Peridynamic and Finite Element Coupling Strategies for the Simulation of Brittle Fracture

A thesis submitted for the degree of Doctor of Philosophy

by

Ilias N. Giannakeas

Department of Civil and Environmental Engineering

College of Engineering Design and Physical Sciences

Brunel University London

Uxbridge, UB8 3PH, United Kingdom

September 2019

Acknowledgements

The completion of this thesis would not have been possible without the guidance and help of my supervisory team. Prof. Hamid Bahai motivated and challenged me throughout the preparation and realization of this research project. His support and consultation helped me to develop not only as a researcher but also as a person. Dr. Theodosios Papathanasiou introduced me to the amazing world of numerical modelling and inspired me to always aim for excellence. Over the past three years he invested his time in teaching me and the content of the present study would be much poorer without his constant mentoring and invaluable contribution. I am also grateful to Dr. Arash S. Fallah who made his support available and helped me in many ways during this project.

I am truly indebted to Brunel University London for sponsoring my PhD studies and for equipping me with the necessary tools to embark on this scientific journey. Being selected as the recipient of the Isambard Kingdom Scholarship is a great honour and it enabled me to pursue my research interests and aspirations.

Of course, I thank my parents, Niko and Stella, for their trust and for making everything possible. Finally, I am grateful to partner, Vasileia, for her love, for always being by my side and for giving me strength every step of the way.

Ilias N. Giannakeas

Brunel University London

Uxbridge, United Kingdom

September 2019

Abstract

The Peridynamic theory is a nonlocal approach, based on an integral formulation that avoids the use of spatial derivatives. This attribute is very desirable in fracture simulations, making Peridynamics a versatile tool for failure analyses. A major disadvantage however is the high computational cost associated with its numerical implementation. The aim of this study is to propose coupling strategies between standard Finite Element methodologies and Peridynamic grids in order to simultaneously exploit the inherent ability of the latter to simulate crack initiation and propagation with the computational efficiency of the former. Initially a coupling technique, where the thermal field is approximated using Finite Elements and the mechanical field using Peridynamics, is applied to a thermal shock problem for refractory ceramics. The results, although very accurate, verify the increased computational cost of Peridynamic simulations. To remedy this, a methodology to couple Peridynamics with finite element solvers for classical continuum theories, restricting the use of particles at the vicinity of the crack tip, is developed. The coupling method introduces fictitious particles inside the finite elements near the coupling interface. This method is selected after comparing three different methodologies with respect to spurious reflections observed during pulse propagation in a 1D bar. A crack tip tracking algorithm and an adaptive expansion/contraction methodology are developed for the dynamic relocation of the Peridynamic patch around the emerging crack fronts. This methodology also employs enrichment of the Finite Elements with Heaviside functions (Extended Finite Element Method) to limit the use of Peridynamics only near the crack tip. The proposed method is used for the simulation of several fracture problems, including the complex case of dynamic crack branching. The results are in close agreement with those obtained using a Peridynamic only approach while featuring significant computational savings.

Table of Contents

List of Figures

List of Tables

List of Abbreviations

ADR	Adaptive Dynamic Relaxation method
BBPD	Bond – Based Peridynamics
CPU	Central Processing Unit
CZM	Cohesive Zone Model
dofs	Degrees of Freedom
FEM	Finite Element Method
GPU	Graphics Processing Unit
LEFM	Linear Elastic Fracture Mechanics
MD	Molecular Dynamics
NLFM	Non-linear Fracture Mechanics
PUM	Partition of Unity Method
RVE	Representative Volume Element
SBPD	State – Based Peridynamics
XFEM	Extended Finite Element Method

1 Introduction

1.1 Motivation

Different failure mechanisms develop when the stresses in a body exceed the material strength, leading to the progressive collapse of the structure. Typical failure mechanisms include the discrete cracks in brittle material, the fracture process zones in concrete and the shear band localization in ductile metals [1]. Fracture and damage analysis are therefore a crucial aspect of structural integrity assessment [2], typically relying heavily on accurate and reliable numerical computations.

Fracture mechanics play a crucial role in the assessment of a structure and the estimation of the remaining life. This is due to the initiation and the propagation of cracks inside the material. Despite the tremendous research over the past decades on the description of the fracture phenomenon, accurate simulation of the process is a major challenge. The complication arises from the vast array of underlying mechanisms that contribute to the process such as: material microstructure, grain boundaries, initial defects, dislocations, loading conditions, environmental conditions, etc. [3].

The introduction of a crack however; complicates the numerical simulation of such phenomena [4] because of **i)** the required mesh refinement around the crack tip, **ii)** the presence of steep gradients in front of the crack and **iii)** the presence of discontinuities in the medium. Predicting crack propagation and nucleation can also prove to be a challenging task using fracture mechanics based on the formulation of classical continuum mechanics [5].

The Peridynamic (PD) theory was introduced by Silling [6] to enable the simulation of dynamic fracture in brittle materials. It assumes non-local interactions between material points/particles and introduces an internal length scale to the simulation [5]. In this setting, crack nucleation and propagation can be naturally simulated through the progressive rupture of interparticle bonds without the introduction of external criteria. Contrary to classical elasticity, its formulation is based on integrals which is very convenient for fracture applications as the introduction of discontinuous displacement fields does not require any special treatment [7].

The implementation of PD however is associated with high computational cost that can be restrictive for large scale simulations. One possibility to reduce the computational burden is to combine the PD theory with classical elasticity formulations using the Finite Element method (FE). The response of the structure is simulated numerically using a coupled PD grid – FE mesh. It is thus attempted to take advantage of the desirable properties of the PD theory

regarding the simulation of fracture and combine it with the robustness and computational efficiency of the FE method.

1.2 Project Overview

1.2.1 *Aims and Objectives*

In this study an algorithm is developed for the numerical simulation of the fracture phenomenon utilizing combined FE meshes with PD grids. The problem domain is divided into two subdomains, Ω^{FE} and Ω^{PD}. The PD model is applied in Ω^{PD} which is limited to areas where nonlinear behaviour and steep strain gradients are expected (e.g. near the vicinity of a crack) while classical elasticity, approximated by the FE method, is applied in Ω^{FE} to describe the response of the remaining structure. Since this approach is intended for crack propagation problems, the algorithm must be able to automatically redefine the location of Ω^{PD} and Ω^{FE}, following the evolution of the crack.

Key ingredients for the successful development and implementation of the proposed algorithm are:

(A) Develop understanding on the application of the PD theory and its limitations and explore various pathways for its efficient combination with the FE method.

(B) An efficient and accurate technique to couple the PD model with the FE method that allows for the independent discretization of each subdomain and minimizes the spurious reflections that are observed in dynamic problems due to model interfaces.

(C) The ability to localize the implementation of the computationally expensive PD theory to specific locations only, such as the vicinity of the crack tip.

(D) Since the method is intended for crack propagation problems, it is desirable to avoid remeshing during the analysis as well as the requirement for *a-priori* knowledge of the final crack path.

(E) An adaptive relocation strategy to automatically redefine the areas where the PD and the FE model is applied during crack propagation.

1.2.2 *Research Novelty*

The novelty of this study can be summarized in the following points:

i) The thermal cracking of alumina specimens is simulated numerically using the FE method to solve the heat transfer problem and subsequently the PD model for its mechanical response. Both cold and hot shock cases are considered, and the results are closely correlated with experimental and numerical observations. The importance

of considering the temperature dependency of the thermal and mechanical material properties is demonstrated through this study.

ii) A comparative study is performed using different coupling methods to evaluate the influence of the method adopted on the spurious reflections observed during pulse propagation. The investigation highlights key parameters that affect the performance of each coupling case. While enforcing a weak coupling with an overlapping length leads to the most accurate energy transmission, coupling approaches that introduce additional "ghost" particles produce comparable accuracy and reduce the computational cost.

iii) The Extended Finite Element Method (XFEM) enrichment is introduced and a coupled XFEM – PD model is developed to allow the localization of Ω^{PD} only near the crack tip. The crack body that now appears in Ω^{FE} is treated with the introduction of Heaviside enrichment functions, limiting the application of the computationally expensive PD model. A convergence study using the J integral value is performed to illustrate the feasibility and effectiveness of the approach. Better convergence is found between the XFEM – PD model and classical elasticity compared to a PD only approach.

iv) A novel adaptive relocation algorithm is developed for the simulation of crack propagation problems. The algorithm does not require any a-priori knowledge of the final crack path. Use of the XFEM enrichment enables the bypass of remeshing and does not impose mesh dependencies on the problem. The results indicate significant improvements in terms of computational efficiency when the XFEM – PD model with the adaptive relocation algorithm is used instead of a PD only model.

1.3 Thesis Structure

This thesis is structured in 7 chapters. In the first chapter, background information on the research topic and an overview on the research objectives are provided.

A review of the relevant literature is included in Chapter 2. State of the art methodologies that are commonly implemented for the numerical simulation of fracture are briefly described. An overview of multiscale methodologies is also included in this chapter with emphasis on the coupling of FE meshes with PD grids.

In Chapter 3, the two numerical methods that are used in this study are defined. First, the formulation of the Bond – Based PD theory is presented with the relevant definitions regarding the appropriate selection of parameters and correction factors. The MATLAB implementation

of the peridynamic theory is validated using two simple benchmarking examples. Then, the formulation of the Classical Elasticity Theory and the approximation of its solution through the FE method are briefly described. The enrichment strategy defined in the Extended Finite Element Method (XFEM) is also presented in this chapter.

The combination of the FE Method and the PD model for uncoupled thermomechanical applications is included in Chapter 4. The thermal cracking problem of ceramics is simulated numerically by employing the FE method to approximate the temperature field and subsequently the PD model is used to simulate the mechanical response of the material. Cold and hot shock conditions are considered and a comparison between the results obtained here with similar numerical and experimental observations from the literature is made. This coupling method, although accurate has been found to have increased computational cost and hence, other types of coupling are pursued in the following chapters.

Chapter 5 is dedicated to the concurrent use of FE meshes and PD grids. In total, three different coupling cases are presented to study the effect of each methodology on the spurious reflections that are generated in dynamic problems. The simple example of waves propagating in a 1D bar is used to compare their accuracy and effectiveness based on time and frequency domain results. The second coupling case is also extended to 2D problems and the importance of establishing an accurate coupling is illustrated through an example where partial energy entrapment occurs.

In Chapter 6, the coupling method that was presented in Chapter 5 is modified to allow the coupling of PD grids with XFEM. This allows for the use of the computationally expensive Peridynamic model only near the vicinity of the crack tip. Furthermore, an adaptive relocation algorithm is also presented that allows the efficient simulation of crack propagation. The performance of the proposed method is evaluated through a series of static and dynamic examples.

Finally, concluding remarks and possible topics for future investigation are discussed in Chapter 7.

2 Literature Review

Almost a century ago, Griffith published his pioneering work on the brittle fracture of glass [8] relating the fracture strength to the flaw size using a simple energy criterion. Subsequent investigations extended Griffith's initial approach to ductile materials and rapidly growing cracks [2]. Without being extensive, some of the major contributions to fracture mechanics are Irwin's introduction of the concept of energy release rate [9], Westergaard solution of sharp cracks [10], Irwin's [11] and Dugdale's [12] works on incorporating a plastic zone correction to account for cases where there is considerable yielding ahead of a crack tip, Wells' [13] introductions of crack-tip-opening displacement parameter, Rise's [14] formulation of the J integral and Paris's investigation on fatigue [15]. These early works have led today to the development of linear elastic fracture mechanics (LEFM) and non-linear fracture mechanics (NLFM) [2]. In the following sections various models that have been proposed in the literature to simulate the fracture phenomenon are discussed.

2.1 Fracture Mechanics using the FE method

Fracture mechanics have been based on the partial differential formulation of classical continuum mechanics, that requires the evaluation of spatial displacement derivatives. Two types of discontinuities can arise in a problem: weak and strong discontinuities [1]. An example of a weak discontinuity is the material heterogeneities that lead to a discontinuous displacement derivative. Strong discontinuities refer to cases where the displacement field itself exhibits a discontinuity. Such is the case of a crack. These cases violate the continuity requirement of the displacement field. In this case, one must consider the crack faces as a boundary to apply the partial differential equation of linear elasticity [5]. Furthermore, stress singularity appears ahead of the crack tip and crack nucleation cannot be simulated within LEFM [3]. The classical theory is enriched with external criteria to simulate crack growth [2] and to predict the direction of crack propagation [16]. In the literature, four major criteria have been suggested: i) the maximum hoop stress or the maximum principal stress, ii) the minimum energy density, iii) the maximum energy release rate and iv) the zero K_{II} criterion [16,17].

Unless the problem geometry and boundary conditions are simple, analytical solution of the underlying partial differential equations is not always possible. Despite the shortcomings of classical continuum theory, it can be applied in a wide spectrum of practical problems using the FE method. In such cases the FE method can be used to find an approximate solution to the problem [18]. Since the approximation is computed using simple algebraic operations, the

method is very suitable for software implementation. It is also noted that the finite difference and the boundary element method [19] can also be employed for the approximation.

The FE method is one of the most widely recognized numerical methods for engineering problems and has already been incorporated in the industry for design purposes due to its robustness and computational efficiency [18]. Many commercial software packages are available in the market that are equipped with powerful mesh generation tools, implicit and explicit solvers, large element libraries, computer aided design interface for the definition of complex geometries and analysis optimization capabilities that allow the user to easily implement the method [20]. In fracture mechanics the FE method has been successfully implemented for the computation of J integral and stress intensity factors and has achieved successes in engineering applications with significant contributions in the estimation of remaining lifetime and structural integrity studies [2].

Since the FE method attempts to approximate the solution of partial differential equations, the shortcomings of classical elasticity with respect to the appearance of cracks in the problem affect the implementation of the method. One of the challenges is the appearance of singular field within the solution domain as discussed earlier. The convergence near the tip can be improved by introducing special collapsed elements or moving the side nodes to the ¼-points [2,21]. Furthermore, the equivalent domain method [22] can be used to improve the approximation of the J contour integral as the use of stress/strain information near the crack tip is avoided. The numerical simulation of crack propagation can also be cumbersome within the FE framework. The evolution of the discontinuity during the simulation imposes topological changes to the problem. The FE mesh must be redefined to capture the new geometry of the discontinuity. The remeshing procedure and the interpolation of the approximation from the old mesh to the new not only increases the computational cost but can also impair the accuracy of the approximation [1]. To avoid this drawback, the Cohesive Zone Model (CZM) and the Extended Finite Element Method (XFEM) are two approaches that have used extensively in the literature to simulate fracture.

The CZM was first introduced by Barenblatt in 1959 [23] for brittle materials and later Dugdale [12] extended the model for ductile materials. Following the pioneering work of Xu and Needleman [24] and Camacho and Ortiz [25], CZM was introduced to computational fracture mechanics. According to this model, the process of fracturing is introduced through the implementation of a traction separation law or a cohesive law. The degrading mechanism is assumed to take place in a zone in front of the crack tip, called the “cohesive zone”, and the fracture is represented through a stress-displacement law across this zone [26]. Stresses are assumed to reduce to zero as the crack opening displacement reaches a critical value.

Through these stress-displacement laws, the cohesive strength (f_t) and the fracture energy (G_c) are introduced into the simulation as material description parameters. Chandra et al [27] showed that the shape of the traction law used in the model is of paramount importance for the accurate description of the macroscopic material behaviour. One for the most significant drawbacks of the method is its mesh dependency. Cohesive zone elements are in essence interface elements inserted between the elements' faces; hence a crack is bound to propagate following paths that depend on inter-element boundaries [28]. In cases where the crack path is not known, remeshing might be required to align element edges with the expected propagation path. During the past years, the CZM has been used widely, especially for situations where the path of the crack is known *a-priori*, either from experimental observations or because of the composition of the structure (e.g. composites) [29]. This mesh dependency can lead to significant inaccuracies of the predicted crack path and inconsistent results depending on the orientation of the element edges [30].

The motivation that drove the development of the XFEM was the need to incorporate arbitrary discontinuities within the simulation. XFEM was first introduced by Belytschko and Black [31] and is based on the partition of unity methodology (PUM). The main idea is to enrich the solution basis of the approximation with special functions that capture the characteristics of the underlying solution. For example, Heaviside functions can be used to capture the displacement jump across a crack, ramp functions for material interfaces and asymptotic solutions for the crack tip singularities [1]. As reported in [32], XFEM are suitable for: i) crack propagation simulations, ii) modelling of grain boundaries, iii) evolution of dislocation and iv) evolution of phase boundaries, as the mesh is decoupled from the geometry and position of the aforementioned entities.

In fracture mechanics, XFEM have been successfully implemented for the determination of stress intensity factors, crack initiation and propagation and fatigue life predictions [33,34]. The general idea of XFEM is based on the PUM to enrich the FE space. Nodes whose element are completely cut by the crack are enriched with jump functions (Heaviside function) while nodes whose element contain the crack tip are enriched with tip enrichment functions [35]. The advent of XFEM allows cracks to propagate independently of the underlying FE mesh and alleviates the need for remeshing at every crack growth step. The crack growth and the direction of propagation are still predicted using criteria based on fracture mechanics parameters. The crack path and the position of the crack tip is monitored through the implementation of a level set function. There are implications however regarding the initiation and the tracking on the crack. As reported in [36] and in [37], crack nucleation can be influenced by the discretization size and requires special treatment. Additionally, tracking the

location of the crack(s) for the definition of the level set functions can be difficult, especially in 3D applications.

Contrary to XFEM and CZM that explicitly model the crack topology prior to performing the calculations [38], the phase-field method is a recently emerged method that represent the discrete cracks through the introduction of a scalar field called the "*phase field*" [39] which represents a smooth transition between the pristine and the damaged material. Phase-fields are based on the variational theory of fracture developed by Francfort and Marigo [40] that aims to address shortcomings of the classical Griffith theory regarding crack nucleation, branching and curved cracks [41]. A key concept of phase fields is the introduction of a length scale parameter that defines the width of the localization band and the diffusion or smearing of the crack. In the limit of vanishing length scale, the original sharp crack problem can be obtained according to the Γ-convergence theorem [42]. An advantage of phase-field models over XFEM and CZM is that the crack location does not need to be tracked and crack growth is modeled through the evolution equation of the phase field however, further investigation is required for the selection and the estimation of the length scale [39].

In light of the difficulties arising in problems where remeshing is required, use of mesh-less (or mesh-free) methods have been studied by many researchers [43,44]. Without being exhaustive, some notable mesh-less models include the element free Galerkin method, the finite point method, the mesh-less local Petrov-Galerkin method, the smooth particle hydrodynamics and the reproducing kernel smooth particle hydrodynamics (see [43,45–50] and the references therein). The main difference between mesh-based methods (such as FEM) and mesh-free methods is that in the case of the former, a predefined mesh with specific relationships between the nodes must be created while in the later nodes are scattered in the domain and on the boundaries of the problem without requiring information on the relationship between the nodes for field variable interpolation [43]. This removes the requirement of a fixed topological connectivity that can be advantageous for problems involving large deformation, fracture and fragmentation [51] and allows the effortless implementation of adaptive refinement schemes [43]. However, there are also disadvantages to the application of mesh-less models. As reported in [43,51] mesh-less methods can suffer from implications regarding the application of boundary conditions, increased simulation time as the shape functions are created during the simulation, stability and accuracy constraints. Nevertheless, mesh-less methods are powerful tools and significant research effort is devoted towards their development.

2.2 Alternative Models to Classical Elasticity

2.2.1 *Generalized Continuum Mechanics*

Damage mechanisms like cracking that take place in small scales (nanometer and femtosecond scales), have an extensive impact and are directly correlated with the observed material's macroscopic behaviour [52]. Hence the need to incorporate the microstructural characteristics is crucial for the accurate simulation and understanding of the fracture phenomenon. Such characteristics however are not captured by classical elasticity. For this reason, scientists have explored different formulations that allow them to take into account these effects.

Enhancing classical elasticity and continuum mechanics to account for the material microstructure has been broadly investigated over the past decades and many theories have been developed [53]. As proposed in [54], these theories can be termed *generalised continuum mechanics*. The Cosserat brothers [55] were the first to suggest such an enhancement. In their mathematical formulation, the total number of degrees of freedom (dofs) was increased by introducing additional micro-rotations at each node and they were the first to introduce couple-stresses [53,56]. The introduction of micro-rotations is well-suited for materials with granular microstructure to describe internal moments [53]. Later investigations extended the Cosserat theory [53] and some landmark publications include the works of Toupin [57] and Mindlin and Tiersten [58]. In these theories, higher order rotation gradients are included in the deformation [59]. Mindlin also introduced the first gradient and the second gradient elasticity theory in [60] and [61]. In this case, the strain energy density depends also on higher order gradients of the deformation field. Notable contributions include the works of Lam et. al. [59] and Fleck and Hutchinson [62]. Following the Cosserat theory, Eringen introduced microrotations within the formulation and his work led to the developments of three theories that are today called "*Micropolar*", "*Microstretch*" and "*Micromorphic*" [63,64]. Among them, the Micromorphic theory is the most general [64].

An interesting advantage of higher order theories is the ability to include microstructural characteristics in the simulations using an internal length scale (usually denoted by l) that appears within the formulation. As reported in [65] gradient elasticity has been successfully implemented to avoid crack tip singularities, simulate wave dispersion and produce size-dependent mechanical behaviour. They depart from the mono-scale formulations of classical elasticity and allow for a multiscale treatment of the medium [66]. However, these advantages come with an increased cost regarding the complexity of methodologies. Additional elastic coefficients are required for the material to be defined that has discouraged engineers and experimentalists to implement them in practical applications [56,66]. Due to the higher order

operator of strain gradient elasticity, the finite element implementation to three-dimensional problems is not straightforward. It is noted that the gradient model suggested by Aifantis introduces only a single additional elasticity coefficient while eliminating the strain singularities ahead of the crack tip [66,67].

2.2.2 *Molecular Dynamics and Atomistic Methods*

When a system is attempted to be described very accurately, finer descriptions of the response must be incorporated (e.g. atomistic, quantum) [68]. Molecular dynamic (MD) simulations have been used over the years to investigate the fracture phenomenon in an atomic lattice scale. One of the fundamental differences between classical continuum mechanics and MD is the inability of the former to incorporate long-range forces. In continuum mechanics, the state of a material point is influenced by the material points that are located in its immediate vicinity. MD on the other hand, allows for long-range interactions between atoms. Fracture (initiation and propagation) can be modelled using the interatomic forces [69] and such simulations could potentially help researchers gain insights and develop a more fundamental understanding of failure [70]. Many observations have been simulated numerically using such models (e.g. crack branching that takes place at elevated crack velocities) and have been validated experimentally [71]. As reported by Askes and Aifantis in [66], many studies have also implemented MD models to fit the parameters of gradient elasticity for various materials. Still, for fracture applications, there are reports in the literature where MD simulations fail to capture the experimental observations [30].

Despite the booming technological advancements in computer science over the past decades and the increase in the available computational power, it is still unfeasible to perform MD simulations for real life structures. In [72], a model with over a billion of atoms was used to simulate the ductile fracture in a face-centred cubic solid under mode I loading. Even though the sheer computational volume of this task is phenomenal, the side of the cube modelled was 0.3 microns and the total duration of the simulation was a few nanoseconds. The small time step required for the temporal resolution of the problem limit MD simulations to short time durations. In fracture simulations high strain rates are typically applied due to this limitation however, the interpretation and the relation of these results to phenomena that take place at lower loading rates is not clear [7]. In many cases, the wave reflections from the geometrical boundaries of the structure need to be incorporated into the simulation to make accurate dynamic brittle fracture predictions [30]. Given the spatial restrictions of MD simulations, such models for larger structures are not feasible yet. These restrictions have led many researchers to explore different pathways and develop various multiscale methodologies, that are discussed in the following sections. Without being exhaustive, studies on the coupling of

atomistic and MD models to continua can be found in [52,70,73–76] and the references therein.

2.2.3 *The Non-local Bond-Based Peridynamic Theory*

The restrictions on the implementation of MD simulations for real engineering applications are evident. According to classical elasticity, material points of infinitesimal volume interact only with other material points that are in direct contact with and fails to account for the long-range forces that have been observed by scientists in experiments [7]. The lack of an internal length scale parameter leads to size independent results and breaks down in smaller scales [56].

To incorporate the long-range forces in continua, Eringen [77] introduced the non-local theory of elasticity. Recent studies illustrate that the lack of nonlocality is one of the reasons classical elasticity breaks down at nanoscales [78]. Non-local elasticity builds a connection between molecular dynamics and continuum mechanics. Non-locality is introduced as integral-type material models whose constitutive model at a point is affected by all the material points that lie within a finite distance from it [79]. Such theories and hypotheses allow the incorporation of the inter-atomic forces as well as an internal length scale [80]. Similar to gradient theories, non-local theories have also the advantage of predicting finite stresses ahead of the crack tip however, many of the early non-local theories developed retain the displacement derivatives, leading to complications when the displacement field is discontinuous [7].

In this category belongs the Peridynamic (PD) theory. In his seminal work [6], Silling presents a reformulation of the elasticity theory to study problems that contain a discontinuity. The PD theory incorporates nonlocal interactions within its formulation and assumes that each material point, or PD particle, interacts with other particles that are within a certain distance from it. These particles are the called the "*family*" or "*neighbourhood*" of a particle and define a spherical region, commonly denoted with H_x. The radius of the spherical region, δ, is called the PD horizon [5,7]. The horizon introduces an internal length scale within the description of the material behaviour that prescribes the extent of these interactions [81]. In [5], the PD theory is termed as a "*strongly*" non-local method while the higher order theories are termed "*weakly*" non-local. This terminology is used due to the explicit incorporation of the long-range forces between the PD particles and make a separation from the theories where the non-locality can be inferred from the appearance of higher order derivatives within the formulation.

The selection and interpretation of the PD horizon has been discussed in many contributions available in the literature (see e.g. [5–7,81]). Specifically, a discussion on the meaning and the selection of the PD horizon has been presented by Bobaru and Hu in [81] where the authors also make suggestions on the appropriate selection of the horizon value.

In some applications, the physics of the problem will dictate the interaction properties that the horizon should capture. In the microscale for instance, the interaction potential drops with respect to the distance between the atoms. In such cases, The concept of nonlocality has the physical meaning of interatomic forces and the PD horizon can be used to describe the extent of the interactions [81]. Furthermore, the horizon can also impose a threshold value to the number of interactions that are considered as including all possible interactions can be a computational burden. The PD horizon introduces a cut-off length to specify the extend over which these interactions are included. Nonlocal interactions also arise when homogenization is performed in heterogeneous materials such as composites. As noted in [5], the distance of these interactions depend on the microstructural features of the material as well as on the constituent material properties. In cases where the long-range interactions are determined by the problem's physics such as the examples mentioned earlier, the horizon size should take a specific value.

In practical engineering applications, where such length scales are not resolved, the horizon and the nonlocal interaction do not have a physical interpretation [5]. An approach recommended by Silling in [6] is to select the PD horizon as such that the PD dispersion curve matches the material's dispersion characteristics. As mentioned in [81], this idea of matching the horizon value is further pursued in [82]. As a general recommendation for the discretization and approximation of macroscale fracture problems, it is suggested in [5] to use horizon values at least three times the discretization length (i.e. $\delta \geq 3\Delta x$) as lower values can lead to grid dependencies on the crack growth orientation. In cases where exact solutions are available or when the problem can be approached with local models (e.g. linear elasticity), the PD horizon can be used as a basis for convergence studies [81]. It should be selected large enough to ensure accuracy during numerical integration but sufficiently small to reduce the computational effort. In [83], it is mentioned for example that the horizon of the PD model can be tailored so the nonlocal J integral value matches exactly the one obtained from a linear elastic model. However, as noted in [84], large horizon values may induce excessive wave dispersion and increase the computational cost without significant accuracy gains. Similar observations have also been reported by Zimmerman [85] and Ha and Bobaru [86] after carrying out convergence studies.

It is also noted that the horizon value does not necessarily need to be constant over the whole problem domain. Approaches that implement variable horizon lengths can be found in [87–91] where the size of the peridynamic horizon is different at specific parts of the structure.

Contrary to classical elasticity, the PD equation of motion is formulated using integrals that avoids the appearance of spatial derivatives. Thus, no changes or special treatment is

required when discontinuous displacement fields are present in the problem domain. Such is the case when problems with strong discontinuities are addressed. An additional benefit within the PD formulation is that fracture can be naturally incorporated into the simulations by modifying the particle interactions. No external phenomenological criteria are required for the initiation of crack nucleation or for the estimation of the propagation direction and length [92]. These characteristics make the PD theory a promising tool for fracture mechanics applications as it provides a unified framework that can readily accommodate discontinuous displacement fields and can simulate fracture without the requirement for additional criteria or *a-priori* knowledge of the propagation path [93].

These properties have attracted the interest of the scientific community and the PD theory has been applied to a variety of fracture problems. A first implementation was carried out by Silling [94] where a plate containing two parallel notches is hit by an impactor. The numerical simulations predicted crack paths that are in close agreement with observations from experimental studies. Impact damage was simulated in the work of Silling and Askari [84]. A simulation of a sphere impacting on a brittle target was carried out containing $185{,}000$ particles where the formation of conical Hertzian cracks was observed on the target. In [95] and [88], a linearized version of the PD theory was introduced and a comparison was made with elasticity using a 1-D bar case study. Simulations of crack propagation and crack branching in brittle materials using PD have been found to be in close agreement compared other numerical methods (e.g. CZM and XFEM) and experimental results [28]. The branching phenomenon was captured without the need to introduce criteria to trigger the splitting of the crack. In the works of Ha and Bobaru [96] and Bobaru and Zhang [30], the PD theory is implemented to study the dynamic crack propagation in brittle materials and identify key parameters that control the appearance of crack branching. The ability of PD to incorporate microstructural properties and material heterogeneities has been also exploited by changing the bond interaction properties between matrix and fibre [97] or different crystals in the body [98]. As described in [95], the PD theory includes an internal length scale l that in the limiting case of $l \to 0$ one retrieves the classical theory of elasticity. This enables the PD theory to be used for multiscale material modelling studies. In [99], it was implemented for the study of polycrystalline ceramics, fracture in anisotropic composite materials and fibre networks. A similar study on granular fracture for polycrystalline materials is presented in [98] where crack initiation and propagation in Iron and AISI 4340 steel crystals is considered, taking into account the micro structure of the material. Furthermore, in [100], fracture of AISI 4340 steel was simulated under the combination of tensile stress and stress corrosion cracking. To reduce the high computational cost of the PD theory when modelling simple structural elements, PD beam and plate elements were developed in [101–104] that are comparable to the

Timoshenko beam and Mindlin plate. An interesting analogy was used by Silling in [105] where the interparticle interactions are described through a simple truss element describing a mass-spring idealization. A truss network was constructed to capture all particle interactions. The implementation of this idealization was realized within the commercial finite element package Abaqus.

The PD formulation presented in [6] is known as "*Bond – Based Peridynamic theory*" (BBPD). The name stems from the pairwise interactions between the pairs of particles. These interaction forces depend only on the relative position of the particles and are assumed equal, opposite and collinear. This assumption imposes a restriction on the effective Poisson ratio of the material. In subsequent work [106], Silling et. al. presented a generalization of the methodology by introducing the concept of a "*state*" giving the name to the method "*State – Based Peridynamic theory*" (SBPD). In this case, particle interactions depend on the collective deformation state of all particles that lie within a finite distance from it. Using State – Based PD the Poisson's ratio restriction is lifted and Bond – Based PD can be extracted as a special case. An alternative that can partially circumvent the restriction on the Poisson's ratio has been presented by Gerstle et al. [107]. Pairwise PD moments where introduced by adding rotational dofs into the model, similar to micropolar elasticity. Due to this similarity, the method is termed "*micropolar peridynamic model*". In the present study only the Bond – Based PD theory is used and for short is referred to as PD. Although the Bond-Based PD model impose the restriction on the value of the Poisson's ratio, it is selected to first evaluate the effectiveness and feasibility of employing coupling and relocation schemes for the simulation of the fracture process. The formulation of the PD model is presented in detail in chapter 3 of this manuscript.

The high computational cost associated with the implementation of the PD theory is one of its biggest disadvantages and can be restrictive for large scale applications [108]. Various methodologies have been devised in the literature to improve the computational efficiency of the PD models. One approach is to adopt a refinement procedure. In [88], local refinement was implemented and the convergence of the PD theory to elasticity was studied in a 1D bar. The local refinement procedure is extended in [87] to 2D static applications where the quadtree partitioning strategy is used to refine the spatial resolution in specific areas and emphasis is given to the change of the horizon value due to discretization change. This approach is adopted by Dipasquale et. al. [91] to study dynamic crack propagation in 2D problems. In this contribution, a trigger is also introduced to adaptively refine the discretization during the evolution of damage. Thus, the number of particles used away from areas that increased accuracy is required is reduced, leading to a more computationally efficient model. In order to

reduce the spurious reflections that appear due to the horizon change when local refinement is used, Ren et. al. [109] introduced the concept of dual horizon.

A different approach to reduce the computational burden is to adopt multiscale numerical models that couple the PD theory with classical elasticity. Many methodologies that were originally developed for the coupling of MD with classical elasticity can be extended or modified to accommodate such applications.

2.3 Multiscale Modelling Approaches

The need of developing approaches for multiscale problems emerged in view of the increasing demand for better understanding and controlling the properties of a product. Implementation of multiscale modelling is in the spotlight of scientific and industrial interest to increase the fidelity of numerical simulations. Multiscale modelling however, is not broadly available and it is restricted to academic cases due to the complexity of its nature and the unavailability of a unified tool to enable researchers implement novel ideas [70]. The notion of combining different models is not new and has been studied by many researchers. Different approaches and combinations of models have been proposed in the literature, aiming to bridge different temporal and spatial scales [52]. There are various reported multiscale methods in the literature. Selection of the appropriate method depends on the case considered (structural, system, material etc.) and on the fine and coarse scale descriptions [52,70]. There are two major multiscale methods: the *hierarchical* and the *concurrent* method.

In the hierarchical method, a small domain/sample of the material that represents its microstructure is computed for certain force-displacement inputs and the response of the domain is stored in the form of a constitutive equation or a database. The discretization employed for this domain is generally much finer compared to the discretization of the problem domain. Then, the original-coarse domain is solved, utilizing the information gathered during the first solution [110]. The domain that represents the microstructure of the materials must be selected in such a way that can be considered representative of the average response of the material. This domain is called *unit cell* for structured microstructures and *representative volume element* for random microstructures (RVE) [111].

In this sense, there is a pre-processing step, prior to the analysis of the structure. The fine domain is solved first and there is a one-way information passing between the two domains without any interaction taking place from the coarser to the finer domain. Although this approach is computationally efficient for simple cases, there are many complexities when modelling problems that exhibit high nonlinearities (e.g. strain localization) or displacement

jumps (e.g. cracks) [112]. Since the information regarding the behaviour of the fine-scale domain is gathered as a pre-processing step, the extracted response is usually simplified and usually refers to linear elastic cases.

Following the concurrent method, the finer and the coarser domains are coupled together and there is no pre-processing step in the simulation. Equilibrium and displacement compatibility are enforced throughout the analysis resulting and the two domains are solved simultaneously. The fine scale domain is inserted in the areas where detailed description of the material response is required [110].

Finally, there are several approaches in the literature [52] that cannot be classified specifically in one of the two previous categories as they exhibit properties of both. These methods are referred to as *semiconcurrent* and *hybrid-semiconcurrent* methods. The difference between the *semiconcurrent* and the hierarchical method is that the fine scale model is not solved before the coarse model, but it is solved at each solution step of the analysis providing *on the fly* the coarse-grained displacement gradient for the prescribed boundary conditions. Still it is different from the concurrent method as a weak coupling is enforced on the boundary [110]. In the hybrid-semiconcurrent method, the fine scale model is solved for a group of expected deformations as in the hierarchical method, however; the fine scale model is kept on standby in case the required response of the microstructure was not mapped during the pre-processing step of the simulation.

This study is focused on studying the feasibility and the potential computational improvements when the PD theory is combined with classical elasticity. The coupling is performed using the discretized equations of motion for each model. For classical elasticity, the discretization is carried out using FEM. This choice is made as it is envisaged that such coupling approaches can be implemented within the environment of commercially available FE software packages to simulate fracture. Such a notion is presented by Talebi et. al. [70] where an open-source framework is developed that interfaces with available libraries (ABAQUS, LAMMPS, LS-DYNA and GMSH). This framework enables the realization of continuum-continuum and atomistic-continuum models for the multiscale simulation of fracture. Nevertheless, other coupling combinations involving Peridynamics are also possible. For instance, a coupling between peridynamics and a mesh-free method is presented in [113]. Peridynamics is combined with the Meshless Local Exponential Basis Functions method, developed in [44], by introducing a transition region between the local and the non-local discretized zones and it was demonstrated that the coupling is patch test consistent and free of ghost forces. Another alternative could potentially be the coupling of Peridynamics with phase-fields models. One of the advantages of selecting phase-fields is that it has already been demonstrated that phase-

fields can be implemented using available FE packages (see e.g. the studies in references [39,41]).

2.4 Concurrent Coupling of FE meshes with PD Grids.

In fracture applications, concurrent coupling methodologies are generally preferred as the representative property of the RVE is violated. The advantages of coupling a computational efficient local theory with the capabilities that are offered in non-local descriptions (e.g. molecular dynamics) have already been recognized [114] within multiscale applications. One of the challenges during concurrent coupling arises when dynamic problems are considered. Due to model mismatch, unrealistic reflections occur when waves cross the different domains. It is noted however that such reflections also appear in cases where local refinement methods are implemented [109]

Substantial effort has been devoted into formulating a methodology that is able to effectively communicate the information between the various descriptions. Various methodologies have been proposed to achieve coupling between continuum with atomistic/molecular descriptions. A recent review can be found in [115]. The coupling methods can be divided into two broad classes: **a)** in the first class, coupling is achieved at a discrete interface [116–118], **b)** in the second class, coupling takes place gradually over a finite zone, often called *overlapping zone* [52,70,119–121]. It is noted that one of the advantages of implementing overlapping zones is that they generally reduce the spurious reflections and allow the two models to have different discretization [52,75,122].

The concurrent coupling of the FE method with PD grids has already been studied by many researchers and various methodologies have been presented. It is preferred that the FE method is used in areas where failure is not expected to happen while the PD model is used to model the behaviour near a failure. Using this approach, it is attempted to combine the computational efficiency of FEs with the inherent ability of the PD theory to accommodate discontinuous fields and microstructural characteristics [98].

Liu and Hong [121] have formulated a methodology of coupling FEs with PD grids that introduces interface elements between the two domains. Two coupling approaches are reported in their work called the *CT* and *VL* coupling schemes. The difference between the two schemes lies in the different distribution of the PD forces within the interface elements. Although the model was applied to static and dynamic problems, in the case of dynamic applications the spurious reflections generated in each case were not studied.

In the work of Seleson et al. [123], the PD and the local classical elastic model are blended together using a force-based coupling scheme. The coupling is derived by a single framework by using a blending function instead of having two models and devise a "*gluing*" process to connect them. Remarkably, this approach eliminates the appearance of ghost forces on the interface. This coupling is also generalized to allow coupling between the PD theory and higher order gradient models.

Kilic and Madenci [124] propose the use of an overlapping region over which both the PD and the FE equations are used. The displacements of the PD particles in the overlapping region are defined through interpolation of the FE nodal values using the shape functions. Although the method is applied to 3D examples, only quasistatic problems are considered. The selection of the overlapping length and its influence on the accuracy of the coupling is not discussed.

In [125], Ha and Lubineau use the Arlequin method presented in [126] to couple the FE method with the non-local elasticity model developed by DiPaola et. al. [127]. This model contains both local and nonlocal interactions within its formulation and the authors point out that the Bond-Based PD model is a suitable alternative. In fact, in subsequent publications [108,128], the same authors introduce the so called "*morphing*" strategy, a modification of the Arlequin method, to couple PD with FEs. In the morphing strategy both local and non-local interactions appear in the formulation of the model and their contributions are controlled by introducing a special weighting function that ensures energy equilibrium. Thus, there are areas of the material that are described though interactions that are purely local, non-local or a combination of both. The effect of the weighting function choice and the length of transitioning area is also investigated [128]. It is noteworthy to mention that in [108], an adaptive strategy is proposed to automatically control the areas where the local and the non-local descriptions are used. A critical damage index based on the loss of material stability is introduced that triggers the switch from local to non-local near damaged areas. The method was successfully implemented for the simulation of crack propagation in three static problems.

A different method to couple FE meshes with PD grids is developed in [118] where the two models are applied to different areas of the problem. Using the linearized formulation of the PD theory, the coupled stiffness matrix is derived by considering force equilibrium at the locations where PD particles and FE nodes coincide. The same approach is also used in [129] to combine the PD theory with the meshless finite point method. In [118] and [129], the coupling was implemented for static problems. In [117], Zaccariotto et. al. employ the same FE - PD coupling to study dynamic and fracture problems. The results of the coupled model are compared to those obtained from PD only solutions. The advantage of their methodology lies in its simplicity as it does not require incorporation of blending functions for the two models

and can be easily extended to commercial software. The appearance of spurious reflections was evaluated by transmitting pulses in 1D and 2D scenarios and measuring the amplitude of the reflected wave for different horizon values. Similar to [108], a trigger is also introduced that is based on the relative displacement between two FE nodes. The trigger signifies the switch from FE nodes to PD particles when the relative elongation exceeds a predefined threshold value. This is important in crack propagation problems as the efficiency of the method is significantly improved. However, since PD particles and FE nodes are required to coincide for the coupling to be enforced, the FE discretization must match that of the PD grid, at least near the coupling location. This requirement can be restrictive as the two meshes are not independent. In a subsequent publication, Zaccariotto et. al. [130], modify the coupling to remove this requirement. Additional, fictitious, PD particles and FE nodes are introduced into the FE and PD domain, respectively. The displacement values of the fictitious particles are computed by interpolating the nodal displacements using the FE shape functions. On the other hand, the displacement values of the fictitious nodes are computed through linear interpolation using the displacement values at the particle locations.

In a very recent publication, Sun and Fish [131] presented a coupling method where the PD model is superimposed onto the classical elasticity model in the area where a crack is present. The coupling is enforced over a region where both models co-exist and a special interface scheme is proposed that introduces fictitious FE nodes and PD particles. The novelty of the superposition-based coupling method is that it avoids the use of blending functions and its performance is evaluated using 1D and 2D static examples. The method leads to very small relative error at the coupling interface and as the authors note, its implementation to wave propagation problems will be studied in future publications.

The plethora of scientific contributions indicate the interest in the development of an efficient and accurate FE – PD coupling procedure. The aim is to reduce the computational cost of the PD model and allow its implementation for the simulation of failure at a structure level. From the contributions mentioned earlier our interest focuses in the methods presented in [108] and [117]. In both studies a criterion was used to signify the transition from a local to a non-local model. Such an approach allows the PD domain to be inserted in targeted areas where large strains develop, and failure is expected to manifest (e.g. possible crack nucleation sites) or to increase the area of the PD domain during crack propagation. The overall computational effort is decreased as the use of the PD model is limited. Whilst both contributions describe a transition from FE to PD, the inverse procedure is yet to be realized. During a fracture simulation, as cracks propagate or new crack nucleate, the PD domain will increase monotonically. Use of the PD model away from the crack tip is however not required and

different pathways to treat the discontinuous displacement field at the crack body can be explored.

3 Local and Non-Local Models for Solid and Fracture Mechanics

3.1 Formulation of Bond – Based Peridynamics

3.1.1 *Definitions*

The PD theory assumes that a material body consists of points, or particles, of infinitesimal volume. The PD equation of motion can be written as [84]:

$$\rho\ddot{\boldsymbol{d}}(\boldsymbol{x},t) = \int_{H_x} \boldsymbol{f}(\boldsymbol{d}(\boldsymbol{x}',t) - \boldsymbol{d}(\boldsymbol{x},t), \boldsymbol{x}' - \boldsymbol{x})\, dV_{x'} + \boldsymbol{b}(\boldsymbol{x},t), \tag{3.1}$$

where, H_x is the "*neighbourhood*" of $\boldsymbol{x}$ within which it interacts with other particles and is the domain of integration, $\boldsymbol{x}'$ are all other particles within the horizon of $\boldsymbol{x}$, $\boldsymbol{f}$ is the pairwise force function and describes the force per unit volume squared $\boldsymbol{x}'$ exerts on $\boldsymbol{x}$, ρ is the mass density of the material, t is the time, $\boldsymbol{d}$ is the displacement vector and $\boldsymbol{b}$ is the external body force field. Unless otherwise stated, bold notation indicates vectors. Figure 3.1 illustrates a PD body before and after deformation, indicating the neighbourhood of interaction of two particles. It is noted here that Eq. (3.1) is defined at the deference configuration. As such, the neighbourhood of $\boldsymbol{x}$ does not change as a result of deformation.

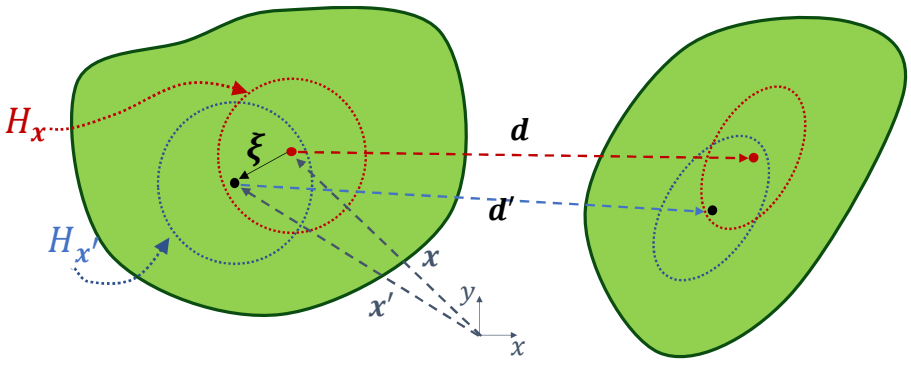

Figure 3.1: Deformation of a PD domain.

Denoting with $\boldsymbol{\xi}$ and $\boldsymbol{\eta}$ the relative position and relative displacement vectors, defined as:

$$\boldsymbol{\xi} = \boldsymbol{x}' - \boldsymbol{x}, \tag{3.2a}$$

$$\boldsymbol{\eta} = \boldsymbol{d}(\boldsymbol{x}',t) - \boldsymbol{d}(\boldsymbol{x},t), \tag{3.2b}$$

then, the PD equation of motion can be written more concisely as:

$$\rho\ddot{\boldsymbol{d}}(\boldsymbol{x},t)=\int_{H_x}\boldsymbol{f}(\boldsymbol{\eta},\boldsymbol{\xi})\,dV_{x'}+\boldsymbol{b}(\boldsymbol{x},t). \tag{3.3}$$

By simple inspection of the expression described in Eq. (3.3), it is evident that spatial derivatives are avoided in the PD equation of motion. The integral formulation of the PD theory makes it powerful tool for failure analyses [5].

The pairwise force function $\boldsymbol{f}$ prescribe the interparticle interactions and holds all the constitute information and properties of the material [84]. The bond forces have the direction of $\boldsymbol{\eta}+\boldsymbol{\xi}$ and must satisfy linear and angular admissibility conditions, as described in detail by Silling in [6]. Considering Newton's third law, leads to the linear admissibility condition expressed as:

$$\boldsymbol{f}(-\boldsymbol{\eta},-\boldsymbol{\xi})=-\boldsymbol{f}(\boldsymbol{\eta},\boldsymbol{\xi}),\quad\forall\boldsymbol{\eta},\boldsymbol{\xi}. \tag{3.4}$$

The linear admissibility condition requires that the bond forces between a pair of particles are equal and opposite. Conservation of the angular momentum leads to the angular admissibility condition, expressed as:

$$(\boldsymbol{\eta}+\boldsymbol{\xi})\times\boldsymbol{f}(\boldsymbol{\eta},\boldsymbol{\xi})=\boldsymbol{0}\,,\quad\forall\boldsymbol{\eta},\boldsymbol{\xi}. \tag{3.5}$$

Effectively, Eq. (3.5) requires that the bond forces are collinear between a pair of particles. Any function that satisfies the linear and angular admissibility conditions, is a valid candidate as a response function and there is no restriction that requires the use of linear functions [5,29]. However, these pairwise interaction assumptions lead to the restriction of Bond – Based PD theory on the value of the Poisson's ratio [7].

The PD horizon is of pivotal importance for the PD theory as it describes the finite distance over which a particle interacts with other particles directly. The collection of all material particles that belong in its horizon define H_x, which is the domain of integration in the equation of motion of a particle. Although the shape of H_x can be arbitrary, it is commonly selected as a disc or a sphere with radius δ, for 2D and 3D applications respectively. Since bond forces vanish for distances greater than δ, then:

$$|\boldsymbol{\xi}|>\delta\Rightarrow\boldsymbol{f}(\boldsymbol{\eta},\boldsymbol{\xi})=\boldsymbol{0},\quad\forall\boldsymbol{\eta}. \tag{3.6}$$

If $\boldsymbol{f}$ is derivable from a scalar *micropotential* w, then the material is said to be *microelastic* and the pairwise force function is written as [132]:

$$\boldsymbol{f}(\boldsymbol{\eta},\boldsymbol{\xi}) = \frac{\partial w(\boldsymbol{\eta},\boldsymbol{\xi})}{\partial \boldsymbol{\eta}}, \forall \boldsymbol{\eta},\boldsymbol{\xi}. \tag{3.7}$$

The micropotential w, represents the bond energy contained in a single bond with dimensions of energy per unit volume squared. The local strain energy density in an area of a body (e.g. within the horizon of a material particle) can be computed by considering the energy stored in all bonds that are connected to a particle. It is expressed as:

$$W = \frac{1}{2}\int_{H_x} w(\boldsymbol{\eta},\boldsymbol{\xi}) dV_x, \tag{3.8}$$

where, the factor $^1/_2$ appears in Eq. (3.8) because each endpoint of the bond contains only half the energy.

Following the definition in [30], a material is called *linear microelastic* when the micropotential w is expressed as:

$$w(\boldsymbol{\eta},\boldsymbol{\xi}) = \frac{c(\boldsymbol{\xi})s^2\|\boldsymbol{\xi}\|}{2}, \tag{3.9}$$

where, $c(\boldsymbol{\xi})$ is the micromodulus function, $\|\cdot\|$ denotes the Euclidean norm and s is the relative bond elongation computed as:

$$s = \frac{\|\boldsymbol{\eta}+\boldsymbol{\xi}\| - \|\boldsymbol{\xi}\|}{\|\boldsymbol{\xi}\|}. \tag{3.10}$$

The micromodulus function contains the information of the material's properties and defines the effective stiffness of the bond that connects two particles. The value of $c(\boldsymbol{\xi})$ can be determined by equating the PD strain energy density to the strain energy density from classical elasticity, under the assumption of the same homogeneous deformation. Micromodulus functions of various shapes have been proposed in the literature. In, [88], the shape of $c(\boldsymbol{\xi})$ is defined as a constant, piecewise linear (conical) and inverted triangular function of $\boldsymbol{\xi}$. In [124], an exponential decay function is proposed to better capture the notion of decreasing forces as the interparticle distance increases. Commonly, the constant and the conical shapes are employed. If $c(\boldsymbol{\xi})$ is assumed constant, its value can be computed as:

$$c(\boldsymbol{\xi}) = c = \begin{cases} \dfrac{48E}{5\pi t\delta^3} & |\boldsymbol{\xi}| \le \delta \text{ and plane strain} \\ \dfrac{9E}{\pi t\delta^3} & |\boldsymbol{\xi}| \le \delta \text{ and plane stress,} \\ \dfrac{2E}{A\delta^2} & |\boldsymbol{\xi}| \le \delta \text{ and 1D} \end{cases} \tag{3.11}$$

where, t *is the thickness and* A is the cross-sectional area.

If $c(\boldsymbol{\xi})$ is assumed to have a conical variation its value is computed as:

$$c(\boldsymbol{\xi}) = \begin{cases} \left(1 - \dfrac{\boldsymbol{\xi}}{\delta}\right)\dfrac{24E}{\pi\delta^3(1-\nu)} & |\boldsymbol{\xi}| \leq \delta \text{ and plane stress} \\ \left(1 - \dfrac{\boldsymbol{\xi}}{\delta}\right)\dfrac{6E}{\delta^2 A} & |\boldsymbol{\xi}| \leq \delta \text{ and 1D} \end{cases}. \tag{3.12}$$

In all cases, $c(\boldsymbol{\xi}) = 0$ if $|\boldsymbol{\xi}| > \delta$. Similar expressions can be obtained for 3D cases. The present study is limited to 1D and 2D applications but the interested reader is referred to [5,7,84,88] and the references therein for more information. It is noted that when $c(\boldsymbol{\xi})$ is conical, better convergence to classical elasticity has been reported in the literature [88,96]. Here either the expression from Eq. (3.11) or Eq. (3.12) is used depending on the example and the application. In each case, the selection is specified explicitly.

Finally, using these definitions and following [30], the pairwise force function for a microelastic material can be written as:

$$\boldsymbol{f}(\boldsymbol{\eta}, \boldsymbol{\xi}) = f(\boldsymbol{\eta}, \boldsymbol{\xi})\frac{\boldsymbol{\eta} + \boldsymbol{\xi}}{\|\boldsymbol{\eta} + \boldsymbol{\xi}\|} = c(\boldsymbol{\xi})s\frac{\boldsymbol{\eta} + \boldsymbol{\xi}}{\|\boldsymbol{\eta} + \boldsymbol{\xi}\|}, \tag{3.13}$$

where, $f(\boldsymbol{\eta}, \boldsymbol{\xi}) = c(\boldsymbol{\xi})s$ is the scalar-valued pairwise force function.

Although the bond constant depends only on the relative position of two particles and describes a linear force-stretch $(f - s)$ interaction relationship, the PD equation of motion leads to a nonlinear system of equations. Alternatively, a linearized formulation was also presented in [6] and has been used extensively in the literature (see e.g. [88,95,133]).

Linearization can be carried out under the assumption of small deformation and the linearized pairwise response function $\boldsymbol{f}^{lin}$ is written as [6,88]:

$$\boldsymbol{f}^{lin}(\boldsymbol{\eta}, \boldsymbol{\xi}) = c(\boldsymbol{\xi})\frac{\boldsymbol{\eta}}{\|\boldsymbol{\xi}\|}. \tag{3.14}$$

Although the validity of the small deformation assumption is ambiguous for fracture simulations as large bond deformations will appear at the vicinity of the crack tip, the linearized PD formulation is compatible with direct solvers. Furthermore, when the linearized equations are used, it is easier to obtain theoretical results such as the properties of waves [5].

3.1.2 *Damage in Peridynamics*

The initial motivation for the development of the PD theory was the investigation of dynamic crack propagation and fragmentation [84]. Material damage is defined on the bond level

between two particles and the fracture process is simulated through the breakage of bond that exceed a predefined threshold value, termed the *critical bond stretch* s_0. Broken bonds are removed from subsequent computations, changing the effective stiffness of the structure, leading to a nonlinear material response. During fracture phenomena this procedure is irreversible and broken bonds remain broken for the remaining computations. In certain applications reversible bond breaking can be used, making the bonds able to re-attach, allowing for the simulation of Van der Waals interactions [132]. In all examples considered here, bond breaking is an irreversible process.

Bond breaking is achieved by introducing a Boolean $\mu(t, \boldsymbol{\eta}, \boldsymbol{\xi})$ in the pairwise response function [105]. When damage is allowed in the simulation, Eq. (3.13) is re-written as:

$$\boldsymbol{f}(\boldsymbol{\eta}, \boldsymbol{\xi}) = c(\boldsymbol{\xi}) s \frac{\boldsymbol{\eta} + \boldsymbol{\xi}}{\|\boldsymbol{\eta} + \boldsymbol{\xi}\|} \mu(t, \boldsymbol{\eta}, \boldsymbol{\xi}). \tag{3.15}$$

Function $\mu(t, \boldsymbol{\eta}, \boldsymbol{\xi})$ is a time-dependent scalar-valued function that monitors which bond have broken and which are intact. Its value can be defined as [105]:

$$\mu(t, \boldsymbol{\eta}, \boldsymbol{\xi}) = \begin{cases} 1, & \text{if } s(t') \leq s_0, \forall 0 \leq t' \leq t \\ 0, & \text{otherwise} \end{cases}. \tag{3.16}$$

The critical stretch value s_0, can be calibrated using measurements on the critical energy release rate G_c, of a brittle material.

The work required to break a single bond can be computed using Eq. (3.9) as [84]:

$$w_c = \int_0^{s_0} c(\boldsymbol{\xi}) s \|\boldsymbol{\xi}\| ds = \frac{c(\boldsymbol{\xi}) s_0^2 \|\boldsymbol{\xi}\|}{2}. \tag{3.17}$$

Then s_0, can be computed by equating the energy required to break all bonds per unit of fracture area to the critical energy release rate G_c. The process is described in detail in [84]. Following, Ha and Bobaru [96], if a constant micromodulus function $c(\boldsymbol{\xi})$ is used in 2D, the value of s_0 is expressed as:

$$s_0 = \sqrt{\frac{4\pi G_C}{9E\delta}}, \tag{3.18}$$

while in the case of a conical $c(\boldsymbol{\xi})$, the above expression becomes:

$$s_0 = \sqrt{\frac{5\pi G_C}{9E\delta}}. \tag{3.19}$$

Thus, the PD theory can naturally incorporate damage by simply removing the bonds whose stretch s exceed the critical stretch s_0 through function $\mu(t, \boldsymbol{\eta}, \boldsymbol{\xi})$. There is no need for any additional criteria to triggering the damage initiation, or estimations of the propagation length and direction within the framework. The evolution of damage can be quantified and monitored using the local damage index $\phi(\boldsymbol{x}, t)$ as [134]:

$$\phi(\boldsymbol{x}, t) = 1 - \frac{\int_{H_x} \mu(t, \boldsymbol{\eta}, \boldsymbol{\xi}) dV_{x'}}{\int_{H_x} dV_{x'}}, \tag{3.20}$$

with $0 \leq \phi(\boldsymbol{x}, t) \leq 1$. When the material is in its pristine condition, the value of the local damage index is $\phi(\boldsymbol{x}, t) = 0$ while $\phi(\boldsymbol{x}, t) = 1$ corresponds to material points that are no longer connected to the rest of the solid. Typically, near a sharp crack that separates two surfaces, $\phi(\boldsymbol{x}, t)$ takes the value of approximately 0.4, as illustrated in Figure 3.2. Higher values however are possible during different damage mechanisms [135].

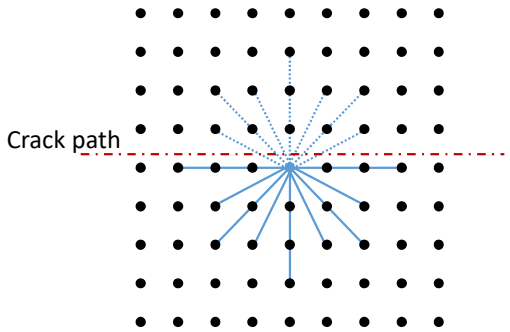

Figure 3.2: Broken bonds of a particle next to the crack path. The total bonds connected to the particle were 28 (when $\delta = 3\Delta x$) and 11 bonds were broken. The local damage index of the particle is 0.39.

Alternative models have been presented in the literature for different applications. In [29], a bilinear constitutive model replaces the linear law to introduce ductility in the simulations. In [100], the value of the critical bond stretch is modified at each time step of the analysis to simulate fracture in a polycrystalline material due to stress corrosion cracking. In [84] a modification of the critical stretch is presented that was found to give better approximations when compared with experimental results from glass fracture.

3.1.3 *Thermomechanical Bond – Based PD Theory*

In many applications it is of interest to examine the influence of the thermal state of a structure on its deformation state and vice versa. Such a problem is described in chapter 4 where the thermal cracking of alumina is studied. The desirable properties of the PD theory for fracture

mechanics can be utilized in thermomechanical problems to investigate the failure of structures under the application of thermal loads. Kilic and Madenci [136,137] were the first to formulate an uncoupled thermomechanical bond-based PD model by introducing a thermal bond stretch in the pairwise force function $\boldsymbol{f}$ and successfully applying their model on fracture problems. Using this methodology, crack propagation was studied in pre-cracked specimens and in thin glass plates subjected to water quenching. Later, Oterkus et. al. [138] introduced a fully coupled thermomechanical model for State-Based PD and the formulation proposed by Kilic and Madenci can be extracted as a special case. In this study we are interested in applying the PD theory in an uncoupled thermomechanical problem and thus the formulation presented by Kilic and Madenci is implemented. Following [136], the pairwise force function defined in Eq. (3.13) can be modified to:

$$\boldsymbol{f}(\boldsymbol{\eta},\boldsymbol{\xi}) = c(\boldsymbol{\xi})(s-\alpha\theta)\frac{\boldsymbol{\eta}+\boldsymbol{\xi}}{\|\boldsymbol{\eta}+\boldsymbol{\xi}\|}, \tag{3.21}$$

where, α is the thermal expansion coefficient and θ is the temperature change, relative to the temperature of the material in the unstressed state. Since the temperature at the location of each PD particle varies, the mean value between material points $\boldsymbol{x}'$ and $\boldsymbol{x}$ is used, defined as: $\theta = \big(\theta(x_j)+\theta(x_i)\big)/2$. The fracture criterion is also redefined by modifying $\mu(t,\boldsymbol{\eta},\boldsymbol{\xi})$ as:

$$\mu(t,\boldsymbol{\eta},\boldsymbol{\xi}) = \begin{cases} 1, & \text{if } s(t')-\alpha\theta \le s_0, \forall 0 \le t' \le t \\ 0, & \text{otherwise} \end{cases}. \tag{3.22}$$

3.1.4 *Discretization of the PD Equation of Motion*

The problem domain can be discretized into a finite number of subdomains and a particle is assigned at the centre of each one. The material volume associated with each subdomain depends on the number of subdivisions and it is attached to each corresponding particle. Although the discretization grid does not have to be necessarily uniform or structured (see e.g. [5,139]), for simplicity only uniform grids are implemented in this study and the discretization length is denoted as Δx. Nevertheless, the concepts described are directly extendible to unstructured or irregular grids. Special considerations however are required when local grid refinement is attempted [87,91].

The integral in the PD equation of motion described in Eq. (3.1), can be approximated numerically through a single quadrature point and can be written as a finite summation as [7]:

$$\rho\ddot{\boldsymbol{d}}_i = \sum_{j=1}^{M} \boldsymbol{f}_{i,j} V_j + \boldsymbol{b}_i, j \neq i \tag{3.23}$$

where, $\boldsymbol{x}_i$ is the location of the i^{th} collocation point (particle), M is the total number of particles that are included in the horizon of the i^{th} particle, V_j is the volume of the j^{th} particle, $\boldsymbol{f}_{i,j}(\boldsymbol{\eta}_{i,j}, \boldsymbol{\xi}_{i,j})$ is the bond force that particle j exerts on particle i and $\boldsymbol{b_i}$ is the body force acting on the i^{th} particle. In the above approximation the quadrature and collocation points coincide. Kilic and Madenci proposed a more elaborate discretization in [116] where the aforementioned discretization can be extracted as a special case.

In Eq. (3.23) either the original or the linearized formulation of the pairwise force function can be used. Substituting Eqs. (3.2), (3.10) and (3.13) in Eq. (3.23) leads to:

$$\rho\ddot{\boldsymbol{d}}_i = \sum_{j=1}^{M} c_{i,j} \frac{\|\boldsymbol{d}_j - \boldsymbol{d}_i + \boldsymbol{x}_j - \boldsymbol{x}_i\| - \|\boldsymbol{x}_j - \boldsymbol{x}_i\|}{\|\boldsymbol{x}_j - \boldsymbol{x}_i\|} \frac{\boldsymbol{d}_j - \boldsymbol{d}_i + \boldsymbol{x}_j - \boldsymbol{x}_i}{\|\boldsymbol{d}_j - \boldsymbol{d}_i + \boldsymbol{x}_j - \boldsymbol{x}_i\|} V_j + \boldsymbol{b}_i, \quad (3.24)$$

where $c_{i,j} = c(\boldsymbol{x}_j - \boldsymbol{x}_i)$ was used for short. Similarly, substituting Eqs. (3.2), (3.10) and (3.14) in Eq. (3.23) leads to:

$$\rho\ddot{\boldsymbol{d}}_i = \sum_{j=1}^{M} c_{i,j} \frac{\boldsymbol{d}_j - \boldsymbol{d}_i}{\|\boldsymbol{x}_j - \boldsymbol{x}_i\|} V_j + \boldsymbol{b}_i, \quad (3.25)$$

If damage is allowed, then $\mu(t, \boldsymbol{\eta}, \boldsymbol{\xi})$ is added in the expression of the pairwise force function, and consequently in Eqs. (3.24) and (3.25) as described in Eq. (3.14).

3.1.5 *Correction Factors in the PD theory*

There are two correction factors that need to be considered to improve the accuracy and the convergence when the PD theory used: **i**) the *volume correction* and **ii**) the *surface correction* factors.

In the discretization described in Eq. (3.23), each particle is located at the centre of each subdomain. Although a particle j might be within the horizon of particle i with $\|\boldsymbol{x}_j - \boldsymbol{x}_i\| \leq \delta$, the volume associated with particle j can be only partial within the horizon of i. This can impair the convergence rate of the integral approximation in Eq. (3.23). The volume correction factor $v(\boldsymbol{\xi}_{i,j})$ is introduced to reduce the effective volume of the particles that are only partially within the horizon of the particle considered. This procedure is expressed as [140]:

$$v(\boldsymbol{\xi}_{i,j}) = \begin{cases} \dfrac{\delta - \|\boldsymbol{\xi}_{i,j}\|}{2r_j} + \dfrac{1}{2}, & \text{if } (\delta - r_j) \leq \|\boldsymbol{\xi}_{i,j}\| \leq \delta \\ 1, & \text{if } \|\boldsymbol{\xi}_{i,j}\| \leq (\delta - r_j) \\ 0, & \text{otherwise} \end{cases}, \quad (3.26)$$

where $\|\boldsymbol{\xi}_{i,j}\| = \|\boldsymbol{x}_j - \boldsymbol{x}_i\|$ and r_j is a constant usually selected equal to half the grid spacing. The length $\delta - r_j$ indicates the distance above which the volume of a node needs to be corrected. When the grid spacing is uniform then one can easily verify that $v_{i,j} = v_{j,i}$.

In the formulation presented in the previous paragraphs, when the PD parameters are computed it was assumed that the particle considered, is completely embedded in the interior of the material and surrounded by other particles. This assumption is true for points that lie in the bulk of the material but ceases to hold for points near the boundaries. If the same parameters are used for all points, regardless of their position, the final stiffness of the material will be lower near the boundaries and higher towards its interior. In the literature this effect is termed the "PD skin-effect" [141]. The skin effect manifests mainly at the geometrical boundaries of the structure but as noted in [142] it can also appear at the crack faces.

Special techniques have been proposed in the literature to compute surface correction factors for the particles whose horizon is interrupted and reduce the effect of this phenomenon. Without being exhaustive, some notable procedures are mentioned here. A comprehensive review and comparison of various surface correction procedures can be found in [143]. In [7] a correction factor is computed by applying simple uniaxial loads on the structure and comparing the resulting response to that of an infinite case. The particles near the boundary will exhibit a directional dependence because of the horizon interruption. A correction is introduced that modifies the bond stiffness to reduce this effect. Instead of modifying the bond stiffness, Gerstle et. al. [144] propose the introduction of an additional fictitious layer that surrounds the initial structure. The motivation is to remove the skin effect by ensuring that the horizon of all nodes that are within the structure is uninterrupted. Finally, in [5], a simple correction is defined based on the volume that is enclosed in the horizon of the particle. If this volume is smaller than that of a particle with uninterrupted horizon, the material is softer than intended.

As stated in [143], none of the correction approaches can truly treat the PD skin effect. Here, the volume correction procedure presented in [5] is employed. The procedure is selected for its effectiveness [143] and its simple implementation that is important later when the domain over which the PD theory is applied is relocated following the evolution of damage. Following this approach, the surface correction factor $\lambda_{i,j}$ can be computed from the expression [5,143]:

$$\lambda_{i,j} = \frac{2V_0}{V_j - V_i}, \tag{3.27}$$

where, V_i and V_j are the actual volume of the horizon for nodes i and j, respectively, and V_0 is the volume of the node that is fully embedded within the material. The two correction factors $v(\boldsymbol{\xi}_{i,j})$ and $\lambda_{i,j}$, are introduced in the discretized equation of motion described in Eqs. (3.24) or (3.25), and modify locally the bond stiffness.

3.2 Solution of the PD equation of motion

As illustrated in the literature, the PD model have been successfully implemented in a wide variety of applications and problems (see e.g. [5,29,7]). Depending on the problem scientists and engineers are trying to address, inertia forces might, or might not, contribute significantly to the system's behaviour. It is important to be able to investigate both the dynamic behaviour of a system as well as find solutions that describe equilibrium states.

3.2.1 *Static Solution*

Under the assumption that the loads are applied sufficiently slowly, and the inertia effects are insignificant, the PD equation of motion expressed in Eq. (3.3) reduces to:

$$\int_{H_x} \boldsymbol{f}(\boldsymbol{\eta}, \boldsymbol{\xi})\, dV_{x'} + \boldsymbol{b}(\boldsymbol{x}, t) = \boldsymbol{0}. \tag{3.28}$$

The above integral can be approximated using the same collocation method that was described in the previous paragraph, using either the original or the linearized expression for the pairwise force function $\boldsymbol{f}(\boldsymbol{\eta}, \boldsymbol{\xi})$. As stated earlier, despite the use of a linear force - stretch relationship from the definition of the $c(\boldsymbol{\xi})$, when the original expression of $\boldsymbol{f}(\boldsymbol{\eta}, \boldsymbol{\xi})$ is used, the resulting system of equations is nonlinear. Three major approaches have been used in the literature to solve this system:

i). In [145], Kilic and Madenci proposed the implementation of the Adaptive Dynamic Relaxation (ADR) method. According to ADR, a fictitious mass and damping is assigned at each particle and Eq. (3.24) is solved directly. After a sufficient number of iterations, the dynamic effects have been dissipated and an equilibrium solution is achieved. This method has been applied in many contributions in the literature as it avoids the solution of a nonlinear system of equations and the computationally expensive matrix inversion.

ii). The conjugate gradient method was proposed by in [146]. The solution of Eq. (3.28) is sought through the minimization of the strain energy of the system and avoids the introduction of any additional fictitious parameters. According to the authors, this

method is superior to ADR as it requires less iterations to approximate the static solution.

iii). Zaccariotto et al. [29] suggested the implementation of a full Newton-Raphson algorithm for the implicit solution of the nonlinear system equations.

In the present study, the full Newton-Raphson approach is adopted for the numerical approximation of the displacement field when the original expression of $\boldsymbol{f}(\boldsymbol{\eta}, \boldsymbol{\xi})$ is implemented in the PD equation of motion. We denote with $g(\boldsymbol{d})$ the expression:

$$\boldsymbol{g}(\boldsymbol{d}) = \int_{H_x} \boldsymbol{f}(\boldsymbol{\eta}, \boldsymbol{\xi})\, dV_{x'} + \boldsymbol{b}(\boldsymbol{x}, t). \tag{3.29}$$

Obviously $g(\boldsymbol{d}) = \boldsymbol{0}$. For an arbitrary test solution $\boldsymbol{d}^n$, $g(\boldsymbol{d}^n)$ is the residual of Eq. (3.29). The same discretization is used in Eq. (3.29) as in Eq. (3.24) leading to:

$$g_i(\boldsymbol{d}_i) = \sum_{j=1}^{M} c \frac{\left\|\boldsymbol{d}_j - \boldsymbol{d}_i + \boldsymbol{x}_j - \boldsymbol{x}_i\right\| - \left\|\boldsymbol{x}_j - \boldsymbol{x}_i\right\|}{\left\|\boldsymbol{x}_j - \boldsymbol{x}_i\right\|} \frac{\boldsymbol{d}_j - \boldsymbol{d}_i + \boldsymbol{x}_j - \boldsymbol{x}_i}{\left\|\boldsymbol{d}_j - \boldsymbol{d}_i + \boldsymbol{x}_j - \boldsymbol{x}_i\right\|} V_j + \boldsymbol{b}_i. \tag{3.30}$$

Using the full Newton-Raphson method, the displacement field can be approximated numerically through [147]:

$$\boldsymbol{d}^{n+1} = \boldsymbol{d}^n - \left[\mathcal{J}_{g(\boldsymbol{d})}\right]^{-1} g(\boldsymbol{d}^n), \tag{3.31}$$

where, $\boldsymbol{d}^{n+1}$ is the next iteration approximation and $\mathcal{J}_{g(\boldsymbol{d})}$ is the Jacobian of $g(\boldsymbol{d})$ is defined as:

$$\mathcal{J}_{g(\boldsymbol{d})} = \frac{\partial g(\boldsymbol{d})}{\partial \boldsymbol{d}}. \tag{3.32}$$

In [148], an algorithm is presented for the approximation of $\mathcal{J}_{g(\boldsymbol{d})}$. Small perturbations in the displacement field are applied and Eq. (3.32) is approximated numerically using a central difference scheme.

Here, use of an analytical expression for $\mathcal{J}_{g(\boldsymbol{d})}$ is preferred as it improves the efficiency of the algorithm. Assume a 2D uniform grid and let n^{PD} be the set of all particles. The total number of particles is $n_p = |n^{PD}|$. Since the grid is uniform then $V_i = V, i = 1, 2, \dots, n^{PD}$. The Jacobian matrix $\mathcal{J}_{g(\boldsymbol{d})}$ has dimensions $2n_p \times 2n_p$ and can be expanded as:

$$\mathcal{J}_{g(\boldsymbol{d})} = \begin{bmatrix} \frac{\partial g_{1,x}}{\partial d_{1,x}} & \frac{\partial g_{1,x}}{\partial d_{1,y}} & \frac{\partial g_{1,x}}{\partial d_{2,x}} & \frac{\partial g_{1,x}}{\partial d_{2,y}} & \cdots & \frac{\partial g_{1,x}}{\partial d_{n_p,x}} & \frac{\partial g_{1,x}}{\partial d_{n_p,y}} \\ \frac{\partial g_{1,y}}{\partial d_{1,x}} & \frac{\partial g_{1,y}}{\partial d_{1,y}} & \ddots & \ddots & & \vdots & \vdots \\ \vdots & \vdots & & \ddots & \ddots & \vdots & \vdots \\ \frac{\partial g_{n_p,y}}{\partial d_{1,x}} & \frac{\partial g_{n_p,y}}{\partial d_{1,y}} & \cdots & \cdots & \cdots & \frac{\partial g_{n_p,x}}{\partial d_{n_p,y}} & \frac{\partial g_{n_p,y}}{\partial d_{n_p,y}} \end{bmatrix} \tag{3.33}$$

where, the notation $\langle\cdot\rangle_{,x}$ and $\langle\cdot\rangle_{,y}$ is used to denote the horizontal and the vertical components, respectively. It is convenient to re-write Eq. (3.30) as:

$$\boldsymbol{g}_i = cV \sum_{j=1}^{M_i} \left(\frac{\boldsymbol{d}_j - \boldsymbol{d}_i + \boldsymbol{\xi}_{i,j}}{\left\|\boldsymbol{\xi}_{i,j}\right\|} - \frac{\boldsymbol{d}_j - \boldsymbol{d}_i + \boldsymbol{\xi}_{i,j}}{\left\|\boldsymbol{d}_j - \boldsymbol{d}_i + \boldsymbol{\xi}_{i,j}\right\|} \right) + \boldsymbol{b}_i. \tag{3.34}$$

where, $M_i \subset n^{PD}$ is a set that contains the particle numbers that are within the horizon of particle i and the cardinality of M_i depends on the value of the PD horizon. It is convenient to write the derivatives in Eq. (3.33) as:

$$\frac{\partial g_{i,\alpha}}{\partial d_{k,\beta}} = cV \sum_{j=1}^{M_i} \frac{\partial}{\partial d_{k,\beta}} \left(\frac{d_{j,\alpha} - d_{i,\alpha} + \xi_{i,j,\alpha}}{\left\|\boldsymbol{\xi}_{i,j}\right\|} - \frac{d_{j,\alpha} - d_{i,\alpha} + \xi_{i,j,\alpha}}{\left\|\boldsymbol{d}_j - \boldsymbol{d}_i + \boldsymbol{\xi}_{i,j}\right\|} \right) \tag{3.35}$$

with $k, i = 1, 2, \ldots, n_p$, $k \neq i$ and $\alpha, \beta = x, y$. By definition, the above derivative vanishes when $k \notin M_i$.

Let $m \in M_i$ and $k = m$. Then, Eq. (3.35) becomes:

$$\frac{\partial g_{i,\alpha}}{\partial d_{m,\beta}} = cV \frac{\partial}{\partial d_{m,\beta}} \left(\frac{d_{m,\alpha} - d_{i,\alpha} + \xi_{i,m,\alpha}}{\left\|\boldsymbol{\xi}_{i,m}\right\|} - \frac{d_{m,\alpha} - d_{i,\alpha} + \xi_{i,m,\alpha}}{\left\|\boldsymbol{d}_m - \boldsymbol{d}_i + \boldsymbol{\xi}_{i,m}\right\|} \right). \tag{3.36}$$

Using Eq. (3.36), we arrive to the following expressions:

$$\frac{\partial g_{i,x}}{\partial d_{m,x}} = cV \left(\frac{1}{\left\|\boldsymbol{\xi}_{i,m}\right\|} - \frac{1}{a_{i,m}} + \frac{\left(d_{m,x} - d_{i,x} + \xi_{i,m,x}\right)^2}{{a_{i,m}}^3} \right). \tag{3.37a}$$

$$\frac{\partial g_{i,x}}{\partial d_{m,y}} = \frac{\partial g_{i,y}}{\partial d_{m,x}} = cV \left(\frac{\left(d_{m,x} - d_{i,x} + \xi_{i,m,x}\right)\left(d_{m,y} - d_{i,y} + \xi_{i,m,y}\right)}{{a_{i,m}}^3} \right) \tag{3.37b}$$

$$\frac{\partial g_{i,y}}{\partial d_{m,y}} = cV \left(\frac{1}{\left\|\boldsymbol{\xi}_{i,m}\right\|} - \frac{1}{a_{i,m}} + \frac{\left(d_{m,y} - d_{i,y} + \xi_{i,m,y}\right)^2}{{a_{i,m}}^3} \right). \tag{3.37c}$$

where, $a_{i,j} = \left\|\boldsymbol{d}_j - \boldsymbol{d}_i + \boldsymbol{\xi}_{i,j}\right\|$.

If we set $k = i$ in Eq. (3.35) then we get:

$$\frac{\partial g_{i,\alpha}}{\partial d_{i,\beta}} = -\sum_{j=1}^{M_i} \frac{\partial g_{i,\alpha}}{\partial d_{j,\beta}} \tag{3.38}$$

Using Eqs. (3.37) and (3.38), the computation of the Jacobian matrix can be vectorized during a computer implementation of the Newton-Raphson solver.

When the linearized formulation is used, the final system of equations becomes linear and can be written in the form $\boldsymbol{Ax} = \boldsymbol{y}$. Thus, a stiffness matrix that describes the interparticle interactions can be assembled. Consider substituting Eq. (3.14) into Eq. (3.28). After discretization of the PD equation of motion we get:

$$\sum_{j=1}^{M} \boldsymbol{f}_{i,j}^{lin} V_j V_i + \boldsymbol{b}_i V_i = \boldsymbol{0}. \tag{3.39}$$

where, both sides of Eq. (3.39) were multiplied by V_i. The term in the summation describes the bond forces acting on each particle. Each bond force $\boldsymbol{f}_{i,j}^{bond}$, can be computed as:

$$\boldsymbol{f}_{i,j}^{bond} = \boldsymbol{f}_{i,j}^{lin} V_j V_i = \frac{c(\boldsymbol{\xi}_{i,j}) v(\boldsymbol{\xi}_{i,j}) \lambda(\boldsymbol{\xi}_{i,j}) V_j V_i}{\|\boldsymbol{x}_j - \boldsymbol{x}_i\|} (\boldsymbol{d}_j - \boldsymbol{d}_i). \tag{3.40}$$

where, in the above expression the correction factors $v(\boldsymbol{\xi}_{i,j})$ and $\lambda(\boldsymbol{\xi}_{i,j})$ have also been introduced to account for the volume and surface correction. The term

$$k_{i,j}^{bond} = \frac{c(\boldsymbol{\xi}_{i,j}) v(\boldsymbol{\xi}_{i,j}) \lambda(\boldsymbol{\xi}_{i,j}) V_j V_i}{\|\boldsymbol{x}_j - \boldsymbol{x}_i\|}, \tag{3.41}$$

describes the stiffness of each bond and has units of force/length. Using the above definitions, the bond forces, $\boldsymbol{f}_{i,j}^{bond}$ can be written in the global coordinate system following the transformation:

$$\boldsymbol{F}_{i,j} = \boldsymbol{R}^T \boldsymbol{K}^{loc} \boldsymbol{R} \boldsymbol{d}_{i,j} = \boldsymbol{K}_{i,j}^{\boldsymbol{PD}} \boldsymbol{d}_{i,j}, \tag{3.42}$$

where, $\boldsymbol{F}_{i,j} = \{f_{i,j,x}, f_{i,j,y}, f_{j,i,x}, f_{j,i,y}\}^T$ is the forcing vector, $\boldsymbol{d}_{i,j} = \{d_{i,x}, d_{i,y}, d_{j,x}, d_{j,y}\}^T$ is the vector containing the displacements of particles i and j, $\boldsymbol{R}$ is the transformation matrix and $\boldsymbol{K}^{loc}$ is the local stiffness matrix of the bond and it is analogous to that of a truss element. Matrices $\boldsymbol{R}$ and $\boldsymbol{K}^{loc}$ are given as:

$$\boldsymbol{R} = \begin{bmatrix} c & s & 0 & 0 \\ -s & c & 0 & 0 \\ 0 & 0 & c & s \\ 0 & 0 & -s & c \end{bmatrix}, \boldsymbol{K}^{loc} = k_{i,j}^{bond} \begin{bmatrix} 1 & 0 & -1 & 0 \\ 0 & 0 & 0 & 0 \\ -1 & 0 & 1 & 0 \\ 0 & 0 & 0 & 0 \end{bmatrix}. \tag{3.43}$$

where, c and s are short for $cos\theta$ and $sin\theta$ with θ being the angle between the bond and the horizontal axis. The final PD stiffness matrix assembled by repeating Eq. (3.42) for all bonds in the problem domain. An approximation of the displacement field $\boldsymbol{d}$ is then obtained by solving the linear system:

$$\boldsymbol{F}^{PD} = \boldsymbol{K}^{PD}\boldsymbol{d}, \tag{3.44}$$

where, $\boldsymbol{F}_i^{PD} = \boldsymbol{b}_i V_i$ is the external force vector acting on the particles.

3.2.2 *Time Integration of the PD Equation of Motion*

Time integration is of pivotal importance for many engineering problems. The schemes that are typically employed to perform time marching in classical models are also applicable for the PD equation of motion [148]. The temporal resolution required to capture the rapid and sudden nature of fracture leads to the necessity of very small time-increments [1]. When a large number of time steps is required explicit time integration schemes can be computationally more efficient compared to the implicit ones as the solution of system of equations is avoided [149]. Additionally, unless the linearized PD theory is employed, the resulting system of equations is also nonlinear, requiring the use of iterative solvers. As such explicit solvers are more efficient. Explicit time marching techniques however are only conditionally stable, and the time discretization step must satisfy the Courant's condition. Various explicit methodologies have been implemented in the literature. The central difference scheme, the velocity – verlet algorithm, forward and backward first order differences are same typical examples [7,84,96,148].

Here the central difference method is used for the time marching. The next step displacements are computed as:

$$\boldsymbol{d}_i^{n+1} = \boldsymbol{d}_i^n + \dot{\boldsymbol{d}}_i^n \Delta t + \frac{1}{2}\ddot{\boldsymbol{d}}_i^n \Delta t^2. \tag{3.45}$$

The next step acceleration is computed using the discretized PD equation of motion from Eq. (3.23). Finally, the next step velocities are computed as:

$$\dot{\boldsymbol{d}}_i^{n+1} = \dot{\boldsymbol{d}}_i^n + \frac{1}{2}\left(\ddot{\boldsymbol{d}}_i^n + \ddot{\boldsymbol{d}}_i^{n+1}\right)\Delta t. \tag{3.46}$$

Although explicit methods are straightforward to use, sufficiently small time-steps must be used to ensure stability. In [84], a stability study was carried out using the linearized PD equation of motion. It was shown that the total error is $O(\Delta t^2) + O(\Delta x^2)$ when no discontinuities are present and $O(\Delta t^2) + O(\Delta x)$ when there are discontinuities. According to [84], for the solution to be stable the maximum time increment must satisfy:

$$\Delta t \leq \Delta t_{critical} = \sqrt{\frac{2\rho}{\sum_{j=1}^{M} \frac{c_{i,j}}{\|\boldsymbol{\xi}_{i,j}\|} V_j}}. \tag{3.47}$$

Since $\Delta t_{critical}$ was computed using the linearized PD equation of motion, its value can be reduced by a factor of 0.9 for problems that contain fracture or when the original formulation is used [84].

3.3 Benchmarking Examples Using The in-house MATLAB Code

Using the definitions in the previous paragraph, an algorithm was developed in MATLAB for the solution of the PD equation of motion. In this paragraph, two benchmarking examples are presented.

3.3.1 *Oscillation of an Initially Loaded 1D bar*

As a first example, the axial vibration of a 1D bar is studied. The discretized PD equation of motion is used to approximate the solution and the results are compared with the analytical solution of classical elasticity. The bar considered is $L = 1.0\text{m}$ long with a cross sectional area $A = 1\text{mm}^2$. The material is linear elastic with Young's modulus $E = 200\text{GPa}$, Poisson's ratio $v = 0.25$ and density $\rho = 2800\text{kg/m}^3$. The bar is assumed to be initially deformed under the application of a distributed load $q = 10\text{N/mm}$. At $t = 0\text{s}$, the load is suddenly removed, and the bar is let free to vibrate for $t_{tot} = 4.0 \cdot 10^{-3}\text{s}$.

First, the derivation of the analytical solution is described. Details on the derivation can be found on a plethora of books on vibrations and dynamics (e.g. [150] and [151]). The bar is assumed fixed at $x = 0$ and free at $x = L$. Furthermore, an initial displacement is applied at the bar due to the external distributed load. The initial and boundary conditions are summarized in Eqs. (3.48) as:

$$u(x,0) = \frac{qLx}{EA} - \frac{qx^2}{2EA} \tag{3.48a}$$

$$\dot{u}(x,0) = 0 \tag{3.48b}$$

$$u(0,t) = 0 \tag{3.48c}$$

$$\frac{\partial u}{\partial x}(L,t) = 0 \tag{3.48d}$$

where, u and $\dot{u}$ are the displacement and the velocity, respectively.

For a prismatic and homogeneous rod, the free-vibration equation can be derived by considering Newton's second law on an infinitesimal small bar segment. Since the material is assumed linear elastic, Hook's law $\sigma = E\varepsilon = E\frac{\partial u}{\partial x}$ can be used leading to:

$$E\frac{\partial^2 u}{\partial x^2} = \rho\frac{\partial^2 u}{\partial t^2}. \tag{3.49}$$

The free-vibration equation can be solved using the separation of variables principle and can be rewritten as the product of $w(x)$ and $k(t)$ using $u(x,t) = w(x)k(t)$. Making this substitution in Eq. (3.49) leads to:

$$\frac{c^2}{w}\frac{d^2 w}{dx^2} = \frac{1}{k}\frac{d^2 k}{dt^2}, \tag{3.50}$$

where, $c = \sqrt{E/\rho}$ is the wave speed in the bar. The left-hand side of Eq. (3.50) depends only on x while the right-hand side only on t. Thus, the common value is a constant, $-\omega^2$. This results into the familiar second order ordinary differential equation for each variable with solutions:

$$\frac{d^2 w}{dx^2} + \left(\frac{\omega}{c}\right)^2 w = 0 \quad \Rightarrow \quad w(x) = A\cos\frac{\omega x}{c} + B\sin\frac{\omega x}{c} \tag{3.51a}$$

$$\frac{d^2 k}{dt^2} + \omega^2 k = 0 \quad \Rightarrow \quad k(t) = C\cos\omega t + D\sin\omega t \tag{3.51b}$$

where, A, B, C and D are constants. Using Eqs (3.51), the solution can be written as:

$$u(x,t) = \left(A\cos\frac{\omega x}{c} + B\sin\frac{\omega x}{c}\right)(C\cos\omega t + D\sin\omega t). \tag{3.52}$$

Using the initial condition from Eq. (3.48b) in Eq. (3.52) and then the boundary condition from Eq. (3.48c) in Eq. (3.52) leads to $D = 0$ and $A = 0$, respectively. Application of the boundary condition from (3.48d) lead to the computation on the natural frequencies of the system as:

$$\omega_n = \frac{(2\nu + 1)\pi c}{2l}, n = 1,2,3, \ldots \tag{3.53}$$

where, ω_n is the natural frequency associated with the n^{th} mode of vibration. Using Eq. (3.53), the equation of vibration can be written for each mode. The general solution of the free-

vibrating bar is given implementing the superposition method for all modes and can be written as:

$$u(x,t) = \sum_{n=1}^{\infty} \sin\frac{(2n+1)\pi x}{2l} C_n \cos\frac{(2n+1)\pi ct}{2l}. \tag{3.54}$$

Finally, using the initial condition from Eq. (3.48a) leads to

$$\sum_{n=1}^{\infty} \sin\frac{(2n+1)\pi x}{2l} C_n = u(x,0). \tag{3.55}$$

Eq. (3.55) is a Fourier sine series and the value of C_n is determined as:

$$\begin{aligned} C_n &= \frac{2}{l}\int_0^l u(u,0)\sin\frac{(2n+1)\pi x}{2l}dx \quad \Rightarrow \\ &= \frac{2}{l}\int_0^l \left(\frac{qLx}{EA} - \frac{qx^2}{2EA}\right)\sin\frac{(2n+1)\pi x}{2l}dx \quad \Rightarrow \\ &= \frac{2q}{EA}\int_0^l x\sin\frac{(2n+1)\pi x}{2l}dx - \frac{q}{lEA}\int_0^l x^2\sin\frac{(2n+1)\pi x}{2l}dx, \end{aligned} \tag{3.56}$$

where, the final integral can be solved using integration by parts. Thus, Eq. (3.52) is finally recast as:

$$u(x,t) = \sum_{n=1}^{\infty} \sin\frac{(2n+1)\pi x}{2l} C_n \cos\frac{(2n+1)\pi ct}{2l}. \tag{3.57}$$

The PD equation of motion is approximated numerically using the collocation method described in paragraph 3.1.4. Two different grids are considered for comparison, one with 100 and one with 1000 nodes, corresponding to $\Delta x = 10\text{mm}$ and 1mm, respectively. In both cases the horizon length is set to $\delta = 3\Delta x$. A fictitious material layer of thickness δ is added on the left side of the bar to apply the boundary condition, as suggested in [7]. The initial condition, defined in Eq. (3.48a), is applied at each particle location. An illustration of the discretization can be found in Figure 3.3. Both the surface and the volume correction factors have been included in this example.

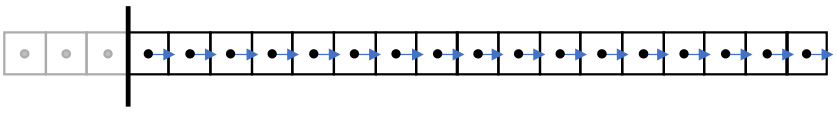

Figure 3.3: Discretization of the 1D bar using the colocation method. Grey boxes indicate the fictitious material layer, added for the application of the boundary conditions.

In Figure 3.4, the displacement of a particle located at $x = 0.5\text{m}$ is plotted during the oscillation of the bar, as a comparison between the analytical with the PD solution. For the analytical solution the first 20 modes of vibration are considered. It is evident that when only 100 particles are used, there is a lag between the two solutions. When the discretization is refined to 1000 particles, the lag is reduced. Still the two solutions are in very close agreement. The effect of different horizon values on the response of the 1D bar is discussed in more depth in the following paragraphs.

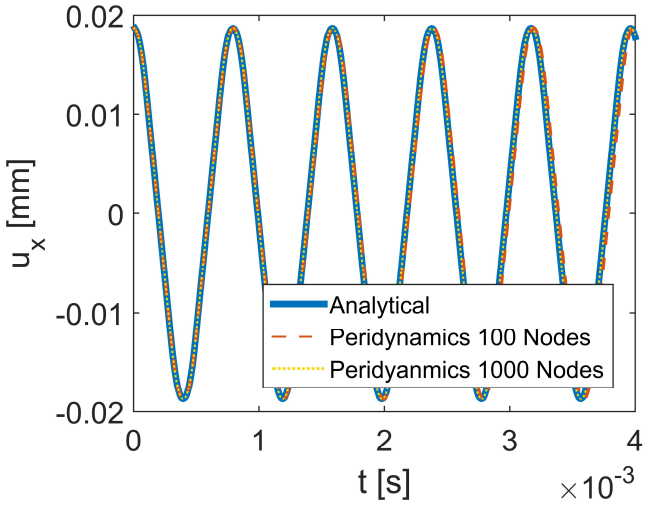

Figure 3.4: Comparison of the PD solution to the analytical solution for

3.3.2 *Static Mode I Crack Propagation*

In this section a Mode I static crack propagation example is considered to evaluate the ability of the algorithm to accurately capture the fracture phenomenon. Consider a plate with an edge breaking crack under plane stress conditions, as illustrated in Figure 3.5 (left). The length of the beam is $L = 0.9\text{mm}$, the height is $H = 0.45\text{mm}$ and the initial crack length $a = 0.3\text{mm}$. The material is linear elastic with Young's Modulus $E = 72\text{GPa}$, Poisson's ratio $v = 0.33$ and energy release rate $G_c = 5\text{J}/\text{m}^2$.

Three uniform grids are used for the discretization of the problem with $\Delta x = 0.015\text{mm}$, 0.009mm and 0.005mm, leading to 3600, 5000 and 16200 total particles, respectively. In all cases the PD horizon is set to $\delta = 3\Delta x$. A displacement control approach is adopted in this example as it leads to a more stable crack propagation. A prescribed displacement $\delta_y = 3 \cdot 10^{-3}\text{mm}$ is applied at the top and bottom left corners. The initial crack geometry is introduced in the PD model by removing the bonds that intersect the crack location. The final bond connectivity is plotted in Figure 3.5 (right).

In total, 100 load increments are used, and the final system of equations is solved using the Newton-Raphson method. The stretch of each bond is monitored during the simulation and if it exceeds the critical value s_0, it is removed from subsequent computations. This process is illustrated in Figure 3.6. The bonds whose stretch value is close to s_0 are plotted with red colour. The prescribed displacement of the load steps presented in Figure 3.6 are $\delta_y = 0.0\text{mm}$, $\delta_y = 0.88 \cdot 10^{-3}\text{mm}$, $\delta_y = 1.7 \cdot 10^{-3}\text{mm}$ and $\delta_y = 2.1 \cdot 10^{-3}\text{mm}$, respectively. High stretch values concentrate near the tip location and the crack propagates in a straight line, as expected for mode I problems.

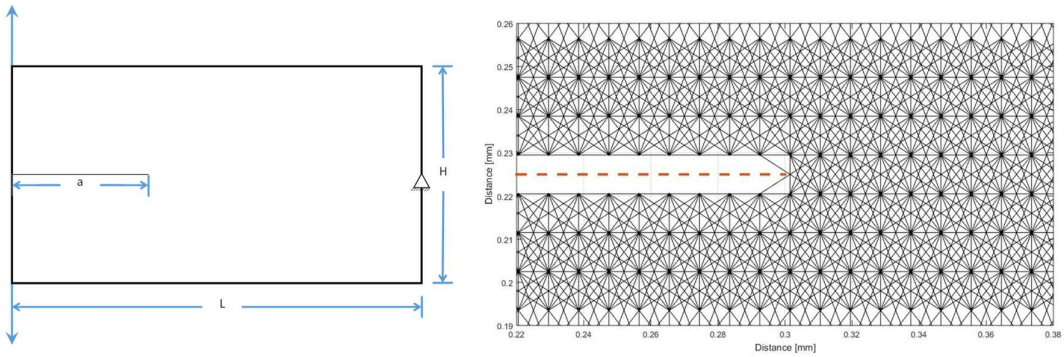

Figure 3.5: Left: Geometry and applied displacement. Right: Bond connectivity near the crack location.

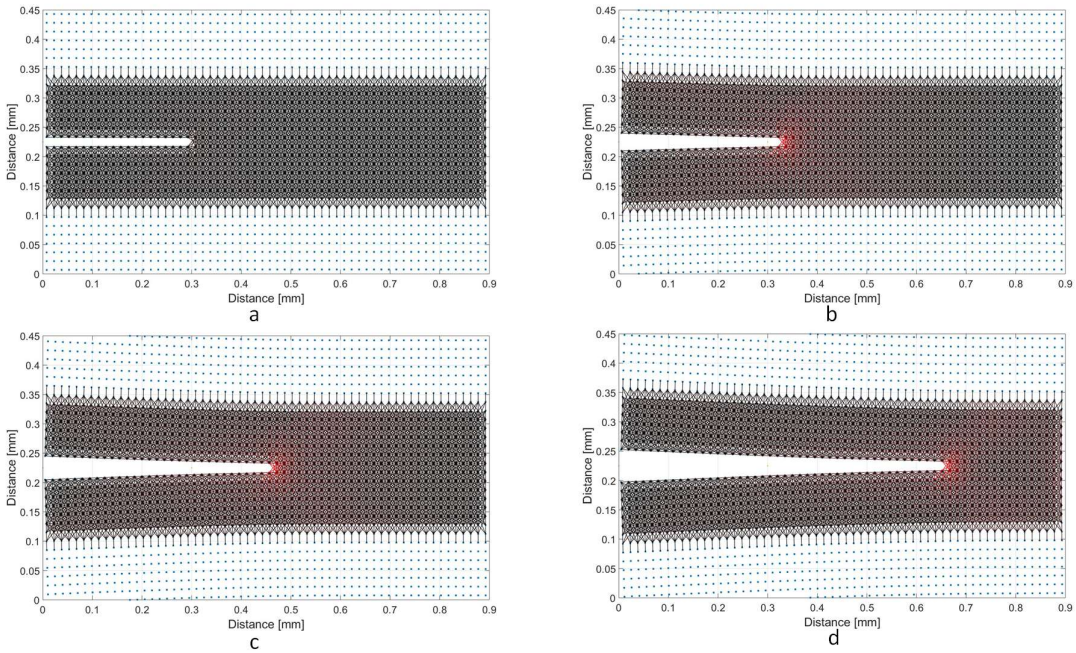

Figure 3.6: Crack path from initial position to the final position before the sudden, unstable fracture for grid spacing $\Delta x = 0.015\text{mm}$. Red denotes bonds that are close to exceeding the critical stretch.

The reaction force at the top left corner is monitored during the propagation and plotted in Figure 3.7 for different grid densities. The same example has been solved by Zaccariotto et. al. in [29] and the results are used for comparison. It is noted that in [29] the authors did not use a volume correction factor nor accounted for the PD skin effect. For consistency, no correction factors are applied in our simulations either. The results of the MATLAB algorithm are in close agreement with those reported in [29]. The final length of the crack is approximately 0.65mm, achieved for a prescribed displacement of 0.0021mm. The same observation was reported in [29].

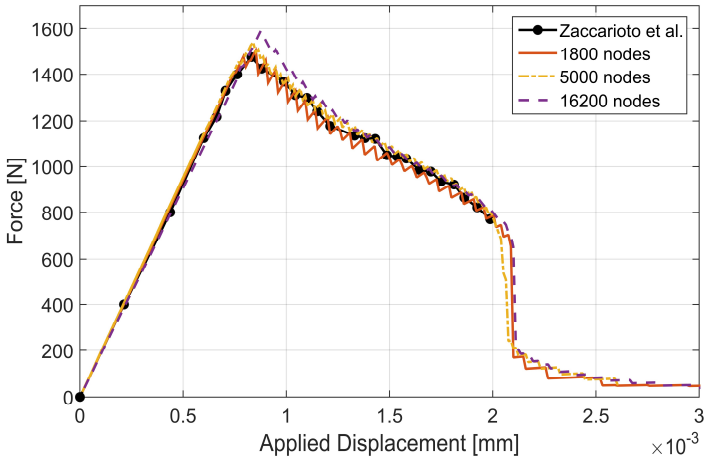

Figure 3.7: Prescribed nodal displacement versus reaction force plot. Results are in good agreement with those published by Zaccariotto et. al. in [29].

3.4 Classical Elasticity and the FE Method

3.4.1 *Strong and Weak Form*

In this paragraph the formulation of linear elasticity is briefly presented. In all situations where a numerical solution is sought, the FE method is used. Denote a problem domain that is modelled using elasticity with Ω^{FE} and its boundary with $\partial\Omega^{FE}$. $\partial_u\Omega$ and $\partial_F\Omega$ denote the portions of $\partial\Omega^{FE}$ where prescribed displacements $\boldsymbol{u}_d$, and forces $\boldsymbol{F}_d$ are applied, respectively. The problem is thus stated as:

Given the initial conditions $\boldsymbol{u}(\boldsymbol{x},0)$ and $\dot{\boldsymbol{u}}(\boldsymbol{x},0)$ and for $\boldsymbol{x} \in \Omega^{FE}$, $t \in [0,T]$, find $\boldsymbol{u}$ such that:

$$\rho\ddot{\boldsymbol{u}} = div\boldsymbol{\sigma} + \boldsymbol{f}_d \text{ on } \Omega^{FE}, \text{with } \boldsymbol{u} = \boldsymbol{u}_d \text{ on } \partial_u\Omega \text{ and } \boldsymbol{\sigma}\cdot\boldsymbol{n} = \boldsymbol{F}_d \text{ on } \partial_F\Omega, \qquad (3.58)$$

where, $\boldsymbol{u}$ is the displacement vector, $\boldsymbol{\sigma}$ is the Cauchy stress tensor, $\boldsymbol{n}$ is the outward unit vector and $\boldsymbol{f}_d$ are the applied body forces. The different formulation between classical elasticity and

the PD theory is apparent when comparing Eq. (3.3) with Eq. (3.58). The volume integral of the pairwise force function $\boldsymbol{f}$, appearing in Eq. (3.3) replaces the divergence of the stress tensor that appears in Eq. (3.58).

To enable the FE discretization of Ω^{FE}, the weak (or variational) formulation of Eq. (3.58) is used [152]. Then the above problem can be rewritten as:

Given the initial conditions $\boldsymbol{u}(\boldsymbol{x},0)$ and $\dot{\boldsymbol{u}}(\boldsymbol{x},0)$ find $\boldsymbol{u}$ such that:

$$\int_{\Omega^{FE}} \rho\ddot{\boldsymbol{u}} \cdot \delta\dot{\boldsymbol{u}} d\Omega + \int_{\Omega^{FE}} \boldsymbol{\varepsilon}(\boldsymbol{u}) : \boldsymbol{E} : \boldsymbol{\varepsilon}(\delta\dot{\boldsymbol{u}})\, d\Omega = \int_{\Omega^{FE}} \boldsymbol{f}_d \cdot \delta\dot{\boldsymbol{u}} d\Omega + \int_{\partial_F\Omega} \boldsymbol{F}_d \cdot \delta\dot{\boldsymbol{u}} dS \quad (3.59)$$

for all admissible $\delta\dot{\boldsymbol{u}}$, where $\boldsymbol{\varepsilon}(\boldsymbol{u}) = \frac{1}{2}(\nabla\boldsymbol{u} + \nabla\boldsymbol{u}^{\boldsymbol{T}})$ is the strain tensor and $\boldsymbol{E}$ is the fourth order elastic tensor.

3.4.2 *Approximation using the FE method*

Unless the geometry and the loading conditions are simple, analytical solution of the partial differential equation (PDE) described in Eq. (3.58) is not always possible [153]. The FE method is employed throughout this study to approximate the solution of the resulting PDE.

The displacement field $\boldsymbol{u}$ is approximated as:

$$\boldsymbol{u}(\boldsymbol{x}^{FE}) \approx \sum_{i=1}^{n_{np}} N_i(\boldsymbol{x}^{FE})\boldsymbol{u}_i = \boldsymbol{NU} \quad (3.60)$$

where, n_{np} is the total number of nodes in the discretization mesh of Ω^{FE}, $\boldsymbol{U}$ is the displacement vector at the FE nodal positions $\boldsymbol{x}^{FE}$ and $N_i(\boldsymbol{x}^{FE})$ are the shape functions. Throughout this study two types of elements are used: 2-noded linear truss elements for 1D problems and 4-noded bilinear plane stress/strain elements for 2D problems.

For the 1D case, the stiffness matrix $\boldsymbol{K}^e$, and lumped mass matrix $\boldsymbol{M}^e$ of the truss element can be taken directly as [154]:

$$\boldsymbol{K}^e = \frac{AE}{l_e}\begin{bmatrix} 1 & -1 \\ -1 & 1 \end{bmatrix} = k^{FE}\begin{bmatrix} 1 & -1 \\ -1 & 1 \end{bmatrix}, \quad (3.61a)$$

$$\boldsymbol{M}^e = \frac{\rho A l_e}{2}\begin{bmatrix} 1 & 0 \\ 0 & 1 \end{bmatrix} \quad (3.61b)$$

where, l_e is the length of the element, E is the Young's Modulus and A is the cross-sectional area of the truss. These element matrices are used directly for the assembly of the global matrices.

For the 2D case, the stiffness and mass matrices are extracted from the variational formulation described in Eq. (3.59) and their values are approximated numerically. The shape functions for a bilinear element are defined as [18]:

$$\boldsymbol{N}^j = \begin{bmatrix} N_1^j & 0 & \cdots & N_4^j & 0 \\ 0 & N_1^j & \cdots & 0 & N_4^j \end{bmatrix}, j = 1, 2, \dots, n_{en} \tag{3.62}$$

where, n_{en} is the total number of elements used for the discretization of Ω^{FE}. Then, using Voigt notation, the strain $\boldsymbol{\varepsilon}(\boldsymbol{x}^{FE}) = \{\varepsilon_{xx}, \varepsilon_{yy}, \varepsilon_{xy}\}^T$ is approximated as:

$$\boldsymbol{\varepsilon}(\boldsymbol{x}^{FE}) \approx \sum_{i=1}^{N_{np}} \boldsymbol{B}_i(\boldsymbol{x}^{FE})\boldsymbol{u}_i = \boldsymbol{BU}, \tag{3.63}$$

where $\boldsymbol{B} = \boldsymbol{B}(\boldsymbol{x}^{FE})$ is defined as:

$$\boldsymbol{B}_i = \begin{bmatrix} \partial N_i/\partial x & 0 \\ 0 & \partial N_i/\partial y \\ \partial N_i/\partial y & \partial N_i/\partial x \end{bmatrix}. \tag{3.64}$$

The discrete form of Eq. (3.59) can thus be written as:

$$\boldsymbol{M}^{cons}\ddot{\boldsymbol{U}} + \boldsymbol{K}^{FE}\boldsymbol{U} = \boldsymbol{F}^{FE}. \tag{3.65}$$

where, $\boldsymbol{F}^{FE}$ is the external force vector, $\boldsymbol{M}^{cons}$ is the consistent mass matrix and $\boldsymbol{K}^{FE}$ is the stiffness matrix with:

$$\boldsymbol{M}^{con} = \sum_{i=1}^{N_{en}} \int_{\Omega_i} \rho \boldsymbol{N}^T \boldsymbol{N} d\Omega \,, \boldsymbol{K}^{FE} = \sum_{i=1}^{N_{en}} \int_{\Omega_i} \boldsymbol{B}^T \boldsymbol{E} \boldsymbol{B} d\Omega \tag{3.66}$$

where, N_{en} is the total number of elements and Ω_i is the integration domain of the i^{th} element. A 2×2 Gauss approximation is used for the evaluation of the integrals in Eq. (3.66). Since explicit time integration is used for the dynamic problems, it is computationally more efficient to use the lumped mass matrix in Eq. (3.65). A simple row summation process is used and the lumped mass matrix $\boldsymbol{M}^{FE}$ is defined as:

$$M_{i,j}^{FE} = \sum_j M_{i,j}^{con} \tag{3.67}$$

and Eq. (3.65) is re-written as:

$$\boldsymbol{M}^{FE}\ddot{\boldsymbol{U}} + \boldsymbol{K}^{FE}\boldsymbol{U} = \boldsymbol{F}^{FE} \tag{3.68}$$

3.4.3 *The Extended Finite Element Method*

The standard FE method is not suitable for problems involving strong or weak discontinuities as it is a piecewise differential approximation. For such problems the mesh needs to be specifically constructed which can be challenging in cases where the discontinuity evolves. The requirement of conforming meshes is avoided with the use of XFEM, introduced in [31] and [155]. Of pivotal importance for the formulation of XFEM is the Partition of Unity Method (PUM) where appropriate enrichment functions are added to the approximation space. The particular choice of enrichment depends on the problem and the extra shape functions are specifically designed to capture known characteristics of the solution field (e.g. the singular field at the crack tip).

Here, the local extrinsic enrichment of the solution field is used where additional dofs are introduced at the nodal points of the elements that are cut by the discontinuity. The approximation of the displacement field can be written as [1]:

$$\boldsymbol{u}(\boldsymbol{x}) \approx \sum_{i=1}^{K} N_i(\boldsymbol{x}^{FE})\boldsymbol{u}_i + \sum_{j=1}^{M} N_j(\boldsymbol{x}^{FE})\psi(\boldsymbol{x}^{FE})\boldsymbol{a}_j, \tag{3.69}$$

where, K is the number of nodal points in the computational domain, $\boldsymbol{u}_i$ are the nodal displacements, $N_i(\boldsymbol{x}^{FE})$ are the standard FE shape functions, M is the number of enriched nodes, $N_j(\boldsymbol{x}^{FE})$ are the shape functions of the enriched part, $\psi(\boldsymbol{x}^{FE})$ is the enrichment function and $\boldsymbol{a}_j$ are the enriched nodal values. In practice, the shape functions of the enriched part are usually selected to be the same as the standard ones. This approach is also adopted in the present study.

Since our strategy employs the PD model ahead of the crack tip, no crack tip enrichment is needed. Hence, the XFEM enrichment will only be used to capture the displacement jump across the crack body. The enrichment function used is the Heaviside sign function given as:

$$H(\boldsymbol{x}^{FE}) = \begin{cases} 1, & \varphi(\boldsymbol{x}^{FE}) > 0 \\ -1, & \varphi(\boldsymbol{x}^{FE}) < 0 \end{cases}, \tag{3.70}$$

where, $\varphi(\boldsymbol{x}^{FE}) = \left\|\boldsymbol{x}^{FE} - \boldsymbol{x}^{FE^*}\right\| sign\left(\boldsymbol{n}_\Gamma \cdot \left(\boldsymbol{x}^{FE} - \boldsymbol{x}^{FE^*}\right)\right)$ is the signed distance function with $\boldsymbol{x}^{FE^*}$ being the closest point to $\boldsymbol{x}^{FE}$ on the discontinuity and $\boldsymbol{n}_\Gamma$ the unit normal on the discontinuity surface [1].

Although the local enrichment of the elements is attractive in XFEM as it limits the additional computational burden, unavoidably some of the elements in the domain will have only a part

of their nodes enriched. These elements are usually termed “blending” or “partially enriched” elements (see [1] and [156]). In these elements the partition of unity concept of the shape functions is violated and this can affect significantly the convergence rate of the solution. In [157], Belytschko et. al. proposed the use of the shifted Heaviside enrichment function that vanishes within the blending elements. The crack tip enrichment commonly employed in the XFEM formulation is replaced by the introduction of the PD domain and only the shifted Heaviside enrichment is introduced in the FE approximation. Thus, the spurious terms that lead to PUM violation are avoided, and no additional treatment or introduction of special blending elements is required for our needs. Using the shifted enrichment, the displacement approximation described in Eq. (3.69) is re-written as:

$$\boldsymbol{u}(\boldsymbol{x}^{FE}) \approx \sum_{\mathrm{i}=1}^{K} N_i(\boldsymbol{x}^{FE})\boldsymbol{u}_i + \sum_{j=1}^{M} N_j(\boldsymbol{x}^{FE})\left(H(\boldsymbol{x}^{FE}) - H\left(\boldsymbol{x}_j^{FE}\right)\right)\boldsymbol{a}_j \tag{3.71}$$

It is noted that the second part of Eq. (3.71) vanishes if no enrichment takes place and the approximation of the displacement field reduces to the familiar FE approximation. Furthermore, only 2D fracture problems are included in this study and the FE mesh is constructed using 4-noded bilinear elements.

The introduction of the enrichment functions in the approximation necessitates modifications to the numerical integration over the enriched elements. The accuracy of Gauss integration can be improved by [1,156,158]: **i**) increasing uniformly the number of Gauss points, **ii**) partitioning the elements into sub-regions that conform with the discontinuity and **iii**) partitioning the elements into regular subregions. Here the numerical integration is performed by dividing the elements into four rectangular sub-regions and perform Gauss integration in each one using a 32×32 grid.

Dynamic crack branching is an open subject in fracture mechanics as no unified theory has been able to explain the phenomenon. Although the theoretical limit of the crack propagation velocity is the Rayleigh wave speed, experimental observations indicate that in some cases this limit is unattainable as branching occurs at lower values [159]. Various numerical models have been used in the literature to study the dynamic phenomenon; the interested reader can refer to [134,160] and the references therein. In their work, Ha and Bobaru [96] implemented the PD theory to study dynamic crack branching. A characteristic of PD is that it does not require additional criteria to signal the initiation of branching. This is something we seek to take advantage of in the proposed methodology. A property that is necessary though is the ability of XFEM to facilitate multiple cracks in a single element as well as crack intersections or junctions.

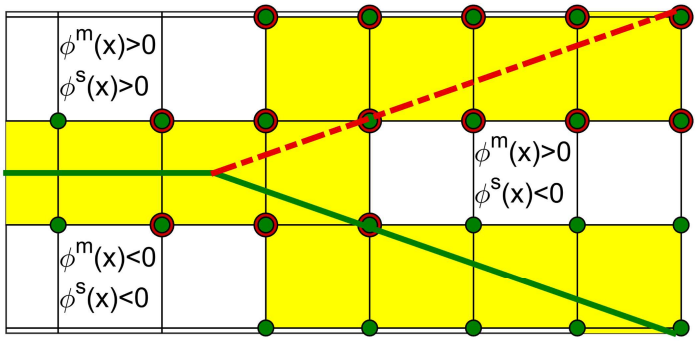

Figure 3.8: Enrichment strategy for multiple cracks and junctions. Green dots represent the nodes enriched due the main crack while red dots the nodes enriched due to the secondary crack.

Daux et. al. [1,161] were the first to implement the junction enrichment function to capture the discontinuous displacement field in an element where crack branching takes place. Later Zi et. al. [162] proposed the enrichment of multiple cracks by overlaying Heaviside step functions. The advantage of this method is that no special treatment is required for the junction as it is captured naturally. Consider the case of a crack with two branches, as illustrated in Figure 3.8. The initial crack and one of the branches are termed *main crack* (solid green line) and the other branch is termed *secondary crack* (dashed red line). A signed distance function $\phi^m(\boldsymbol{x}^{FE})$ and $\phi^s(\boldsymbol{x}^{FE})$ is assigned to the main and the secondary crack, respectively. The yellow elements are the elements whose basis functions have been enriched while the white elements are standard bilinear elements. The nodes whose support is intersected by the main crack are enriched in the absence of the secondary crack, indicated with green dots. Subsequently, the nodes whose support is intersected by the secondary crack are enriched in the absence of the main crack, indicated by larger red dots. Consequently, the elements that are cut by multiple cracks or contain a junction will be enriched multiple times. This happens because a single step function is not adequate to capture the complex discontinuous displacement field in these elements [163]. Following [163], the displacement field in an element with multiple cracks is approximated as:

$$\boldsymbol{u}(\boldsymbol{x}^{FE}) \approx \sum_{i=1}^{K} N_i(\boldsymbol{x}^{FE})\boldsymbol{u}_i + \sum_{j=1}^{M} N_j^m(\boldsymbol{x}^{FE})\left(H(\boldsymbol{x}^{FE}) - H\left(\boldsymbol{x}_j^{FE}\right)\right)\boldsymbol{a}_j^m + \sum_{k=1}^{G} N_j^s(\boldsymbol{x}^{FE})\left(H(\boldsymbol{x}^{FE}) - H(\boldsymbol{x}_k^{FE})\right)\boldsymbol{a}_k^s \tag{3.72}$$

where, M and G are the total number of nodes due to the main and the secondary crack, respectively, $\boldsymbol{a}_j^m$ are the enriched dofs associated with the main crack and $\boldsymbol{a}_k^s$ are the dofs

associated with the secondary crack. In the element where the crack junction takes place, the approximation is modified to:

$$\boldsymbol{u}(\boldsymbol{x}^{FE}) \approx \sum_{i=1}^{K} N_i(\boldsymbol{x}^{FE})\boldsymbol{u}_i + \sum_{j=1}^{M} N_j^m(\boldsymbol{x}^{FE})\left(H(\boldsymbol{x}^{FE}) - H\left(\boldsymbol{x}_j^{FE}\right)\right)\boldsymbol{a}_j^m + \sum_{k=1}^{G} N_j^s(\boldsymbol{x}^{FE})\left(J(\boldsymbol{x}^{FE}) - J(\boldsymbol{x}_k^{FE})\right)\boldsymbol{a}_k^s \tag{3.73}$$

where, $J(\boldsymbol{x}^{FE})$ is the junction function defined as:

$$J(\boldsymbol{x}^{FE}) = \begin{cases} H\left(\varphi^m(\boldsymbol{x}^{FE})\right), & \varphi^m(\boldsymbol{x}^{FE}) < 0 \\ H\left(\varphi^s(\boldsymbol{x}^{FE})\right), & \varphi^m(\boldsymbol{x}^{FE}) > 0 \end{cases} \tag{3.74}$$

Depending on the specific element and the problem addressed (i.e. is there a crack in Ω^{FE}? how many cracks exist in the same element? do the cracks intersect?) either the displacement approximations described in Eqs. (3.71), (3.72) or (3.73) is used.

Following [1], the XFEM approximation for a 2D problem can be written more compactly by introducing:

$$N_i^{std}(\boldsymbol{x}^{FE}) = \begin{bmatrix} N_i(\boldsymbol{x}^{FE}) & 0 \\ 0 & N_i(\boldsymbol{x}^{FE}) \end{bmatrix} \tag{3.75a}$$

$$N_i^{enr}(\boldsymbol{x}^{FE}) = \begin{bmatrix} N_i(\boldsymbol{x}^{FE})\left(H(\boldsymbol{x}^{FE}) - H\left(\boldsymbol{x}_j^{FE}\right)\right) & 0 \\ 0 & N_i(\boldsymbol{x}^{FE})\left(H(\boldsymbol{x}^{FE}) - H\left(\boldsymbol{x}_j^{FE}\right)\right) \end{bmatrix} \tag{3.75b}$$

and the XFEM approximation is written as:

$$\boldsymbol{u}(\boldsymbol{x}^{FE}) \approx \boldsymbol{N}^{std}\boldsymbol{u} + \boldsymbol{N}^{enr}\boldsymbol{a} = \boldsymbol{N}^{enh}\overline{\boldsymbol{u}}, \tag{3.76}$$

where, $\boldsymbol{N}^{enh} = \{\boldsymbol{N}^{std}, \boldsymbol{N}^{enr}\}$ and $\overline{\boldsymbol{u}} = \{\boldsymbol{u}^T, \boldsymbol{a}^T\}^T$.

Similarly, the matrices of derivatives are defined as:

$$B_i^{std}(\boldsymbol{x}^{FE}) = \begin{bmatrix} \partial N_i/\partial x & 0 \\ 0 & \partial N_i/\partial y \\ \partial N_i/\partial y & \partial N_i/\partial x \end{bmatrix} \tag{3.77a}$$

$$B_i^{enr}(\boldsymbol{x}^{FE}) = \begin{bmatrix} \partial N_i/\partial x\left(H(\boldsymbol{x}^{FE}) - H\left(\boldsymbol{x}_j^{FE}\right)\right) & 0 \\ 0 & \partial N_i/\partial y\left(H(\boldsymbol{x}^{FE}) - H\left(\boldsymbol{x}_j^{FE}\right)\right) \\ \partial N_i/\partial y\left(H(\boldsymbol{x}^{FE}) - H\left(\boldsymbol{x}_j^{FE}\right)\right) & \partial N_i/\partial x\left(H(\boldsymbol{x}^{FE}) - H\left(\boldsymbol{x}_j^{FE}\right)\right) \end{bmatrix}. \tag{3.77b}$$

The strain field can thus be approximated as:

$$\boldsymbol{\varepsilon}(\boldsymbol{x}^{FE}) \approx \boldsymbol{B}^{std}\boldsymbol{u} + \boldsymbol{B}^{enr}\boldsymbol{a} = \boldsymbol{B}^{enh}\overline{\boldsymbol{u}}, \tag{3.78}$$

where, $\boldsymbol{B}^{enh} = \{\boldsymbol{B}^{std}, \boldsymbol{B}^{enr}\}$. Using these definitions in the weak formulation of the problem the stiffness matrix $\boldsymbol{K}^{FE}$, and the consistent mass matrix $\boldsymbol{M}^{con}$, can be obtained, in an analogous way to the process described for the FE case. The stiffness matrix can be computed using:

$$\boldsymbol{K}^{FE} = \begin{bmatrix} \boldsymbol{K}^{std,std} & \boldsymbol{K}^{std,enr} \\ \boldsymbol{K}^{enr,std} & \boldsymbol{K}^{enr,enr} \end{bmatrix}, \tag{3.79}$$

where,

$$\boldsymbol{K}^{std,std} = \sum_{i=1}^{N_{en}} \int_{\Omega_i} (\boldsymbol{B}^{std})^T \boldsymbol{D}\boldsymbol{B}^{std} d\Omega \tag{3.80a}$$

$$\boldsymbol{K}^{std,enr} = \sum_{i=1}^{N_{en}} \int_{\Omega_i} (\boldsymbol{B}^{std})^T \boldsymbol{D}\boldsymbol{B}^{enr} d\Omega \tag{3.80b}$$

$$\boldsymbol{K}^{enr,std} = \sum_{i=1}^{N_{en}} \int_{\Omega_i} (\boldsymbol{B}^{enr})^T \boldsymbol{D}\boldsymbol{B}^{std} d\Omega \tag{3.80c}$$

$$\boldsymbol{K}^{enr,enr} = \sum_{i=1}^{N_{en}} \int_{\Omega_i} (\boldsymbol{B}^{enr})^T \boldsymbol{D}\boldsymbol{B}^{enr} d\Omega \tag{3.80d}$$

Similarly, the consistent mass matrix can be computed. The superscripts std and enr that appear in Eqs. (3.75) – (3.80) refer to the standard and the enriched dofs. It is noted that for an element that contains two cracks or the junction of two cracks, the dimensions of local stiffness matrix will be 24×24, referring to 8 standard and 16 enriched dofs.

Problems under both static and dynamic conditions will be considered using the XFEM formulation. As mentioned in a previous paragraph, explicit time integration schemes are commonly used to capture the fracture process. However, use of the consistent mass matrix can increase significantly the computational burden. In their work, Belytschko et. al. [164] pointed out that if conventional mass lumping techniques are implemented, the critical time step tends to zero as the discontinuity approaches the nodes of the element [165]. A method to circumvent this restriction was proposed by Menouillard et. al. in [166], the lumped mass matrix was approximated by considering kinetic energy conservation for some special motions of the body. The methodology provides a lower bound on the critical time step, even in cases where the discontinuity coincides with a nodal position.

Menouillard derived the lumped mass matrix for the case where a Heaviside enrichment is used. Xu et. al. [163] followed the formulation of Menouillard to propose a mass lumping approximation when the shifted Heaviside enrichment is used. The methodology is also extended to cases where multiple discontinuities are present. Consider a 2D bilinear element. Following [163] and [166], the element mass associated with the enriched nodes of the element is computed as:

$$m = \rho \int \psi^m(\boldsymbol{x}^{FE})^2 \, d\Omega, \tag{3.81}$$

where, $\psi^m(\boldsymbol{x}^{FE}) = \sum_{j=1}^{4} N_j^m(\boldsymbol{x}^{FE}) \left(H(\boldsymbol{x}^{FE}) - H\left(\boldsymbol{x}_j^{FE}\right) \right)$ is the particular enrichment function selected (in this case the shifted Heaviside enrichment) and ρ is the density. Then, the element mass is distributed to the nodes of the elements and subsequently, to the respective dofs. Xu et. al. [163] present a weighting procedure for the distribution of the mass considering the area of each subarea in the element that is defined by the crack. The integral in Eq. (3.81) can be approximated numerically using the Gauss integration procedure that was described earlier. Then, the weighted mass for each node can be approximated following [163] by creating a uniform grid within the element and using the expression:

$$m_J = \frac{n_{subJ}^{intI}}{n_{ele}^{int} \cdot n_{subJ}^{nodeI}} \cdot m, \tag{3.82}$$

where, $J = 1, 2, 3, 4$ is the element node number, n_{subJ}^{intI} is the number of grid points in the subarea that contains node J, n_{ele}^{int} is the total number of grid points and n_{subJ}^{nodeI} is the number of nodes in the subarea that contains node number J. An illustration of the mass approximation is presented in Figure 3.9. In this case $n_{ele}^{int} = 16$, $n_{sub1}^{intI} = 3$, $n_{sub2}^{intI} = n_{sub3}^{intI} = n_{sub4}^{intI} = 13$, $n_{sub1}^{nodeI} = 1$ and $n_{sub2}^{nodeI} = n_{sub3}^{nodeI} = n_{sub4}^{nodeI} = 3$. Following Eq. (3.82) the mass values associated with each node are $m_1 = 3/16\, m$ and $m_2 = m_3 = m_4 = 13/(3 \cdot 16)\, m$.

The process is repeated if multiple cracks or a junction exists in the element. For the secondary crack in the example depicted in Figure 3.8, Eq. (3.81) would be repeated in the absence of the main crack and the subscript $(\cdot)^m$ would be replaced with $(\cdot)^s$. The weighted mass is computed again using Eq. (3.82) but this time the mass is associated with the dofs of the secondary crack.

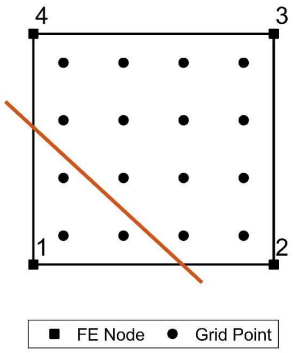

Figure 3.9: Illustration of the mass approximation for a FE cut by a crack.

For the standard dofs, the mass is computed using the conventional row summation technique on the consistent mass matrix as:

$$\boldsymbol{M}_{i,i}^{std,std} = \sum_{j} M_{i,j}^{consistent}. \tag{3.83}$$

Then the final mass matrix is:

$$\boldsymbol{M}^{FE} = \begin{bmatrix} \boldsymbol{M}^{std,std} & \boldsymbol{0} \\ \boldsymbol{0} & \boldsymbol{M}^{enr,enr} \end{bmatrix}, \tag{3.84}$$

where, $\boldsymbol{M}^{enr,enr}$ is the diagonal lumped mass matrix associated with the enriched dofs. The elements of $\boldsymbol{M}^{enr,enr}$ are defined using Eq. (3.82). Finally, using the definitions in Eqs. (3.79) and (3.84), the discretized system of equations is written in matrix notation as:

$$\boldsymbol{M}^{FE}\ddot{\overline{\boldsymbol{u}}} + \boldsymbol{K}^{FE}\overline{\boldsymbol{u}} = \boldsymbol{F}^{FE}. \tag{3.85}$$

Obviously, in the absence of enrichment, Eq. (3.85) reduces to Eq. (3.68).

4 Uncoupled Thermomechanics using FE meshes and PD grids

In a solid body, the thermal and deformation states are interdependent. In certain cases, this interdependency can be neglected leading to uncoupled thermomechanical models in which, only the influence of the temperature field on the deformation is present. In this chapter the thermomechanical response of ceramic specimens is investigated. Alumina specimens are subjected to sudden and extreme temperature variations that lead to the formation of cracks. As a simplification, it is assumed here that the thermal cracking does not affect the heat transfer and the uncoupled solutions will be used. This hypothesis has been used extensively in the literature (e.g. [167]), as cracks are expected to appear parallel to the direction of heat transfer.

The FE method is used first to approximate the evolution of the temperature field through the solution of the heat transfer problem. Subsequently, the PD model simulates the mechanical response of the specimen due to the application of the resulting thermal load. Besides, due to the brittle nature of ceramics, the PD theory is a suitable candidate for the simulation of the fracture process. The two solutions are not used concurrently but instead sequentially. Therefore, one-way information passing is achieved from the FE to the PD model. This way it is attempted to combine the use of FE mesh with PD grid for the analysis of this problem. The benefits of this approach are:

i). The numerical solution of the heat transfer problem, assuming local interactions, is already well understood [138]. Since the assumption for uncoupled thermomechanical analysis is applicable, available analytical solutions could also be used for simple cases. Blocking this option in our study is the temperature dependency of the thermal and mechanical material properties as well as the effects associated with radiative heat transfer. This leads to a nonlinear heat transfer problem and the resulting temperature field is approximated numerically with the FE method.

ii). The computational efficiency of the FE method for the approximation of partial differential equations is exploited to simulate the temperature distribution as, according to our assumption, heat transfer is not affected from the onset of fracture.

iii). The inherent ability of the PD theory to simulate complex crack patterns is beneficial as multiple cracks are expected to nucleate and propagate in the material.

iv). The time integration procedure implemented for the thermal transfer and the mechanical problem becomes independent. The temporal resolution requirement during heat transfer can be different that the resolution required for the mechanical response [168]. Additionally, different solvers might be used for each case (i.e. explicit or implicit) depending on the application.

4.1 Thermal Cracking of Ceramic Refractories

Ceramics and refractories are an extremely diverse family of materials that have met wide applicability across many industries. They exhibit high compressive strength, hardness and melting point, low thermal and electrical conductivity as well as the ability to maintain their properties at elevated temperatures. Due to their excellent performance under elevated temperatures, typical applications include: dies for metal forming, liquid steel technologies, thermal barrier coatings and others [169,170]. Aluminium oxide (Al_2O_3) and zirconia (ZrO_2) are two commonly used engineering oxide ceramics [171]. However, the inherent brittle nature of ceramic materials makes them prone to cracking when subjected to sudden temperature variations. Due to its paramount importance, thermal shock induced cracking in ceramic materials has been studied by many researchers over the last decades. Plentiful studies in the literature, both numerical and experimental, aim to investigate the maximum temperature change a brittle material can withstand prior to cracking, thus estimating its thermal shock resistance [172–175,167,176]. Furthermore, thermal fatigue due to repeated temperature fluctuations is of high academic and industrial interest [177,178].

Investigations on the thermal induced stress field, have illustrated that specimens undergoing cold shock develop tensile stresses near the boundary and compressive stresses in the interior [167,175]. The reversed effect is observed during heating of the specimen where tensile stresses develop in the interior. Lu and Fleck [175] presented a systematic classification of solids based on their thermal resistance. Cracking of the material was investigated assuming a pre-existing crack embedded in the area under tension and the resulting stresses were compared with the maximum allowed. Bahr et al. [179] investigated the emerging crack patterns after water quenching of pre-heated quartz and glass plates and simulated the crack evolution using multiple-crack models [167].

Early investigations were carried out assuming pre-existing crack or cracks in the medium. More recent studies on thermal shock employ elaborate lattice [180], nonlocal ([181] and [182]) and gradient ([173] and [183]) models to simulate the initiation and propagation of cracks as well as approaches for the incorporation of microstructural characteristics [184,185]. Additionally, studies on the induced thermal stresses have illustrated that it is crucial to

account for temperature dependent material parameters in the simulations [168,174]. Usually, materials tend to exhibit a softening behaviour as the temperature increases due to decrease of Young's modulus. As reported in [174], not considering the temperature dependency of the material properties tends to lead to underestimation of the actual thermal shock resistance. In their work, Papathanasiou et al. [168] carried out a detailed investigation on the thermomechanical response of ceramic refractories under extreme temperature changes. The nonlinear heat equation was solved using the FE method for a 2D problem, taking into consideration radiation heat exchange and temperature dependant thermal and elastic material properties. The calculated temperature field was subsequently used to determine the induced stress field and the results were compared with those arising from linear models for different values of the Biot number.

As state earlier, the FE method is used to approximate the temperature field and subsequently, the PD model simulates the mechanical response of the specimen. First, the experimental and numerical results for cold shocked alumina specimens reported by Li et. al. in [182], are compared with the results of the proposed method for validation purposes. It is noted that in [182], an analytical solution of the heat transfer problem was used as input to a damage model to capture the fracture process. Then the proposed method is used to simulate cold and hot shocked specimens, considering the temperature dependence of the material properties. To the best of the authors' knowledge, numerical simulations for hot shock related analysis are scarcer, while some experimental procedures have been reported to yield results that are not easily reproducible [186]

4.2 Problem Definition

Thermal shock is divided into two distinct categories: "*hot*" shock and "*cold*" shock. During hot shock, an object is introduced to an environment of elevated temperature and the temperature of the material increases rapidly. On the other hand, in cold shock, the object is introduced to an environment of much lower temperature and its temperature rapidly decreases. Both scenarios are crucial for the identification of the maximum temperature variations a material can withstand prior to failure.

Here, the problem of thin rectangular alumina (Al_2O_3) specimens subjected to sudden and extreme temperature variations is studied numerically. Both cold and hot shock scenarios are considered to investigate the different damage mechanisms that develop in each case. For the cold shock case the pre-heated (to a specified temperature T_0) specimen is assumed to undergo sudden heat exchange with a surrounding fluid of temperature $T_\infty = 293.15\mathrm{K} \ll T_0$. In the hot shock case, the specimen is assumed initially at room temperature $T_0 = 293.15\mathrm{K}$

and then heated due to exposure at an ambient with temperature $T_\infty \gg T_0$. Various values of T_0 for the cold shock and T_∞ for the hot shock will be considered during the simulations.

In all cases heat transfer is assumed to take place only in the xy plane. Figure 4.1, illustrates the physical and numerical model under investigation. The specimen's half-length and thickness are $L = 5H$ and $W = 0.2H$ respectively where H is half the height. Taking advantage of the system's symmetry along $y-$ and $x-$ axes, only one quadrant of the initial domain is simulated. Adiabatic conditions apply to the edges that coincide with lines of symmetry. Convection and radiation losses occur on the other two edges, as shown in Figure 4.1. Initially the specimen is assumed to be at a uniform temperature T_0 and stress free. The material is linear, isotropic, homogeneous and in pristine condition at the initial configuration.

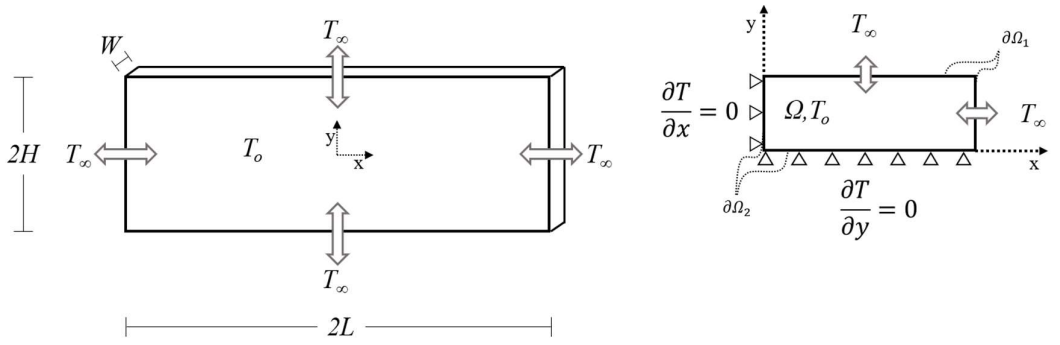

Figure 4.1: Physical (left) and numerical (right) model of the alumina specimen subjected to 2D heat transfer.

Due to the severe temperature variations refractories experience throughout their lifetime, it is imperative to include the temperature dependency of the thermal and elastic properties. This is reflected by the vast scientific effort to accurately capture the variation of these parameters in a wide range of temperatures [187–190]. Based on experimental data for polycrystalline alumina, the temperature dependency of the specific heat capacity c_p and thermal conductivity k can be approximated with adequate accuracy by inverse power laws [168]:

$$k(T) = k_0 + k_1 T^{-1}, \ \mathrm{Wm^{-1}K^{-1}}, \tag{4.1a}$$

$$c_p(T) = c_0 + c_1 T^{-1}, \ \mathrm{Jkg^{-1}K^{-1}} \tag{4.1b}$$

where, T is the absolute temperature, k_0, k_1, c_0 and c_1 are constants with values -4.5536, 12227, 1429.4 and -197620, respectively. Although more elaborate and accurate functions have been described in [187], the expressions from Eqs. (4.1) are adopted here due to their simple form. It is obvious that as temperature increases, the specific heat capacity increases

while the thermal conductivity decreases. This is expected, as materials at higher temperatures tend to store heat instead of conducting it [168,189].

The temperature field is determined considering thermal convection and radiation/irradiation between the material and its environment. Heat exchange can be estimated through the implementation of the Newton cooling law and Stefan-Boltzmann law. To fully characterize heat transfer, two additional parameters must be defined: the emissivity $\varepsilon \in [0,1]$ and the heat transfer coefficient h. Heat exchange can then be written as:

$$q_{\text{surf}} = q_{\text{conv}} + q_{\text{rad}} = h(T - T_{\infty}) + \varepsilon\sigma(T^4 - T_s^4), \tag{4.2}$$

where, $\sigma = 5.67\ 10^{-8}\ \text{W}^{-2}\text{K}^{-4}$, is the Stefan-Boltzmann constant and T_s is the temperature at the surface of the solid. Following [168], heat loss due to radiation is taken as $\varepsilon = 0.80$.

Estimation of the convective heat transfer coefficient h, is crucial for the accurate simulation of the heat transfer between alumina and the surrounding environment. Various experimental configurations have been proposed in the literature (e.g. [191,192]) but as reported in [169], the results exhibit high dispersion. Following [182], the value $h = 50{,}000\ \text{Wm}^{-2}\text{K}^{-1}$ is employed, as a representative value of the heat transfer between a liquid and a solid (water quenching for cold shock or molten steel for hot shock).

The temperature dependence of alumina's mechanical properties needs also to be accounted for. The elastic modulus E and fracture toughness K_C, decrease as the temperature increases while, the thermal expansion coefficient α and Poisson's ratio v, increase. Despite the fact that the temperature dependency of the thermal expansion coefficient is in general nonlinear, a simple linear function can approximate the experimental observations with adequate accuracy [168,189]. Determining the fracture toughness of a material during the initiation of a crack is difficult [2]. Experimental studies have illustrated that the fracture toughness of high purity alumina tends to decrease as temperature increases. Following the observations reported in [193], the fracture toughness of alumina, expressed in terms of stress intensity, is assumed to decrease linearly as temperature increases. In the subsequent analyses, the use of the Bond-Based PD model restricts the values of the Poisson's ratio to $v = 0.33$ for plane stress problems [29]. Nevertheless, the temperature variation of the Poisson's ratio is also included for completeness. Although the Poisson's ratio of the refractory material selected is different than the value enforced by the PD theory (which is independent of the temperature variation) the results obtained indicate that the prediction of failure due to thermal shock is reasonably accurate. The elastic and mechanical properties of alumina are calculated using:

$$E(T) = E_0[1 - \lambda_1(T - T_0)] \tag{4.3a}$$

$$v(T) = v_0[1 + \lambda_2(T - T_0)] \tag{4.3b}$$

$$a(T) = a_0[1 + \lambda_3(T - T_0)] \tag{4.3b}$$

$$K_C(T) = K_0[1 - \lambda_4(T - T_0)]. \tag{4.3b}$$

where, $E_0 = 370\text{GPa}$, $v_0 = 0.25$, $a_0 = 6 \cdot 10^{-6}\text{K}^{-1}$ and $K_0 = 3.3\text{MPa}\sqrt{\text{m}}$ are the elastic modulus, Poisson's ratio, thermal expansion coefficient and fracture toughness of polycrystalline alumina at room temperature and $\lambda_1 = 1.2 \cdot 10^{-4}\text{K}^{-1}$, $\lambda_2 = 6.9 \cdot 10^{-5}\text{K}^{-1}$, $\lambda_3 = 9 \cdot 10^{-4}\text{K}^{-1}$, and $\lambda_4 = 1.567 \cdot 10^{-4}\text{K}^{-1}$ are constants. Using Eqs. (4.1) and (4.3), the temperature dependency of the thermal and elastic material properties is illustrated in Figure 4.2. In the following paragraphs, the fracture process will be related to the critical energy release rate G_C. An estimate of the fracture toughness (using Linear Elastic Fracture Mechanics for relatively brittle materials like alumina and plane stress assumptions) is $G_C = K_{IC}^2/E$.

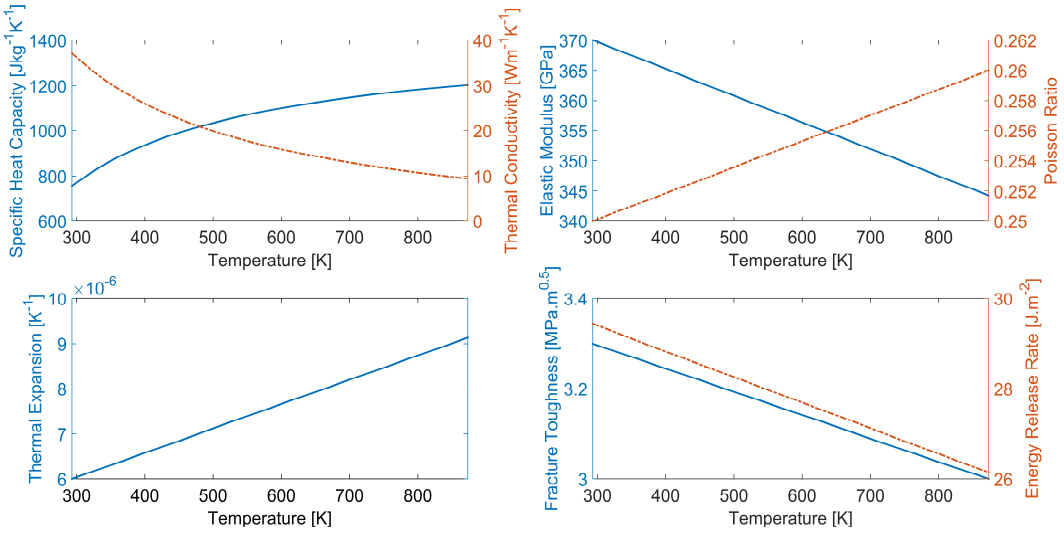

Figure 4.2: Temperature dependency of thermal and elastic properties for polycrystalline alumina (Al_2O_3).

4.3 Heat transfer simulation

When the thermal properties are assumed constant, solution of the mixed boundary problem illustrated in Figure 4.1, can be obtained directly from available analytical solutions [194]. When the thermal properties are functions of temperature, analytical solutions are not possible and the temperature field needs to be approximated numerically [195]. The FE method is commonly employed for the approximation of complex thermomechanical problems when

analytical solutions are not available. Here, Lagrange elements with bilinear interpolation of the temperature field are used for the solution of the nonlinear heat transfer problem [168].

Following the derivation presented in [168], the nondimensional spatial and temporal parameters introduced are:

$$\hat{\xi}_x = H^{-1}x \tag{4.4a}$$

$$\hat{\xi}_y = H^{-1}\mathrm{y} \tag{4.4b}$$

$$\hat{t} = H^{-2}\kappa t \tag{4.4c}$$

where, the accent $\langle\hat{\cdot}\rangle$ is employed to indicate nondimensional values, $\kappa = k_{\mathrm{ref}}/(\rho c_{p,\mathrm{ref}})$ is the thermal diffusivity and k_{ref} and $c_{p,\mathrm{ref}}$ are the thermal conductivity and specific heat capacity at room temperature, respectively. The nondimensional temperature field:

$$\hat{\theta} = {T_0}^{-1}T, \tag{4.5}$$

is introduced. The governing equations and the FE solution approach adopted are the same as in Papathanasiou et al. [168].

The mechanical response of the specimen is approximated by implementing the PD theory. The pairwise force function described in Eq. (3.21) is used in the PD equation of motion and following the same collocation method described in paragraph 3.1.4 for its discretization lead to:

$$\rho\ddot{\boldsymbol{d}}_i = \sum_{j=1}^{M} v(\boldsymbol{\xi}_{i,j})\lambda(\boldsymbol{\xi}_{i,j})c(\boldsymbol{\xi}_{i,j})\left(s_{i,j} - \alpha\theta_{i,j}\right)\frac{\boldsymbol{d}_j - \boldsymbol{d}_i + \boldsymbol{x}_j - \boldsymbol{x}_i}{\left\|\boldsymbol{d}_j - \boldsymbol{d}_i + \boldsymbol{x}_j - \boldsymbol{x}_i\right\|}V_j, \tag{4.6}$$

where, the body forces $\boldsymbol{b}_i$ have been neglected as they are not relevant for this problem and $s_{i,j}$ is used for short to denote the stretch of the bond that connects particle i and j. Furthermore, the volume correction $v(\boldsymbol{\xi}_{i,j})$ and surface correction $\lambda(\boldsymbol{\xi}_{i,j})$ factors are also introduced in Eq. (4.6). The shape of the micromodulus $c(\boldsymbol{\xi})$ is assumed to be constant and its value is computed as described in Eq. (3.11) for a plane stress problem.

Using the characteristic length and time scales introduced in Eqs. (4.4), the position vector $\hat{\boldsymbol{x}}$ and the displacement vector $\hat{\boldsymbol{d}}$, are defined as $\hat{\boldsymbol{x}} = H^{-1}\boldsymbol{x}$ and $\hat{\boldsymbol{d}} = H^{-1}\boldsymbol{d}$. The following nondimensional values can then be defined:

$$\hat{\ddot{\boldsymbol{d}}} = \left(\frac{k_{\mathrm{ref}}}{c_{p,\mathrm{ref}}\rho}\right)^{-2} H^3\ddot{\boldsymbol{d}} \tag{4.7a}$$

$$\hat{c}(\boldsymbol{\xi}_{i,j}) = \frac{9E}{\pi\hat{\delta}^3\widehat{W}} = \frac{9E}{\pi\delta^3 W}H^4 = c(\boldsymbol{\xi}_{i,j})H^4 \tag{4.7b}$$

$$\hat{V} = \widehat{\Delta x}^2\widehat{W} = H^{-3}V \tag{4.7c}$$

where, $\widehat{\Delta x}$ is the lattice spacing considered for the spatial discretization. Using Eqs. (4.7) into Eq. (4.6), the dimensionless uncoupled equation of motion is obtained as:

$$\frac{{k_0}^2}{\rho {c_0}^2 H^2}\ddot{\widehat{\boldsymbol{d}}}_i = \sum_{j=1}^{M}\hat{C}_{i,j}\left(s_{i,j} - \alpha\hat{\theta}_{i,j}\right)\frac{\widehat{\boldsymbol{d}}_j - \widehat{\boldsymbol{d}}_i + \widehat{\boldsymbol{x}}_j - \widehat{\boldsymbol{x}}_i}{\left\|\widehat{\boldsymbol{d}}_j - \widehat{\boldsymbol{d}}_i + \widehat{\boldsymbol{x}}_j - \widehat{\boldsymbol{x}}_i\right\|}\hat{V}_j, \tag{4.8}$$

where, $\hat{C}(\boldsymbol{\xi}_{i,j}) = v(\boldsymbol{\xi}_{i,j})\lambda(\boldsymbol{\xi}_{i,j})c(\boldsymbol{\xi}_{i,j})$. Similar to the previous examples, boundary conditions are applied by introducing an additional fictitious material layer of thickness δ. The nondimensional temperature field $\hat{\theta}$, approximated using the FE method, is subsequently applied on the PD model thorough $\hat{\theta}_{i,j}$.

4.4 Numerical Results

4.4.1 *Cold Shock and Model Verification*

The sudden nature of material cracking during cold shock has impaired scientists to experimentally observe and monitor the phenomenon [191]. Additionally, the rapid fracture of the material creates complex crack patterns that are difficult to simulate when implementing traditional continuum fracture mechanics. The tensile stresses developing on the surface of the material leads to the initiation of surface breaking cracks [175]. Many methodologies have been proposed for the approximation of the stress field and stress intensity factors. More recent studies, also incorporate microstructural characteristics as well as effects due to the presence of micro cracks in the medium [185,196]. A distinctive characteristic of the final crack patterns that emerge, is the varying crack length that forms hierarchical classes of cracks [173,182]

Table 4.1: Temperature independent properties employed as specified in [182].

Thermal and Mechanical Properties for Al_2O_3		
E	370,000	MPa
ρ	3980	$\mathrm{kg/m^3}$
G_c	24.3	$\mathrm{J/m^2}$
h	50,000	$\mathrm{W/(m^2 \cdot K)}$
k	31	$\mathrm{W/(m \cdot K)}$
c	880	$\mathrm{J/(kg \cdot K)}$
a	$7.5 \cdot 10^{-6}$	$\mathrm{K^{-1}}$

The efficiency of the Bond-Based PD theory for numerical simulations of thermal shock cracking is evaluated by comparing the present methodology with the numerical and experimental results for Al_2O_3 specimens reported in [182]. To ensure compatibility and comparability of the results, the temperature dependency of the thermal and mechanical properties and the radiative heat transfer is initially neglected and the material parameters used in [182] are employed. The parameters used are summarized in Table 4.1.

Due to the geometry of the model, tensile stresses at the surface of the specimen are virtually uniform along the length. For that reason, to avoid de-bonding of wide areas of the upper surface and accurately capture the crack nucleation sites, sufficiently small time-steps must be used, otherwise cracks become time-step dependent. The transient solution allows for the extraction of dynamic characteristics. However, due to the restrictive maximum time step calculated from Eq. (3.47), dynamic simulation of the whole phenomenon is computationally unfeasible.

During the numerical experiments, it was observed that the fracture process can be divided into three phases: nucleation, propagation and arrest (Figure 4.3). The nucleation phase is very rapid and short in duration. The tensile stresses that develop on the outer boundary of the specimen lead to the formation of small cracks. These cracks however start to further propagate in the interior of the material after all initial cracks have formed. This signifies the beginning of the propagation phase. Finally, as the cracks propagate, they enter the compressive stresses that develop in the interior of the specimen and their extension is arrested. Similar observations have been reported in the literature [172,175,179].

Hence, the transient solution of the PD equation of motion is used to simulate crack nucleation and subsequently an incremental static solution (ignoring inertia effects) is used for the propagation phase till the final arrest. This allows for the simulation of the nucleation phase using a sufficiently small time increment that satisfies the stability criterion of the explicit time marching method while the final propagation of each crack is predicted using large time steps. Comparisons with similar numerical and experimental results from the relevant literature, that are presented in the following paragraphs, indicate that this approach leads to results of reasonable accuracy. To further accelerate the simulation, the loading (temperature) increment was increased during the static analysis, following a geometric sequence of $n = 300$ steps with common ratio, $r = 1.02$. That is, the discrete form of Eq. (4.8) is solved using the temperature distribution, calculated from the FE solution, at time instants $\Delta\hat{t}_{\mathrm{n}} = \Delta\hat{t}_0 r^{n-1}$. The initial time step during the transient solution is $\Delta\hat{t}_0 = 3.0\ 10^{-9}$ and the maximum time step $\Delta\hat{t}_{\max} = 0.05$. The nondimensional time step parameters $\Delta\hat{t}_{\mathrm{n}}$, $\Delta\hat{t}_0$ and $\Delta\hat{t}_{\max}$ are also

defined using Eq. (4.4). The solution implemented in each phase and the corresponding time step is illustrated schematically in Figure 4.3.

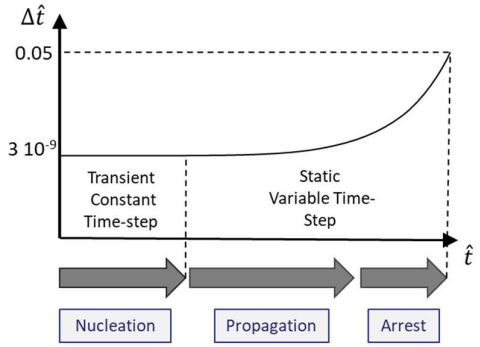

Figure 4.3: Variation of the time-step during the simulation of cold shock.

The geometry of the specimen is $50\text{mm} \times 10\text{mm} \times 1\text{mm}$, $(L \times H \times W)$ and only one quarter of the domain is considered. The half-height of the specimen is $H = 5\text{mm}$. The solution domain is discretized using $52{,}416$ particles corresponding to a grid spacing $\widehat{\Delta x} = 0.01$. A fictitious material layer of length $\hat{\delta}$ is added to enforce the boundary conditions and the PD horizon is set to $\hat{\delta} = 3.015\widehat{\Delta x}$, following the observations on macroscale problems reported in the literature [84,97,197]. The simulation is carried out for a total time $\hat{t}_{\text{total}} = 1$. A 200×40 structured grid was implemented for the FEM discretization. The temperature at the location of each PD particle is computed using linear interpolation on the results from the FEM (see Figure 4.4).

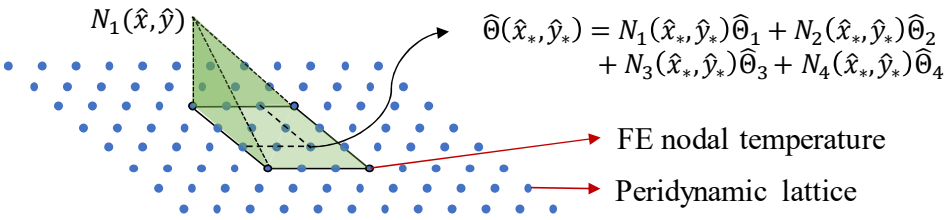

Figure 4.4: Qualitative illustration of the temperature field interpolation at the PD particles.

First, the evolution of the thermal shock induced cracks in an alumina specimen preheated at $T_0 = 773.15\text{K}$ and quenched into a fluid at room temperature $(T_\infty = 293.15\text{K})$, is investigated. In Figure 4.5, the initiation, propagation and final crack patterns are illustrated at various time steps. In the left column, the displacement of each PD particle in the lattice is displayed (displacements have been magnified by a factor of 100 for clarity). In the right column, the local damage index $\phi(\boldsymbol{x}, t)$ from Eq. (3.20) is illustrated to enhance visualization of the crack location.

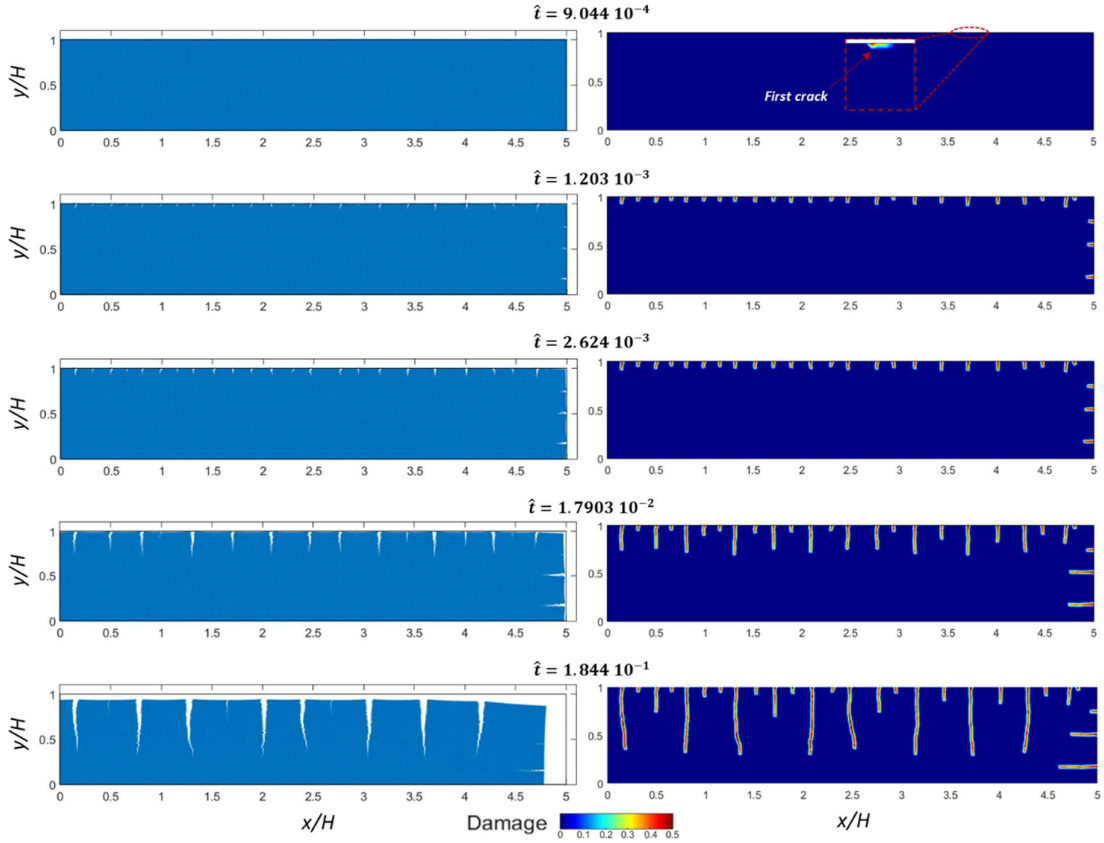

Figure 4.5: Crack evolution for a specimen preheated at $T_0 = 773.15\text{K}$ and quenched into water at ambient temperature ($T_\infty = 293.15\text{K}$).

According to the numerical results, the first crack nucleates at approximately $\hat{t} = 9.044\ 10^{-4}$ while the last one nucleates at $\hat{t} = 1.203\ 10^{-3}$, as illustrated in the first two rows of Figure 4.5. These time instants indicate the initiation and the completion of the nucleation phase. It is noted that after a crack nucleates, it does not start to propagate towards the interior of the material till after all cracks have emerged. This happens after $\hat{t} = 1.203\ 10^{-3}$ and at $\hat{t} = 2.624\ 10^{-3}$ the propagation of the cracks is illustrated. Very small variations in the crack lengths at the initial stages result to the formation of a periodic and hierarchical crack pattern, which is distinctive of cold shocked specimens. This is illustrated at $\hat{t} = 1.7903\ 10^{-2}$, where the hierarchical classes are evident. The mechanism responsible for this pattern is stress flow deviation from the short cracks due to shielding by the larger ones. At $\hat{t} = 1.844\ 10^{-1}$, the PD model predicts that crack propagation has been terminated for all cracks. In total three clear crack length classes can be identified in the final crack pattern.

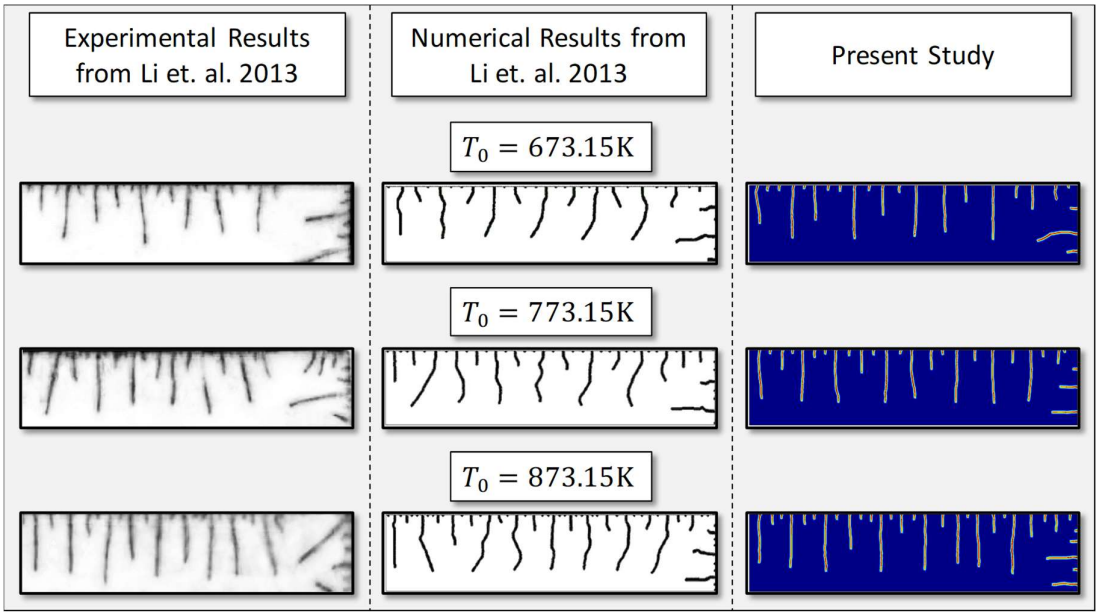

Figure 4.6: Comparison of the final crack paths obtained using the proposed method with the experimental and the numerical results presented by Li et. al. in [182].

The analysis is repeated for initial temperatures $T_0 = 673.15\text{K}$ and $T_0 = 873.15\text{K}$. The results for each temperature case are compared in Figure 4.6 with the experimental and numerical results presented by Li et. al. in [182]. The figures taken from [182] have been processed digitally to enhance clarity. The proposed approach can capture the periodic and hierarchical crack pattern that is typical in cold shock for all T_0 cases considered. Furthermore, it was also possible to capture the increase in the crack density that is observed when the difference between T_0 and T_∞ increases. Thus, using the proposed combination of FEM and PD is possible to replicate the phenomenon.

Aiming for a more detailed comparison, using the results presented in [182], the dimensionless crack length, defined as $\hat{l} = l/H$, is computed for all the initial temperatures considered. Following [182] the comparison presented in Figure 4.7, is carried out using the ratio N/N_{tot}, where, $N(\hat{l}_1, \hat{l}_2)$ is the number of cracks with crack length $\hat{l}_1 \leq \hat{l} \leq \hat{l}_2$ and N_{tot} is the total number of cracks. It is thus possible to compare the length of the cracks for each temperature and the number of cracks in each length level and identify the crack clusters that define the hierarchical levels.

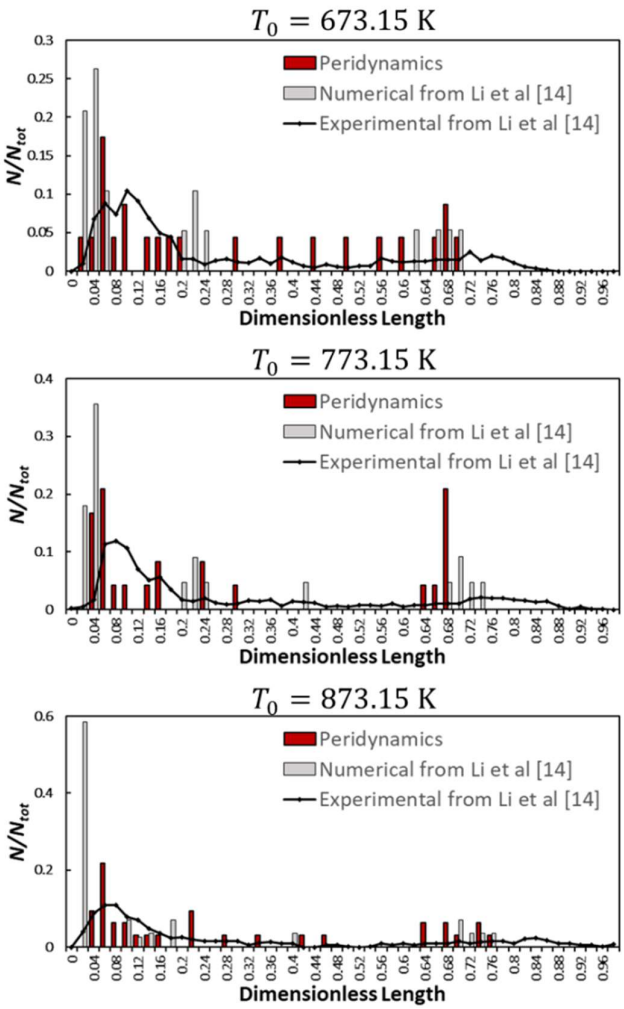

Figure 4.7: Histograms comparing the number of cracks at each length level between the numerical and experimental results presented in [182] and here.

Commenting on Figure 4.7, it is identified that the crack lengths in each hierarchical level, as derived from the numerical procedure suggested in [182], exhibit very small dispersion with respect to a central value. At the same time, these length class clusters appear to be slightly misplaced compared to the experimental results, (grey bars and black line in Figure 4.7). On the other hand, the crack lengths produced with the PD model exhibit a wider distribution that in the mean sense appears to describe better the experimental observations. In the case of the short hierarchical level specifically, the central value around which the numerical results of [182] cluster, underestimate the experimental findings. However, the results of the proposed method fit better underneath the curve. As the initial temperature increases, the length of the shortest hierarchical level shifts to the left. This effect was captured by both numerical models, with the PD model leading to better approximations. Although both models predict that the crack length of the longest hierarchical level increases with increasing initial temperature,

based on the available experimental results, both models underestimate the final nondimensional lengths of the longest cracks. In this case, the method presented in [182] produces slightly better approximations.

When such large temperature differences are considered, the nonlinear effects related to thermal dependent moduli and radiation heat transfer need to be included. The strong influence of temperature depended material properties on the thermal stresses has been documented in the literature [168,174]. Therefore, the numerical simulations are repeated using this time the nonlinear heat transfer model. The constant properties presented in Table 4.1 are now replaced by those reported in Figure 4.2. Furthermore, due to the nonlinearities in the heat transfer equations, the finite element mesh was increased to $50{,}000$ elements to accurately approximate the temperature variation. The solution procedure is otherwise identical to the one followed in the previous section.

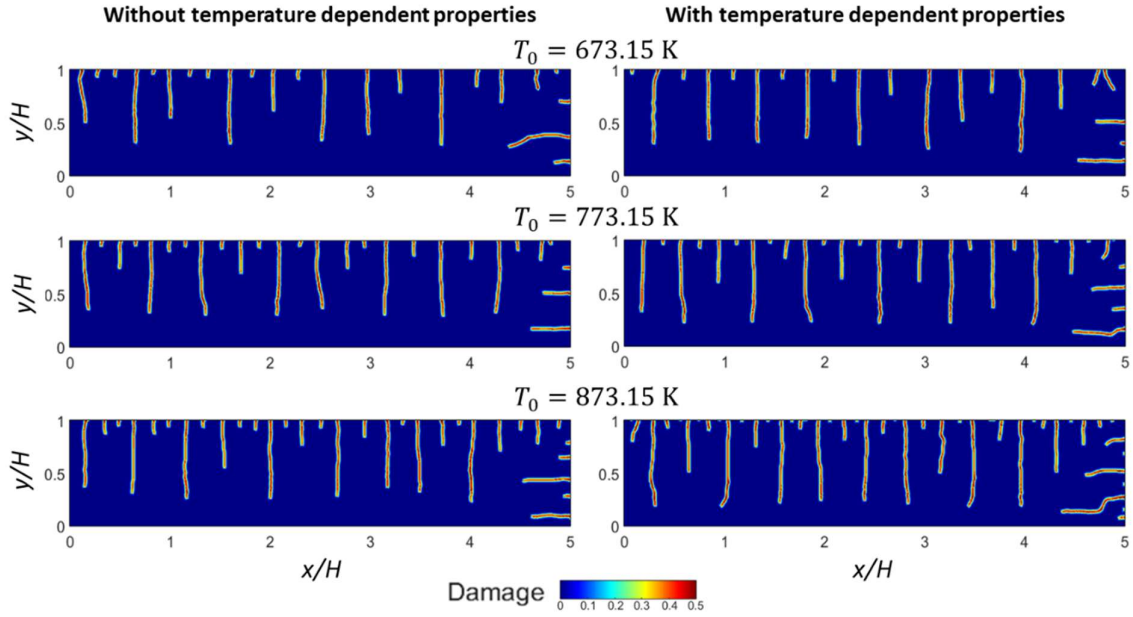

Figure 4.8: Comparison of the final crack patterns after the introduction of the temperature dependent material properties ($\hat{t} = 1.00$).

Figure 4.8 offers a comparison between the results from the proposed procedure, with (right column) and without the temperature dependency (left column). Each row in Figure 4.8 depicts the local damage index $\phi(\boldsymbol{x}, t)$ at $\hat{t} = 1.00$ for $T_0 = 673.15\text{K}$, 773.15K and 873.15K, respectively. It is evident that for higher initial temperatures, the heat flux within the material intensifies and the crack spacing is decreased, leading to an increase in the total number of cracks. This agrees well with the experimental and numerical results presented in [182] as well as similar observations in the literature (e.g. [172,177,181]). The transient algorithm

successfully predicted that cracks will nucleate on the material boundary. Subsequently, the static algorithm predicted multi-crack propagation till their final arrest. The spacing of the cracks tends to be even across the boundary and final crack patterns illustrate hierarchical and periodic classes. Increasing the initial temperature T_0, the density of the crack patterns and the length of the longest crack class increases [177]. In the cases presented here, it was possible to clearly identify three hierarchical classes. When the temperature dependency of the thermal and mechanical material properties is included into the simulations, the length of the longest crack level is increased, while the lower crack levels still follow the distribution observed experimentally [182].

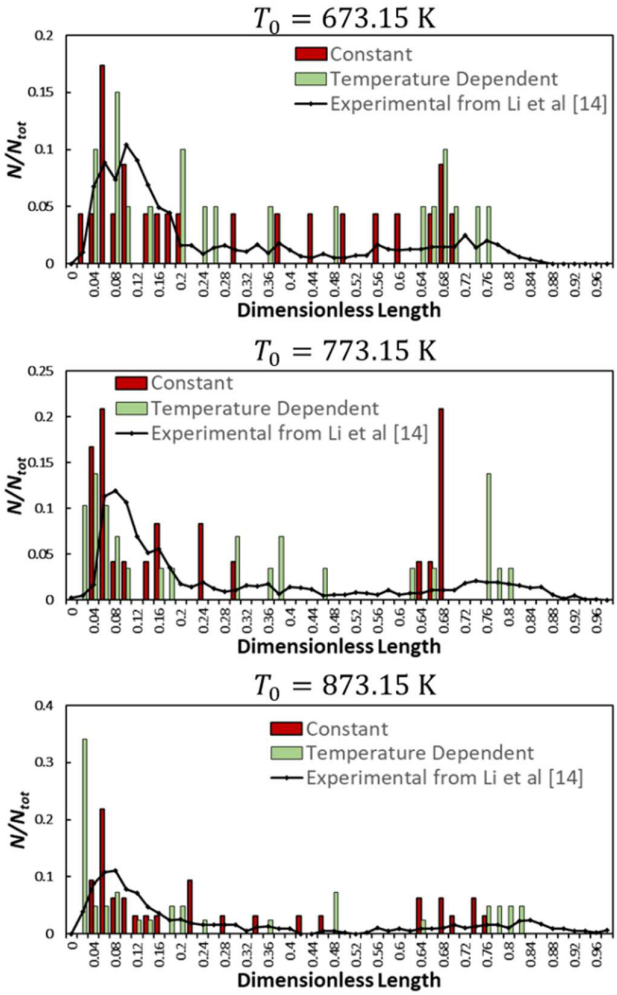

Figure 4.9: Comparison of the number of cracks at each length level before and after the introduction of the temperature dependent material properties.

When the temperature dependency is not included, the time instant of first nucleation is $\hat{t} = 16.52\,10^{-4}$, $\hat{t} = 9.04\,10^{-4}$ and $\hat{t} = 5.76\,10^{-4}$ for initial temperature $T_0 = 673.15\text{K}$, $T_0 = 773.15\text{K}$ and $T_0 = 873.15\text{K}$, respectively. In the cases considered, the PD model predicts

that cracks initiate when the temperature difference on the surface of the material is approximately $106\mathrm{K}$. When the temperature dependency is included, the first crack appeared at $\hat{t} = 17.06\ 10^{-4}$, $\hat{t} = 6.25\ 10^{-4}$ and $\hat{t} = 3.16\ 10^{-4}$ for initial temperature $T_0 = 673.15\mathrm{K}$, $T_0 = 773.15\mathrm{K}$ and $T_0 = 873.15\mathrm{K}$, respectively. After the introduction of the variable material properties, steeper temperature gradients develop in the interior of the material and thus, thermal stresses increase. This explains why cracks appeared sooner compared to the constant properties. At $T_0 = 673.15\mathrm{K}$, the first crack appears at comparable time in both cases due to the higher value of the fracture toughness assumed here.

In Figure 4.9, the experimental data presented in [182] (black line) are plotted against the ones derived by the present FEM-PD method. Apart from the linear heat transfer model (red bars), the more realistic nonlinear heat transfer based results are shown using green bars. It is evident from the three plots in Figure 4.9 that the fully nonlinear model can predict better the formation of larger cracks. The clusters of green bars in higher values of the nondimensional length appear to follow more accurately the line produced by experimental data. The methodology proposed here can approximate the experimental findings over the full spectrum of crack lengths for various initial temperatures.

Qualitatively, the methodology presented here produces crack patterns that are in close agreement with the numerical and experimental results presented in [182]. Differences between the models can be traced back in the use of a transient solution for the first part of the simulation and the limitation on the Poisson ratio (here $v = 0.33$). Finally, as mentioned earlier, both the numerical model presented in [182] and the present model underestimate the length of the longest cracks when the temperature dependency on the thermal and mechanical material properties is neglected. This shortcoming is remedied by the incorporation of nonlinear effects in the heat transfer model.

Concluding the analysis of cold shock, it is necessary to mention that the rapid evolution of cracks is one of the key fracture characteristics of cold shocked specimens. The use of the transient solution during the nucleation phase, allows for the evaluation of crack propagation velocities. In the following, the average crack propagation velocity is estimated for the first crack that nucleates at each initial temperature T_0, when the temperature dependent properties are used. For $T_0 = 673.15\mathrm{K}$, the first crack nucleates at $\hat{t}_1 = 1.7059\ 10^{-3}$ and propagates till $\hat{t}_2 = 1.7061\ 10^{-3}$, for a total length of $\hat{l} = 0.105$. The average velocity, expressed as a dimensional value for convenience, is approximately $v_{\mathrm{average}} = 1113\mathrm{m/s}$. Similarly, for $T_0 = 773.15\mathrm{K}$ and $T_0 = 873.15\mathrm{K}$, the average velocities are $v_{\mathrm{average}} = 1033\mathrm{m/s}$ and $v_{\mathrm{average}} = 719\mathrm{m/s}$, respectively. Typical Rayleigh wave speeds c_R, for alumina

materials are in the region of $5858\mathrm{m/s}$ [198]. The results obtained from the numerical simulations suggest propagation velocities well below c_R. In [199], Rosakis notes that although the Rayleigh wave speed is the maximum, theoretically attainable, crack velocity for Mode I fracture of ceramics, experimental observations suggest only lower velocity levels are actually attainable. When the crack tip velocity is within the range of approximately $0.35\sim0.5c_R$, crack branching is observed. The range of the crack velocities predicted from the PD model during cold shock are below the crack branching velocities and agree with the straight crack patterns observed during experiments. Therefore, the results presented appear to be in agreement with the expected values and provide insights on the rapid nature of the phenomenon.

4.4.2 *Hot Shock Simulation*

In applications like metal forming and gas turbines, refractories are subjected to extremely high temperatures. During a hot shock, the surface of the material tries to expand and compressive stresses develop near its boundaries while tensile stresses develop in the interior of the material [168,175]. Due to the tensile stresses that develop in the interior, cracks initiate inside the material and propagate towards its boundary [174].

Various techniques have been suggested in the literature to reproduce damage in specimens due to hot shock, under laboratory conditions. These set ups however are more demanding compared to the ones used for cold shock. Open flame burners are probably the simplest set up but the supplied heat flux is not easy to be quantified accurately [172,200]. It is noted (as also mentioned in [186]) that the ASTM standardized procedure for flame burners was withdrawn due to reproducibility issues. The use of laser apparatus on the other hand, can be only applied on a very limited area that can impair the applicability of the method [186], [201,202], although the energy supplied is known. Melt immersion tests produce the most representative temperature changes a refractory can experience in metal forming applications. This is due to the direct contact of the specimen with the melt, but the procedure is very costly [203]. Due to these inefficiencies, experimental results for the cases under consideration are not available. However, the results of the numerical model will be compared with general observations from the literature on hot shocked specimens.

Similar to the cold shock simulations described in the previous section, the temperature field is approximated numerically using the FEM algorithm. Subsequently the interpolated temperature field is used in the uncoupled PD model to simulate the mechanical response. A structured mesh with a 200×40 grid was used for the finite element calculations while 52416 particles were used for the spatial discretization of the PD equation of motion. The geometry of the model, boundary conditions and application of heat transfer is identical to that described

in the previous sections. Since in hot shock the maximum stresses take longer to manifest compared to the cold shock [168,174], the whole phenomenon is simulated under the assumption of static conditions.

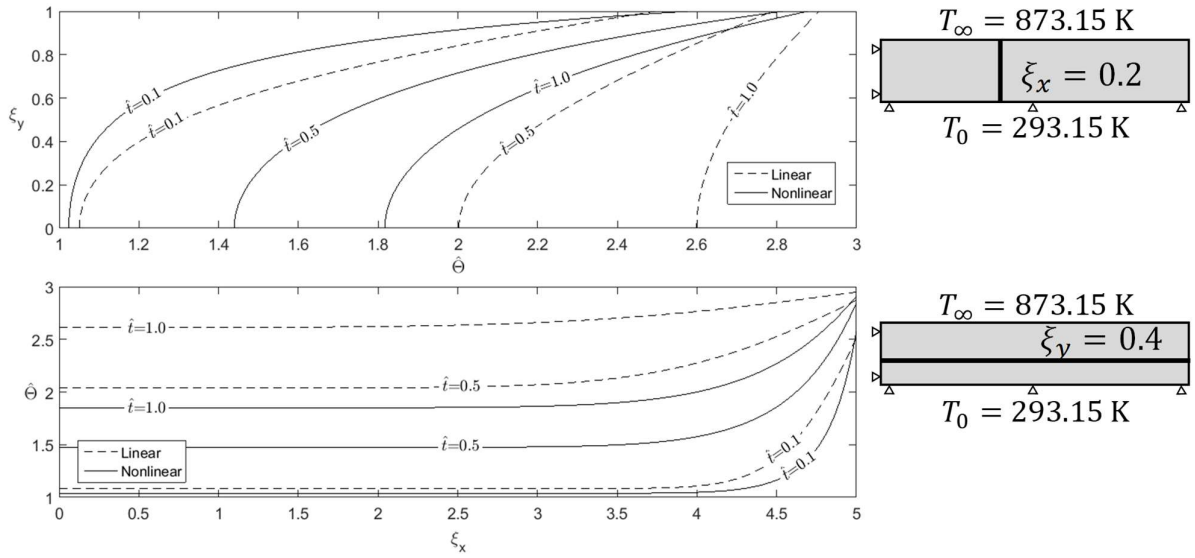

Figure 4.10: Temperature variation along a vertical and horizontal cross section at various time instants corresponding to initial temperature $T_0 = 293.15$ K and $T_\infty = 873.15$ K.

Both the linear and non-linear heat transfer solutions will be used to simulate thermal induced fracture of a material body that undergoes rapid temperature increase. The heat transfer coefficient is again assumed equal to $50{,}000\ \mathrm{Wm^{-2}K^{-1}}$, to simulate the heat exchange between a hot liquid and a cool solid. Such conditions are typical for metal forming and die casting. The temperature variation and a comparison between the temperature field from the linear and the non-linear solution can be found in Figure 4.10. The temperature fields are extracted from a specimen, initially at ambient temperature $(T_0 = 293.15\mathrm{K})$, suddenly exposed to an environment of higher temperature $(T_\infty = 873.15\mathrm{K})$. It is evident that intense heat transfer takes place at the boundary of the material which is explained from the Biot number, calculated at room temperature as $\mathrm{Bi} = k_{\mathrm{ref}}^{-1} Hh = 6.74$. In the same figure, the nonlinear solution exhibits steeper temperature gradients, while the linear predicts a smoother transition of the temperature from the boundary to the interior of the material. Furthermore, from the thermomechanical analysis carried out in [168], it can be seen that the nonlinear solution predicts higher compressive stresses at the boundary of the material while the linear solution predicts higher tensile stresses in the interior of the material.

As a first case, the temperature dependence of the thermal and mechanical material properties is neglected and the properties at room temperature, presented in Figure 4.2, are implemented

for the whole duration of the simulation. To investigate the influence of the surrounding temperature, the simulation was repeated for $T_\infty = 673.15\text{K}, T_\infty = 773.15\text{K}$ and $T_\infty = 873.15\ \text{K}$.

For all thermal shock magnitudes considered, damage initiated in the interior of the material and propagated towards the upper boundary (Figure 4.11, left column). Damage is concentrated near the left end, forming a crack at the centre of the specimen (left end of one quadrant modelled here). This crack formation is compatible with the statements in the relevant literature [175] and can be explained from the tensile stresses developing in the interior of the material. Comparing the crack formed during hot shock with the cracks that emerged during cold shock, it is evident that damage is not restricted to the vicinity of the crack, but PD bonds break in a wider area, leading to material weakening around the crack. Furthermore, only a single crack formed during hot shock that almost completely split the specimen in half.

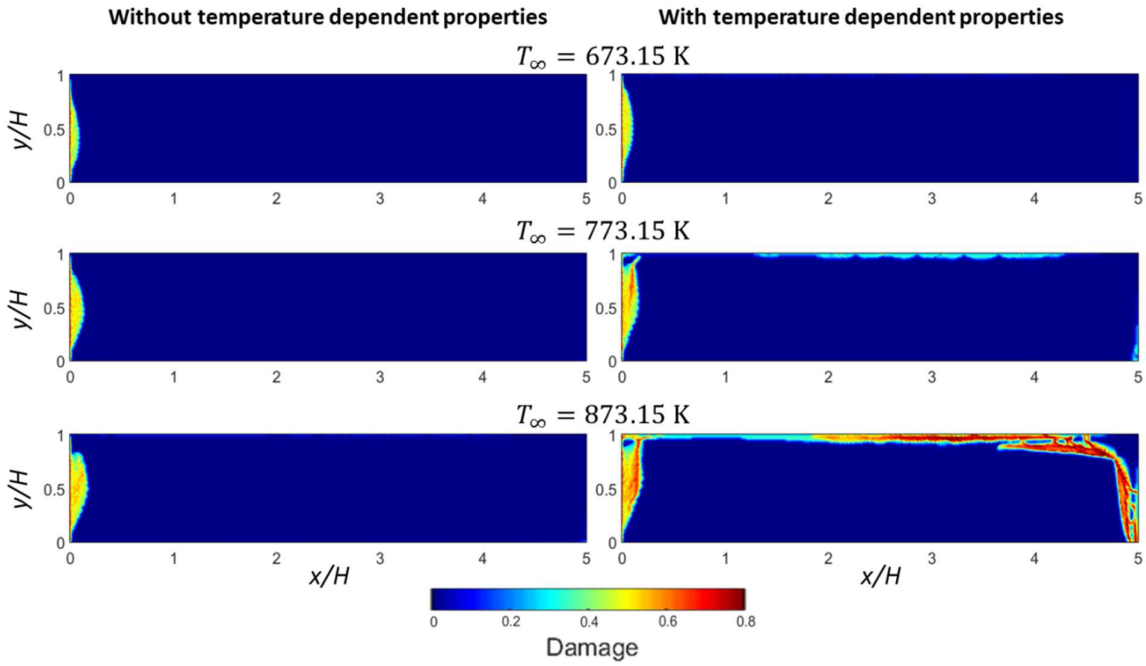

Figure 4.11: Comparison of damage in a hot shocked specimen after the introduction of the temperature dependent parameters for different shock magnitudes.

As a second case, the temperature dependency of the material parameters, illustrated in Figure 4.2, is included. The nonlinear solution of the heat transfer problem, presented in the previous paragraph, is employed for the approximation of the temperature field. Figure 4.11 illustrates a comparison of the results for the two cases, at the end of the simulation $(\hat{t} = 1.00)$. When the temperature dependency is included in the simulations (right column of Figure 4.11), a total of three damage types can be identified: **i)** a single crack splits the material

in two (similar to the previous case), **ii)** surface damage appears on the exposed surfaces of the material and **iii)** a crack at the upper right corner forms when $T_\infty = 873.15$ K. When $T_\infty = 673.15$ K, the introduction of the temperature dependent parameters has led to material weakening in a wider area around the main crack at $x/H = 0$, as well as to some limited damage at the heat transfer boundary. Increasing the surrounding temperature to $T_\infty = 773.15$ K during hot shock, further intensifies the damage at the boundary. At $T_\infty = 873.15$ K, a third type of damage manifests and crack initiates at the corner of the specimen.

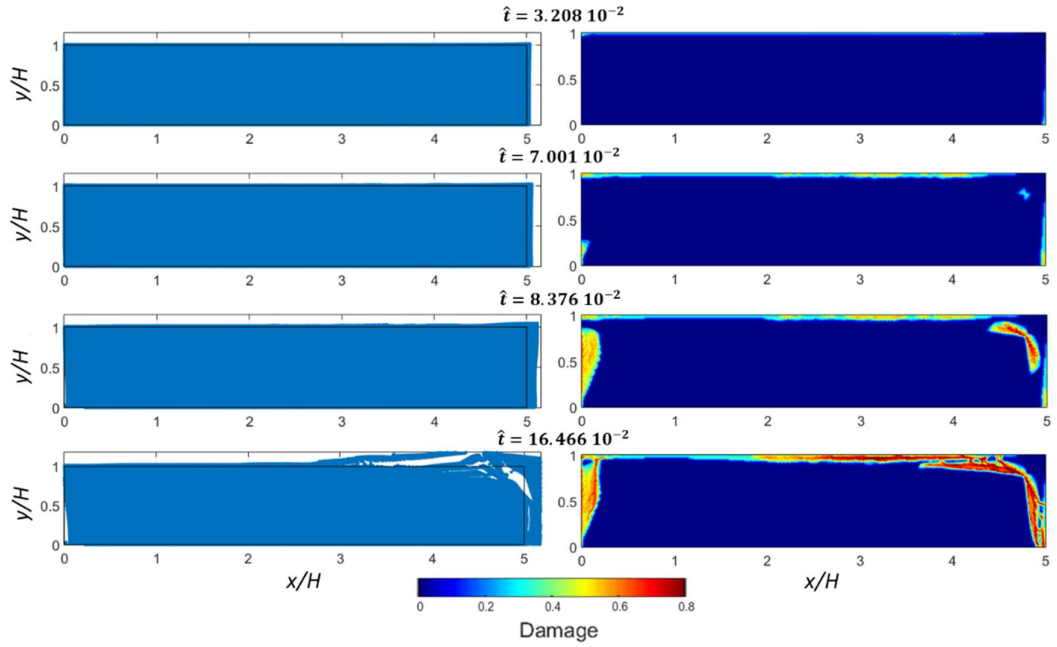

Figure 4.12: Evolution of damage in a hot shocked alumina specimen from $T_0 = 293.15$ K to $T_\infty = 873.15$ K.

A timeline of the damage evolution for a specimen suddenly subjected to an environment at $T_\infty = 873.15$K, is illustrated in Figure 4.12. Damage first manifests at the boundary of the material. It initiates at approximately $\hat{t} = 0.0107$ and quickly spreads to almost the full length of the boundaries at $\hat{t} = 0.0321$. The second damage mechanism that appears is the crack at the boundary that initiates at $\hat{t} = 0.0519$, followed closely by the last one, the corner crack, that initiates at $\hat{t} = 0.0659$. At $\hat{t} = 0.1647$ complete fracture of the specimen occurred, and the simulation was terminated.

Although both the cold and hot shocked numerical simulations predict damage at the material boundary when the temperature dependence of the material properties is included, the damage mechanisms behind each phenomenon is inherently different. In Figure 4.13, a close-

up of the PD lattice near the top boundary is illustrated for a cold shock and hot shock case. The red lines represent the broken bonds between the particles at the initial stages of the damage. During cold shock, the tensile stresses near the boundary break locally the horizontal bonds, creating the crack nucleation sites. During hot shock on the other hand, it is the vertical bonds that brake, while the horizontal bonds remain intact. This leads to the formation of weakened material layers that at later stages of the simulation, detach from the rest of the solid (see Figure 4.12 at $\hat{t} = 0.1647$).

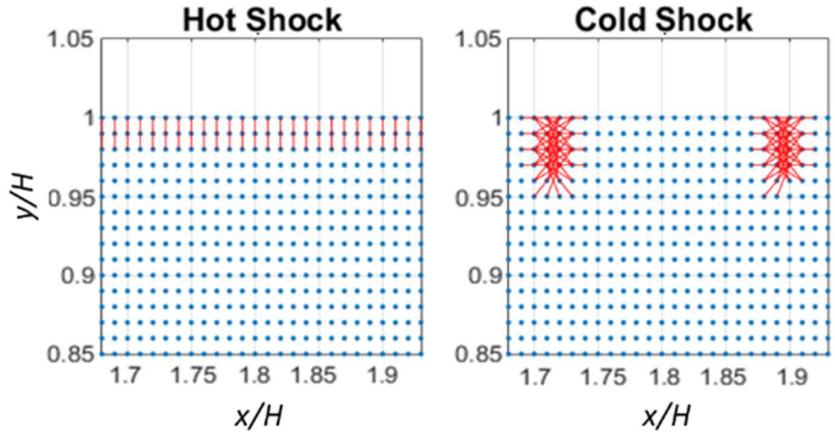

Figure 4.13: Comparison of broken bonds for a hot and cold shocked specimen.

When the temperature dependency of the material parameters is not included in the simulations, surface damage does not manifest at the material surface. This can be attributed to two main reasons. Firstly, at higher temperatures, the material fracture toughness decreases, and the material becomes more susceptible to fracture. The second reason becomes apparent considering the thermal stresses that develop in the material during hot shock. When the thermal material properties are not constant, the thermomechanical solution predicts higher compressive stresses near the material boundary compared to when the material properties are not constant [168]. In the literature, it has been pointed out that during hot shock, spalling at the material surface is possible, if the thermal induced compressive stresses are high enough [175,195]. The fracture mechanism of spalling and the simulated damage at the material boundary appear to have similar characteristics and the present methodology could be a good candidate for simulations regarding the material response undergoing a rapid increase in temperature. Referring again to Figure 4.12, surface damage precedes the formation of a crack near the boundary as well as the corner crack. This agrees with the thermomechanical response of alumina during heating as the compressive stresses near the upper boundary reach their maximum value prior to the tensile stresses in the interior of the material [168,175].

Interestingly, the corner crack initiates at an angle close to 45^o and subsequently propagates following the boundaries of the specimen. Figure 4.14 illustrates a close-up of the corner crack along with the temperature field acting on the material. During the thermomechanical investigation of refractories carried out in [168], development of shear stresses near the corners of the domain were observed. The shear stresses computed in [168] are presented in the middle of Figure 4.14, while at the top of Figure 4.14, the PD damage index from the present study is reported at the same time instant.

Considering a material point at the vicinity of the corner, its temperature will be different compared with neighbouring material points in both the vertical and horizontal direction (due to smooth isothermal lines). This temperature difference leads to distortion of the differential areas in close proximity to the corner and the development of shear stresses. This distortion effect is further magnified by the temperature dependence of the thermal expansion coefficient of alumina. The simultaneous combination of shear and compressive stresses on the material points near the corner could explain the fracture during the numerical simulations. It is noted however that in this case the assumption that an uncoupled thermomechanical approach can be used is no longer valid as heat transfer is no longer parallel to the direction of the crack propagation. Although the present approach is capable of producing same initial observations, a fully coupled approach will also capture the effect of fracture on the temperature distribution.

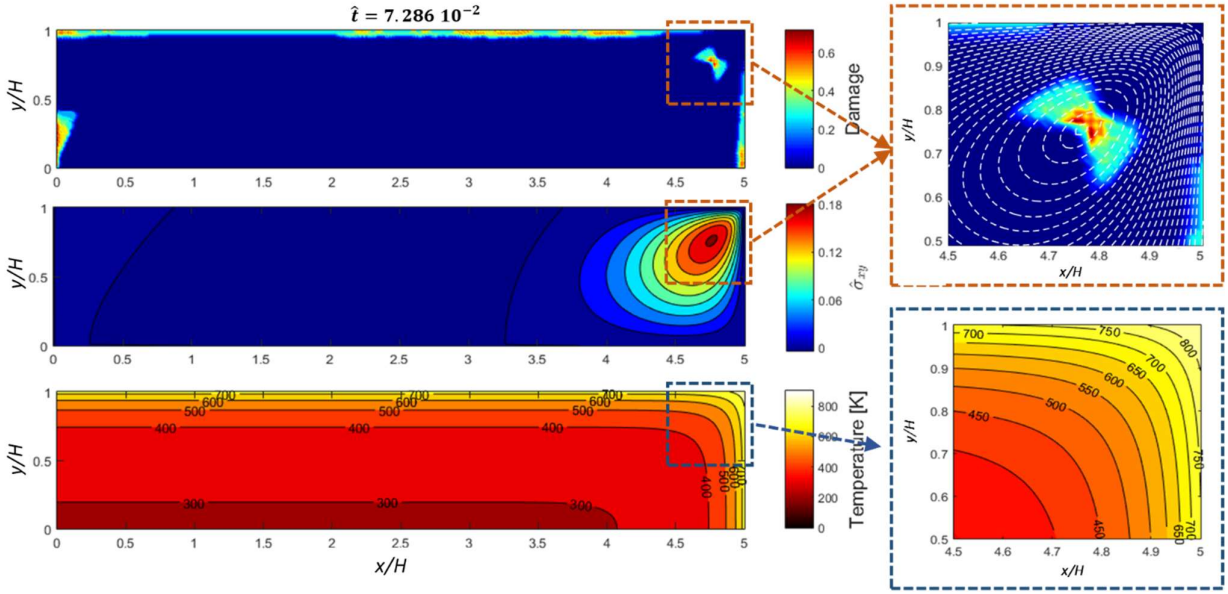

Figure 4.14: Close-up of the damage (upper plot), the shear stress field (middle plot) and the smooth isothermal contours near the corner of the material (lower plot).

5 Coupling Approaches for FE-PD Models and Wave Reflections in Dynamic Problems

5.1 The Problem Domain Ω and the Subdomains Ω^{PD} and Ω^{FE}

Let Ω be the computational domain of the problem and $\partial\Omega$ its boundary. For simplicity, and without loss of generality, in this study we assume absence of body forces and external loads are applied only on $\partial\Omega$. $\partial_u\Omega$ and $\partial_F\Omega$ are the portions of the boundary where the prescribed displacements $\boldsymbol{u}_d$ and external forces $\boldsymbol{F}_d$ are applied. Then, Ω is divided into two subdomains where the PD theory and the classical elasticity are applied, denoted with Ω^{PD} and Ω^{FE}, respectively, with $\Omega = \Omega^{FE} \cup \Omega^{PD}$. As discussed during the literature review, coupling between two different models is usually performed: **a**) at a discrete interface [116–118] in which case $\Omega^{FE} \cap \Omega^{PD} = \emptyset$ or **b**) gradually over a zone where both descriptions coexist, often called the "*overlapping zone*" [52,118–121], in which case $\Omega^{FE} \cap \Omega^{PD} = \Omega^{coupl}$. The two different approaches are illustrated schematically in Figure 5.1.

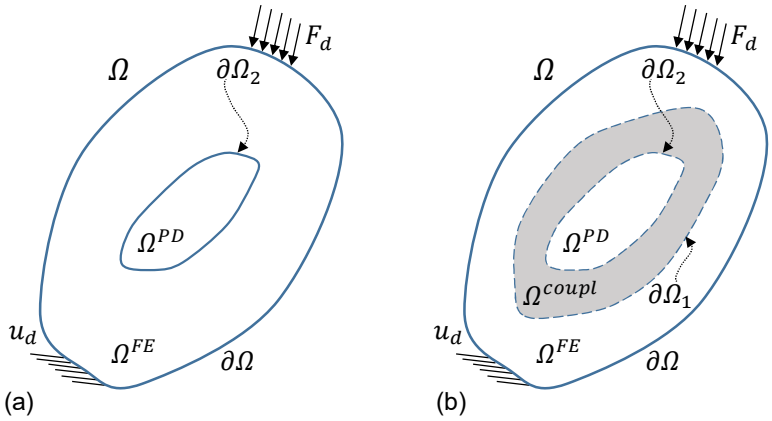

Figure 5.1: Subdivision of Ω into Ω^{PD} and Ω^{FE} when a) coupling is enforced at a discrete interface or b) gradually over a region.

We limit ourselves to the configuration illustrated in Figure 5.1 with the restriction $\partial\Omega \cap \partial\Omega_1 = \partial\Omega \cap \partial\Omega_2 = \partial\Omega_1 \cap \partial\Omega_2 = 0$ on the boundaries. This configuration is a desirable situation for our applications because: **i)** use of the computationally expensive PD model is limited, **ii)** its application can be focused to specific locations and **iii)** the PD model is defined away from the portions $\partial_u\Omega$ and $\partial_F\Omega$ where the boundary conditions are enforced. This circumvents the difficulties regarding the application of boundary conditions on an nonlocal model [6,107,117]. However, despite being located away from the geometrical boundaries, the PD skin effect still

manifests. For this reason, use of a surface correction procedure is very important as it will improve the accuracy of the coupling between the two different models, as it will be discussed in the following sections.

5.2 Definition of the Coupling Approaches in 1D

Although the PD theory can be advantageous in certain problems, the high computational cost associated with its implementation is very restrictive. It is thus desirable to limit the use of PD in areas where finer descriptions are required and use a more computational efficient method for the remaining domain. Coupling different numerical model leads to the development of fictitious forces near the interface. In dynamic problems, spurious reflections are observed due to model mismatch [52]. In this paragraph, three different approaches are presented to couple FE meshes with PD grids.

5.2.1 *Problem Description*

Consider the 1D bar depicted in Figure 5.2. The bar domain Ω, consists of the subdomains Ω^{FE} and Ω^{PD}, as defined in the previous paragraph. Ω^{FE} consists of the two ends of the bar while Ω^{PD} contains the middle part of the bar. This simple 1D bar problem is used to identify the fundamental mechanisms and phenomena associated with spurious wave reflections during pulse propagation. In this setting, a wave propagating in the bar will cross a FE-PD and a PD-FE coupling. Test cases of propagating pulses with different shapes are considered to identify the parameters (e.g. PD horizon δ, effect of discretization size in each model) that are crucial.

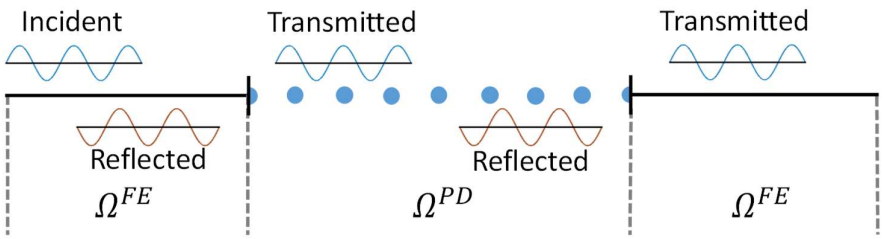

Figure 5.2: Incident and reflected wave in a 1D bar.

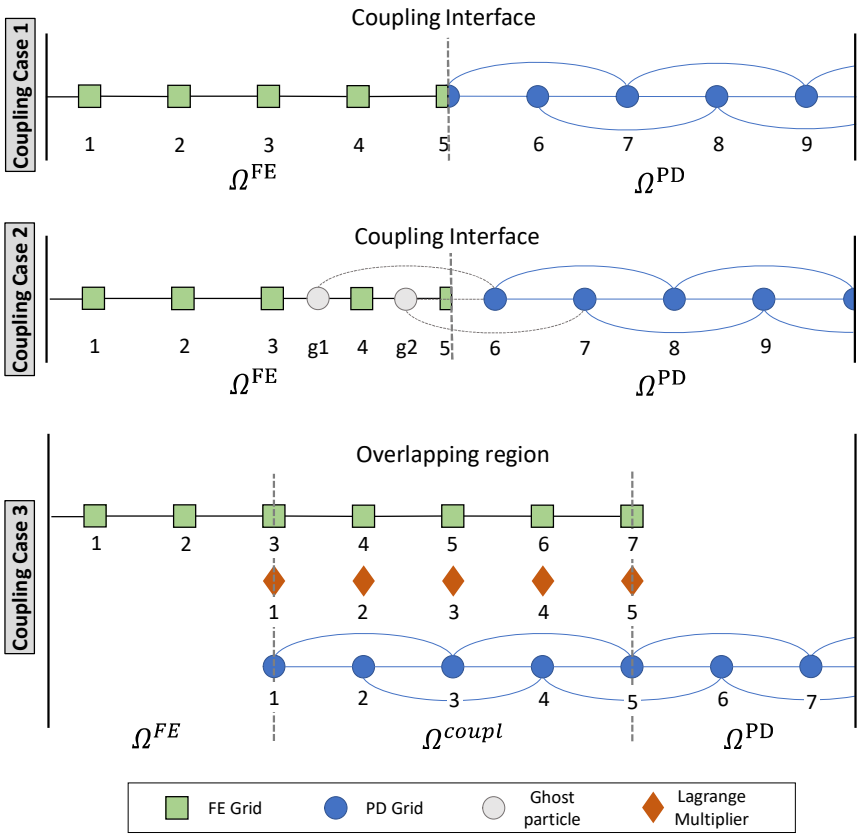

Figure 5.3: Illustration of the three approaches implemented in this study to couple FE meshes with PD grids. First two methods couple the two domains at an interface while the third one performs the coupling over an overlapping region.

A crucial point of this study is the effect of different coupling approaches on the reflected wave energy. To evaluate each strategy three approaches are presented below:

i). The first approach (Coupling Case 1 - Figure 5.3) involves a simple coupling between the two models at a discrete interface, that is termed "*coupling interface*" hereafter. In 2D applications the coupling interface is a curve (see $\partial\Omega_2$ in Figure 5.1(a)) and reduces to a single point in 1D. Force equilibrium and continuity requirements are enforced on the interface to achieve information passing between the two models. Following this approach, it is required that a FE node and a PD particle coincide at the interface location. In the present study, this is the only case where such a requirement is enforced.

ii). The second approach (Coupling Case 2 - Figure 5.3) introduces additional PD particles within the FE mesh, that will be referred to as "*ghost particles*" in the subsequent sections. Recently, an approach very similar to this coupling case was presented in [117,118]. Just like Coupling Case 1, the coupling is enforced at an interface that

reduces to a single point in the 1D problem considered here. The difference is that there is no requirement for coincident FE nodes and PD particles at the interface location. Circumventing this requirement is very desirable for 2D and 3D problems as the discretization approach adopted in each model becomes independent.

iii). The third approach included in this comparison in an energy coupling method (Coupling Case 3 - Figure 5.3), proposed by Aubertin et al. [75]. In this case, the two models overlap and coexist in Ω^{coupl}. Contrary to Coupling Cases 1 and 2, this time Ω^{coupl} is defined over a region of the bar.

These three cases are implemented and the formulation that enforces the coupling between the different models is described in the following paragraphs. The aim of this comparison is to evaluate the efficiency and the ability of each methodology to achieve accurate information passing between Ω^{FE} and Ω^{PD}. Focal point of the comparison is the generation of spurious reflections during pulse propagation. These fictitious artefacts are one of the biggest issues when such coupling approaches are adopted [52] and can lead to erroneous results. To ensure comparability of the results, it is noted that in all the examples presented in this chapter $c(\boldsymbol{\xi})$ is assumed constant and it is computed through Eq. (3.11).

5.2.2 *Coupling Case 1*

The first coupling approach presented here is a simple coupling of the two models using a single interface node. The FE and the PD model "share" this node to achieve wave propagation across the interface. Although this is a very simplistic approach, it is used as a benchmarking tool for comparison with the other two coupling methods. For convenience examples for all approaches are described using $\delta = 2\Delta x$. It is noted however that the formulation remains the same for larger values of δ. Assuming that the interface is at node α (e.g. $\alpha = 5$ in Figure 5.3), to ensure continuity between the models at the interface it is required that:

$$u_\alpha = d_\alpha = u_{int}. \tag{5.1}$$

It is reminded that $\boldsymbol{u}$ and $\boldsymbol{d}$ denote the FE and PD displacements respectively.

The interface node is subjected to forces from the FE model on the left side and the PD model on the right side and thus, the motion of node α is described from:

$$m_{int}\ddot{u}_{int} = \Sigma F^{FE} + \Sigma F^{PD}, \tag{5.2}$$

where, $m_{int} = m_{\alpha}^{FE} + m_{\alpha}^{PD}$, m_{α}^{FE} and m_{α}^{PD} are the mass contributions from the FE and PD model respectively, and ΣF^{FE} and ΣF^{PD} are the total forces applied from the FE and the PD model respectively.

Combining Eqs. (3.39), (3.61), (5.1) and (5.2), the final system of equations for Coupling Case 1 can be derived. Assuming small displacements (i.e. $|\boldsymbol{\eta}| < |\boldsymbol{\xi}|$), the linearized expression of the pairwise force function $\boldsymbol{f}(\boldsymbol{\eta}, \boldsymbol{\xi})$ is used and the final system of equations can be written in the familiar form $\boldsymbol{M\ddot{U}} + \boldsymbol{KU} = \boldsymbol{0}$. For a single truss element, the stiffness matrix is given as described in Eq. (3.61a). Substituting the value of the $c(\boldsymbol{\xi})$ from Eq. (3.11) into Eq. (3.41), the stiffness of a bond is computed as:

$$k_{i,j}^{bond} = \frac{2E}{\delta^2 A} \frac{v(\boldsymbol{\xi}_{i,j})\, \lambda(\boldsymbol{\xi}_{i,j}) V_j V_i}{\beta \Delta x^{PD}} = k^{PD} \frac{v(\boldsymbol{\xi}_{i,j})}{\beta}. \tag{5.3}$$

Since this is a 1D model with a uniform grid spacing Δx^{PD}, then the distance between two particles is a multiple of Δx^{PD}, i.e. $\|\boldsymbol{x}_j - \boldsymbol{x}_i\| = \beta \Delta x^{PD}$. Additionally, the volume correction factor $v(\boldsymbol{\xi}_{i,j})$ takes the value 0.5 when $\|\boldsymbol{x}_j - \boldsymbol{x}_i\| = \delta$. With these definitions, the stiffness matrix of the coupled system near the dof of node α is:

$$K = \begin{array}{c} \\ \alpha-2 \\ \alpha-1 \\ \alpha \\ \alpha+1 \\ \alpha+2 \\ \alpha+3 \\ \\ \end{array} \begin{array}{c} \begin{array}{cccccc} \alpha-2 & \alpha-1 & \alpha & \alpha+1 & \alpha+2 & \alpha+3 \end{array} \\ \begin{bmatrix} \ddots & & & & & \\ 2k^{FE} & -k^{FE} & 0 & 0 & 0 & 0 \\ -k^{FE} & 2k^{FE} & -k^{FE} & 0 & 0 & 0 \\ 0 & -k^{FE} & k^{FE}+1.25k^{PD} & -k^{PD} & -0.25k^{PD} & 0 \\ 0 & 0 & -k^{PD} & 2.25k^{PD} & -k^{PD} & -0.25k^{PD} \\ 0 & 0 & -0.25k^{PD} & -k^{PD} & 2.5k^{PD} & -k^{PD} \\ 0 & 0 & 0 & -0.25k^{PD} & -k^{PD} & 2.5k^{PD} \\ & & & & & \ddots \end{bmatrix} \end{array} \tag{5.4}$$

Stiffness contributions from both the PD and the FE domain appear at the interface position (node α). Furthermore, as also stated in [117,130], when such couplings are enforced the bandwidth of the final stiffness matrix changes due to the nonlocal nature of PD theory. By inspecting the final stiffness matrix, it is evident that the stiffness contributions from the PD model to nodes α and $\alpha + 1$ is different compared to nodes $\alpha + 2$ and $\alpha + 3$. This happens because the horizon of the nodes near the interface has been interrupted. This is avoided when the second coupling case is used. As noted earlier, it was assumed here that $\delta =$

$2\Delta x^{PD}$. The final stiffness matrix for other values of the PD horizon can be computed following the same procedure.

5.2.3 *Coupling Case 2*

In the second coupling case, ghost particles are inserted within the FE domain (Coupling Case 2 - Figure 5.3). These particles are termed "*ghost particles*" because their respective dofs can be eliminated in the final system of equations through static condensation. The reason why ghost particles are introduced in Ω^{FE} is twofold: firstly, it allows for the computation of the forces that are applied at the interface location and secondly, the horizon of the nodes that are located close to the coupling interface is not interrupted. The number of ghost particles is such that the PD horizon of the first particle in the PD model is complete.

Denote with $\boldsymbol{x}^{PD}$ and $\boldsymbol{x}^{FE}$, the location vectors of the PD particles and FE nodes, respectively. Let n_g be the number of ghost particles, i.e., the number of PD particles with $\boldsymbol{x}^{PD} \in \Omega^{FE}$ and $\boldsymbol{d}^g$ their displacements. Continuity between the two models is enforced by interpolating the nodal displacements of the FE model at the positions of the ghost particles using the FE shape functions. Thus, $\boldsymbol{d}^g$ is computed as:

$$\boldsymbol{d}_i^g = \boldsymbol{N}(\boldsymbol{x}_i^{PD})\boldsymbol{u}. \tag{5.5}$$

The introduction of ghost particles does not imply any coincident FE nodes and PD particles on the interface. The forces acting on the interface from the PD model are computed by considering the forces of each individual bond that crosses the coupling interface. Using the definition of the bond force described in Eq. (3.40), the motion of the interface node α is described as (again $\alpha = 5$, for the purposes of this example):

$$m_\alpha \ddot{u}_\alpha = (k^{FE}u_\alpha - k^{FE}u_{\alpha-1}) + \boldsymbol{f}^{lin}_{(\alpha+1),(g1)} + \boldsymbol{f}^{lin}_{(\alpha+1),(g2)} + \boldsymbol{f}^{lin}_{(\alpha+2),(g2)}\,. \tag{5.6}$$

Combining Eqs. (3.39), (3.61), (5.5) and (5.6), the final system of equations for the second coupling case is formed. Again, using the linearized PD formulation, it is possible to construct the stiffness matrix of the system. Using Eq. (5.5), the displacements of the ghost particles can be written in terms of the FE nodal displacements as:

$$d_{g1} = N_{\alpha-2}u_{\alpha-2} + N_{\alpha-1}u_{\alpha-1} \text{ and } d_{g2} = N_{\alpha-1}u_{\alpha-1} + N_\alpha u_\alpha. \tag{5.7}$$

Thus, Eq. (5.6) can be re-written as:

$$\begin{aligned} m_\alpha \ddot{u}_\alpha = {} & 0.25k^{PD}N_{\alpha-2}u_{\alpha-2} - (k^{FE} - 1.5k^{PD}N_{\alpha-1})u_{\alpha-1} \\ & + (k^{FE} + 1.25k^{PD}N_\alpha)u_\alpha - 1.25k^{PD}d_{\alpha+1} - 0.25k^{PD}d_{\alpha+2}. \end{aligned} \tag{5.8}$$

In Eq. (5.9), a portion of the coupled stiffness matrix is presented to illustrate the final stiffness contributions at the coupling interface, i.e. the dof associated with node α.

$$K = \begin{array}{c} \\ \alpha-2 \\ \alpha-1 \\ \alpha \\ \alpha+1 \\ \alpha+2 \\ \alpha+3 \\ \\ \end{array} \begin{array}{c} \begin{array}{cccccc} \alpha-2 & \alpha-1 & \alpha & \alpha+1 & \alpha+2 & \alpha+3 \end{array} \\ \begin{bmatrix} \ddots & & & & & & \\ & 2k^{FE} & -k^{FE} & & & & \\ & -k^{FE} & 2k^{FE} & -k^{FE} & & & \\ & 0.25k^{PD}N_3 & -k^{FE}+1.5k^{PD}N_4 & k^{FE}+1.25k^{PD}N_5 & -1.25k^{PD} & -0.25k^{PD} & \\ & -0.25k^{PD}N_3 & -1.25k^{PD}N_4 & -k^{PD}N_5 & 2.5k^{PD} & -k^{PD} & -0.25k^{PD} \\ & & -0.25k^{PD}N_4 & -0.25k^{PD}N_5 & -k^{PD} & 2.5k^{PD} & -k^{PD} \\ & & & & -0.25k^{PD} & -k^{PD} & 2.5k^{PD} \\ & & & & & & \ddots \end{bmatrix} \end{array} \tag{5.9}$$

Comparing the stiffness matrices of the first two coupling approaches from Eqs.(5.4) and (5.9) it is obvious that the nonlocality of PD has also been transferred to the interface node while the horizon of the particles near the interface is not interrupted. Due to the static condensation the dofs of the ghost particles do not appear in the final stiffness matrix. It is noted that the stiffness matrix in Eq. (5.9) is valid only when the PD horizon is $\delta = 2\Delta x^{PD}$ and the ghost particles $g1$ and $g2$ lie between nodes $(\alpha-2, \alpha-1)$ and $(\alpha-1, \alpha)$ respectively. Of course, similar expressions can be derived for other values of the horizon and ghost particle location.

5.2.4 *Coupling Case 3*

In the third case, coupling is not realised at a single point but occurs along an overlapping region Ω^{coupl}, where the two models coexist (Coupling Case 3 - Figure 5.3). Coupling between the two domains is enforced in a weak sense through the implementation of Lagrange multipliers. This methodology has been presented by Aubertin et al. [75]. Similar approaches include the Arlequin method [126] and the bridging domain method [204]. In the work of Aubertin et al. [75], FE were coupled with MD. Here, the methodology presented in [75], is adopted and modified so that the PD theory is used instead of MD.

First, the variation of the PD kinetic and strain energy is defined. The variation of the total potential energy can be approximated numerically using the same collocation method that was used for the PD equation of motion as:

$$\delta W_{Kin}^{PD} \approx \sum_{i=1}^{N} m_i \ddot{\boldsymbol{d}}_i \cdot \delta \dot{\boldsymbol{d}}_i, \tag{5.10}$$

where, N is the total number of PD particles in Ω^{PD}. Implementing Eqs. (3.7) and (3.8) the variation of the potential energy is computed as:

$$\delta W_{Pot}^{PD} = \frac{1}{2}\int_{\Omega^{PD}}\int_{H_x} \frac{\partial w(\boldsymbol{\eta},\boldsymbol{\xi})}{\partial \boldsymbol{\eta}} \cdot \delta\dot{\boldsymbol{\eta}} dV_{x'}\, dV_x = \\ = \frac{1}{2}\left(\int_{\Omega^{PD}}\int_{H_x} \boldsymbol{f}(\boldsymbol{\eta},\boldsymbol{\xi}) \cdot \delta\dot{\boldsymbol{d}}' dV_{x'}\, dV_x - \int_{\Omega^{PD}}\int_{H_x} \boldsymbol{f}(\boldsymbol{\eta},\boldsymbol{\xi}) \cdot \delta\dot{\boldsymbol{d}} dV_{x'}\, dV_x\right) \tag{5.11}$$

where, the definition $\dot{\boldsymbol{\eta}} = \dot{\boldsymbol{d}}' - \dot{\boldsymbol{d}}$ was used to arrive to the last expression. Similarly, we approximate the above with a finite summation:

$$\delta W_{Pot}^{PD} \approx \frac{1}{2}\left(\sum_{i=1}^{N}\sum_{j=1}^{N_H} \boldsymbol{f}\left(\boldsymbol{\eta}_{i,j},\boldsymbol{\xi}_{i,j}\right) \cdot \delta\dot{\boldsymbol{d}}_j V_j V_i - \sum_{i=1}^{N}\sum_{j=1}^{N_H} \boldsymbol{f}\left(\boldsymbol{\eta}_{i,j},\boldsymbol{\xi}_{i,j}\right) \cdot \delta\dot{\boldsymbol{d}}_i V_j V_i\right) \tag{5.12}$$

where, i, j are dummy variables to denote different particles and N_H is the number of particles within the horizon of particle i. Using the definitions of $\boldsymbol{\eta}$ and $\boldsymbol{\xi}$ from Eqs. (3.2) we get that:

$$\boldsymbol{\eta}_{i,j} = \boldsymbol{d}_j - \boldsymbol{d}_i = -\left(\boldsymbol{d}_i - \boldsymbol{d}_j\right) = -\boldsymbol{\eta}_{j,i} \tag{5.13a}$$

$$\boldsymbol{\xi}_{i,j} = \boldsymbol{x}_j^{PD} - \boldsymbol{x}_i^{PD} = -\left(\boldsymbol{x}_i^{PD} - \boldsymbol{x}_j^{PD}\right) = -\boldsymbol{\xi}_{j,i} \tag{5.13b}$$

Using Eqs. (3.4) and (5.13), the first term of Eq. (5.12) can be written as:

$$\sum_{i=1}^{N}\sum_{j=1}^{N_H} \boldsymbol{f}\left(\boldsymbol{\eta}_{i,j},\boldsymbol{\xi}_{i,j}\right) \cdot \delta\dot{\boldsymbol{d}}_j V_j V_i = \sum_{i=1}^{N}\sum_{j=1}^{N_H} \boldsymbol{f}\left(-\boldsymbol{\eta}_{j,i},-\boldsymbol{\xi}_{j,i}\right) \cdot \delta\dot{\boldsymbol{d}}_j V_j V_i \\ = -\sum_{i=1}^{N}\sum_{j=1}^{N_H} \boldsymbol{f}\left(\boldsymbol{\eta}_{(j),(i)},\boldsymbol{\xi}_{(j),(i)}\right) \cdot \delta\dot{\boldsymbol{d}}_j V_j V_i \tag{5.14}$$

By interchanging the dummy variables in the last expression δW_{Pot}^{PD} is then approximated as:

$$\delta W_{Pot}^{PD} \approx -\sum_{i=1}^{N}\sum_{j=1}^{N_H} \boldsymbol{f}\left(\boldsymbol{\eta}_{i,j},\boldsymbol{\xi}_{i,j}\right) \cdot \delta\dot{\boldsymbol{d}}_j V_j V_i \tag{5.15}$$

If no external forces or body forces are applied in the PD domain, the problem can be stated as:

Given the initial conditions $\boldsymbol{d}(\boldsymbol{x}^{PD}, 0)$ and $\dot{\boldsymbol{d}}(\boldsymbol{x}^{PD}, 0)$, find $\boldsymbol{d}$ such that:

$$\sum_{i=1}^{N} m_i \ddot{\boldsymbol{d}}_i \delta\dot{\boldsymbol{d}}_i - \sum_{i=1}^{N}\sum_{j=1}^{N_H} \boldsymbol{f}\left(\boldsymbol{\eta}_{i,j},\boldsymbol{\xi}_{i,j}\right) \cdot \delta\dot{\boldsymbol{d}}_j V_j V_i = 0, \tag{5.16}$$

for every possible $\delta\dot{\boldsymbol{d}}$. Similar derivations can be found in [5,75,125]. It is noted that both the original and the linearized version of the PD theory can be used in Eq. (5.16).

Coupling in the overlapping region is achieved by introducing a coupling operator that will compare the velocities of the two models. Other coupling operators have been proposed in the literature as well. They enforce the coupling by considering the displacement fields (termed L^2 coupling) or the displacement field and its spatial derivatives (termed H^1 coupling). The interested reader can refer to [126,205] and the references therein for more information. Following Aubertin et al. [75], a "*mediator space*" $\mathcal{M}$ is introduced where the velocities are projected, such that the velocity field is now defined only on discrete points that belong to a subset of Ω^{PD}. The velocities are projected on $\mathcal{M}$ using a suitable projection operator Π, a scalar product p and Lagrange multipliers $\boldsymbol{\lambda}$, such that:

$$\forall \delta\boldsymbol{\lambda} \in \mathcal{M}, p\left(\delta\boldsymbol{\lambda}, \Pi\dot{\boldsymbol{u}} - \Pi\dot{\boldsymbol{d}}\right) = 0 \tag{5.17}$$

Similar to the case of molecular dynamics [75], the discrete nature of PD implies that Lagrange multipliers are defined at the location of PD particles in the overlapping region. The final coupled system can be written as:

Given the initial conditions $\boldsymbol{u}(\boldsymbol{x}^{FE}, 0)$, $\dot{\boldsymbol{u}}(\boldsymbol{x}^{FE}, 0)$, $\boldsymbol{d}(\boldsymbol{x}^{PD}, 0)$ and $\dot{\boldsymbol{d}}(\boldsymbol{x}^{PD}, 0)$ find $\boldsymbol{u}$ and $\boldsymbol{d}$ such that:

$$\int_{\Omega^{FE}} a^{FE}(\boldsymbol{x})\rho\ddot{\boldsymbol{u}} \cdot \delta\dot{\boldsymbol{u}} d\Omega + \int_{\Omega^{FE}} a^{FE}(\boldsymbol{x})\boldsymbol{\varepsilon}(\boldsymbol{u}) : \boldsymbol{E} : \boldsymbol{\varepsilon}(\delta\dot{\boldsymbol{u}})\, d\Omega + p(\boldsymbol{\lambda}, \Pi\delta\dot{\boldsymbol{u}}) = 0 \tag{5.18a}$$

$$\sum_{i=1}^{N} a^{PD}(\boldsymbol{x}) m_i \ddot{\boldsymbol{d}}_i \cdot \delta\dot{\boldsymbol{d}}_i - \sum_{i=1}^{N}\sum_{j=1}^{N_H} a^{PD}(\boldsymbol{x}) \boldsymbol{f}\left(\boldsymbol{\eta}_{i,j}, \boldsymbol{\xi}_{i,j}\right) \cdot \delta\dot{\boldsymbol{d}}_i V_j V_i - p\left(\boldsymbol{\lambda}, \Pi\delta\dot{\boldsymbol{d}}\right) = 0 \tag{5.18b}$$

$$p\left(\delta\boldsymbol{\lambda}, \Pi\dot{\boldsymbol{u}} - \Pi\dot{\boldsymbol{d}}\right) = 0 \tag{5.18c}$$

for all admissible $\delta\dot{\boldsymbol{u}}, \delta\dot{\boldsymbol{d}}$ and $\delta\boldsymbol{\lambda}$. The functions $a^{FE}(\boldsymbol{x})$ and $a^{PD}(\boldsymbol{x})$ define a partition of unity in the problem domain with $a^{FE}(\boldsymbol{x}) + a^{PD}(\boldsymbol{x}) = 1$. This is to ensure conservation of energy across the overlapping domain Ω^{coupl}, as they distribute the energy between the two models. These functions are often called "*blending functions*" [52]. They can be defined (using the partition of unity property) through:

$$a^{FE}(\boldsymbol{x}) = \begin{cases} 1, & \boldsymbol{x} \in \Omega^{FE} \\ h(\boldsymbol{x}), & \boldsymbol{x} \in \Omega^{coupl} \\ 0, & \boldsymbol{x} \in \Omega^{PD} \end{cases} \tag{5.19}$$

Selection of the appropriate function $h(\boldsymbol{x})$ to distribute the energies is not straightforward and can be case dependent [117]. In [205] and [120] it was demonstrated that when the L^2 coupling is implemented in the Arlequin method, which is very similar to the coupling implemented here, selection of Heaviside functions to distribute the energy can lead to ill-posed problems. To

avoid this, continuous functions were selected to define the energy distribution (Figure 5.4). Two cases are used for comparison: **i**) a linear function with $h(x) = \frac{x_1 - x}{x_1 - x_0}$ and **ii**) a cubic function with $h(x) = 1 - 3\left(\frac{x - x_0}{x_1 - x_0}\right)^2 + 2\left(\frac{x - x_0}{x_1 - x_0}\right)^3$.

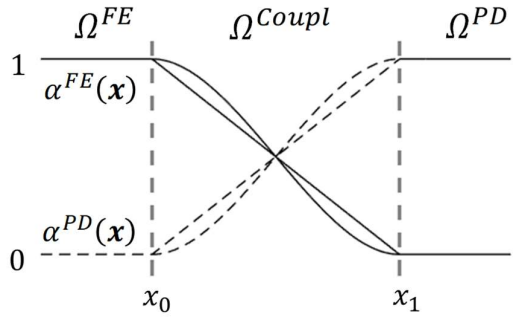

Figure 5.4: Blending functions $a^{FE}(x)$ and $a^{PD}(x)$.

Following [75] and after discretization of Eqs. (5.18), and using matrix notation, we arrive at:

$$\boldsymbol{a}^{FE}\boldsymbol{M}\ddot{\boldsymbol{u}} + \boldsymbol{a}^{FE}\boldsymbol{K}\boldsymbol{u} + \boldsymbol{C}^{FE}\boldsymbol{\Lambda} = \boldsymbol{0}, \tag{5.20a}$$

$$\boldsymbol{a}^{PD}\boldsymbol{m}\ddot{\boldsymbol{d}} - \boldsymbol{a}^{PD}\boldsymbol{f}^{PD} - \boldsymbol{C}^{PD}\boldsymbol{\Lambda} = \boldsymbol{0}, \tag{5.20b}$$

$$\boldsymbol{C}^{FE}\dot{\boldsymbol{u}} - \boldsymbol{C}^{PD}\dot{\boldsymbol{d}} = \boldsymbol{0}, \tag{5.20c}$$

where, $\boldsymbol{C}^{FE}$ and $\boldsymbol{C}^{PD}$ are the coupling matrices of the FE and PD, respectively and $\boldsymbol{a}^{FE}$ and $\boldsymbol{a}^{PD}$ are diagonal weighting matrices. The FE velocities $\dot{\boldsymbol{u}}$ are projected on the mediator space $\mathcal{M}$ and then interpolated on the location of the PD particles in the overlapping region through the FE shape functions. The matrix $\boldsymbol{C}^{FE}$ contains the shape function values that define this interpolation. $\boldsymbol{C}^{PD}$ is a scalar Boolean matrix associating each Lagrange multiplier with a PD particle.

5.3 Time Domain Analyses using the FE-PD models

5.3.1 *Time Integration*

In this chapter, time integration for Coupling Cases 1 and 2, is performed implementing the central difference method [206] (i.e. Newmark-β with $\beta = 0$ and $\gamma = 0.5$) for both FE and PD models. The displacements of the next time step $(n+1)$ are computed through:

$$\boldsymbol{u}^{n+1} = \boldsymbol{u}^n + \dot{\boldsymbol{u}}^n \Delta t + \tfrac{1}{2}\ddot{\boldsymbol{u}}^n \Delta t^2 \tag{5.21a}$$

$$\boldsymbol{d}_i^{n+1} = \boldsymbol{d}_i^n + \dot{\boldsymbol{d}}_i^n \Delta t + \tfrac{1}{2}\ddot{\boldsymbol{d}}_i^n \Delta t^2 \tag{5.21b}$$

Subsequently, the accelerations at the next step are found using the next step displacements $\boldsymbol{u}^{n+1}$ and $\boldsymbol{d}_i^{n+1}$ from the FE and PD equations of motion. Finally, the velocities of the next step are:

$$\dot{\boldsymbol{u}}^{n+1} = \dot{\boldsymbol{u}}^{n} + \frac{1}{2}(\ddot{\boldsymbol{u}}^{n} + \ddot{\boldsymbol{u}}^{n+1})\Delta t, \tag{5.22a}$$

$$\dot{\boldsymbol{d}}_i^{n+1} = \dot{\boldsymbol{d}}_i^{n} + \frac{1}{2}\left(\ddot{\boldsymbol{d}}_i^{n} + \ddot{\boldsymbol{d}}_i^{n+1}\right)\Delta t. \tag{5.22b}$$

For the time integration of the third coupling approach, the predictor-corrector procedure presented in [75] is adopted. It has been shown that this procedure can reduce the generated spurious reflections. According to this procedure, each model is first solved individually, disregarding the coupling terms, and then the velocities and accelerations are updated in the overlapping domain using the Lagrange multipliers. This procedure is briefly presented here.

First the next step displacements $\boldsymbol{u}^{n+1}$ and $\boldsymbol{d}^{n+1}$ are computed using Eqs. (5.21). Then, a prediction of the next step accelerations $\ddot{\boldsymbol{u}}^{n+1,*}$ and $\ddot{\boldsymbol{d}}^{n+1,*}$ is made as:

$$\ddot{\boldsymbol{u}}^{n+1,*} = -\boldsymbol{M}^{-1}\boldsymbol{a}^{FE^{-1}}\boldsymbol{a}^{FE}\boldsymbol{K}\boldsymbol{u}^{n+1} = -\boldsymbol{M}^{-1}\boldsymbol{K}\boldsymbol{u}^{n+1}, \tag{5.23a}$$

$$\ddot{\boldsymbol{d}}^{n+1,*} = \boldsymbol{m}^{-1}\boldsymbol{a}^{PD^{-1}}\boldsymbol{a}^{PD}\boldsymbol{f}^{PD} = \boldsymbol{m}^{-1}\boldsymbol{f}^{PD}. \tag{5.23b}$$

Using the predicted accelerations, a prediction of the next step velocities $\dot{\boldsymbol{u}}^{n+1,*}$ and $\dot{\boldsymbol{d}}^{n+1,*}$ is made using Eqs. (5.22). Following [75], the Lagrange multipliers are computed using the predicted velocities as:

$$\boldsymbol{\Lambda}^{n+1} = \boldsymbol{A}^{-1}\boldsymbol{B}^{n+1} \tag{5.24}$$

with $\boldsymbol{A} = \frac{\Delta t}{2}\left(\boldsymbol{C}^{FE^T}\boldsymbol{M}^{-1}\boldsymbol{a}^{FE^{-1}}\boldsymbol{C}^{FE} + \boldsymbol{C}^{PD^T}\boldsymbol{m}^{-1}\boldsymbol{a}^{PD^{-1}}\boldsymbol{C}^{PD}\right)$ and $\boldsymbol{B}^{n+1} = \boldsymbol{C}^{FE^T}\dot{\boldsymbol{u}}^{n+1,*} - \boldsymbol{C}^{PD^T}\dot{\boldsymbol{d}}^{n+1,*}$. Using the Lagrange multipliers calculated from Eq. (5.24), the velocities are adjusted as:

$$\dot{\boldsymbol{u}}^{n+1} = \dot{\boldsymbol{u}}^{n+1,*} - \frac{1}{2}\boldsymbol{M}^{-1}\boldsymbol{a}^{FE^{-1}}\boldsymbol{C}^{FE}\boldsymbol{\Lambda}^{n+1} \tag{5.25a}$$

$$\dot{\boldsymbol{d}}^{n+1} = \dot{\boldsymbol{d}}^{n+1,*} + \frac{1}{2}\boldsymbol{m}^{-1}\boldsymbol{a}^{PD^{-1}}\boldsymbol{C}^{PD}\boldsymbol{\Lambda}^{n+1}, \tag{5.25b}$$

and the accelerations as:

$$\ddot{\boldsymbol{u}}^{n+1} = \ddot{\boldsymbol{u}}^{n+1,*} - \boldsymbol{M}^{-1}\boldsymbol{a}^{FE^{-1}}\boldsymbol{C}^{FE}\boldsymbol{\Lambda}^{n+1} \tag{5.26a}$$

$$\ddot{\boldsymbol{d}}^{n+1} = \ddot{\boldsymbol{d}}^{n+1,*} + \boldsymbol{m}^{-1}\boldsymbol{a}^{PD^{-1}}\boldsymbol{C}^{PD}\boldsymbol{\Lambda}^{n+1}, \tag{5.26b}$$

5.3.2 *Pulse Propagation and Spurious Reflections in a 1D bar*

Wave propagation test cases are simulated numerically for the 1D bar illustrated in Figure 5.2. It is assumed that the Young's modulus of the bar is $E = 200\ \mathrm{GPa}$, the cross-sectional area is $A = 10^{-6}\ \mathrm{m}^2$, the density is $\rho = 7850\ \mathrm{kg/m}^3$ and the total length is $l = 1.2\ \mathrm{m}$. The bar is divided into three equal parts with the middle one being modelled using the PD theory and the other two with FEs. When Coupling Case 3 is used, the PD domain is extended within the FE domain to create the overlapping region. The extension length is denoted with l^{coupl}.

Test cases with different pulse shapes are carried out. The displacement of the node at the free end of the bar is prescribed to simulate a rightward traveling incident wave. Incident pulses with two different shapes are used: a Gaussian with $\boldsymbol{u}(\mathbf{0},t) = a_1 e^{-\frac{1}{2}\left(\frac{t-a_2}{a_3}\right)^2}$ and a modulated pulse with $\boldsymbol{u}(0,t) = \frac{a_1}{2}\sin(2\pi f_1 t) - \frac{a_1}{2}\sin(2\pi f_2 t)$. The following parameters are selected for the pulses: $a_2 = 4\times10^{-6}$, $a_3 = 1\times10^{-6}$, $f_1 = 5\times10^5\ \mathrm{Hz}$ and $f_2 = 5.25\times10^5\ \mathrm{Hz}$. In both cases, the amplitude of the pulse is $a_1 = 10^{-4}\ \mathrm{m}$. The frequency content of each pulse shape is illustrated in Figure 5.5 where $|P(f)|$ is the amplitude spectrum.

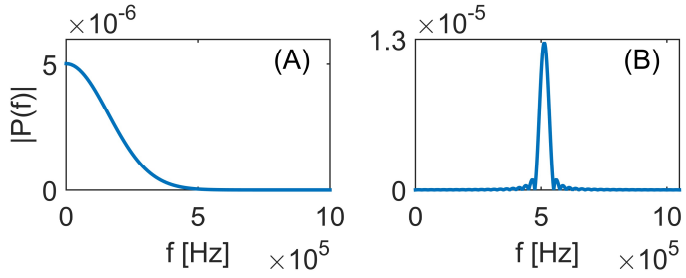

Figure 5.5: Frequency content of the a) Gaussian and b) modulated incident pulses

Coupling Case 1 is used first to as an illustration example of the spurious reflections that are generated. Both models have identical discretization lengths with $\Delta x^{FE} = \Delta x^{PD} = 2\cdot10^{-4}\mathrm{m}$ and the PD horizon is $\delta = 3\Delta x^{PD}$. A time step $\Delta t = 10^{-8}\ \mathrm{s}$ is used and the duration of the analysis is $t_{tot} = 2.3\times10^{-4}\ \mathrm{s}$. The duration of the analysis was selected as such that traveling pulses do not reach the end of the bar to avoid boundary reflections. In Figure 5.6, the spurious reflections that appear every time the pulse crosses a coupling interface (dashed line) are illustrated. Even with a simple approach like this it is possible to achieve accurate information passing between FE-PD and PD-FE interfaces given that a very fine discretization is used. For the model parameters selected, the amplitude of the reflected wave is approximately $3\cdot10^{-7}\ \mathrm{m}$. As it will be shown later, the accuracy of this coupling method

deteriorates very fast as the discretization becomes coarser and this approach will only be used for comparison purposes.

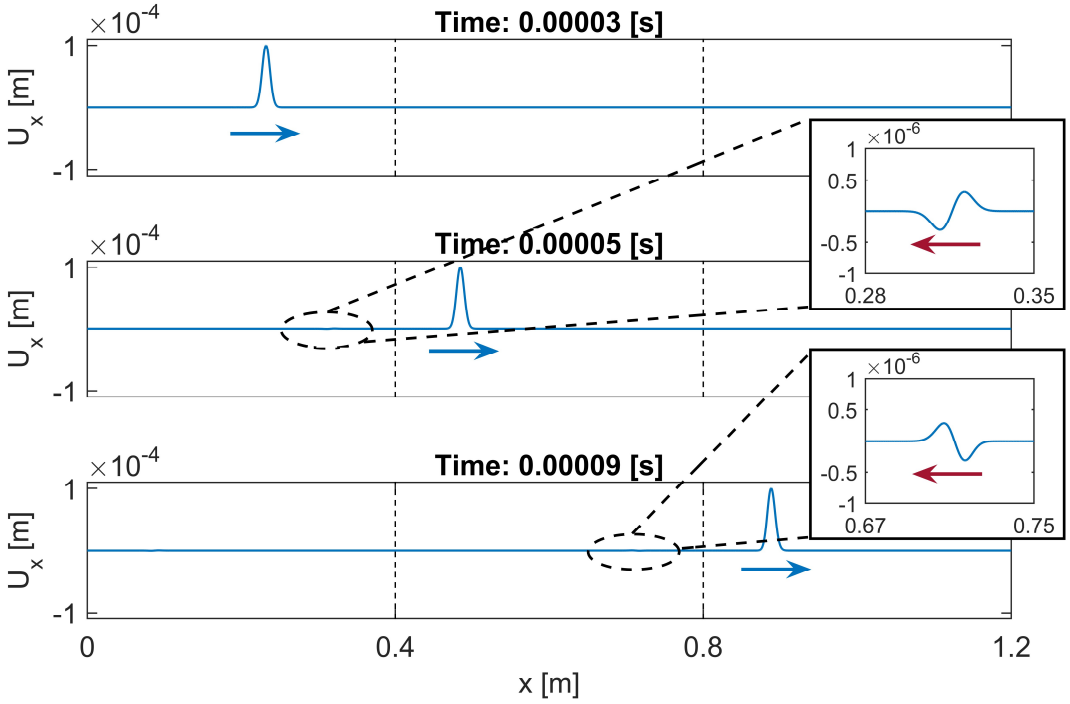

Figure 5.6: Spurious reflections when Coupling Case 1 is used. Vertical dashed lines indicate the interface positions.

The focus is now shifted to Coupling Cases 2 and 3. To better quantify and compare the accuracy of each coupling case, the total energy within each domain is computed. As the pulse propagates through the bar, the total energy (strain and kinetic) is transferred from the FE domain (E_{tot}^{FE}) to the PD domain (E_{tot}^{PD}) and finally back to the FE domain. As an example, the energy transferring between the two domains using Coupling Case 2 is illustrated in Figure 5.7 for the modulated incident pulse. The pulse crosses the FE-PD interface at approximately $t = 1.19 \cdot 10^{-4}$s and the energy is transferred from the FE to the PD domain. At $t = 2.03 \cdot 10^{-4}$s, the pulse crosses the PD-FE interface and the energy is transferred back to the FE domain. For comparison, the total energy in an equivalent FE only model is also plotted with grey dashed line. If the coupling is adequately accurate, the spurious reflections generated should be minimal and all the energy should be transferred back to the FE domain. The accuracy of the coupling method is tested by comparing the amount of energy that was transferred to the right-hand side FE model compared to the initially provided energy. The percent error between the two energies (energy drift) is used in the following as a measure of accuracy.

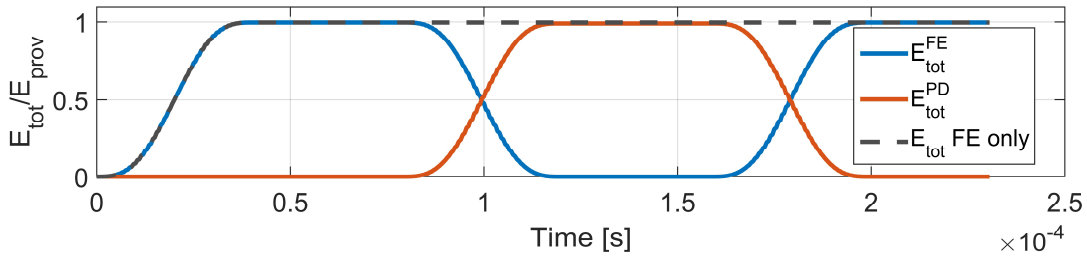

Figure 5.7: Energy transfer between the FE and the PD domain for the modulated pulse when the second coupling case is used.

Figure 5.8 depicts the energy drift when Coupling Case 2 is used, for different values of the PD horizon δ and discretization length Δx^{PD}, for both the modulated and the Gaussian incident pulses. As δ increases, much finer grids are required to achieve comparable accuracy. It is noted that for macroscale problems, the horizon is typically set to 3 to 4 times the discretization length, as higher values can induce excessive dispersion and increase the required computational time, while lower values will lead to grid dependent crack paths [7,84,207].

As Δx^{PD} and δ increases, total reflection of the incident wave is observed (energy drift =1 in Figure 5.8). This is attributed to the cut-off frequency of the discrete PD model being well below the frequency content of the pulse. Here by "*cut-off frequency*" we refer to the high frequency limit above which the discretized system does not support traveling waves. In such cases, the pulse never enters the PD domain and is reflected back to the FE domain. The parameters Δx^{PD} and δ are of outmost importance as they control the model's cut-off frequency. The definition and computation of the cut-off frequency of the discrete PD model is discussed in depth in the following paragraph.

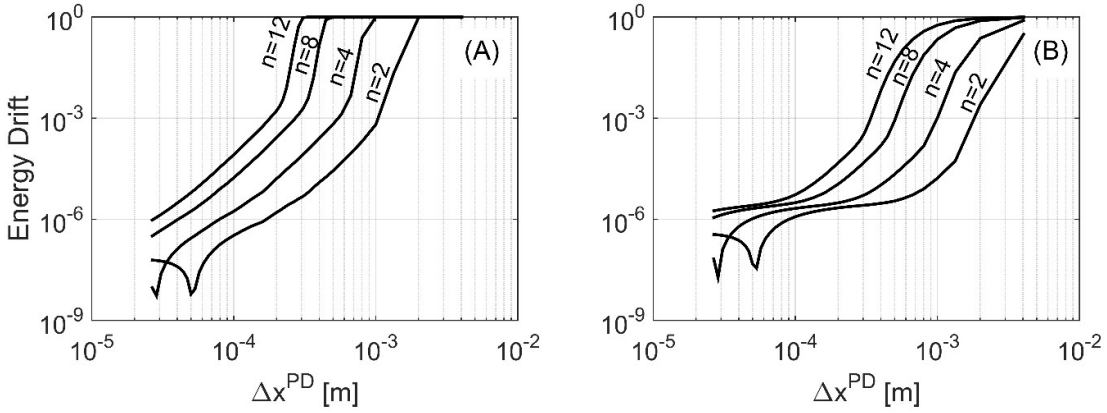

Figure 5.8: Energy drift using the second coupling case for (a) the modulated and (b) the gaussian incident pulse and for PD horizon $\delta = n\Delta x^{PD}$ (the horizontal axis is in log scale).

When the third coupling case is implemented, two additional parameters need to be taken into consideration, namely, the overlapping length l^{coupl} and the choice of blending function $h(\boldsymbol{x})$ that is implemented within the formulation. In [75], numerical tests were carried out using a linear blending function. Here a cubic blending function is also tested. In [205] and [120], a more detailed analysis on the selection of blending functions can be found for the Arlequin method. The problem parameters are the same as before and the number of Lagrange multipliers in the coupling region is the same as the corresponding PD particles.

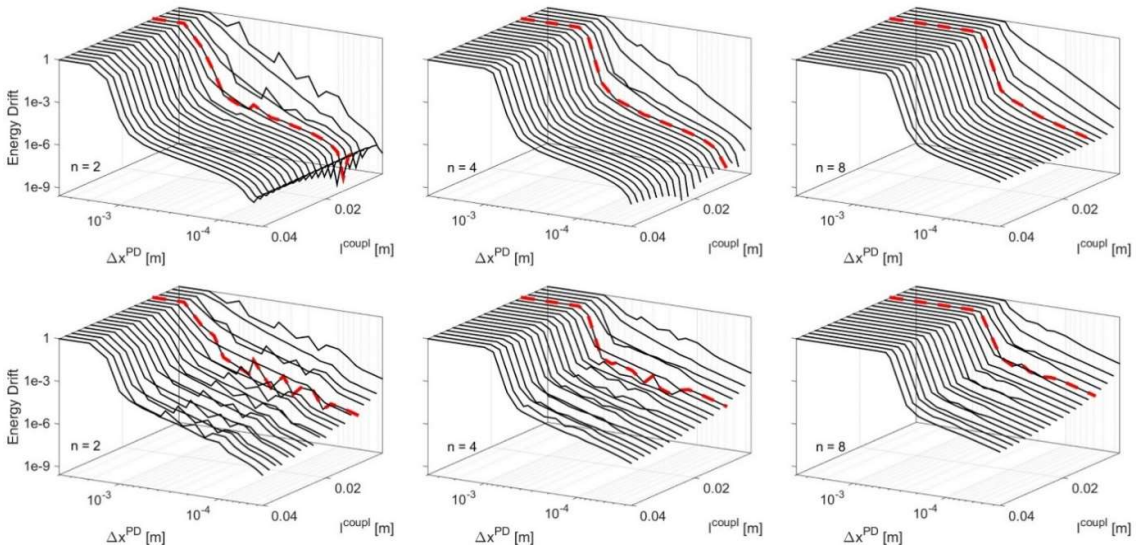

Figure 5.9: Energy drift waterfall plots using the third coupling case for a modulated pulse. The top row corresponds to results using the cubic blending function while the bottom to the linear. The dashed (red) line indicates the case of $l^{coupl} = 0.01$ m. The PD horizon is given as $\delta = n\Delta x^{PD}$ (Δx^{PD} axis is in log scale).

Using the modulated pulse, a parametric investigation is performed for different values of Δx^{PD}, δ and l^{coupl}. In Figure 5.9, waterfall plots of the resulting energy drift are presented. In all cases, the conditions for total wave reflection remain unaffected by the choice of blending function and l^{coupl}. However, higher values of l^{coupl} can improve the accuracy of the coupling. Furthermore, by implementing a cubic blending function instead of a linear in the formulation, the accuracy of the coupling is improved for the same values of Δx^{PD}, δ and l^{coupl}. This is intuitively expected since the transition is smoother in this case. Increasing the value of l^{coupl} increases the computational cost of the method as additional PD particles and Lagrange

multipliers are introduced. For the cases considered, an overlapping length of approximately $l^{coupl} = 0.01\ \mathrm{m}$ seems a fair compromise between accuracy and computational cost.

Using $l^{coupl} = 0.01\ \mathrm{m}$ and a cubic blending function, the energy drift is also computed for the Gaussian pulse and the results are plotted in Figure 5.10. Comparing Figure 5.8 and Figure 5.10, both coupling approaches exhibit total wave reflection under the same conditions, indicating that the cut-off frequency is not affected by the coupling strategy. In both cases the higher frequency content of the modulated pulse requires refinement of the PD domain to ensure transmission. Furthermore, the accuracy achieved is comparable between the two approaches for the specific choice of parameters. If, however, the linear blending was implemented further refinement would be necessary.

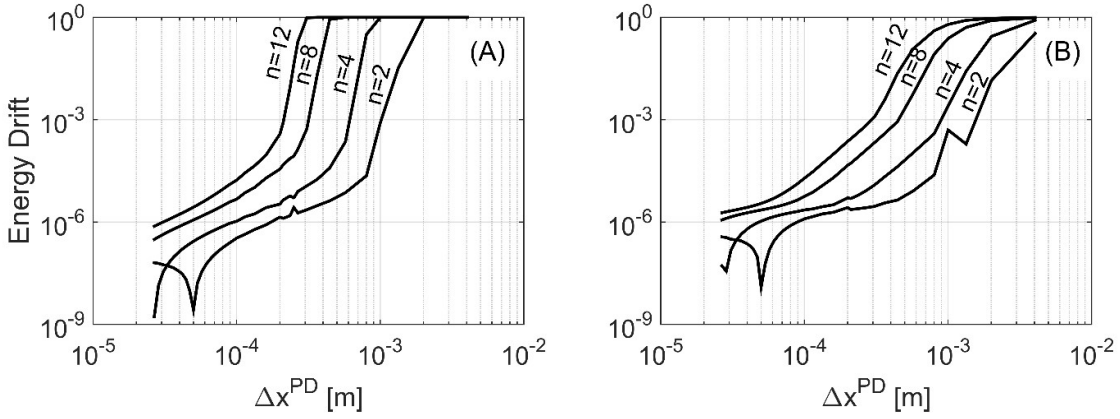

Figure 5.10: Energy drift using the third coupling case with cubic blending function and $l^{coupl} = 0.01\ \mathrm{m}$ for (a) the modulated and (b) the gaussian incident pulse with PD horizon $\delta = n\Delta x^{PD}$ (the horizontal axis in log scale).

To make this investigation more general, it is of interest to continue the analysis in the frequency domain. To this end, in the next section, the linearized PD theory is coupled with a continuum directly instead of a FE approximation. Furthermore, a brief derivation of the PD dispersion curve from the discretized equation of motion is presented as it provides insights on the cut-off frequency and its dependence on Δx^{PD} and δ that is pivotal in minimizing the spurious reflections.

5.4 Reflection – Transmission in a 1D Continuum – PD Bar

5.4.1 *Dispersion curve for Bond-Based PD*

According to the theory of linear elasticity, the phase velocity of a travelling wave is independent of its angular frequency ω and wavenumber κ, leading to a linear relation

between ω and κ. In discretized systems however, this relation is nonlinear. Along the interface of two models with different dispersion relationships, spurious reflections occur as the incident wave travels with different speeds in each domain [208].

In PD theory, waves of higher frequency will travel slower than lower frequency waves. In [209], the dispersion characteristics of gradient and nonlocal elasticity are elasticity are compared. Similar observations are reported for nonlocal elastic models with different weight functions while strain gradient models produce both normal and anomalous dispersion. The dispersion needs to be taken into consideration when coupling domains that are described by different models. Additionally, discrete models exhibit a cut-off frequency that can lead to full reflection of the incident pulse. In [6], [95] and [210], the PD dispersion curve was extracted by substituting solutions with the form $u = Ue^{i(\kappa x - \omega t)}$ into the linearized PD equation of motion and solving the resulting integral in the eigenvalue problem. In [211] the dispersion relation was derived for different micromoduli while in [102] they are given for PD beams and plates. The dispersive characteristic of the PD theory can be also used to match the experimentally observed dispersion as presented in [212].

Considering a 1D bar of infinite length and using the idealization that the bar consists of a repeating series of masses and springs, the dispersion curve of PD is derived after substitution of Eq. (3.14) in the discretized equation of motion from Eq. (3.23). If each particle interacts only with those that is in direct contact with (i.e. $\delta = \Delta x$) and Δx is uniform then, the equation of motion for a particle becomes:

$$\ddot{d}_n = c^2 \frac{d_{n-1} - 2d_n + d_{n+1}}{\Delta x^2} \tag{5.27}$$

where, the volume correction is also included. When $d = De^{i(\omega t + \kappa x)}$, the following relationship is extracted:

$$\omega = \frac{2}{\delta}\sqrt{\frac{E}{\rho}}\sin\left(\frac{\kappa \Delta x}{2}\right). \tag{5.28}$$

In the limit when $\kappa\Delta x$ is very small, we can use the approximation $\sin(\kappa\Delta x/2) = \kappa\Delta x/2$ and Eq. (5.28) leads to $\omega/\kappa \approx c$. Thus, the PD dispersion relation approximates the one extracted from the local theory of elasticity. This observation has already been described in [6]. Similarly, in [209] it is reported that nonlocal elasticity with a linearly decreasing weighting function $w(r)$ with $w(0) = 1$ and $w(\Delta x) = 0$, leads to the same dispersion relationship as the mass-spring model with nearest interactions (i.e. $\delta = \Delta x$).

Following the same procedure, the dispersion relation for various horizon lengths can be derived. As a general case, with $\delta = n\Delta x$, the dispersion relation can be written as:

$$\omega = \frac{2}{n\Delta x}\sqrt{\frac{E}{\rho}}\sin\left(\frac{\kappa\Delta x}{2}\right)G_n\left(\frac{\kappa\Delta x}{2}\right), \tag{5.29}$$

where $G_n(x)$ is a function whose expression depends on the value of the PD horizon δ. Expressions for $G_n(x)$ are given in Table 5.1, for $n = \delta/\Delta x = 1,2,3 \text{ and } 4$. As expected, for $\kappa\Delta x \to 0$ then $G_n(x) \to n$ and Eq. (5.29) reduces to the dispersion relationship obtained from classical elasticity. The derivation of $G_n(x)$ for $n = 1,2,3 \text{ and } 4$ is presented in Appendix .

A comparison between the dispersion relation for different δ using Eq. (5.29) is illustrated in Figure 5.11. In the same figure, the linear elasticity case has also been included. It is noted that when the value of the PD horizon is $\delta = \Delta x$, the relationship coincides with that for a 2-node linear finite element. The figure is plotted for wave numbers $\kappa \in (0, \pi/\Delta x)$ representing only the positive half of the first Brillouin zone. The parameters assumed are $E = 200\ \text{GPa}$, $\rho = 7850\ \text{kg/m}^3$, $\Delta x = 2 \cdot 10^{-4}\ \text{m}$ and $l = 0.4\ \text{m}$. An important feature for this study is that the PD cut-off frequency depends not only on the discretization length Δx but also on the value of the horizon δ. In Figure 5.11, the angular frequencies ω_0, that define the cut-off frequency are indicated for each value of δ. Values have been nondimensionalized with respect to $c = \sqrt{E/\rho}$ and l.

Table 5.1: Table of expressions for $G_n(x)$.

n	$G_n(x)$
1	1
2	$\sqrt{2\cos(x)+2}$
3	$\sqrt{\frac{32}{6}\sin^4(x) - 8\sin^2(x) + 4\cos^2(x) + 5}$
4	$\sqrt{4\cos^2(x)\cos^2(2x) + \frac{32}{3}\sin^4(x) - 16\sin^2(x) + 4\cos^2(x) + 8}$

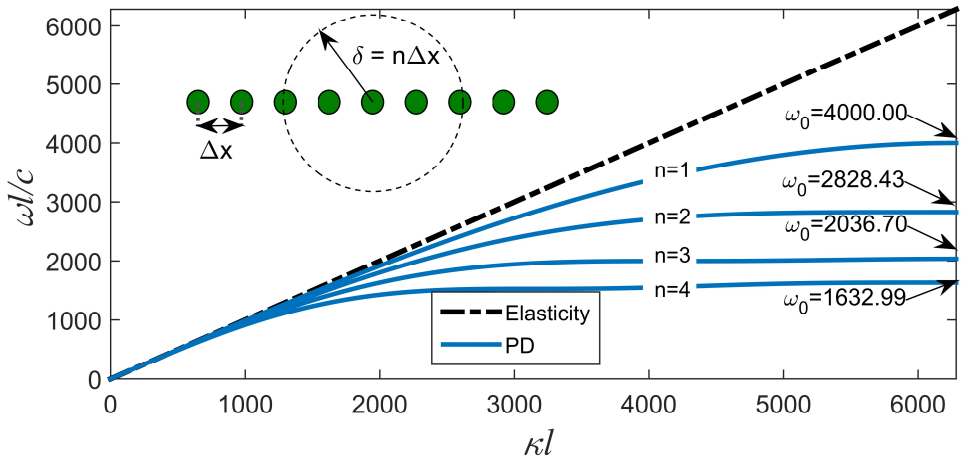

Figure 5.11: Comparison of dispersion curves between elasticity and the PD theory with $\delta = n\Delta x$.

5.4.2 *Continuum – PD coupling and Frequency Domain Analyses*

Coupling of linearized PD theory with continuum directly allows to perform our analyses in the frequency domain and assume rightward travelling harmonic pulses propagating in an infinite bar. The domain Ω (see Figure 5.12), is divided into two subdomains Ω^{PD} and Ω^{cont}, with $\Omega^{PD} \cup \Omega^{cont} = \Omega$ and $\Omega^{PD} \cap \Omega^{cont} = \Omega^{coupl}$. The classical theory of elasticity will be used to describe the behaviour of the Ω^{cont} domain while the PD theory will be used for Ω^{PD}. It is noted that for Coupling Cases 1 and 2 we have that $\Omega^{coupl} = 0$. The PD theory is used in the middle of the bar with $\Omega^{PD} = [-l, l]$, while the rest of the bar is modelled using continuum elasticity with $\Omega^{cont} = \Omega^{cont,1} \cup \Omega^{cont,2} = (-\infty, -l] \cup [l, +\infty)$.

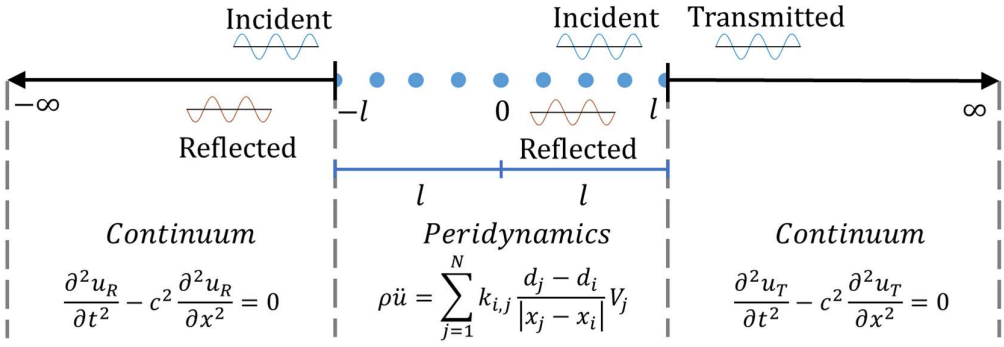

Figure 5.12: Continuum-PD coupling in an infinite 1D bar using a discrete interface.

A sinusoidal incident wave is assumed to be travelling from $-\infty$ towards the left coupling interface at $-l$. Part of the wave will be reflected towards $-\infty$ while the rest will be transmitted into Ω^{PD}. Similarly, at l, part of the pulse will transmit to $\Omega^{cont,2}$, while the remaining energy will reflect into Ω^{PD}. Hence, in $\Omega^{cont,1}$, there are two pulses, the initial incident pulse and the reflection from the first interface. In $\Omega^{cont,2}$, on the other hand, only the finally transmitted pulse exists. The infinite length of the bar prevents the interference from boundary reflections. Denoting with u_R, u_T and d the displacement fields in $\Omega^{cont,1}$, $\Omega^{cont,2}$ and Ω^{PD} respectively, we assume solutions in the form $u_R = U_R e^{-i\omega t}$, $u_T = U_T e^{-i\omega t}$ and $d_i = D_i e^{-i\omega}$ and the governing equations become:

$$c^2 \frac{d^2 U_R}{dx^2} + \omega^2 U_R = 0 \tag{5.30a}$$

$$-\omega^2 m_i D_i = \sum k \frac{D_j - D_i}{|x_j - x_i|} V_j V_i \tag{5.30b}$$

$$c^2 \frac{d^2 U_T}{dx^2} + \omega^2 U_T = 0, \tag{5.30c}$$

where U_R and U_T are solutions in the form:

$$U_R = e^{i\kappa x} + Re^{-i\kappa x} \text{ and} \tag{5.31a}$$

$$U_T = Te^{i\kappa x}, \tag{5.31b}$$

with R and T being the reflection and transmission coefficients, respectively [213]. Energy conservation implies $E_R + E_T = 1$, where $E_R = |R|^2$ is the reflected energy and $E_T = |T|^2$ is the transmitted energy. Using these definitions, the ability of a pulse to be transmitted across a coupling interface is evaluated.

Realization of Coupling Cases 1 and 2 for the discretized PD equation of motion with the continuum solution is carried out following the procedure presented in sections 5.2.2 and 5.2.3, respectively. The first coupling case requires the position of PD particles at the interface positions $x_1 = -l$ and $x_n = l$, where n is the total number of PD particles (see Figure 5.13). Continuity and force equilibrium requirements are enforced at the interface positions resulting in the following equations:

$$U_R(-l) = D_1 \rightarrow D_1 = e^{-i\kappa l} + Re^{i\kappa l} \tag{5.32a}$$

$$U_T(l) = D_n \rightarrow D_n = Te^{i\kappa l} \tag{5.32b}$$

$$\Sigma F(-l) = 0 \tag{5.32c}$$

$$\Sigma F(l) = 0 \tag{5.32d}$$

Using as an example the case where $\delta = 2\Delta x$, Eqs. (5.32c) and (5.32d) become:

$$\left(k_{1,2} + k_{1,3}\right)D_1 - k_{1,2}D_2 - k_{1,3}D_3 - EAi\kappa e^{i\kappa l}R = -EAi\kappa e^{-i\kappa l} \tag{5.33a}$$

$$-k_{n,n-1}D_{n-1} - k_{n,n-2}D_{n-2} + \left(k_{n,n-1} + k_{n,n-2}\right)D_n - EAi\kappa e^{i\kappa l}T = 0 \tag{5.33b}$$

where in the above, D_1, D_2, D_3, D_{n-2}, D_{n-1} and D_n are the particle displacements corresponding to the particles with positions $\boldsymbol{x} = -l, -l + \Delta x, -l + 2\Delta x, l - 2\Delta x, l - \Delta x$ and l respectively. Combining Eqs. (5.30), (5.31), (5.32) and (5.33) the system of equations can be solved for the R and T coefficients.

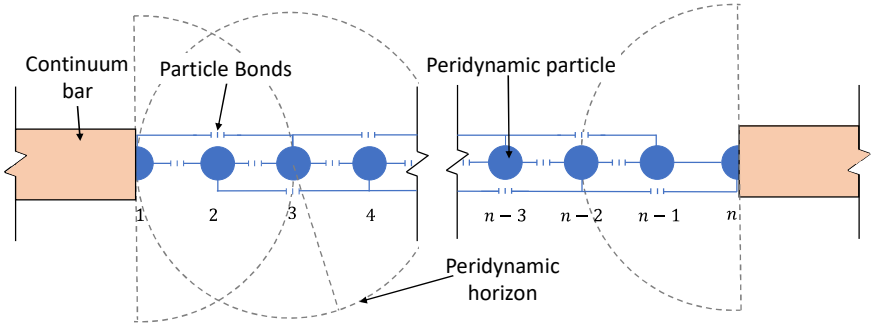

Figure 5.13: Illustration of coupling PD with continuum using the first coupling approach.

In the same manner, the system of equations for Coupling Case 2 can be constructed. Without loss of generality the example $\delta = 2\Delta x$ is implemented leading to the introduction of two ghost particles at each side of the PD domain (see Figure 5.14). The continuity and force equilibrium requirements lead now to the following equations:

$$U_R\left(x_{g1}\right) = D_1 \rightarrow D_1 = e^{i\kappa x_{g1}} + Re^{-i\kappa x_{g1}}, \tag{5.34a}$$

$$U_R\left(x_{g2}\right) = D_2 \rightarrow D_2 = e^{i\kappa x_{g2}} + Re^{-i\kappa x_{g2}} \tag{5.34b}$$

$$U_T\left(x_{g3}\right) = D_{n-1} \rightarrow D_{n-1} = Te^{i\kappa x_{g3}} \tag{5.34c}$$

$$U_T\left(x_{g4}\right) = D_n \rightarrow D_n = Te^{i\kappa x_{g4}} \tag{5.34d}$$

$$\Sigma F(-l) = 0 \tag{5.34e}$$

$$\Sigma F(l) = 0 \tag{5.34f}$$

where, x_{g1}, x_{g2}, x_{g3} and x_{g4} are the positions of the ghost particles corresponding to the locations $\boldsymbol{x} = -l - \Delta x/2, -l - 3\Delta x/2, l + \Delta x/2$ and $l + 3\Delta x/2$ respectively. Although the force equilibrium of the second coupling case, described in Eqs. (5.34e) and (5.34f), looks similar to that of the first coupling case, described in Eqs. (5.32c) and (5.32d), it correlates the sum of the internal forces of each bond that crosses the interface with the internal forces from elasticity. For the example considered here, Eqs. (5.34e) and (5.34f) are expressed as:

$$k_{1,3}D_1 + \left(k_{2,3} + k_{2,4}\right)D_2 - \left(k_{1,3} + k_{2,3}\right)D_3 - k_{2,4}D_4 - i\kappa EAe^{i\kappa l}R = -i\kappa EAe^{-i\kappa l} \tag{5.35a}$$

$$-k_{n-1,n-3}D_{n-3} - \left(k_{n-1,n-2} + k_{n,n-2}\right)D_{n-2} + \left(k_{n-1,n-2} + k_{n-1,n-3}\right)D_{n-1} + k_{n,n-2}D_n - i\kappa EAe^{i\kappa l}T = 0 \tag{5.35b}$$

Finally, combining Eqs. (5.30), (5.31), (5.34) and (5.35) the R and T coefficients are computed for the second coupling case.

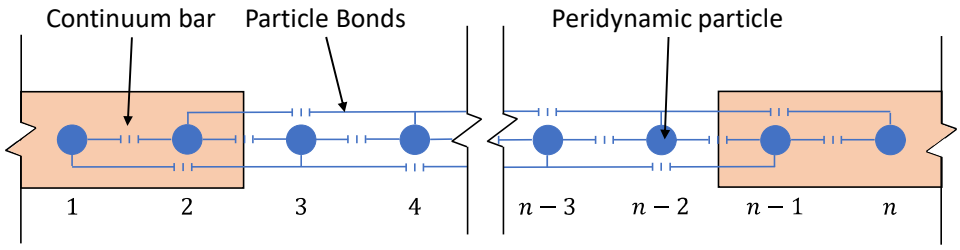

Figure 5.14: Coupling of PD with continuum using the second coupling case.

For Coupling Case 3 to be implemented, Ω^{PD} is extended within $\Omega^{cont,1}$ and $\Omega^{cont,2}$ by a length $l^{coupl} = x_B - x_A = x_D - x_C$ to create the overlapping regions $\Omega^{coupl,1}$ and $\Omega^{coupl,2}$, over which the coupling scheme is enforced (Figure 5.15). The assumption of solutions in the form given by Eqs. (5.31) is no longer valid within these domains. Assuming a linear blending function $a(x) = 1 - (x - x_A)/l^{coupl}$, an analytical derivation of the unknown fields $U_1(\boldsymbol{x})$ and $U_2(\boldsymbol{x})$ is sought.

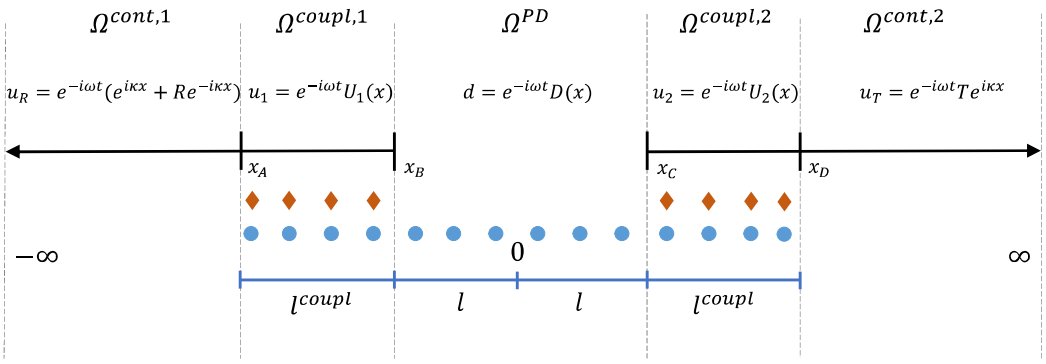

Figure 5.15: Illustration of continuum to PD coupling using the third approach. Circles indicate the PD particles, diamonds the Lagrange multipliers and solid line the continuum bar.

Using Eq. (5.18a) and substituting $u_1 = e^{-i\omega t}U_1(\boldsymbol{x})$ in $\Omega^{coupl,1}$, the following differential equation is written:

$$a(x)U_{1,xx} + a(x)_{,x}U_{1,x} + \frac{\omega^2\rho}{E}a(x)U_1 = \sum_{j=1}^{n}\frac{\Lambda_j}{EA}\delta\left(x - x_{\lambda_j}\right), x_A \leq \boldsymbol{x} \leq x_B \qquad (5.36)$$

where, $\delta(\cdot)$ is the Dirac delta function. A solution in the form $\lambda_j = e^{i\omega t}\Lambda_j(x)$ was assumed for the Lagrange multipliers and n and x_{λ_j} is the total number and the positions of the Lagrange multipliers. A similar equation can be written for $\Omega^{coupl,2}$.

Using the change of variables $z = a(x)$, Eq. (5.36) becomes:

$$zU_{1,zz} + U_{1,z} + b_1^2 zU_1 = \sum_{j=1}^{n} b_2\Lambda_j\delta\left(z - \widehat{x_{\lambda_j}}\right), 0 \leq z \leq 1 \qquad (5.37)$$

where, $b_1 = \sqrt{\rho\omega^2 l^2/E}$ and $b_2 = l/EA$ are two constants and $\widehat{x_{\lambda_j}} = (l^{coupl} + x_A - x_{\lambda_j})/l^{coupl}$. This differential equation can be solved using the Hankel transform [214,215]. The solution obtained in $\Omega^{coupl,1}$ is given as:

$$U_1 = C_1 J_0(b_1 z) + C_2 Y_0(b_1 z) + \sum_{j=1}^{n}\frac{\pi}{2}b_2\Lambda_j H\left(z - \widehat{x_{\lambda_j}}\right)\left(J_0\left(b_1\widehat{x_{\lambda_j}}\right)Y_0(b_1 z) - J_0(b_1 z)Y_0\left(b_1\widehat{x_{\lambda_j}}\right)\right) \qquad (5.38)$$

where, C_1 and C_2 are two constants, J_k and Y_k are the Bessel functions of the first and second kind with order k and $H(\cdot)$ is the Heaviside function. As can be seen from Eq. (5.38), as $z \to 0$ (i.e. $x \to x_B$), $U_1 = C_1 J_0(0) + C_2 Y_0(0) \to -\infty$. This solution is not accepted as a finite result is expected and hence $C_2 = 0$.

On the interface between $\Omega^{coupl,1}$ and $\Omega^{cont,1}$, continuity and equilibrium conditions need to be satisfied. This leads to the following two equations:

$$U_R|_{x=x_A} = U_1|_{x=x_A} \rightarrow$$
$$Re^{-i\kappa x_A} - C_1 J_0(b_1) - \sum_{j=1}^{n}\frac{\pi}{2}b_2\Lambda_j\left(J_0\left(b_1\widehat{x_{\lambda_j}}\right)Y_0(b_1) - J_0(b_1)Y_0\left(b_1\widehat{x_{\lambda_j}}\right)\right) = -e^{i\kappa x_A} \qquad (5.39)$$

and:

$$\left.\frac{dU_R}{dx}\right|_{x=x_A} = \left.\frac{dU_1}{dx}\right|_{x=x_A} \rightarrow$$
$$i\kappa Re^{-i\kappa x_A} + C_1\frac{b_1 J_0(b_1)}{l^{coupl}} - \sum_{j=1}^{n}\frac{\pi b_2 b_1}{2l^{coupl}}\Lambda_j\left(J_1(b_1)Y_0\left(b_1\widehat{x_{\lambda_j}}\right) - J_0\left(b_1\widehat{x_{\lambda_j}}\right)Y_1(b_1)\right) = i\kappa e^{i\kappa x_A} \qquad (5.40)$$

Similarly, the same procedure can be repeated in $\Omega^{coupl,2}$ to relate the transmission coefficient T with the solution U_2. Using Eqs. (5.18b), (5.18c), (5.39) and (5.40), the system of equations can be solved to compute the reflected and transmitted energy across the different domains.

The accuracy of the third coupling approach can be improved using a cubic (Hermitian) blending function with $a(x) = 1 - 3\left(\frac{x-x_A}{l^{coupl}}\right)^2 + 2\left(\frac{x-x_A}{l^{coupl}}\right)^3$ in Eq. (5.36). In this case, the unknown displacement fields are approximated numerically through finite elements in $\Omega^{coupl,1}$ and $\Omega^{coupl,2}$.

The FEs are coupled on one end with continuum using the first coupling approach and at the other end with PD using the third coupling approach Figure 5.16. To avoid interference in the final $R-T$ diagrams due to the connection of the FE with the continuum, an extremely fine FE mesh was used, with $\Delta x^{FE} = 2 \times 10^{-5}\text{m}$, to approximate as closely as possible the continuum case. For the solution of this configuration, Eqs. (5.20) are implemented in the frequency domain with the addition of continuity and force balance conditions, using equations (5.32a,b) and (5.32c,d) respectively, between the FEs and the continuum at positions x_A and x_D.

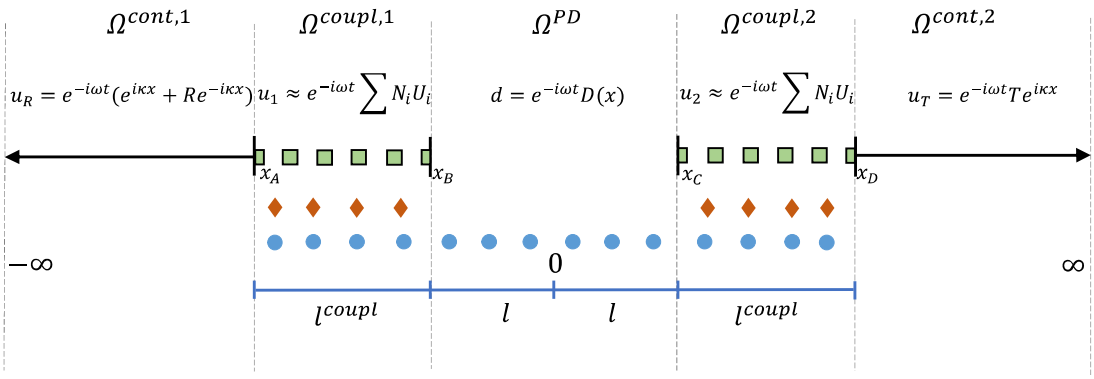

Figure 5.16: Third coupling case with finite elements in the coupling zone connected with continuum.

Using the same model parameters as in the time-domain analyses (i.e. $E = 200\,\text{GPa}$, $A = 10^{-6}\,\text{m}^2$, $\rho = 7850\,\text{kg/m}^3$ and $l = 0.2\,\text{m}$ as the half-length of the PD domain), the transmission and reflection coefficients were computed with ω ranging from 0 to $4 \cdot 10^7$ rad/s for various values of Δx^{PD} and $\delta = n\Delta x^{PD}$. In Figure 5.17, Reflection – Transmission diagrams are reported for all coupling cases considered, for different PD discretization length Δx^{PD} values, while keeping the PD horizon constant $\delta = 2\Delta x^{PD}$. Red lines indicate the part of the initial energy that was reflected ($|R|^2$) while blue lines indicate the transmitted energy ($|T|^2$). Similarly, in Figure 5.18, the PD discretization length is kept constant, with $\Delta x^{PD} = 2 \cdot$

10^{-4}m, and different values are used for the PD horizon. In all cases, energy conservation is satisfied. Results are presented in a nondimensional form with respect to the wave speed c and the length of Ω^{PD}, $2l = 0.4$ m.

All coupling approaches considered can achieve accurate wave propagation with minimal reflections for relatively small values of ω, as $|R|^2$ is close to 0 and $|T|^2 = 1$. As the frequency increases, the accuracy of the coupling deteriorates. When the forcing frequency of the pulse is close to or exceeds the cut-off frequency total reflection occurs and the transmitted energy vanishes. The PD discretization length Δx^{PD} implemented in Figure 5.18 is the same as that in Figure 5.11. For all cases, total reflection occurs at the frequency value predicted from the PD dispersion curve regardless of the coupling method chosen. Furthermore, the influence of Δx^{PD} and δ on the model's cut-off frequency is illustrated.

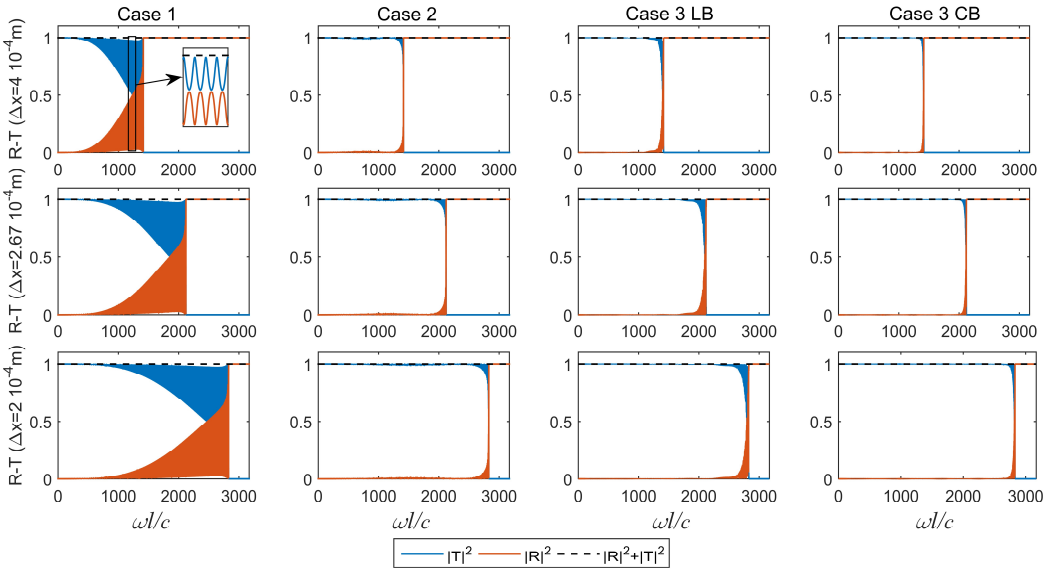

Figure 5.17: Reflection – Transmission diagrams for Coupling Cases 1, 2 ,3 with a linear blending function (LB) and 3 with a cubic blending function (CB). The PD horizon was set to $\delta = 2\Delta x^{PD}$. Each row corresponds to a different PD discretization Δx^{PD}.

Using the results reported in Figure 5.17 and Figure 5.18, Coupling Case 3 with a cubic blending function leads to the best results, followed by Coupling Case 2. Through these numerical tests, the improvement of implementing a cubic blending function within the formulation of the third coupling case is also highlighted as the coupling remains accurate for values closer to the cut-off frequency. It is noted here that for the results presented, the overlapping length was set to $l^{coupl} = 10\Delta x$. The coupling could be further improved by increasing the overlapping length as illustrated in Figure 5.19. The accuracy of the coupling is

improved, even for frequencies very close to the cut-off frequency however, the computational cost is increased as additional PD particles and Lagrange multipliers are used.

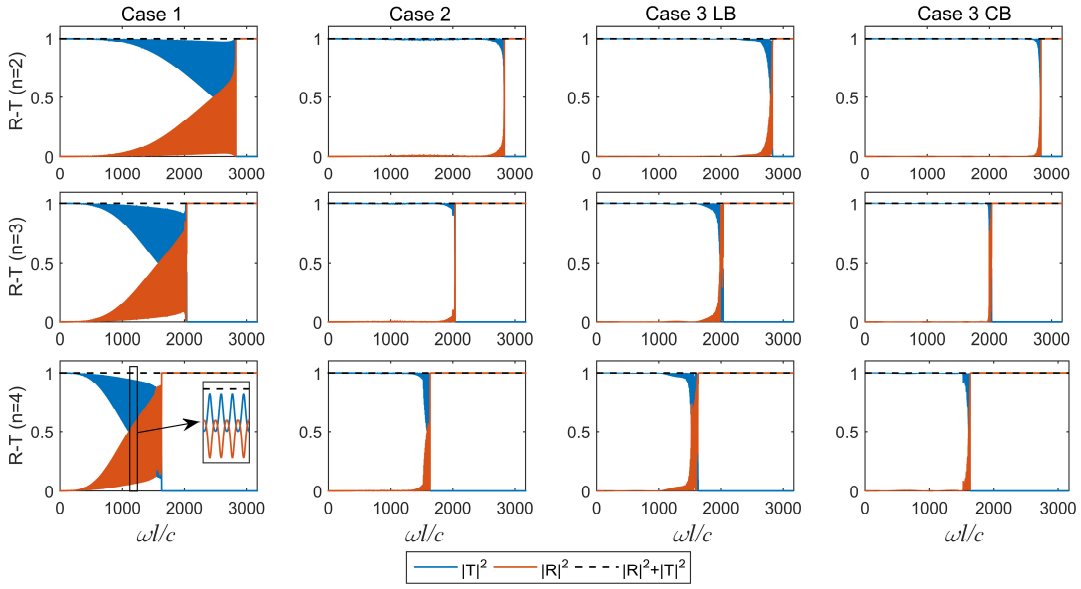

Figure 5.18: Reflection – Transmission diagrams for Coupling Cases 1, 2 ,3 with a linear blending function (LB) and 3 with a cubic blending function (CB). The PD discretization was set to $\Delta x^{PD} = 2 \times 10^{-4}\mathrm{m}$. Each row corresponds to a PD horizon value given as $\delta = n\Delta x^{PD}$.

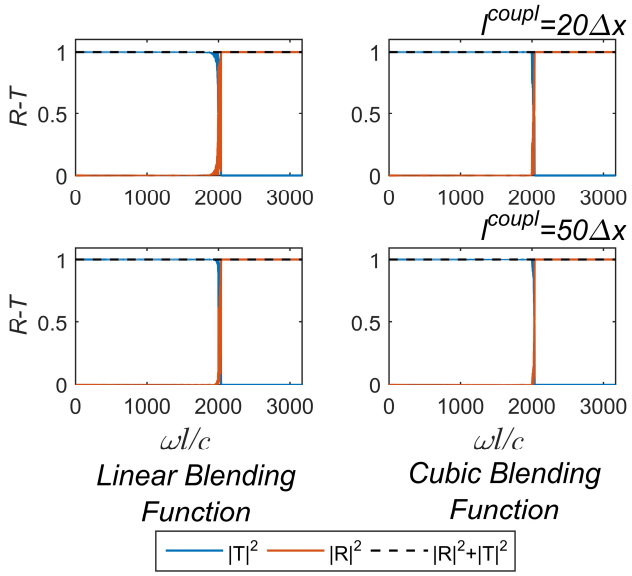

Figure 5.19: Influence of the overlapping length l^{coupl} when Coupling Case 3 is used with either the linear or the cubic blending function. The PD discretization and horizon values were set to $\Delta x^{PD} = 2 \cdot 10^{-4}\mathrm{m}$ and $\delta = 3\Delta x^{PD}$.

Finally, of major importance is the implementation of the surface correction factor (Figure 5.20). Coupling Case 3 is less affected from the skin effect which appears at the particles near

the boundary of Ω^{PD} where the value of the blending function is almost zero (i.e. energy has been transferred to Ω^{cont}). The first two coupling approaches are affected though, as the coupling interface is located near the area where the skin effect manifests. Comparing Figure 5.20 with the corresponding diagrams from Figure 5.18, the accuracy of the coupling is affected significantly if appropriate correction is not implemented.

Coupling Case 3 can lead to the most accurate coupling between PD and continua, given that an appropriate blending function and an adequately large overlapping region is provided. This increases the computational burden of the method and creates ambiguities on the a-priori selection of blending functions in 2D and 3D problems. On the other hand, coupling approaches similar to Coupling Case 2 or the method presented in [117], achieve comparable accuracy with lower cost and are easier to implement. The simplistic coupling presented in the first method should be avoided not only because it leads to strong reflections for relatively small frequencies but also because it requires conforming meshes that are problematic in problems involving higher dimensions.

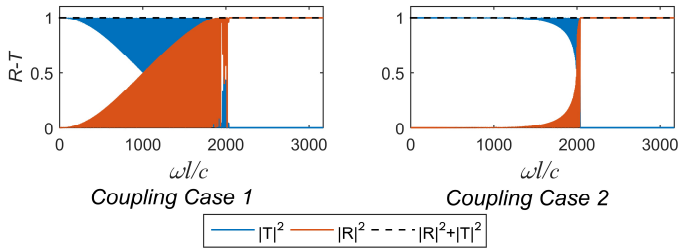

Figure 5.20: Influence of the surface correction for Coupling Cases 1 and 2 with $\Delta x^{PD} = 2 \cdot 10^{-4}\mathrm{m}$ and $\delta = 3\Delta x^{PD}$.

5.5 Coupled FE-PD model in 2D

5.5.1 *Extension of the Second Coupling Case to 2D Problems*

The second coupling case is extended to 2D problems to further illustrate the importance of considering the cut-off frequencies of both the PD and FE models when addressing dynamic examples. The only thing that differs in the formulation of the second coupling case is the computation of the forces applied on the interface. In the 1D bar example, the computation of PD interfacial forces required to simply identify which bonds cross the interface (i.e. bonds that connect a ghost and a normal particle) and what is the total force of these bonds. In 2D the interface between the two descriptions is no longer a point but a line and thus it is necessary to compute the exact location where each bond crosses the interface. This is the

location where PD forces are applied on the interface. In the following examples the linearized PD theory is coupled with 4-noded bilinear finite elements.

Continuity between the FE and PD model is enforced again at the location of the ghost particles through interpolation using the FE shape functions as expressed in Eq. (5.5). The coefficients of the interpolation can be stored in a matrix $\boldsymbol{C}_g$ and thus we have:

$$\boldsymbol{d}^g = \boldsymbol{C}_g \boldsymbol{u}. \tag{5.41}$$

Following the same interpolation, the acceleration $\ddot{\boldsymbol{d}}^g$ and velocity $\dot{\boldsymbol{d}}^g$ of the ghost particles can also be computed. Force equilibrium is enforced on the coupling interface by considering the forces acting on it from the FE, $\boldsymbol{f}^{inter,FE}$, and the PD, $\boldsymbol{f}^{inter,PD}$, domain. To compute $\boldsymbol{f}^{inter,PD}$, the forces from all the bonds that cross the interface need to be evaluated and applied on the location that the bond crosses the interface. In Figure 5.21, a PD particle, a ghost particle and a finite element on the interface have been isolated as an illustration. The bond between the PD particle i and the ghost particle j, crosses the coupling interface at (x_A, y_A). This is the location that the force is applied with regards to the force equilibrium between the two approximations.

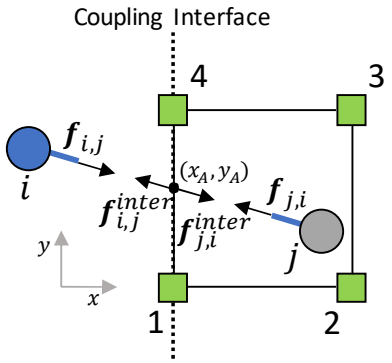

Figure 5.21: Close-up near the coupling interface indicating the point of application of the bond force on the coupling interface.

The force $\boldsymbol{f}_{i,j}^{inter}$ on the interface due to the PD particle i and the ghost particle j is equal to the bond force connecting the two particles, i.e. $\boldsymbol{f}_{i,j}^{inter} = -\boldsymbol{f}_{i,j}$. Furthermore, due to the linear momentum described in Eq. (3.4), we get that $\boldsymbol{f}_{i,j} = -\boldsymbol{f}_{j,i}$. Thus, the force acting on the interface can be computed in the global coordinate system using Eq. (3.42) as:

$$\boldsymbol{f}_{i,j}^{inter} = k_{i,j}^{bond} \begin{bmatrix} -c^2 & -c \cdot s & c^2 & c \cdot s \\ -c \cdot s & -s^2 & c \cdot s & s^2 \end{bmatrix} \boldsymbol{d}_{i,j}^{inter}, \tag{5.42}$$

where, $\boldsymbol{f}_{i,j}^{inter} = \{f_{i,j,x}^{inter}, f_{i,j,y}^{inter}\}^T$ and $\boldsymbol{d}_{i,j}^{inter} = \{d_{i,x}, d_{i,y}, d_{j,x}^g, d_{j,y}^g\}^T = \{\boldsymbol{d}_i, \boldsymbol{d}_j^g\}^T$. It is convenient to separate the contributions from the PD particles and the ghost particles in $\boldsymbol{f}_{i,j}^{inter}$. Then Eq. (5.42) is rewritten as:

$$\boldsymbol{f}_{i,j}^{inter} = k_{i,j}^{bond} \begin{bmatrix} -c^2 & -c \cdot s \\ -c \cdot s & -s^2 \end{bmatrix} \boldsymbol{d}_i + k_{i,j}^{bond} \begin{bmatrix} c^2 & c \cdot s \\ c \cdot s & s^2 \end{bmatrix} \boldsymbol{d}_j^g = \boldsymbol{A}_1 \boldsymbol{d}_i + \boldsymbol{A}_2 \boldsymbol{d}_j^g \tag{5.43}$$

To compute $\boldsymbol{f}^{inter,PD}$, the force contributions $\boldsymbol{f}_{i,j}^{inter}$ from all the bonds that cross the coupling interface are considered. Here it is assumed that the bond force $\boldsymbol{f}_{i,j}^{inter}$ is applied on the FE at the position of intersection of the bond with the coupling interface (point x_A, y_A in Figure 5.21). The point of application is defined using a 2D Dirac delta function $\delta(x - x_A, y - y_A)$. Finally, $\boldsymbol{f}^{inter,PD}$ is computed by integrating $\boldsymbol{f}_{i,j}^{inter}$ on the FEs as an externally applied point force as:

$$\begin{aligned} \boldsymbol{f}^{inter,PD} &= \sum_{m=1}^{m_{tot}} \int \boldsymbol{N}^T \boldsymbol{f}_{i,j}^{inter} \delta(x - x_A, y - y_A) d\Gamma = \sum_{m=1}^{m_{tot}} \boldsymbol{N}_{x=x_A,y=y_A}^T \boldsymbol{f}_{i,j}^{inter} \\ &= \sum_{m=1}^{m_{tot}} \boldsymbol{N}_{x=x_A,y=y_A}^T \left(\boldsymbol{A}_1 \boldsymbol{d}_i + \boldsymbol{A}_2 \boldsymbol{d}_j^g\right) = \boldsymbol{C}_F \boldsymbol{d} + \boldsymbol{C}_{F,g} \boldsymbol{d}^g, \end{aligned} \tag{5.44}$$

where m_{tot} is the total number of bonds that cross the coupling interface. Effectively, the bond force has been distributed to the FE nodes that lie on the interface through its shape functions. In the last term of Eq. (5.44), matrices $\boldsymbol{C}_F$ and $\boldsymbol{C}_{F,g}$ are assembled from the terms $\sum_{m=1}^{m_{tot}} \boldsymbol{N}_{x=x_A,y=y_A}^T \boldsymbol{A}_1$ and $\sum_{m=1}^{m_{tot}} \boldsymbol{N}_{x=x_A,y=y_A}^T \boldsymbol{A}_2$, respectively. Then, for the FE equations of motion we can write:

$$\boldsymbol{K}^{FE} \boldsymbol{u} - \boldsymbol{f}^{inter,PD} = \boldsymbol{K}^{FE} \boldsymbol{u} - \boldsymbol{C}_F \boldsymbol{d} - \boldsymbol{C}_{F,g} \boldsymbol{d}^g = \boldsymbol{0}. \tag{5.45}$$

Finally, Eqs. (3.44), (3.68), (5.41) and (5.44) can be written as a global system of equations for the displacements $\boldsymbol{U}$ at the FE nodes, $\boldsymbol{d}$ of the PD particles and $\boldsymbol{d}^g$ of the ghost particles. This system has the form:

$$\begin{bmatrix} \boldsymbol{K}^{FE} & \boldsymbol{C}_F & \boldsymbol{C}_{F,g} \\ \boldsymbol{0} & \boldsymbol{K}^{PD} & \boldsymbol{K}^{PD,g} \\ \boldsymbol{C}_g & \boldsymbol{0} & -\boldsymbol{I} \end{bmatrix} \begin{bmatrix} \boldsymbol{u} \\ \boldsymbol{d} \\ \boldsymbol{d}^g \end{bmatrix} = \begin{bmatrix} \boldsymbol{F}^{FE} \\ \boldsymbol{F}^{PD} \\ 0 \end{bmatrix}, \tag{5.46}$$

where, $\boldsymbol{K}^{PD,g}$ contains the interactions between ghost and normal PD particles and it is defined similar to the $\boldsymbol{K}^{PD}$. The first row in the matrix in Eq. (5.46) represents the stiffness and coupling terms due to the interface from Eq. (5.45). The last set of equations in Eq. (5.46) (FE interpolation at the ghost nodes) is $\boldsymbol{d}^g = \boldsymbol{C}_g \boldsymbol{u}$. Using static condensation, the system can be

written in the form $\boldsymbol{K}^c\boldsymbol{U}^c = \boldsymbol{F}^c$. The stiffness matrix $\boldsymbol{K}^c$, displacement vector $\boldsymbol{U}^c$ and force vector $\boldsymbol{F}^c$ of coupled system are now defined as:

$$\boldsymbol{K}^c = \begin{bmatrix} \boldsymbol{K}^{FE} + \boldsymbol{C}_{F,g}\boldsymbol{C}_g & \boldsymbol{C}_F \\ \boldsymbol{K}^{PD,g}\boldsymbol{C}_g & \boldsymbol{K}^{PD} \end{bmatrix}, \boldsymbol{U}^c = \begin{bmatrix} \boldsymbol{u} \\ \boldsymbol{d} \end{bmatrix} \text{ and } \boldsymbol{F}^c = \begin{bmatrix} \boldsymbol{F}^{FE} \\ \boldsymbol{F}^{PD} \end{bmatrix}. \tag{5.47}$$

For simplicity, and without loss of generality, in the examples presented in the following sections it is assumed that no external forces are applied on the PD particles leading to $\boldsymbol{F}^{PD} = \boldsymbol{0}$. Furthermore, it can be seen that $\boldsymbol{K}^c$ is not symmetric. This was also evident in the stiffness matrix presented in Eq. (5.9). Similar coupling approaches, like the one presented in [117,118], lead to analogous results. It is noted that the symmetry of $\boldsymbol{K}^c$ is not lost when energy coupling methods are implemented, like the Arlequin method presented in [120].

5.5.2 *Verification of the 2D Model*

To validate the coupling in 2D, a pulse propagating in a solid under plane stress conditions is considered. The boundary conditions and geometry are illustrated in Figure 5.22 (left). The length and the height of the plate are $L_x = 0.5\text{m}$ and $L_y = 0.25\text{m}$ respectively, with a thickness of $t = 0.001\text{m}$. The inner dimensions define the FE domain Ω^{FE} are given as $L_{x1} = 0.2\ \text{m}$ and $L_{y1} = 0.1\ \text{m}$. Thus, the plate is modelled with FE apart from an area in the center, defining Ω^{PD}, that is modeled using PD. The time profile of the input pulse is Gaussian with $u(x = L_x, t) = ae^{-\frac{(t-\beta)^2}{2c^2}}$, $\alpha = 10^{-4}\ \text{m}$, $\beta = 10^{-5}\ \text{s}$ and $c = 2\ 10^{-6}\ \text{s}$. The y displacements are constrained at the top and bottom edges while the x displacements are constrained at the left edge of the plate. The material is assumed elastic and isotropic with $E = 200\ \text{GPa}$, $v = 1/3$ and $\rho = 7850\ \text{kg/m}^3$.

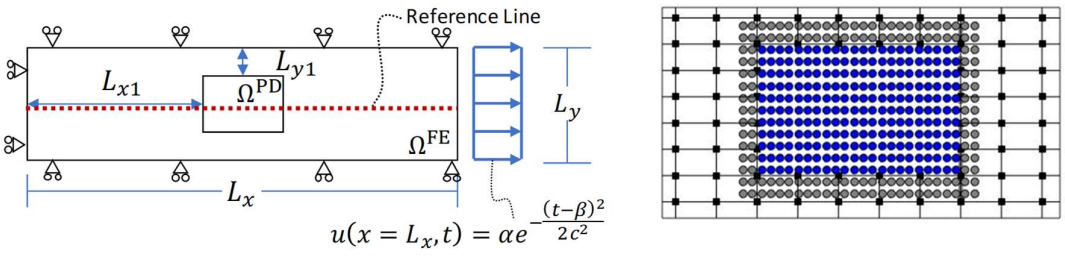

Figure 5.22: (Left) Problem geometry and boundary conditions. (Right) Example of a coupled FE-PD model in 2D, black squares indicate FE nodes, blue circles PD particles and grey circles PD ghost particles.

The coupled problem was discretized with $\Delta x^{FE} = \Delta y^{FE} = 2 \cdot 10^{-3}\text{m}$, and $\Delta x^{PD} = \Delta y^{PD} = 2.07 \cdot 10^{-4}\text{m}$. The length of the PD horizon is set to $\delta = 5\Delta x^{PD}$. In total $123{,}492$ particles were used in the PD domain out of which $7{,}330$ where ghost particles. The FE element domain was discretized using $30{,}000$ elements corresponding to $30{,}450$ nodes. The total simulation time is $t_{to} = 1 \cdot 10^{-4}s$ with steps $\Delta t = 5 \cdot 10^{-8}\text{s}$. The standard FE solution was obtained using a uniform grid with $\Delta x^{FE} = \Delta y^{FE} = 2 \cdot 10^{-3}\text{m}$. In Figure 5.22 (right) an example of the discretization of Ω^{FE} and Ω^{PD} is illustrated. The location of the PD particles is independent of the FE nodal locations, thus simplifying the process. If the first coupling case was to be implemented, refinement of the FE mesh would be required near the interface for the FE nodes to coincide with the PD particles.

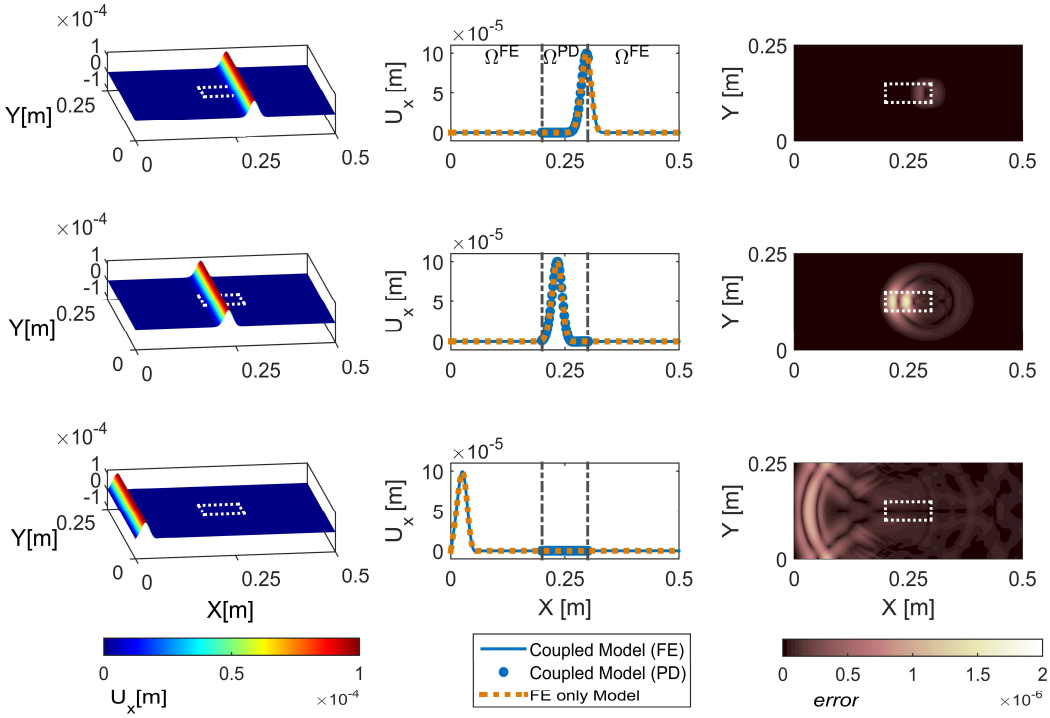

Figure 5.23: Comparison of the coupled model with FE solution at three different time steps. Left column: U_x displacements in the plate. White lines indicate the PD-FE interface. Middle column: Comparison of the U_x displacements along the reference line illustrated in Figure 5.22 with the FE solution. Right column: Plot of the error magnitude during each time step.

In the left column of Figure 5.23 the propagation of the Gaussian pulse is illustrated at time instants $t = 4.4 \cdot 10^{-5}\text{s}$, $t = 5.7 \cdot 10^{-5}s$ and $t = 9.9 \cdot 10^{-5}\text{s}$. Similar to the 1D case, each time the pulse crosses a PD-FE interface, a reflection is generated. Since a much finer discretization was implemented in the PD domain compared to the FE domain, the cut-off frequency of the PD domain was higher than that of the FE domain allowing the pulse to be

transferred. This can also be seen in the middle column of Figure 5.23 where the displacements along the reference line, illustrated in Figure 5.22, are compared for the coupled and the FE-only solutions. Compared to the amplitude of the pulse, the amplitude of spurious reflections is negligible, and the two solutions agree well. To further compare the two solutions, the L_2 norm of error is employed. Since the nodal points of the two solutions do not coincide in the Ω^{PD} region, the solution in the PD region is interpolated onto the FE nodal points through linear interpolation. The magnitude of error is defined as:

$$error = \|\boldsymbol{u}^{FE\ only} - \widehat{\boldsymbol{u}}^{coupled}\|_2, \tag{5.48}$$

where $\widehat{\boldsymbol{u}}^{coupled}$ contains the interpolated values of the coupled model $\boldsymbol{u}^{coupled}$ onto the FE nodes. The magnitude of the L_2 norm is plotted in the right column of Figure 5.23. As expected, discrepancies first appear when the pulse crosses for the first time the FE-PD interface and reach the maximum value of $2.02 \cdot 10^{-6}$ when the pulse exits the PD domain. It is noted that the error here is not only due to the generated reflections but also due to differences in the numerical dispersion characteristics of the two solution methods. Still, the two solutions are in very good agreement in the whole computational domain.

5.5.3 *Partial Trapping of Pulses in FE-PD models*

According to the findings of the 1D study, if the cut-off frequency of the PD domain in the previous example was not high enough to allow the pulse to be transmitted accurately, the spurious reflections generated would be more severe and affect the accuracy of the simulation. It is desirable that the PD domain will be localized only in a small area of the computational domain, where fracture is expected. To accurately capture these phenomena, a very fine discretization is usually required. It is thus expected that in practical applications, the PD grid will be much finer than the FE mesh. Since the frequency content of the pulse was low enough to be transmitted within the coarse FE description, it was also able to propagate within the PD domain. In this case, consideration of the dispersion curves for each model is needed to make sure that the cut-off frequency of the FE domain is high enough to allow the pulse to be transmitted. At the same time, the cut-off frequency of the PD domain needs to be higher to reduce the spurious reflections due to the coupling. Consideration of the FE cut-off frequency is of equal importance to the PD one to achieve accurate coupling. This is evident in cases where the source of the pulse is located within the PD domain. One such case is considered in the next example.

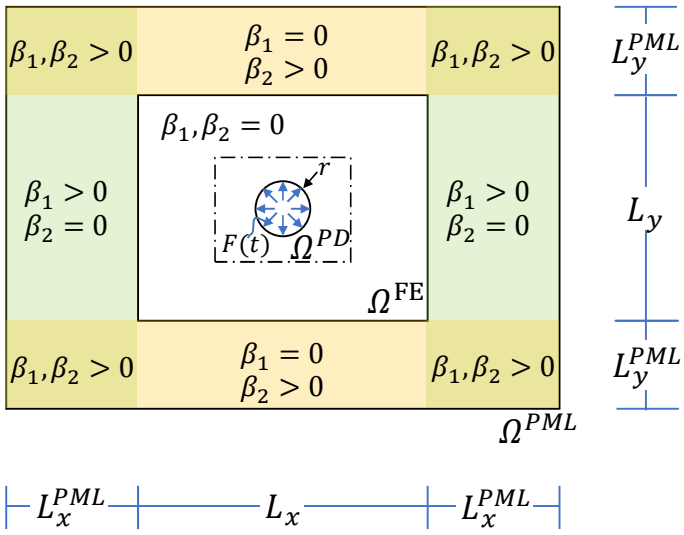

Figure 5.24: A PML layer is added around Ω^{FE}. Within the PML region the material becomes anisotropic and attenuates the outward going pulses.

Table 5.2: Summary of model parameters.

Parameter	Value	Parameter	Value
$L_x = L_y$	0.5m	t_{tot}	$2 \cdot 10^{-4}$s
$L_{x1} = L_{y1}$	0.2m	Δt	$2 \cdot 10^{-7}$s
$L_x^{PML} = L_y^{PML}$	0.3m	$\Delta x^{PD} = \Delta y^{PD}$	$3.11 \cdot 10^{-4}$m
t	1mm	$\Delta x^{PML} = \Delta y^{PML}$	$9.37 \cdot 10^{-4}$m
r	3mm	$\Delta x^{FE} = \Delta y^{FE}$ (fine)	$13 \cdot 10^{-4}$m
E	200GPa	$\Delta x^{FE} = \Delta y^{FE}$ (coarse)	$33 \cdot 10^{-4}$m
v	1/3	F_{max}	$1.06 \cdot 10^{4}$MPa
δ	$3\Delta x^{PD}$	ρ	7850 Kg/m^3

Assuming an infinite plate with a hole at its centre, the area around the hole is modelled with PD while the rest of the plate with FE. To avoid interference due to the boundary conditions of the numerical model, the computational domain is truncated by adding a Perfectly Matched Layer (PML) to attenuate outward traveling waves. In a recent study, unbounded problems were addressed using the PD differential operator and Sommerfeld boundary conditions [216].

The PML was originally proposed by Berenger for applications in electromagnetic waves [217] and was later extended to applications involving elastic waves [218]. Here, the convolution PML (C-PML) proposed in [219] for time-domain analyses, is employed. In the PML region, the coordinate variables $x_i, i = 1,2$ of the problem are transformed into the stretched coordinate variables $\tilde{x}_i$, in each direction, given as [220] [218]:

$$\tilde{x}_i = \int_0^{x_i} s_i(x_i, \omega) dx_i \,, i = 1,2, \tag{5.49}$$

where, ω is the angular frequency and s_i are the stretched coordinate functions, proposed by Kuzuoglu and Mittra [221]:

$$s_i(x_i\omega) = \kappa_\iota(x_i,\omega) + \frac{\beta_i(x_i)}{\alpha_i(x_i) + i\omega} \tag{5.50}$$

Three coordinate-wise functions are introduced in Eq. (5.50), $\beta_i(x_i) \geq 0, \kappa_\iota(x_i,\omega) \geq 1$ and $\alpha_i(x_i) \geq 0$. $\beta_i(x_i)$ controls the attenuation in the PML region while $\kappa_\iota(x_i,\omega)$ and $\alpha_i(x_i)$ enhance the attenuation of evanescent waves. In [219], it was shown that when near-grazing waves do not manifest, the selection $\kappa_\iota(x_i,\omega) = 1$ and $\alpha_i(x_i) = 0$ simplifies the PML computations as one of the convolution terms disappears without affecting significantly the accuracy. Since this is applicable to the case considered here, these values are adopted. The function $\beta_i(x_i)$ is defined in [219,220] and the references therein as:

$$\beta_i(x_i) = \beta_i^{\max}\left(\frac{x_i - x_i^0}{2d_i}\right)^3, \tag{5.51}$$

where $\beta_i^{\max} = -(4c_p \log_{10} R_0)/(2d_i)$, $R_0 = 10^{-8}$ is the theoretical reflection coefficient at normal incidence, x_i^0 is the location of the PML interface and d_i is the PML thickness in each direction.

The coordinate stretching performed in the PML region leads to a non-homogeneous differential operator. To extract the original one, artificial anisotropy is introduced to the material. The FE equation of motion now is:

$$\boldsymbol{M\ddot{U}} + \boldsymbol{Z\dot{U}} + \boldsymbol{KU} + \boldsymbol{g} = \boldsymbol{F}^{ext} \tag{5.52}$$

where, $\boldsymbol{M, Z, K}$ are the mass, damping and stiffness matrices and $\boldsymbol{g}$ is a convolution term defined in [53]. More details in on the finite element implementation of the PML can be found in [53] while a PML formulation for State-Based PD can be found in [222]. The geometry of the problem is illustrated in Figure 5.24 along with the definition of the coordinate-wise function β_i in different areas of the plate. A radial pressure is applied at the walls of the hole with $F(t) = F_{max} e^{-\frac{1}{2}\left(\frac{t-a_2}{a_3}\right)^2}$. The problem solution is repeated two times, the first time the FE discretization was refined to minimize the spurious reflections generated while the second time, a coarser FE mesh was used. In both solutions the PD and the FE discretization in the PML was not changed. The model parameters are summarized in Table 5.2. The displacements are constrained on the outer perimeter of the PML as according to [219], this improves the stability during time marching.

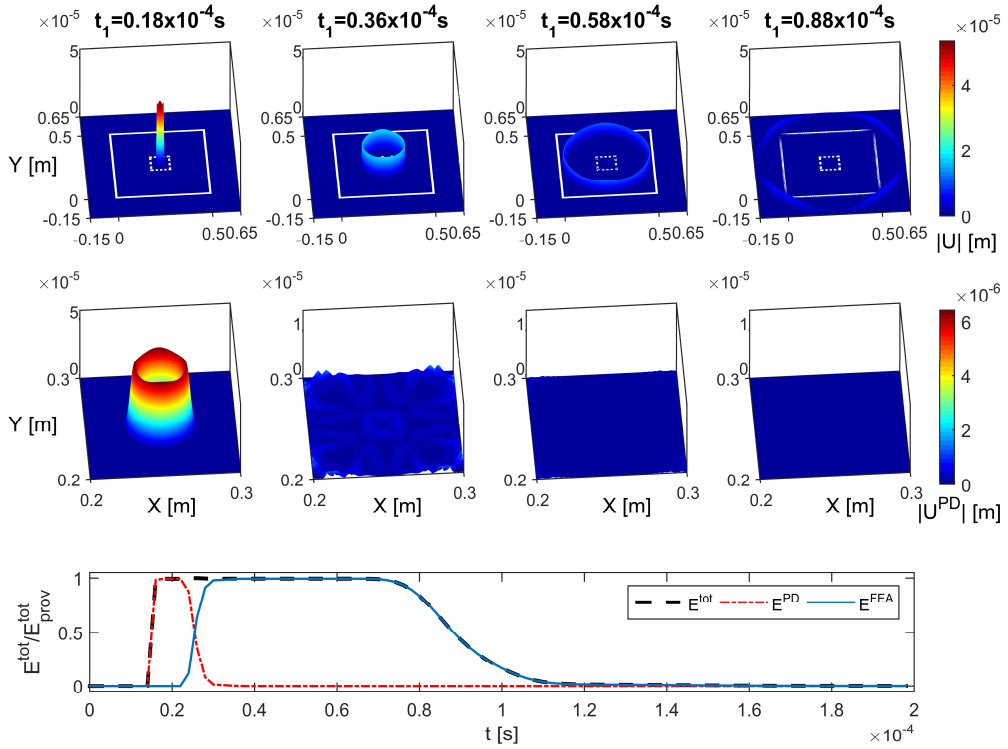

Figure 5.25: Pulse propagation with close-up in Ω^{PD} and energy transferring using the fine FE mesh.

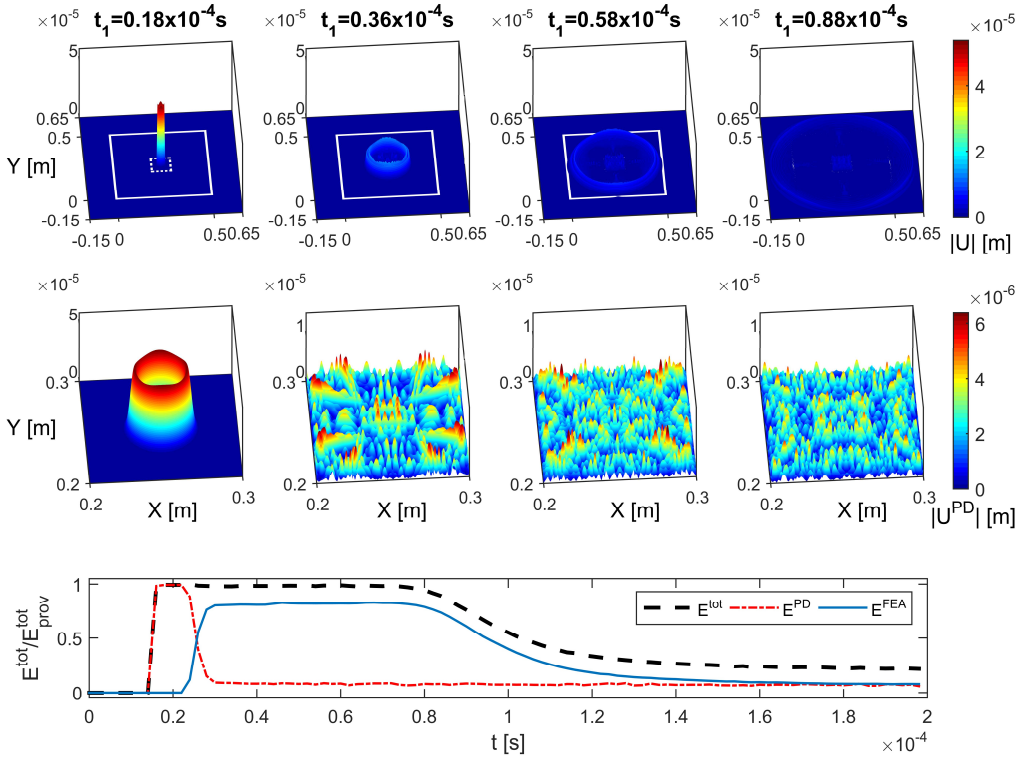

Figure 5.26: Pulse propagation with close up in Ω^{PD} and energy transferring using the coarse FE mesh. Approximately 16% of the total energy is trapped within the PD domain.

The results using the finer and coarser discretization are illustrated in Figure 5.25 and Figure 5.26. The displacement magnitude $|\boldsymbol{U}| = \sqrt{U_x^2 + U_y^2}$ is plotted at different time instants as the pulse propagates along the PD-FE and FE-PML interfaces till it is finally attenuated. In the same figures, the total energy in the PD and the FE model is also included. When the fine FE discretization is used, the pulse propagates without significant reflections across the PD-FE interface. The total energy provided into the PD model is transferred to the FE model and subsequently exits the domain (vanishes due to the introduction of the PML). On the other hand, when the coarse mesh is used, only part of the energy is transmitted to the FE domain while approximately 16% of the energy is trapped within the PD domain.

By making the FE mesh coarser, the cut-off frequency is reduced, and significant spurious reflections are generated at the interface. These reflections are trapped in the PD domain and are unable to reach the PML region. In practice, if the frequency content of the propagating pulse is known beforehand, the discretization parameters of the numerical descriptions will be selected accordingly. However, application of impact-like loads in the PD domain will excite the whole frequency spectrum of the finer model. It is thus desired that the two models have similar cut-off frequencies to minimize the reflected energy. In problems involving dynamic crack propagation, mismatch between the two descriptions will lead to accumulation of the trapped energy within the PD domain that will lead to erroneous and unrealistic results.

6 The PD Snail – An Adaptive Algorithm for the Simulation of Crack Propagation using a Coupled XFEM – PD Model

In Chapter 5 an efficient and accurate way to couple FE meshes with PD grids was presented. This allowed the simulation of wave propagation problems where the application of Ω^{PD} was focused at a specific part of the structure. In order to achieve the objectives set-out for this project, we need to develop two additional characteristics into the final algorithm to improve its efficiency during fracture simulations: **i)** the ability to localize Ω^{PD} near the crack tip area only and **ii)** an adaptive relocation strategy for Ω^{PD} and Ω^{FE} to follow the evolution of damage.

The localization of Ω^{PD} near the vicinity of the tip introduces a complication; a part of the crack remains within Ω^{FE}. Treatment of the discontinuous displacement field that now appears in the domain of classical elasticity is required. One possible way to address this is by considering the crack faces as geometrical boundaries and create specific meshes that conform to the crack geometry. In a recent publication [223], Ni et. al. used the FE-PD coupling proposed in [118] and [117] and localized Ω^{PD} near the crack tip. Although such implementation is straightforward, if Ω^{PD} is relocated, remeshing is required to include the updated crack length. Here it is preferred to enrich the elements that are cut by the crack body with the shifted Heaviside enrichment from the XFEM formulation. This is illustrated schematically in Figure 6.1.

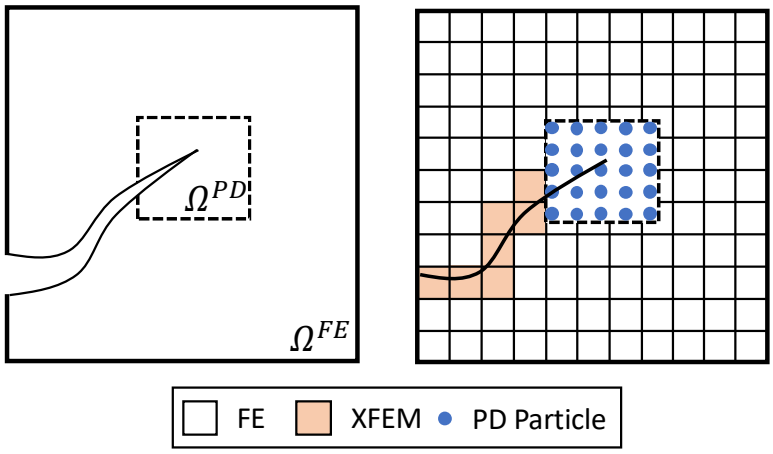

Figure 6.1: Localization of Ω^{PD} only near the crack tip. The crack body remains in Ω^{FE} and the elements cut are enriched according to XFEM.

The introduction of the XFEM enrichment not only reduces the required computational effort since Ω^{PD} is further limited but also, the discretization mesh used for Ω^{FE} is independent with

respect to the crack location. It is noted here that a different way of combining PD with XFEM was presented in [224]. The PD operator derived in [225] is used to augment the XFEM approximation and both models act on the whole computational domain. The PD operator is used to guide the crack during its propagation, alleviating the challenging implementation of external criteria (i.e. level set functions, maximum stress criteria, crack growth criteria). Our proposed methodology differs in that PD and XFEM are used for different parts of the domain and the stress state near the crack tip is exclusively approximated using the PD theory.

In the contributions of Zaccariotto et. al. [117] and Han et. al. [108], an adaptive procedure is presented to increase the area of Ω^{PD}, following the propagation of the crack. In both contributions specific triggers are used to control the switch from FE nodes to PD particles. This has been proven to be an efficient way to simulate fracture as Ω^{PD} is initially small and expands only when needed. In the case of problems with multiple cracks however, constantly expanding the PD domain will eventually lead to restrictions with regards to the computational requirements of the model. The relocation strategy that is presented in this chapter has also the ability to transition from PD particles to FE nodes and thus keep the computational cost small throughout the whole simulation. The introduction of the XFEM enrichment has the added benefit of avoiding remeshing in Ω^{FE} during the relocation.

6.1 XFEM-PD Coupling and Modification of the Force Equilibrium

6.1.1 *XFEM-PD Coupling and Localization of the PD Model*

As stated earlier, localization of the PD model near the vicinity of the crack tip leads to the appearance of discontinuous displacement fields in Ω^{FE} as at least part of the crack body will not be captured by the PD model. Although in the PD theory the appearance of a strong discontinuity is handled naturally, special treatment needs to be employed in the case of classical elasticity. Therefore, the Extended Finite Element Method, presented in section 3.4.3 is introduced into the model. The elements that are cut by the crack are locally enriched with Heaviside functions to capture the displacement jump at the crack body. This new addition needs to be incorporated into the coupling methodology to enforce the coupling between the XFEM and the PD. Contrary to section 5.5.1 where the coupling was formulated and applied using the linearized formulation of the PD theory, here the formulation is presented for the more general case where the original formulation is used, as the assumption for small displacements no longer holds for fracture problems. Finally, a modification is introduced in the coupling that changes the way forces are applied from the PD model to the XFEM model.

Still, the discretization of the two models remain independent and there is no requirement of coincident FE nodes and PD particles.

Let n^{PD} be the set of all PD particles in a problem domain Ω. We denote with $n_g = \{\boldsymbol{x}^{PD}: \boldsymbol{x}^{PD} \in \Omega^{FE}\}$ the set of ghost particles and with $n_n = \{\boldsymbol{x}^{PD}: \boldsymbol{x}^{PD} \in \Omega^{PD}\}$ the set of normal particles. Then $n^{PD} = n_n \cup n_g$ while $n_n \cap n_g = \emptyset$ since a particle is either normal or ghost. The total number of ghost and normal particles in Ω is defined by the cardinality of the sets $|n_g|$ and $|n_n|$, respectively. Similarly, n^{FE} is the set of all FE nodes and n_{std} and n_{enr} contain the standard and enriched FE nodes. The displacement vectors of the FE nodes and PD particles are given as $\overline{\boldsymbol{u}} = \{\boldsymbol{u}^T, \boldsymbol{a}^T\}^T$ and $\boldsymbol{d} = \{(\boldsymbol{d}^n)^T, (\boldsymbol{d}^g)^T\}^T$ where $\boldsymbol{d}^n$ and $\boldsymbol{d}^g$ refer to the normal and ghost particle dofs, respectively.

The introduction of XFEM requires a modification on the expression that enforces continuity between Ω^{FE} and Ω^{PD}. Evidently, some of the ghost particles will be located in elements that are cut by the crack and have been enriched. Since the enrichment vanishes outside these elements [1], then $\boldsymbol{d}^g$ can be computed using:

$$\boldsymbol{d}_k^g = \sum_{\mathrm{i}=1}^{K} N_i(\boldsymbol{x}_k^{PD})\boldsymbol{u}_i + \sum_{j=1}^{M} N_j(\boldsymbol{x}_k^{PD})\left(H(\boldsymbol{x}_k^{PD}) - H\left(\boldsymbol{x}_j^{FE}\right)\right)\boldsymbol{a}_j\,, k = 1, 2, \dots, |n_g|, \qquad (6.1)$$

where, the FE approximation from Eq. (3.71) is used and K and M are the standard nodes and enriched nodes, respectively. Clearly, the second term of Eq. (6.1) vanishes if a particle is located in an element away from the crack body and the interpolation reduces to $\boldsymbol{d}_k^g = \sum_{\mathrm{i}=1}^{K} N_i(\boldsymbol{x}_k^{PD})\boldsymbol{u}_i$ which is the same expression as in Eq. (5.41). The interpolation from Eq. (6.1) can be re-written using matrix notation as:

$$\boldsymbol{d}^g = \boldsymbol{C}_{g,1}\boldsymbol{u} + \boldsymbol{C}_{g,2}\boldsymbol{a} = \boldsymbol{C}_g\overline{\boldsymbol{u}}. \qquad (6.2)$$

where, $\boldsymbol{C}_{g,1}$ and $\boldsymbol{C}_{g,2}$ are the matrices of coefficients that couples the displacements of the ghost particles $\boldsymbol{d}^g$ with the displacements of the standard $\boldsymbol{u}$ and enriched $\boldsymbol{a}$ nodal values, respectively. From the definitions given earlier, the dimensions of matrix $\boldsymbol{C}_g$ are $2n_g \times 2n^{FE}$. Similar expressions are derived for the velocity $\dot{\boldsymbol{d}}^g$ and the acceleration $\ddot{\boldsymbol{d}}^g$ of the ghost particles.

The goal is to develop a coupled XFEM-PD model with the ability to adaptively redefine Ω^{FE} and Ω^{PD}, following the propagation of the crack. Each time Ω^{FE} and Ω^{PD} are relocated, the location of the coupling interface (e.g. $\partial\Omega_2$ in Figure 5.1) is also updated. In the coupling

presented in section 5.5.1, force equilibrium is taken on $\partial\Omega_2$. To this end, the computation of the intersection between the coupling interface and each bond is required. In cases where Ω^{PD} and Ω^{FE} are constructed at the beginning of the analysis and remain unchanged throughout, this requirement is not significant. However, when the location and the shape of $\partial\Omega_2$ is not static during the simulation, re-computation of the bond – interface intersection can be challenging and computationally demanding. Instead, we can assume that a bond force is applied in the interior of the FE, and specifically, at the location of the ghost particle. A comparison of the two idealizations is illustrated schematically in Figure 6.2 where a FE on $\partial\Omega_2$ and a bond pair that crosses $\partial\Omega_2$ have been isolated. These two approaches are very similar to the *CT* and *VL* coupling schemes presented by Liu and Hong in [121].

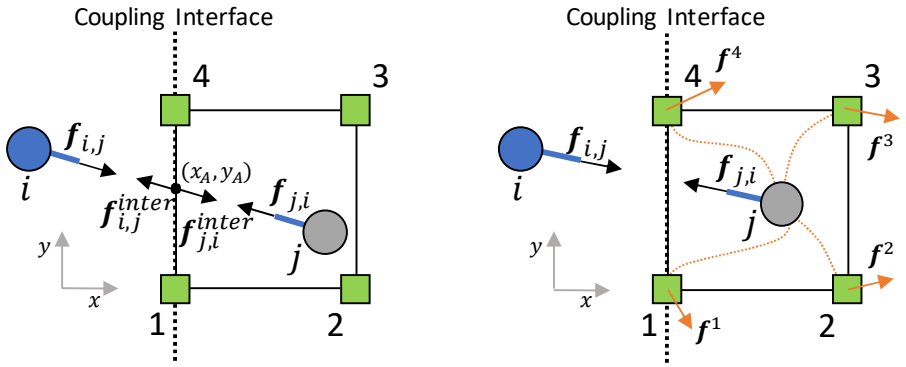

Figure 6.2: Comparison of the two approaches regarding the application of the bond forces. On the left, the bond force is applied on the intersection of the bond with the coupling interface [226] and it is effectively distributed on the two nodes that lie on $\partial\Omega_2$. On the right the bond force is applied in the interior or the element and the force is distributed to all 4 nodes of the element.

The bond force $\boldsymbol{f}_{i,j}$ between particles i and j is computed using Eq. (3.13) after discretization. From linear and angular momentum conservation we also get that $\boldsymbol{f}_{i,j} = -\boldsymbol{f}_{j,i}$. We consider $\boldsymbol{f}_{i,j}$ to be an external concentrated force acting inside the element at the location $\boldsymbol{x}_j^{PD}$. The point of application of the concentrated force can be defined using a 2D Dirac function $\delta\left(x - x_j^{PD}, y - y_j^{PD}\right)$. Let n be the total number of bonds that connect ghost particle j with a normal particle. The total force $\boldsymbol{f}_j^g$, applied at $\boldsymbol{x}_j^{PD}$ is:

$$\boldsymbol{f}_j^g = \sum_{i=1}^{n} -\boldsymbol{f}_{i,j}\, V_i, j = 1, 2, \dots, |n_g|. \tag{6.3}$$

The force vector $\boldsymbol{f}^I$, where $I = 1, 2, 3, 4$ is the element nodal numbers (see e.g. Figure 6.2) is computed by integrating $\boldsymbol{f}_j^g$ over the volume of the element as:

$$\boldsymbol{f}^I = \sum_{j=1}^{j_{total}} \int \boldsymbol{N}^T \boldsymbol{f}_j^g \delta\left(x - x_j^{PD}, y - y_j^{PD}\right) d\Omega = \sum_{j=1}^{j_{total}} \boldsymbol{N}^T_{x=x_j^{PD}, y=y_j^{PD}} \boldsymbol{f}_j^g, \tag{6.4}$$

where, j_{total} is the total number of ghost particles in the element. In essence, $\boldsymbol{f}_j^g$ is distributed to the nodes of the element through the FE shape functions evaluated at the location of the ghost particle. Comparing Eqs. (5.44) and (6.4) the difference between them is the different location where the FE shape functions are evaluated. The bond forces $\boldsymbol{f}_{i,j}$ in Eq. (6.3) are computed using the original formulation of the PD theory, however, the linearized definition from Eq. (3.40) can also be used. Iterating this procedure over all the FE elements, the vector of forces $\boldsymbol{f}^C$, that the PD ghost particles apply on the FE elements can be expressed in the global system as:

$$\boldsymbol{f}^C = \boldsymbol{C}_F \boldsymbol{f}^g, \tag{6.5}$$

where, $\boldsymbol{C}_F$ is a $2n^{FE} \times 2n_g$ matrix with the coefficients that distribute the forces that are applied on the PD ghost particles to the FE dofs, and $\boldsymbol{f}^g$ is a vector that contains the forces applied on the ghost particles. In both cases, the interpolation described in Eqs. (6.1) and (6.4) is performed by evaluating the FE shape functions at the location of the ghost particles. This simplifies the computation of the coupling matrices $\boldsymbol{C}_F$ and $\boldsymbol{C}_g$. In fact, $\boldsymbol{C}_F = \left(\boldsymbol{C}_g\right)^T$.

Then, the equation of motion in Ω^{FE} becomes:

$$\boldsymbol{M}^{FE} \ddot{\overline{\boldsymbol{u}}} + \boldsymbol{K}^{FE} \overline{\boldsymbol{u}} = \boldsymbol{F}^{FE} + \boldsymbol{f}^C. \tag{6.6}$$

Finally, combining Eqs. (3.23), (6.4) and (6.6) the final system of equations is formed. For dynamic problems, time integration is performed using the central difference scheme. For static problems on the other hand, the final system of equations is solved using the Newton-Raphson solver. Let $\boldsymbol{U} = \{(\overline{\boldsymbol{u}})^T, (\boldsymbol{d}^n)^T, (\boldsymbol{d}^g)^T\}^T$, be the vector of displacements for all dofs in the coupled system. Following section 3.2.1, when the inertia forces are neglected the final system of equations can be written as:

$$\boldsymbol{g}(\boldsymbol{U}) = \begin{bmatrix} \boldsymbol{g}^{FE} \\ \boldsymbol{g}_i^{PD,n} \\ \boldsymbol{g}^{PD,g} \end{bmatrix}, \tag{6.7}$$

where,

$$\boldsymbol{g}^{FE} = \boldsymbol{K}^{FE} \overline{\boldsymbol{u}} - \boldsymbol{F}^{FE} - \boldsymbol{f}^C \tag{6.8a}$$

$$\boldsymbol{g}_i^{PD,n} = \sum_{j=1}^{M} \boldsymbol{f}_{i,j} V_j + \boldsymbol{b}_i, i = 1,2,\dots,|n_n| \tag{6.8b}$$

$$\boldsymbol{g}^{PD,g} = \boldsymbol{C}_g \bar{\boldsymbol{u}} - \boldsymbol{d}^g. \tag{6.8c}$$

The Jacobian of the coupled system $\mathcal{J}_{\boldsymbol{G}}$ is required for the implementation of the implicit solution. Thus, we need to define the components of:

$$\mathcal{J}_{\boldsymbol{g}} = \frac{\partial \boldsymbol{g}}{\partial \boldsymbol{U}} = \begin{bmatrix} \frac{\partial \boldsymbol{g}^{FE}}{\partial \boldsymbol{U}} \\ \frac{\partial \boldsymbol{g}_i^{PD,n}}{\partial \boldsymbol{U}} \\ \frac{\partial \boldsymbol{g}^{PD,g}}{\partial \boldsymbol{U}} \end{bmatrix} = \begin{bmatrix} \frac{\partial \boldsymbol{g}^{FE}}{\partial \bar{\boldsymbol{u}}} & \frac{\partial \boldsymbol{g}^{FE}}{\partial \boldsymbol{d}^n} & \frac{\partial \boldsymbol{g}^{FE}}{\partial \boldsymbol{d}^g} \\ \boldsymbol{0} & \frac{\partial \boldsymbol{g}^{PD,n}}{\partial \boldsymbol{d}^n} & \frac{\partial \boldsymbol{g}^{PD,n}}{\partial \boldsymbol{d}^g} \\ \frac{\partial \boldsymbol{g}^{PD,g}}{\partial \bar{\boldsymbol{u}}} & \boldsymbol{0} & \frac{\partial \boldsymbol{g}^{PD,g}}{\partial \boldsymbol{d}^g} \end{bmatrix}. \tag{6.9}$$

The following components can be derived in straightforward manner:

$$\frac{\partial \boldsymbol{g}^{FE}}{\partial \bar{\boldsymbol{u}}} = \boldsymbol{K}^{FE}, \frac{\partial \boldsymbol{g}^{PD,g}}{\partial \bar{\boldsymbol{u}}} = \boldsymbol{C}_g, \frac{\partial \boldsymbol{g}^{PD,g}}{\partial \boldsymbol{d}^g} = -\boldsymbol{I} \tag{6.10}$$

where, $\boldsymbol{I}$ is the identity matrix with dimensions $2n^g \times 2n^g$. Then, using Eqs. (6.3), (6.5) and (6.7), the remaining entries in Eq. (6.9) are defined as:

$$\frac{\partial \boldsymbol{g}^{FE}}{\partial \boldsymbol{d}^n} = -\frac{\partial \boldsymbol{f}^C}{\partial \boldsymbol{d}^n} = -\boldsymbol{C}_F \frac{\partial \boldsymbol{f}_j^g}{\partial \boldsymbol{d}_i^n} = -\boldsymbol{C}_F \mathcal{J}_{g,n}^{PD}, j = 1,2,\dots,|n_g| \text{ and } i = 1,2,\dots,|n_n| \tag{6.11a}$$

$$\frac{\partial \boldsymbol{g}^{FE}}{\partial \boldsymbol{d}^g} = -\frac{\partial \boldsymbol{f}^C}{\partial \boldsymbol{d}^g} = -\boldsymbol{C}_F \frac{\partial \boldsymbol{f}_j^g}{\partial \boldsymbol{d}_i^g} = -\boldsymbol{C}_F \mathcal{J}_{g,g}^{PD}, j = 1,2,\dots,|n_g| \text{ and } i = 1,2,\dots,|n_g| \tag{6.11b}$$

$$\frac{\partial \boldsymbol{g}^{PD,n}}{\partial \boldsymbol{d}^n} = \frac{\partial}{\partial \boldsymbol{d}_j^n}\left(\sum_{k=1}^{M} \boldsymbol{f}_{i,k} V_k\right) = \mathcal{J}_{n,n}^{PD}, j = 1,2,\dots,|n_n| \text{ and } i = 1,2,\dots,|n_n| \tag{6.11c}$$

$$\frac{\partial \boldsymbol{g}^{PD,n}}{\partial \boldsymbol{d}^g} = \frac{\partial}{\partial \boldsymbol{d}_j^g}\left(\sum_{k=1}^{M} \boldsymbol{f}_{i,k} V_k\right) = \mathcal{J}_{n,g}^{PD}, j = 1,2,\dots,|n_g| \text{ and } i = 1,2,\dots,|n_g| \tag{6.11d}$$

The matrices $\mathcal{J}_{g,n}^{PD}$, $\mathcal{J}_{g,g}^{PD}$, $\mathcal{J}_{n,n}^{PD}$ and $\mathcal{J}_{n,g}^{PD}$can be computed using the expressions from Eqs. (3.37) and (3.38). The final Jacobian of the coupled system of equations can now be written as:

$$\mathcal{J}_{\boldsymbol{g}} = \begin{bmatrix} \boldsymbol{K}^{FE} & -\boldsymbol{C}_F \mathcal{J}_{g,n}^{PD} & -\boldsymbol{C}_F \mathcal{J}_{g,g}^{PD} \\ 0 & \mathcal{J}_{n,n}^{PD} & \mathcal{J}_{n,g}^{PD} \\ \boldsymbol{C}_g & 0 & -\boldsymbol{I} \end{bmatrix} \tag{6.12}$$

and the iterative solver as:

$$\boldsymbol{U}^{n+1} = \boldsymbol{U}^k - \left[\mathcal{J}_{g(\boldsymbol{U})}\right]^{-1} \boldsymbol{g}(\boldsymbol{U}). \tag{6.13}$$

6.1.2 *Static Example: Plate under multiaxial loading conditions*

First a static example is presented to evaluate the error between the solution approximated using the coupled model with the solution approximated using FEs only. Consider a plate under plane stress conditions. The plate is assumed to behave elastically, it is in its pristine condition and bond breaking is not allowed within Ω^{PD} (i.e. the plate will remain undamaged after the load application). The geometry of the plate, the boundary conditions and the applied load are illustrated in Figure 6.3. This example is used to demonstrate the accuracy of the combined FE-PD model to accurately capture the response of a problem under both normal and shear loads.

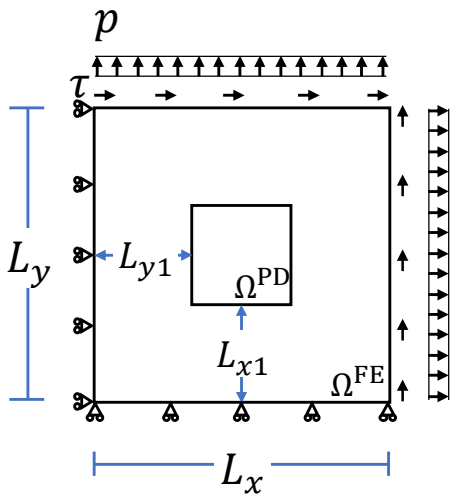

Figure 6.3: Illustration of the problem set-up for the first verification example.

Table 6.1: Summary of the problem parameters for the first verification problem.

Parameter	Value	Parameter	Value
L_x	5 mm	$\Delta x^{PD} = \Delta y^{PD}$	0.01 mm
L_{x1}	1.5 mm	$\Delta x^{FE} = \Delta y^{FE}$	0.05 mm
L_y	5 mm	δ	$4\,\Delta x^{PD}$
L_{y1}	1.5 mm	p	1 MPa
t	1 mm	τ	1 MPa
E	1 GPa	ν	1/3

Application of Ω^{PD} is restricted to a small area in the interior of the plate and it is completely enclosed by Ω^{FE}. Again, utilizing such an approach avoids difficulties in the PD theory with regards to the application of boundary conditions [6,107,117]. Thus, in this example, all loads and boundary conditions are applied on the boundary of Ω^{FE}. The problem is solved assuming

static conditions and the inertia terms are neglected in the PD and elastic equation of motion. The problem parameters are summarized in Table 6.1.

The same problem is also solved using a FE only model. In both cases, 4-node bilinear elements are used to approximate the solution of the partial differential equation of elasticity. To assess the accuracy of the FE-PD model, the relative error of the displacement magnitude between the FE-PD model and the FE only model is computed at the FE nodal locations. Since the nodal points do not necessarily coincide in Ω^{PD}, the solution in the PD region is interpolated at the FE nodal locations using linear interpolation. The relative error is computed as:

$$error = \frac{\|\boldsymbol{u}^{FE\ only} - \boldsymbol{u}^{FE-PD}\|}{\|\boldsymbol{u}^{FE\ only}\|} \tag{6.14}$$

where, $\boldsymbol{u}^{FE\ only}$ and $\boldsymbol{u}^{FE-PD}$ are the displacement fields approximated by the FE only and the FE-PD models, respectively. The magnitude of the displacement field $\|\boldsymbol{u}^{FE-PD}\|$ and the absolute value of the relative error are plotted in Figure 6.4. A good agreement can be seen between the results of the two models. The maximum absolute value of the relative error is approximately 0.75%. It can also be seen that the error between the two solutions is mainly concentrated near the interface where the FE and PD coupling is enforced. This observation is also reported in similar coupling approaches [130].

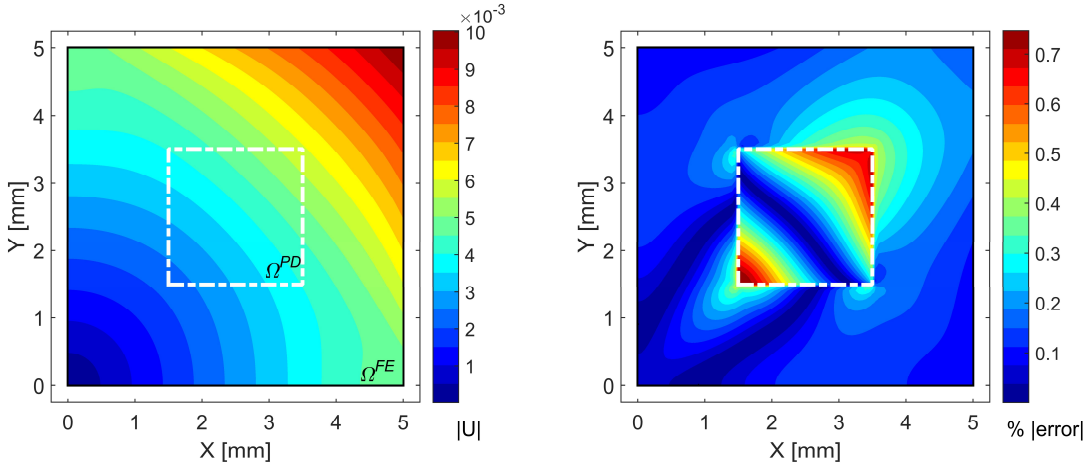

Figure 6.4: Left: Magnitude of the displacement field. Right: Relative % error between the FE and the FE-PD solutions.

6.1.3 *Dynamic Example: Pulse Propagation in a 2D plate*

The problem presented in section 5.5.2 is repeated here using the modified coupling approach. The material parameters and the discretization in each domain is kept the same.

The geometry of the problem and the location of Ω^{PD} and Ω^{FE} is the same as indicated in Figure 5.22. To avoid division with zero, the error is now defined using Eq. (5.48).

The propagation of the Gaussian pulse is plotted in Figure 6.5 at three time instants, $t_1 = 0.19 \cdot 10^{-4}$ s, $t_2 = 0.56\ 10^{-4}\ s$ and $t_3 = 0.79 \cdot 10^{-4}$ s. The evolution of the error between the coupled FE-PD model and the solution of classical elasticity approximated using FEs only can be seen at the bottom of Figure 6.5. For $t = t_1$the pulse has not reached yet the coupling interface and there is no error between the FE-PD and the FE only model. At time instant $t = t_2$ the pulse has crossed the coupling interface and now lies within Ω^{PD} in the middle part of the plate. A small reflection appears at the interface with a maximum amplitude of $0.7 \cdot 10^{-6}$m. This corresponds to 0.7% of the amplitude of the input pulse. The reflection is captured more accurately in the error plot. Finally, at $t = t_3$, the whole pulse has been transferred back to Ω^{FE}. As the pulse crosses once more the coupling interface, a reflection is generated. Avoiding completely the spurious reflections is not possible. Contrary to section 5.5.2, the original formulation of the PD theory is used here with the modification with regards to the way the bond forces are applied on the FEs. A comparison between the two solutions can be made using the error plots. Both approaches lead to comparable accuracy and the spurious reflections are kept small.

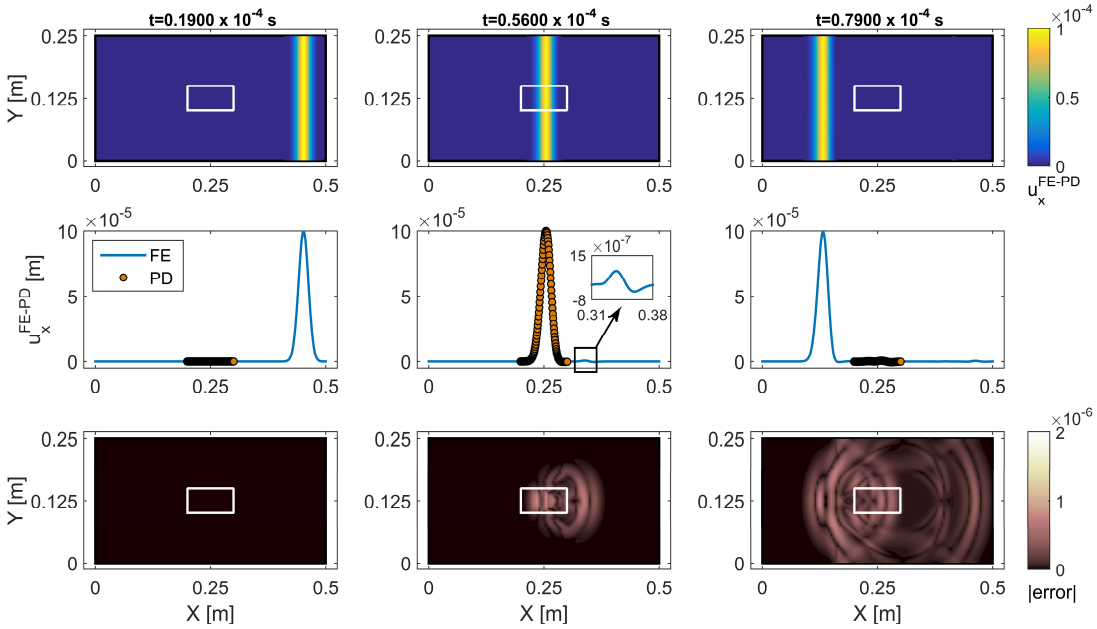

Figure 6.5: Pulse propagation in the coupled FE-PD model captured at three time instants. In the top row $\boldsymbol{u}_x$ is plotted for the whole plate, in the middle $\boldsymbol{u}_x$ is plotted along the reference line indicated in

Figure 5.22 and the bottom row indicates the evolution of the relative error between the FE-PD model and a FE only solution.

When the pulse crosses the coupling interface $\partial\Omega_2$, part of the total energy is transferred from Ω^{FE} to Ω^{PD}. The total energy, E_{tot}^{FE} and E_{tot}^{PD}, is computed within Ω^{FE} and Ω^{PD}, respectively, and plotted in Figure 6.6 versus time. In the same plot, the time instants illustrated in Figure 6.5 are also indicated. At $t_1 = 0.19 \cdot 10^{-4}$s the pulse has not crossed $\partial\Omega_2$ and $E_{tot}^{PD} = 0$ while at $t_2 = 0.56 \cdot 10^{-4}$s the pulse is within Ω^{PD} and E_{tot}^{PD} takes its maximum value with $E_{tot}^{PD}/E_{prov} = 0.20$. Finally, at $t_3 = 0.79 \cdot 10^{-4}\,s$ the whole pulse is again within Ω^{FE}. If no reflections appeared the energy in Ω^{PD} should go back to 0. Despite the appearance of spurious reflections, E_{tot}^{PD} at the end of the simulation is low with $E_{tot}^{PD}/E_{prov} = 1.26 \cdot 10^{-5}$. No dissipation mechanisms have been incorporated in this analysis and the total energy is conserved.

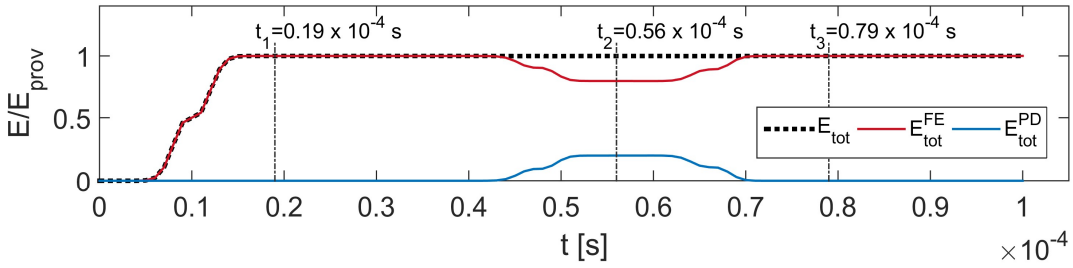

Figure 6.6: Energy distribution between Ω^{FE} and Ω^{PD}.

6.2 Convergence Study of the XFEM-PD Model

In this section an example featuring a strong discontinuity within the problem domain is considered. Contrary to similar publications in the literature (see e.g. [7,130]), Ω^{PD} is localized near the crack tip while the crack body remains within Ω^{FE}. The discontinuity within Ω^{FE} is treated with the incorporation of the XFEM enrichment.

To enable comparisons with results available in the literature, the example of a double edge-notched plate under plane stress conditions presented in [83] is adopted and recreated here. This example is used to present a more rigorous study for the performance of the XFEM-PD model. The dimensions of the plate are assumed $L = H = 10\text{cm}$, $h = 0.1\text{cm}$ and the length of the crack $a = 5\text{cm}$ on each side of the plate. The plate is assumed to behave elastically with Young's modulus $E = 72\text{GPa}$ and Poison's ratio $v = 1/3$. A uniform tensile pressure $p = 1\text{MPa}$ is applied in the vertical direction along the top and bottom edges of the specimen. Due

to symmetry, only the left half of the plate is modelled, with symmetric boundary conditions being applied on the right edge. Following [83], $c(\boldsymbol{\xi})$ is assumed to have a conical shape and its value is computed using Eq. (3.12). For comparison, three different configurations are used to approximate the resulting displacement field (see also Figure 6.7): **i**) Case 1 – FE only, **ii**) Case 2 – PD only, **iii**) Case 3 – coupled XFEM-PD. In Case 3 the shifted Heaviside enrichment, discussed in section 3.4.3, has been employed to treat the displacement jump from the crack body in Ω^{FE}. Furthermore, Ω^{PD} is constructed as a square patch with $L^{PD} = H^{PD} = 0.04\text{m}$, centered at the location of the crack tip.

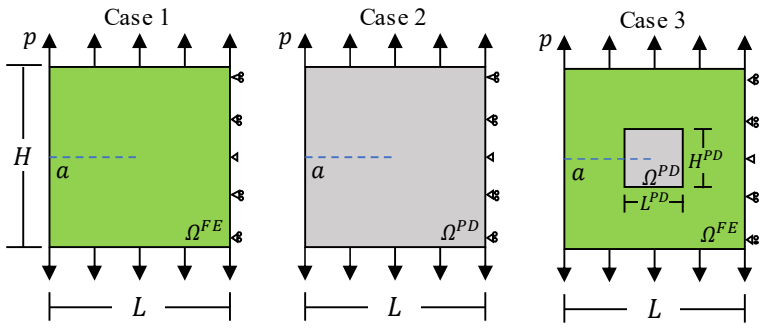

Figure 6.7: Schematic illustration of the three models used for the comparison.

The commercial software package Abaqus is employed to carry out the FE approximation in Case 1. The FE mesh is defined using $10{,}662$ quadratic elements with $32{,}451$ nodes. Near the crack tip region special crack-tip (collapsed) elements are used. The solution obtained from Case 1 is assumed to be a very close approximation to the exact solution and is used as a benchmark for comparison with the other cases. The numerical approximation of the solution for Cases 2 and 3 is carried out using a MATLAB algorithm.

The discretization in Ω^{PD} for Cases 2 and 3 is $\Delta x^{PD} = \Delta y^{PD} = 5 \cdot 10^{-4}\text{m}$ and the PD horizon is set to $\delta = 4\Delta x^{PD}$. In Case 3, Ω^{FE} is discretized using $\Delta x^{FE} = \Delta y^{FE} = 3 \cdot 10^{-3}\text{m}$. Furthermore, an additional fictitious material layer of PD particles, with thickness equal to δ, is added in Case 2 for the application of the boundary conditions, as suggested in [7]. In both Cases 2 and 3 the discretization is uniform for simplicity. In total, the discretization led to $81{,}600$ dofs for Case 2 ($40{,}800$ PD particles) while for Case 3 the total number of dofs is $17{,}844$ ($7{,}744$ PD particles and $1{,}156$ FE nodes of which 22 are enriched). It is evident that coupling FE with PD can significantly reduce the total number of dofs compared to using a PD only analysis, while achieving similar discretization near the crack tip. The benefits, in terms of computational efficiency, will be discussed more in the next paragraphs.

The simulated displacement fields for each of the cases considered are presented in Figure 6.8. In the same figure, a black dotted line is used to indicate the coupling interface $\partial\Omega_2$ in Case 3. For easier comparison the plots have been created using the same colour scales. A very close agreement can be seen between the results for all three cases. Additionally, in Figure 6.9, the plate is plotted in its deformed state as simulated using Case 3. The introduction of the shifted Heaviside enrichment at the elements cut by the crack, enables the FE method to facilitate discontinuous displacement fields and capture the displacement jump at the crack body. It is this property that allows the PD domain to be limited only in the area near the crack tip, without unmerging nodal displacements or specifically constructing the FE mesh to conform to the crack geometry. This will prove invaluable in the following paragraphs were crack propagation problems are considered. Notice also how using the definition from Eq. (6.1) the ghost particles that are positioned within an enriched element are able to follow the deformation.

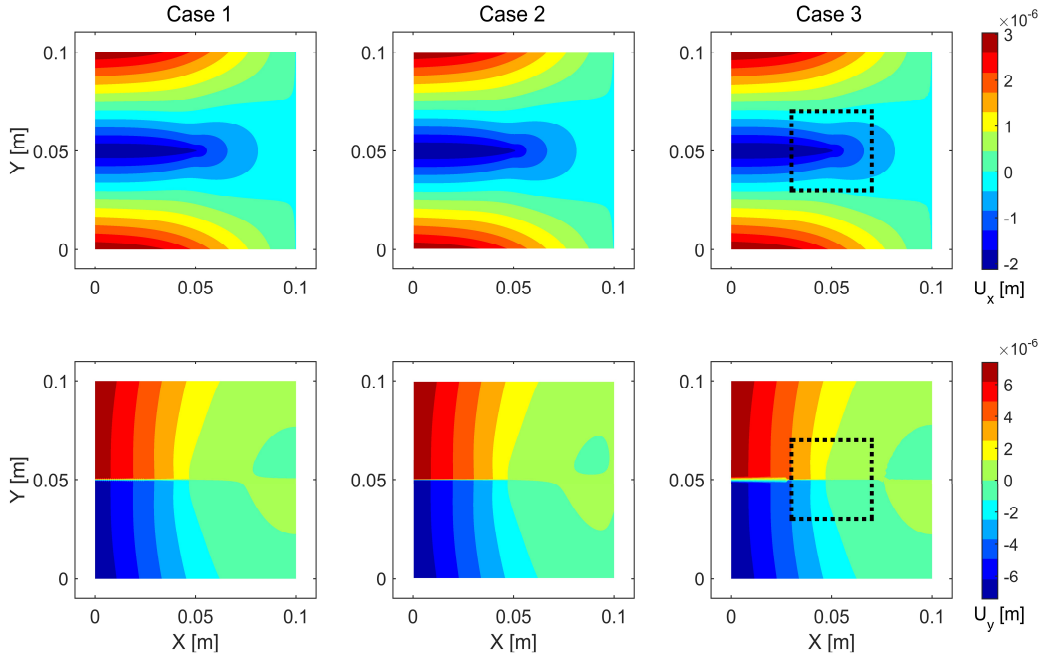

Figure 6.8: Comparison of the displacement fields approximated used each model. A black dotted line indicates the XFEM-PD boundary $\partial\Gamma_2$ in Case 3.

The aim is to examine the performance and the convergence of the XFEM-PD model more rigorously and systematically. To this end, the J contour integral is employed to allow for the comparison of the stress state near the crack tip. The J contour integral was introduced by Rice [14] has been used extensively both for linear and nonlinear fracture mechanics [2]. The formulation of the nonlocal J integral for the PD theory can be found in the works of Silling and

Lehoucq [227] and Hu et. al. [83]. It is defined on a closed contour ∂R that contains the crack tip and separates layers, R_1 and R_2, of thickness δ, as illustrated in Figure 6.10. Two convergence studies are typically employed in PD [5,83,86,143] namely **i**) m −convergence where the PD horizon δ is kept constant while the discretization length is reduced and the solution converges to the nonlocal solution and **ii)** δ − convergence where the ratio $\delta/\Delta x$ is kept constant and the solution converges to the classical solution as the PD theory converges to classical elasticity theory for $\delta \to 0$ [95]. A study on the convergence of the nonlocal J integral using both convergence types can be found in [83].

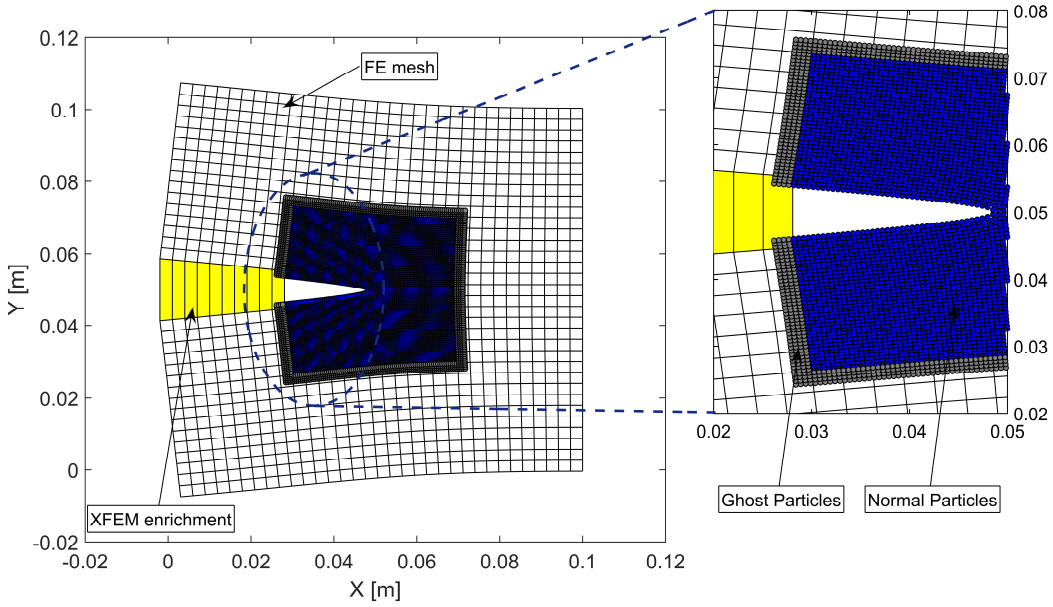

Figure 6.9: Deformation of the double cantilever beam using Case 3. White squares indicate standard FE, yellow squares the enriched elements, blue dots the normal PD particles and grey dots the ghost particles. Displacements have been magnified by a factor of 1000 for clarity.

Following [83] and [228], the nonlocal J integral can be approximated as:

$$J = \sum_{i=1}^{n_c} W_i n_{i,x} \Delta x^{PD} - \sum_{k=1}^{n_1} \sum_{m=1}^{n_2} \boldsymbol{f}(\boldsymbol{\eta}_{k,m}, \boldsymbol{\xi}_{k,m}) \cdot \left(\frac{\partial \boldsymbol{u}_m}{\partial \boldsymbol{x}} + \frac{\partial \boldsymbol{u}_k}{\partial \boldsymbol{x}} \right) h A_k A_m. \tag{6.15}$$

where W_i is the strain energy density of particle i, n_c, n_1 and n_2 are the number of particles on ∂R, R_1 and R_2 respectively, A_k is the area associated with particle k and $n_{i,x}$ is the horizontal component of the outward unit normal vector on the contour. To avoid inaccuracies in the approximation of the nonlocal J integral, care must be given to select contours for which

the definition of areas R_1 and R_2 is possible. The spatial displacement derivatives that appear in Eq. (6.15), can be approximated numerically using a central difference scheme as:

$$\frac{\partial \boldsymbol{u}(\boldsymbol{x})}{\partial x} \approx \frac{\boldsymbol{u}(x + \Delta x^{PD}, y) - \boldsymbol{u}(x - \Delta x^{PD}, y)}{2\Delta x^{PD}}. \tag{6.16}$$

Using Case 1, the J integral value for the double notched plate is computed as $J^{Abaqus} = 12.89\mathrm{Pa} \cdot \mathrm{m}$. This value was acquired after convergence tests with local refinement in the vicinity of the crack tip and it matches the one reported in [83] for the same problem. Therefore, it is considered a very close approximation to the analytical solution and will be used subsequently as a benchmarking tool. It is noted that Abaqus computes the J integral using the domain integration method that is considered more robust compared to the direct contour approximation that is used in Eq. (6.15) [229]. For Cases 2 and 3, the J integral is approximated using Eqs. (6.15) and (6.16). In all cases, the contour path is defined as a square, centred at the crack tip, with edge length l^c (Figure 6.10). The path is selected as a square for consistency and for compatibility with Case 3 where Ω^{PD} is also square.

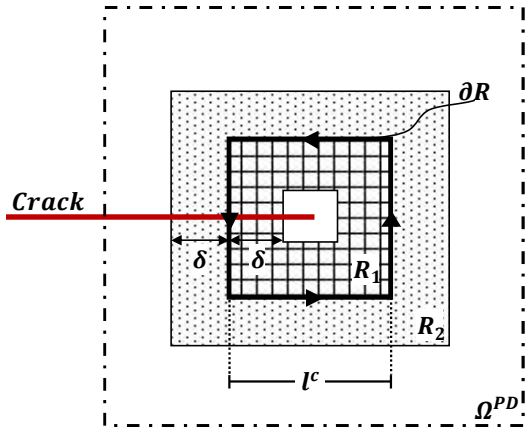

Figure 6.10: Definition of the contour region for the calculation of the nonlocal J-integral according to Hu et. al. [83].

Although the path independence of the J integral approximation in Eq. (6.15) has already been studied in [83], it is important to establish that this property is not affected by the XFEM-PD coupling in Case 3. Using again the same discretization (i.e. $\Delta x^{FE} = \Delta y^{FE} = 3 \cdot 10^{-3}\mathrm{m}$, $\Delta x^{PD} = \Delta y^{PD} = 5 \cdot 10^{-4}\mathrm{m}$ and $\delta = 4 \cdot \Delta x^{PD}$), the J integral is evaluated for different values of l^c. The results are compared with J^{Abaqus} in terms of the relative % error.

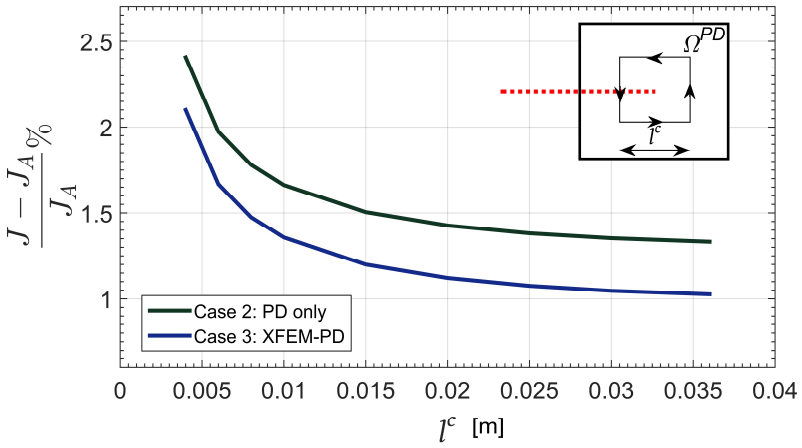

Figure 6.11: Comparison of the relative error between the J integral computed from Cases 2 and 3 with J^{Abaqus} for different contour paths.

In all cases we allow $0.004 \leq l^c \leq 0.036$ in order to ensure the feasibility of the contour, i.e. there is adequate clearance to define the areas R_1 and R_2 required for Eq. (6.15). Figure 6.11 illustrates the relative error for different l^c values. The results exemplify that the J integral approximation does not vary significantly for different contour paths. In fact, the maximum variation on the J integral value is approximately 1.06% in both cases. The relative error is higher for paths closer to the crack tip. Typically, paths near the tip are avoided due to numerical inaccuracies. Still, Figure 6.11, indicates that the variation is small, and the path independence is satisfied. The results in Figure 6.11 also indicate that Case 3 leads to slightly better estimations of the J integral value. This slight improvement could be due to the different way boundary conditions are applied in the PD theory. In the XFEM-PD model on the other hand, the boundary conditions are applied on Ω^{FE}.

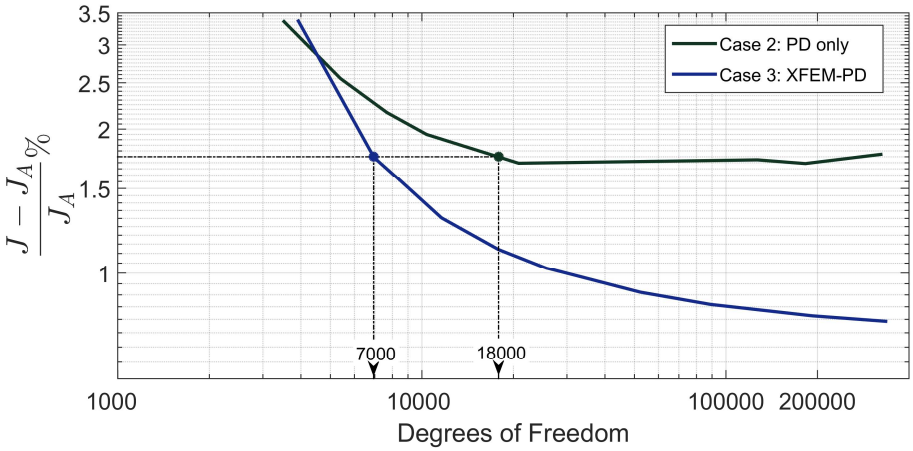

Figure 6.12: Convergence of the J integral value approximated using Cases 2 and 3 to J^{Abaqus} versus the total number of dofs. Logarithmic scale is used for both axes.

To illustrate the reduction of the dofs when Case 3 is used instead of Case 2, a convergence study is presented for different values of the discretization length Δx^{PD}. The J integral is computed each time using a square contour with $l^c = 0.02\text{m}$. In Case 3 the discretization of Ω^{FE} remains unchanged and equal to $\Delta x^{FE} = \Delta y^{FE} = 3 \cdot 10^{-3}\text{m}$. The relative error to J^{Abaqus} is plotted versus the total number of dofs in the final system of equations in Figure 6.12. Using Case 2 the relative error exhibits a plateau at approximately 1.7%. A similar observation was reported in [83] for the same example. Although the convergence rate for Case 3 also deteriorates as the discretization of Ω^{PD} becomes finer, the accuracy is improved. As reported in [230], use of XFEM with geometrical enrichment near the crack tip can achieve rates up to $O(h^2)$. Although such convergence rates are not achieved here with the coupled XFEM-PD models, the convergence is improved compared to using a PD only model. On the same figure the total dofs required to achieve 1.75% accuracy is indicated with dotted lines for each case. Case 3 requires less than half the dofs to achieve the same accuracy as Case 2. This increase of performance in Case 3 can be traced back to the fact that for the same number of dofs, Case 3 achieves a finer discretization in Ω^{PD} as the total number of dofs is dedicated in this area only. For very small numbers of dofs, the coupling between the two models however becomes inaccurate.

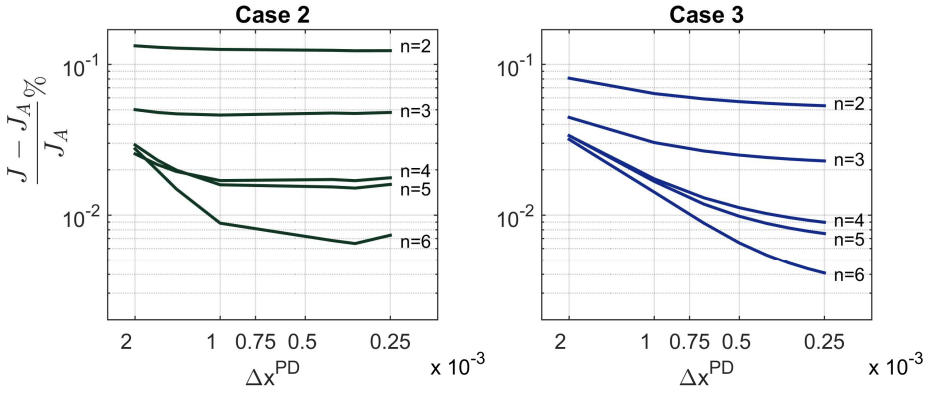

Figure 6.13: Convergence of the J integral value approximated using Cases 2 and 3 for different values of the PD discretization Δx^{PD} and the PD horizon $\delta = n \cdot \Delta x^{PD}$

The convergence of the J integral value is also presented for different values of the PD horizon $\delta = n \cdot \Delta x^{PD}$, with $n = 2, 3, 4, 5$ and 6 and $l^c = 0.02\text{m}$. The results are plotted in Figure 6.13 versus the PD discretization length Δx^{PD}. When very coarse discretization is used in Ω^{PD}, the relevant error of Case 3 can be higher compared to Case 2 as the coupling between the two models becomes inaccurate. Higher values of the PD horizon improve the convergence in both cases, while in Case 2, it also affects the value where it exhibits the plateau. As discussed

in [83], appropriate selection of n and Δx^{PD} can be made to match exactly the PD solution with classical elasticity. Low values of δ however, can lead to mesh dependencies during crack propagation while high values induce excessive dispersion and increase the computational cost [84,207].For macroscale 2D fracture problems values $n \geq 3$ are typically selected [143]. For the computation of the nonlocal J integral, the value $n = 4$ seems a fair compromise between accuracy and computational cost.

Apart from the accuracy improvement the XFEM-PD models exhibit compared to the PD only model, the efficiency of the numerical approximation is also boosted significantly in terms of computational time and memory requirements. This development is directly related to the reduction of the total dofs. To illustrate this improvement, the required time to solve the resulting system of equations was evaluated for each case, using different values of Δx^{PD} in Ω^{PD}. The analyses were carried out using a system with 16GB total memory and an i7 8700K CPU, running at default settings. For all analyses, the PD horizon was set as $\delta = 4\Delta x^{PD}$ while for Case 3 the discretization of Ω^{FE} was also kept constant with $\Delta x^{FE} = \Delta y^{FE} = 3 \cdot 10^{-3}\text{m}$. In both cases, the same Newton-Rapson solver was used to solve the final system of equation. MATLAB's backslash operator is called to solve the system of equations. The required CPU time for each case as well as the relative speed up between Case 2 and Case 3 are plotted in Figure 6.14.

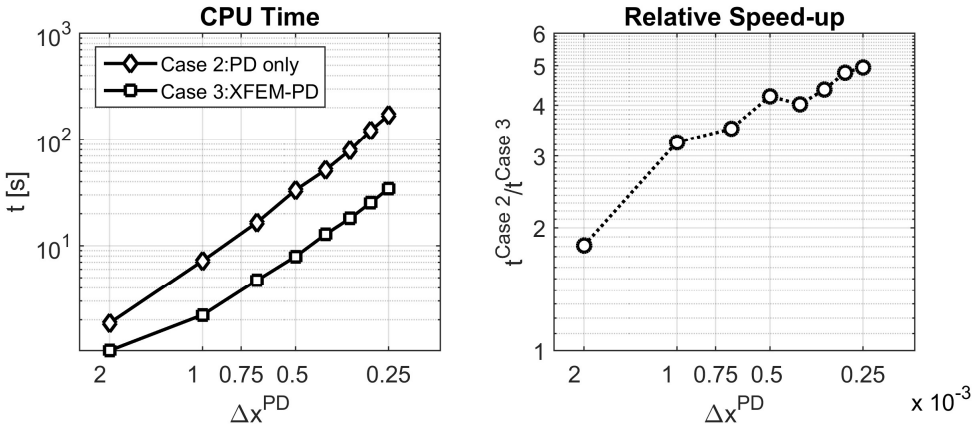

Figure 6.14: Comparison of the CPU time needed for each case (left) and the relative speed-up between Case 2 and Case 3 (right). Both axes are plotted in logarithmic scale.

Employing a coupled model can reduce the required computational effort while achieving the same discretization in Ω^{PD}. For example, the CPU time elapsed when $\Delta x^{PD} = 5 \cdot 10^{-4}\text{m}$ is $t^{\text{Case 2}} = 170.1s$ and $t^{\text{Case 3}} = 34.38s$ for Cases 2 and 3, respectively. There are two main reasons that contribute towards the reduction of the CPU time: **i**) the reduction in terms of total

dofs that lead to a computationally more manageable system of equations and **ii**) use of classical elasticity away from the crack tip, assumes a local description, that further boosts the computational efficiency by increasing the sparsity of the stiffness matrix, i.e. reduces the required algebraic operations in the numerical approximation.

Case 3 entails the additional cost of enforcing the coupling between the two domains. When coarse discretization is implemented in Ω^{PD}, this additional cost becomes significant compared to the total simulation time and the relative speed up is small, despite the implementation of a local model away from the crack tip. As the PD discretization becomes finer, particularly when $\Delta x^{PD} < \Delta x^{FE}$, which is expected to be the typical case for practical applications, the computational gains are highlighted. Compared to Case 2, Case 3 can achieve a speed-up up to 5 times faster. Thus, the incorporation of XFEM notions can significantly increase the computational efficiency of a coupled model. It is noted here that these results are not meant to be used as a suggestion on the selection of the discretization parameters Δx^{PD} and Δx^{FE}. They do offer however an indication on the potential gains that a coupled model can offer. Proper selection of the discretization parameters for each domain is particularly important for dynamic problems as they influence the spurious reflections generated when a pulse crosses the coupling interface [226].

6.3 Adaptive Relocation during Crack Propagation

In this section the algorithm for the adaptive relocation of Ω^{PD} is presented. Aiming towards the overall reduction of the total dofs in the final system of equations, application of the PD theory is restricted to the vicinity of the crack tip(s) only. Similar strategies have been already proposed in the literature in a plethora of publications. Here we mention only two contributions due to their relevance with the present study. In [117] and [130] the FE mesh and the PD grid are coupled in a similar way to the method implemented here. The authors also addressed crack propagation problems by continually increasing the domain where the PD theory is applied. A criterion based on the relative elongation between FE nodes is used to trigger the conversion of FE nodes to PD particles. This contribution is noteworthy as the methodology is also extended to 3D applications. Another notable contribution is the so called "*morphing*" strategy, presented in [231–233]. In this case, a unified framework is used that incorporates both the local and the non-local force interactions. The local and non-local contribution at a material point is defined through weighting functions that ensure energy equilibrium.

The difference with the current approach is that Ω^{PD} is attempted to be localized near the location of the crack tip only. Use of PD to capture the displacement jump near the crack body

increases unnecessarily the computational cost of the solution. Thus, the methodology presented here allows to switch from FEs to PD particles in order to capture the propagation of the crack but also switch PD particles back to FEs in areas where the PD model is no longer needed. One way to achieve this is to redefine Ω^{PD} and Ω^{FE} at each solution step, making sure that Ω^{PD} contains the crack tip location. This approach however can be cumbersome in static problems and when complex crack patterns are considered. Instead, the strategy followed here is the adaptive relocation of Ω^{PD} through a two-step process:

Step 1 – Expansion Step: As the crack propagates within Ω^{PD} it will eventually reach the XFEM-PD coupling interface, $\partial\Omega_2$. The area where the PD theory is applied needs to be expanded to ensure that the crack tip is always within Ω^{PD}. Consequently, $\partial\Omega_2$ is shifted, and additional PD particles are introduced to cover the updated location of Ω^{PD}. The FEs that are now located within the new boundary are deactivated and their contribution is removed from $\boldsymbol{K}^{FE}$ and $\boldsymbol{M}^{FE}$.

Step 2 – Contraction Step: After Ω^{PD} has been expanded, the PD particles that are away from the crack tip are no longer required as the displacement jump due to the crack body can be captured with the XFEM enrichment. During this step $\partial\Omega_2$ is shifted again, focusing around the crack tip(s) and Ω^{PD} is restricted to a smaller area. The approximation of the solution switches back to the FE method in the area that is no longer inside Ω^{PD}. Additional enriched dofs with their respective functions are introduced in Ω^{FE} to capture the updated crack location.

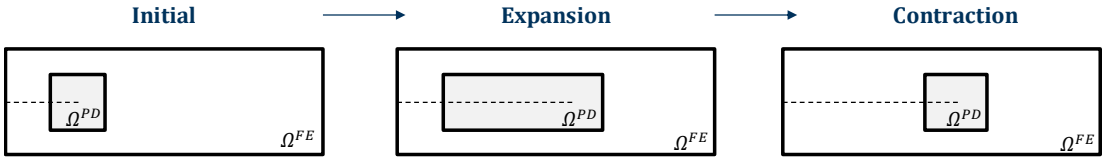

Figure 6.15: Schematic illustration of the two-step process for the adaptive relocation of Ω^{PD}.

The location of Ω^{PD} is updated and follows the propagation of the crack through the two-step process, as illustrated in Figure 6.15. Because Ω^{PD} virtually propagates through the expansion/contraction steps, leaving behind a trail of Heaviside functions, the algorithm is termed the "*Peridynamic snail*". The advantage of this two-step process is that each time a small portion of Ω^{PD} and Ω^{FE} is modified, minimizing the requirement for interpolations and allowing for the crack pattern to first emerge naturally within Ω^{PD} prior to the relocation. A requirement that arises during the contraction step, is the need for information regarding the

vicinity of the tip and the geometry of the crack. This is necessary to identify which particles are no longer needed and update the location of $\partial\Omega_2$ as well as to define the enrichment functions. A tracking methodology is thus required to monitor the evolution of the crack.

6.3.1 *Crack Tracking Algorithm*

The requirement to monitor the location of the crack during the simulation is counter-intuitive for the PD theory. In fact, one of the attractive properties of PD is the ability to incorporate damage and simulate its evolution without the need for special algorithms that are intended to monitor its location and the path it has travelled during the simulation [5]. A simple approach is implemented here to identify the location of the crack tip at each time step, leading to a piecewise linear estimation of the crack path.

The current location of the crack tip is estimated numerically using the PD local damage index $\phi(\boldsymbol{x}^{PD}, t)$, defined in Eq. (3.20). Consider a square plate with an edge breaking crack, as illustrated in Figure 6.16 (a). The process is based on the observation that when taking the gradient of the local damage index, the vector field near the crack will point towards the location of the crack body and converge near the location of the tip. It is thus expected that the Laplacian of local damage index (i.e. $\nabla \cdot \nabla\phi(\boldsymbol{x}^{PD}, t)$) will exhibit a local minimum at this location. The gradient and the Laplacian of $\phi(\boldsymbol{x}^{PD}, t)$ are plotted in Figure 6.16 (b) and (c), respectively. The exact value of $\nabla \cdot \nabla\phi(\boldsymbol{x}^{PD}, t)$ is not of interest here, just the location where the minimum appears. In the examples presented here, the Laplacian of $\phi(\boldsymbol{x}^{PD}, t)$ has been normalized with respect to its minimum value. The location of the local minimum is indicated in the same figure with a red triangle. In Figure 6.16 (d) a schematic representation of a PD grid and the bonds that connect the particles is illustrated. The bonds that are intersected due to the crack have been removed from the grid. It is not easy to pinpoint exactly the location of the crack tip in the PD model as the bonds cannot be directly related to geometrical information. Still, the approach followed can lead to very good estimations.

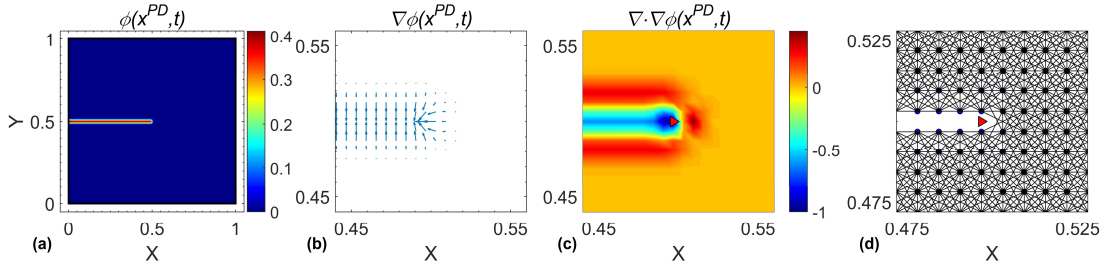

Figure 6.16(a): Illustration of a plate with an edge crack using the local damage index $\phi(\boldsymbol{x}^{PD}, t)$, (b) and (c): Close-up near the location of the tip for $\nabla\phi(\boldsymbol{x}^{PD}, t)$ and $\nabla \cdot \nabla\phi(\boldsymbol{x}^{PD}, t)$ and (d): representation

of a PD grid and the bond network. A red triangle indicates the location of the tip as identified from the tracking algorithm.

The Laplacian $\nabla \cdot \nabla \phi(\boldsymbol{x}^{PD}, t)$, is computed numerically during the simulation and the current location of the crack tip is stored in an array to be used during the contraction step of the relocation process. This tracking method can be also used to monitor the damage evolution when multiple cracks are present in the problem. The performance of the tracking methodology is evaluated by using the cold case from section 4.4.1. Specifically, the method is applied on the results presented in Figure 4.5.

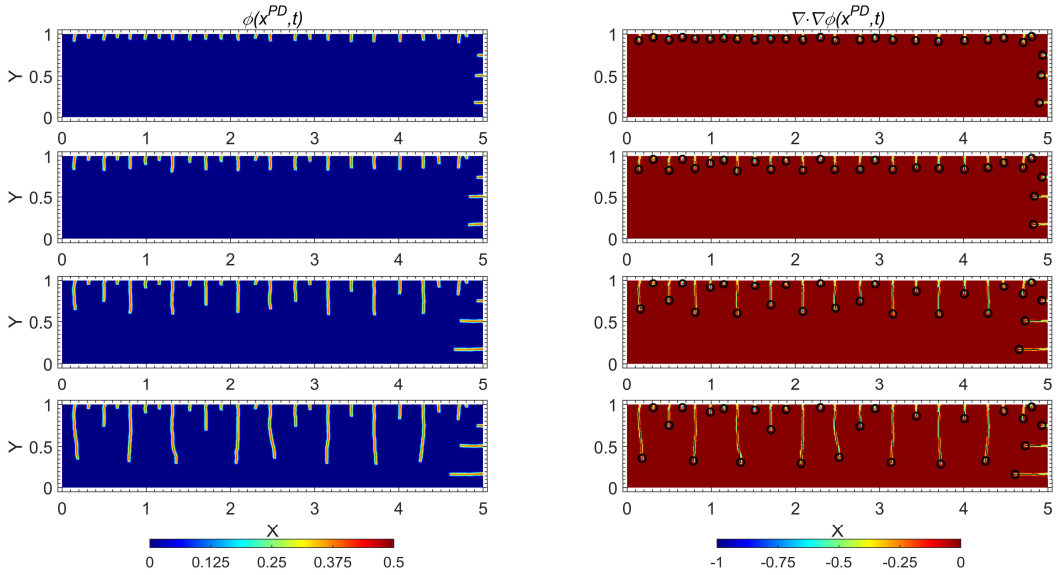

Figure 6.17: Application of the tracking algorithm on the damage evolution of an alumina specimen under cold shock [234].

The tracking process for the cold shocked alumina at different time steps, is illustrated in Figure 6.17. Using this approach, it was possible to capture automatically the propagation and the arrest of each individual crack. The current location of the crack tip is indicated with a black circle and the path it followed with a black line. At each time step that the tracking algorithm is executed, possible tip locations are identified. To sort which tip location corresponds to which crack, a straight line is used to connect each crack with each possible tip location. The local damage index is then computed along each of the lines and the tip corresponds to the crack that produces the highest value. The method is applied by simply comparing a current with a previous step and no prior knowledge regarding the direction of propagation is required. In the examples presented here for instance, some of the cracks propagate in the vertical direction while others in the horizontal. It is noted here that the robustness of the method is an important issue. False positive indications of a crack tip can lead to erroneous results and affect

significantly the adaptive algorithm. For the examples considered here, this simplistic approach provides adequate accuracy.

6.3.2 *Expansion Step*

The expansion and the contraction steps are performed sequentially to achieve the adaptive relocation of Ω^{PD}. It is desirable during the relocation process to limit as much as possible the remeshing requirements for Ω^{FE}. With regards to the crack body that appears within Ω^{FE}, this requirement is lifted with the introduction of the XFEM enrichment. However, in order to achieve relocation, the area where Ω^{FE}, Ω^{PD} and the coupling interface $\partial\Omega_2$ are defined, needs to be updated. Since the shape and the size of Ω^{PD} will vary during the simulation, at least partial redefinition of the grid is unavoidable. Remeshing of Ω^{FE} can be avoided however by initially discretizing with FEs the whole problem domain Ω. Then, Ω^{PD} is overlaid on Ω^{FE} and $\partial\Omega_2$ is defined along the element edges. The dofs associated with FE nodes with $\boldsymbol{x}^{FE} \in \Omega^{PD}$ as well as the stiffness and mass contributions of the elements within Ω^{PD} are removed from $\boldsymbol{K}^{FE}$ and $\boldsymbol{M}^{FE}$, respectively. During relocation, the FE mesh remains unchanged by activating and deactivating the appropriate elements while no restrictions are applied with regards to its initial definition.

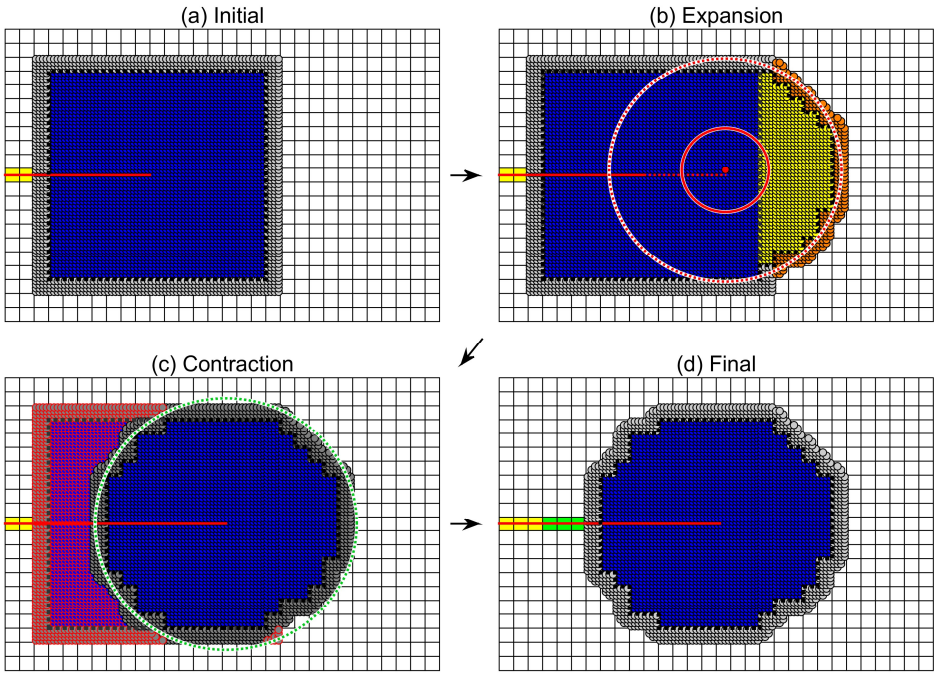

Figure 6.18: Illustration of the relocation process through the successive application of the expansion and contraction steps.

An example of the expansion/contraction process is illustrated in Figure 6.18. For simplicity, uniform discretization is used for both Ω^{PD} and Ω^{FE}. Initially, Ω^{PD} is constructed as a square, centred at crack tip. Blue and grey dots indicate normal and ghost particles, respectively. White squares have been used to indicate the FE mesh while yellow squares indicate the elements that are cut by the crack body and have been enriched. As the crack propagates, it will eventually reach the coupling interface $\partial\Omega_2$ (see Figure 6.18 (b)).

During the expansion step knowledge of the location of the tip or the crack is not required. The expansion step is activated when:

$$\|\boldsymbol{x}^{PD,b} - \boldsymbol{x}^{PD,*}\| < l^{crit}, \tag{6.17}$$

where, $\boldsymbol{x}^{PD,b}$ are the PD particles that lost at least one bond in the current step increment t, $\boldsymbol{x}^{PD,*}$ is the closest point to $\boldsymbol{x}^{PD,b}$ on $\partial\Omega_2$ and l^{crit} is a threshold distance. The term step increment refers to time and load increments for dynamic and static problems, respectively.

Eq. (6.17) is the *expansion trigger* within the algorithm to identify the location where expansion is required. Let $\boldsymbol{x}^{PD,Exp}$ be the set of $\boldsymbol{x}^{PD}$ that violates Eq. (6.17) i.e.:

$$\boldsymbol{x}^{PD,Exp} = \left\{\boldsymbol{x}^{PD} \in \boldsymbol{x}^{PD,b} : \|\boldsymbol{x}^{PD} - \boldsymbol{x}^{PD,*}\| > l^{crit}\right\} \tag{6.18}$$

Then Ω^{PD} must be expended for each entry in $\boldsymbol{x}^{PD,Exp}$ till the expansion trigger is no longer violated at any location. Multiple expansions might be required within a single expansion step depending on the number and the locations defined by $\boldsymbol{x}^{PD,Exp}$. The threshold value ensures that a minimum distance of l^{crit} covers at any given time step a damaged particle. As such, it is the location of the damaged particles that drive the activation of the expansion step regardless of the exact position of the crack. This property allows to easily reshape Ω^{PD} even when complex crack patterns or multiple cracks are considered (see branching example in the following sections). A particle that has tripped the expansion trigger is illustrated in Figure 6.18 (b) with a red dot and the distance l^{crit} around the particle is plotted with a solid red line.

How much the area of Ω^{PD} expands during the expansion step is defined through the expansion length l^{Exp}. Since the final crack path is not known, the expansion is performed in a radial sense, centred at the location of the expansion trigger, to allow for all possible directions of crack propagation. A circle with radius l^{Exp}, is plotted in Figure 6.18 (b) with a dashed red line to define the part of Ω^{FE} that will switch to Ω^{PD} in the subsequent steps. The expansion domain is defined as:

$$\Omega^{Exp} = \{\boldsymbol{x}^{FE} \in \Omega^{FE} : \|\boldsymbol{x}^{FE} - \boldsymbol{x}^{PD,Exp}\| < l^{Exp}\} \tag{6.19}$$

Obviously $\Omega^{Exp} \subseteq \Omega^{FE}$ and $\partial\Omega^{Exp}$ is its boundary. Thus, for the next step:

$$\Omega^{PD,t+\Delta t} = \Omega^{PD,t} \cup \Omega^{Exp}, \tag{6.20a}$$

$$\Omega^{FE,t+\Delta t} = \Omega^{FE,t} \backslash \Omega^{Exp}, \tag{6.20b}$$

The superscripts $t + \Delta t$ and t are used to denote the current and next step. The new coupling interface $\partial\Omega_2^{t+\Delta t}$ is now updated and it is the boundary of $\Omega^{PD,t+\Delta t}$, illustrated with a black dotted line in Figure 6.18 (b). The FEs that lie within Ω^{Exp} are deactivated by removing their contribution from $\boldsymbol{K}^{FE}$ and $\boldsymbol{M}^{FE}$ and additional normal and ghost PD particles are introduced to discretize Ω^{Exp} and enforce the coupling, indicated by yellow and orange dots, respectively, in Figure 6.18 (b).

The displacement, velocity and acceleration of the PD particles that were added in Ω^{Exp} need to be initialized. Let n^a be the total number of the added particles. The same interpolation can be used as in Eq. (6.1):

$$\boldsymbol{Y}_k^a = \sum_{\mathrm{i}=1}^{K} N_i(\boldsymbol{x}_k^{PD})\boldsymbol{X}_i\,, k = 1,2,\dots n^a \tag{6.21}$$

where, K is the total number of FE nodes, $\boldsymbol{Y}_k^a$ and $\boldsymbol{X}_i$ can be replaced by $\boldsymbol{d}_k^a, \dot{\boldsymbol{d}}_k^a$ or $\ddot{\boldsymbol{d}}_k^a$ and $\boldsymbol{u}_i, \dot{\boldsymbol{u}}_i$ or $\ddot{\boldsymbol{u}}_i$ respectively.

6.3.3 *Contraction Step*

The expansion step and the contraction step are independent. A trigger can also be used to activate the contraction step such $k < k^{crit}$. Here we define k to be the number of times the expansion step has been executed. By setting $k^{crit} = 1$, the contraction step is activated after each expansion step. Other definitions of the trigger for the contraction step are also possible. For example, a limit can be set based on the total number of dofs in the system to keep in control the memory requirements of the solution.

During the contraction step, the area of Ω^{PD} is limited to a certain distance from the location of the crack tip, $\boldsymbol{x}^{tip}$. This limits the use of the PD theory and improves the computational efficiency. Similar to the expansion step, a threshold value, l^{Con}, is used to define the part of Ω^{PD} that will remain unchanged (green dotted line in Figure 6.18 (c)). The current location of the tip is computed using the tracking algorithm. Just like the expansion step converts part of Ω^{FE} into Ω^{PD}, the contraction step converts part of Ω^{PD} into Ω^{FE}. The part of the domain that needs to be converted is defined as:

$$\Omega^{Con} = \left\{ \boldsymbol{x}^{FE} \in \Omega^{PD} : \left\| \boldsymbol{x}^{FE} - \boldsymbol{x}^{tip} \right\| > l^{Con} \right\} \tag{6.22}$$

and its boundary as $\partial\Omega^{Con}$. The particles that are inside the contracted PD domain are defined as $\boldsymbol{x}^{PD,n} = \{\boldsymbol{x}^{PD} \in \Omega^{PD} \backslash \Omega^{Con}\}$. The particles that will remain in the subsequent steps are defined as:

$$\boldsymbol{x}^{PD,f} = \{\|\boldsymbol{x}^{PD} - \boldsymbol{x}^{PD,n}\| < \delta\} \tag{6.23}$$

i.e. $\boldsymbol{x}^{PD,f}$ contains the particles in $\boldsymbol{x}^{PD,n}$ and all the particles in $\boldsymbol{x}^{PD}$ that are located within one horizon distance δ of the particles in $\boldsymbol{x}^{PD,n}$. The particles in $\boldsymbol{x}^{PD,n}$ are the new normal particles while the additional particles in $\boldsymbol{x}^{PD,f}$ are needed to be used as ghost particles and enforce the coupling. The normal and the ghost particles after the contraction are indicated with blue and grey dots, respectively, in Figure 6.18 (c). In the same figure, red circles indicate the particles that are not contained in $\boldsymbol{x}^{PD,f}$ and that are removed from subsequent computations. The elements in Ω^{Con} are activated again and their stiffness and mass contributions are added back to $\boldsymbol{K}^{FE}$ and $\boldsymbol{M}^{FE}$, respectively. Furthermore, the elements in Ω^{Con} that are cut by the crack body are enriched, and the signed distance function $\varphi(\boldsymbol{x}^{FE})$ is updated. The enrichment is necessary since after moving the coupling interface $\partial\Omega_2$, an additional segment of the crack body now exists in Ω^{FE}.

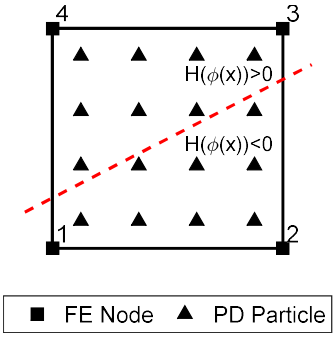

Figure 6.19: Illustration of a FE cut by a crack and the PD particles it contains.

Since the FE nodes in Ω^{Con} are activated, their values need to be also initialized. The initialization of the values depends on whether the support of the node is cut by the crack body or not. If it is not cut, linear interpolation is implemented using the PD values that enclose the FE node. This interpolation procedure is also used in [130]. If, however, the crack intersects the nodal support, the enriched dofs must also be considered. Since the values of the enriched dofs do not have a physical meaning, their values cannot be easily related to information from

the PD model. In this case, the initialization is performed in an approximate manner through least squares fitting.

Consider the isolated element in Figure 6.19. Let $n_1 = 4$ be the total FE nodal numbers and $n_2 = 16$ the number of PD particle numbers inside the element. The FE nodes have been enriched with shifted Heaviside functions to capture the discontinuous displacement field due to the crack (red dash line). Considering the displacement field and using Eq. (6.1), we write:

$$\boldsymbol{d}_k = \sum_{\mathrm{i}=1}^{n_1} N_i(\boldsymbol{x}_k^{PD})\boldsymbol{u}_i + \sum_{j=1}^{n_1} N_j(\boldsymbol{x}_k^{PD})\left(H(\boldsymbol{x}_k^{PD}) - H\left(\boldsymbol{x}_j^{FE}\right)\right)\boldsymbol{a}_j\,, k = 1, \dots, n_2. \tag{6.24}$$

The above expression describes an overdetermined system of equations (32 equations with 16 unknowns in this example). Denoting with:

$$\boldsymbol{y} = \left[(\boldsymbol{d}_1)^T, \dots, \left(\boldsymbol{d}_{n_2}\right)^T\right]^T, \boldsymbol{A} = \begin{bmatrix} [\boldsymbol{N}(\boldsymbol{x}_1^{PD})]\ [\boldsymbol{\Psi}^{enr}(\boldsymbol{x}_1^{PD})] \\ \vdots \\ [\boldsymbol{N}(\boldsymbol{x}_k^{PD})]\ [\boldsymbol{\Psi}^{enr}(\boldsymbol{x}_k^{PD})] \end{bmatrix} \text{ and} \\ \boldsymbol{b} = \left[(\boldsymbol{u}_1)^T, \dots, \left(\boldsymbol{u}_{n_1}\right)^T, (\boldsymbol{a}_1)^T, \dots, \left(\boldsymbol{a}_{n_1}\right)^T\right]^T \tag{6.25}$$

the vector of inputs, the matrix of coefficients and the unknown vector, respectively, then:

$$\boldsymbol{b} = (\boldsymbol{A}^T\boldsymbol{A})^{-1}\boldsymbol{A}^T\boldsymbol{y}. \tag{6.26}$$

Eq. (6.26) describes the least square estimation of $\boldsymbol{b}$ and allows for the approximation of the enriched dofs values. For short, $\boldsymbol{\Psi}^{enr}(\boldsymbol{x}_1^{PD})$ is used to denote the second term of Eq. (6.24). The velocity and acceleration fields are estimated in an analogous manner.

After the initialization of the FE values is completed, the PD particles that are not contained in $\boldsymbol{x}^{PD,f}$ can be removed and the domains are updated as:

$$\Omega^{PD,t+\Delta t} = \Omega^{PD,t} \backslash \Omega^{Con}, \tag{6.27a}$$

$$\Omega^{FE,t+\Delta t} = \Omega^{FE,t} \cup \Omega^{Con}, \tag{6.27b}$$

The updated $\partial\Omega_2^{t+\Delta t}$ is the boundary of $\Omega^{PD,t+\Delta t}$ and it is indicated with a black dotted line in Figure 6.18 (c) and (d). The additional FE that have been enriched due to the contraction of Ω^{PD} are indicated in Figure 6.18 (d) with green colour. It is also possible to see in Figure 6.18 that after the execution of the expansion/contraction steps, the PD domain has been displaced, following the propagation of the crack. The incorporation of the XFEM enrichment for the description of the discontinuous displacement field near the crack body alleviates the need for remeshing each time the contraction step is executed, and an additional part of the

crack appears in Ω^{FE}. Still, local modification of $\boldsymbol{K}^{FE}$ and $\boldsymbol{M}^{FE}$ is required to account for the relocation of the two domains.

The requirement for information on the current location of the crack tip arises due to the appearance of $\boldsymbol{x}^{tip}$ in the definition of Ω^{Con}. Furthermore, the crack path or more precisely, the location of the crack body is required for the computation of the signed distance function $\varphi(\boldsymbol{x})$ and the definition of the Heaviside functions for Eq. (6.24). Tracking the curve (or the surface in 3D) that defines the crack can give rise to complications when complex crack patterns appear. This necessity however is not related only to the use of XFEM. Even if approaches like the phantom node [235] or the local re-mesh were followed, the crack tracking requirement would persist.

6.3.4 *Parameter Selection*

The behaviour of the expansion/contraction steps depends on the definition of the parameters l^{crit}, l^{Exp} and l^{Con}. These values are auxiliary and do not arise from the formulation of the problem. Nevertheless, the following observations can be made that corelate the values of these parameters. Consider the simplified illustration in Figure 6.20; after the application of the contraction step, Ω^{PD} is limited within a circle of radius l^{Con}, centered at the crack tip (orange circle). The crack can propagate within a distance of l^{crit} of the orange circle without triggering the expansion step (green circle).

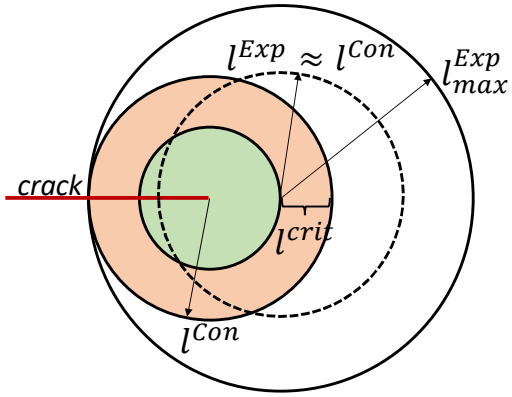

Figure 6.20: Schematic illustration of the relationship between l^{crit}, l^{Exp} and l^{Con}.

Let the crack propagate in a straight line and trigger the expansion step. If $l^{Exp} < l^{crit}$ then Ω^{Exp} would be empty and no expansion occurs through Eqs. (6.20). Furthermore, there is a maximum value $l^{Exp}_{max} = 2l^{Con} - l^{crit}$ above which the expanded domain will cover a larger portion of the crack compared to the initial domain. This is counterproductive for the purposes of this algorithm. Thus l^{Exp} is bounded as:

$$l^{crit} < l^{Exp} \leq 2l^{Con} - l^{crit} \tag{6.28}$$

Additionally, if $l^{Exp} > l^{Con}$ then the contraction step might cancel out substantial portion of the expansion if they are used in turn. Therefore, in the following paragraphs, it is selected $l^{Exp} \approx l^{Con}$. Thus, Eq. (6.28) is satisfied for $l^{Con} > l^{crit}$.

6.3.5 *Implementation of the Expansion/Contraction Steps for Static and Dynamic Problems*

A flowchart with an overview of the expansion/contraction steps can be found in Figure 6.21. The implementation of these steps depends on whether a static or a dynamic problem is considered. During a dynamic simulation the expansion trigger is checked after each time increment to evaluate if every damaged particle is sufficiently covered (see Figure 6.22). Subsequently the contraction step is used to reduce the application of the PD theory. Static simulations however require a different approach. When the solution has converged for a given load increment the expansion trigger is evaluated. If it is not satisfied, Ω^{PD} is expanded and the same load increment is re-evaluated (see Figure 6.22). This process is repeated till the expansion trigger is not tripped and the solution is accepted for this load increment. After this the contraction step can be executed. Thus, multiple expansion steps might be required for a single load increment till Ω^{PD} is sufficiently large to facilitate the initial and the propagated crack location. This is required because the direction and the propagation length are not known and in static problems even small increases in the load step can lead to large crack extension. This feature is particularly important for unstable crack propagation and it is one of the reasons why relocation through the expansion/contraction method was preferred compared to a direct relocation.

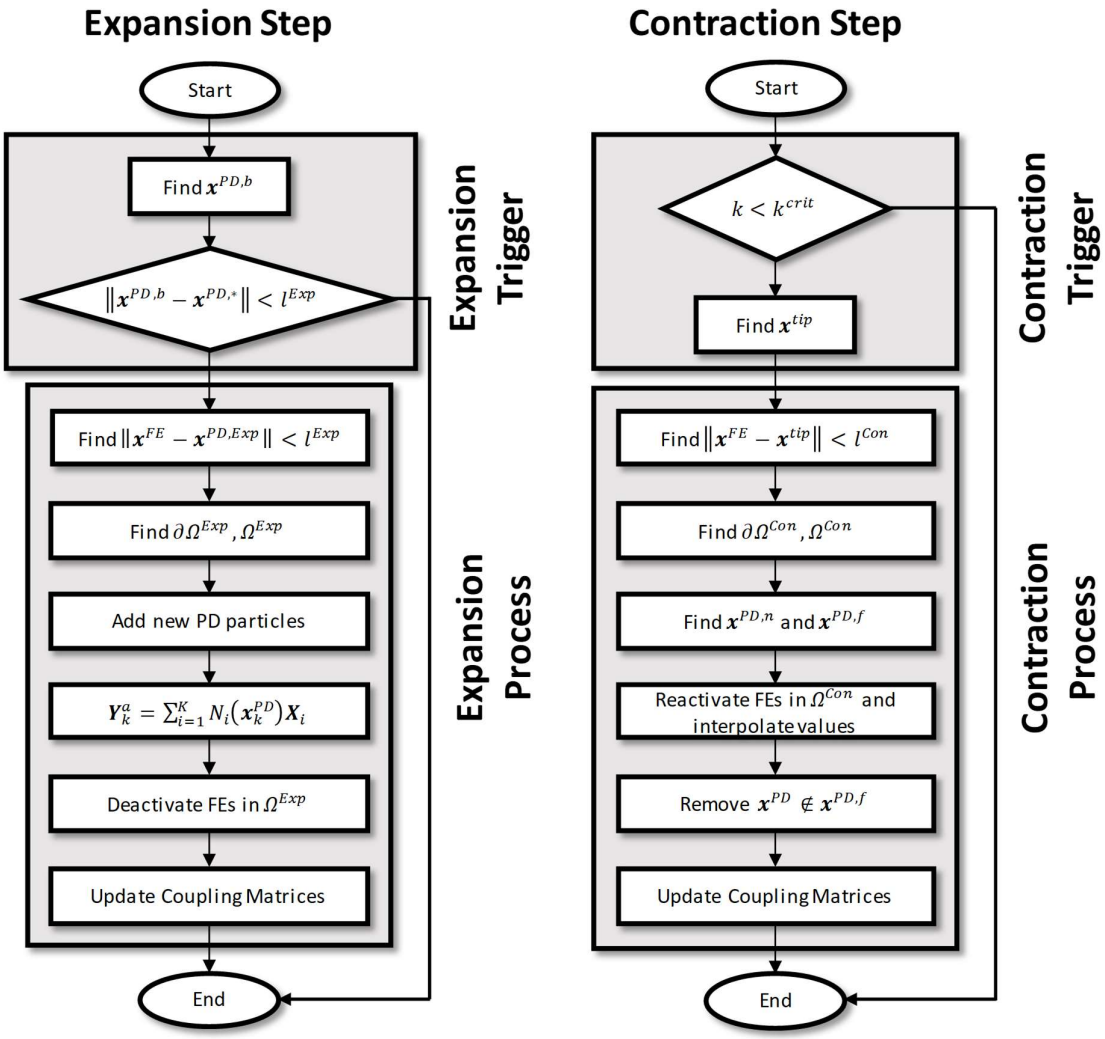

Figure 6.21: Flowchart for the Expansion and the Contractions steps.

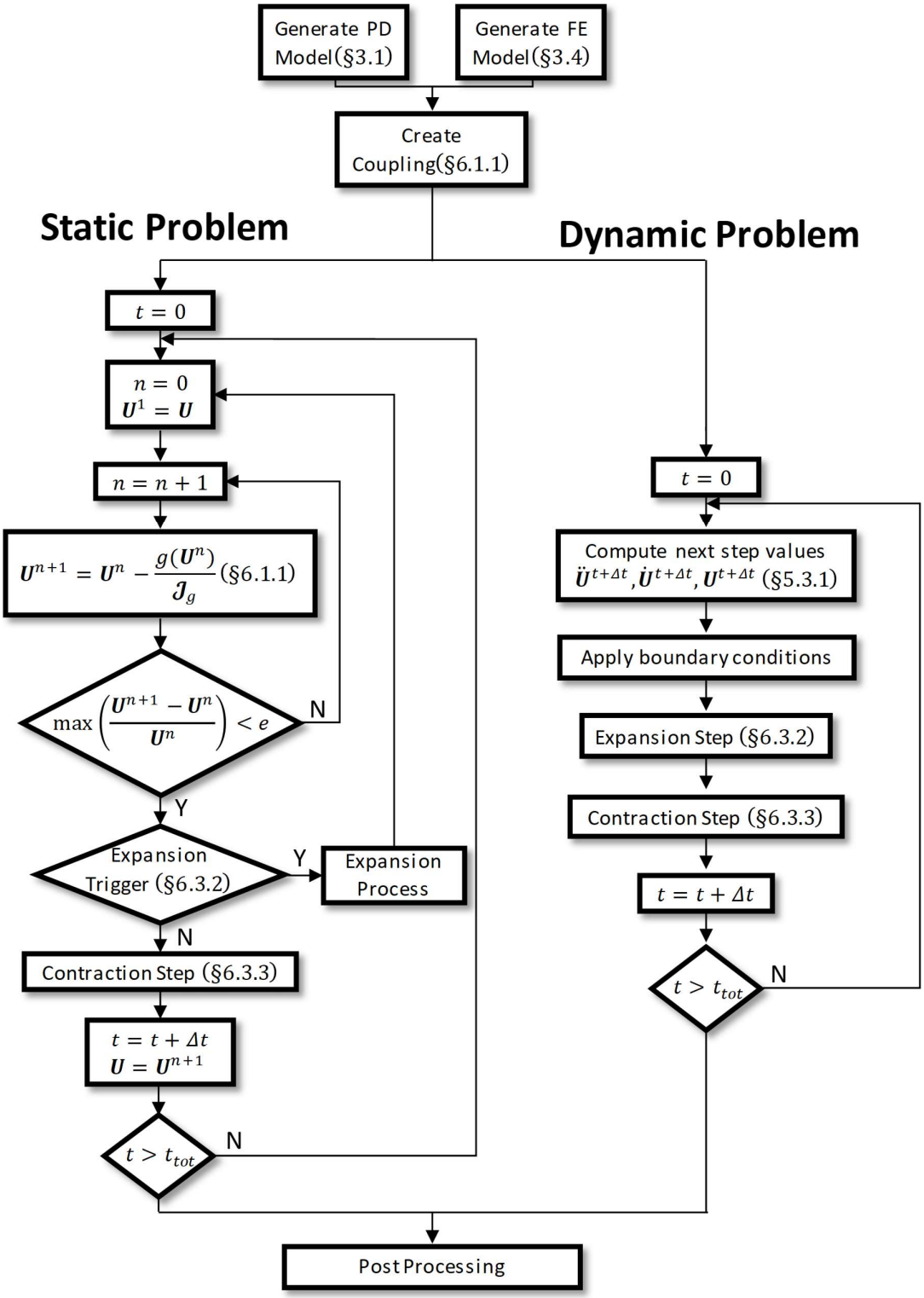

Figure 6.22: Overview of the differences in the implementation of the expansion/contraction steps in static and dynamic problems.

6.4 Simulation of Static and Dynamic Crack Propagation with Adaptive Relocation

The feasibility and effectiveness of the adaptive relocation methodology is evaluated using the results of three crack propagation problems. Both static and dynamic examples are considered to test its performance on various applications.

6.4.1 *Example 1: Static Mode I Propagation in a Double Cantilever Beam*

As a first example the problem of a double cantilever beam with a pre-existing edge breaking crack $a = 0.3\text{mm}$ is considered. Linear elastic material behaviour is assumed under plane stress conditions. The Young's modulus is $E = 75\text{GPa}$, Poisson's ratio $v = 1/3$ and the energy release rate $G_c = 5\text{N/m}$. External loads are assumed to be applied slowly, so that the inertia terms can be neglected. To ensure stable crack propagation, a displacement control approach is adopted. Two clamps are fixed at the bottom and top left corners, as illustrated in Figure 6.23, and are displaced by $\delta_y = 1.5 \cdot 10^{-3}\text{mm}$. The reaction force at the clamps is monitored during the propagation of the crack.

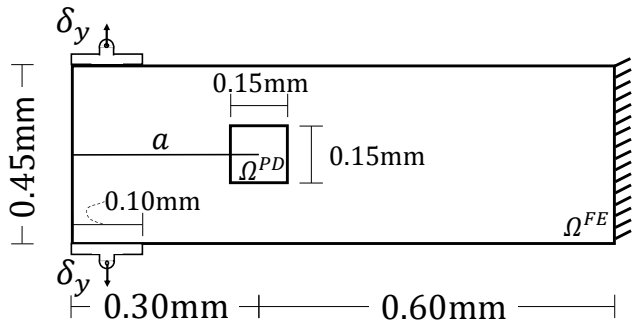

Figure 6.23: Geometry and boundary conditions of the double cantilever beam with a pre-existing crack.

Initially, Ω^{PD} is defined as a square, with side 0.15mm, centered at the crack tip. The discretization parameters are defined as $\Delta x^{PD} = \Delta y^{PD} = 2.5 \cdot 10^{-3}\text{mm}$ and $\Delta x^{FE} = \Delta y^{FE} = 10 \cdot 10^{-3}\text{mm}$ for the PD and FE domains respectively. The PD horizon is assumed $\delta = 4\Delta x^{PD}$ and a conical shape is assumed for $c(\boldsymbol{\xi})$, defined in Eq. (3.12). The parameters used for the expansion/contraction steps are $l^{crit} = 3\,\delta$, $l^{Exp} = 8\,\delta$ and $l^{Con} = 9\,\delta$. In total $17{,}716$ dofs are used after the discretization of the problem domain ($9{,}248$ PD dofs and $8{,}468$ FE dofs). Although this example is simple in the sense that the crack is expected to propagate in a straight line, it is used to illustrate certain aspects of the methodology. The prescribed displacement is applied over 200 increments and the solution of the system of equations is

approximated using the Newton-Raphson iterative solver. The solution of static crack propagation problems with peridynamics has been studied in [223] using different modifications of a Newton-Raphson solver. After each load increment, the expansion trigger from Eq. (6.17) is evaluated to determine if the updated geometry of the crack is sufficiently covered by the PD domain. The contraction step is executed after each expansion to minimize the total number of dofs in the system.

In Figure 6.24, the crack propagation using the proposed methodology is presented at three different load increments. In the left column of Figure 6.24, white and yellow squares indicate the standard and enriched FEs, respectively, and a grey line is used to indicate the location of $\partial\Omega_2$. The local damage index, $\phi(\boldsymbol{x}^{PD}, t)$, is plotted in the region of the PD domain to indicate the crack location. In the right column of Figure 6.24, the deformed configuration is plotted near Ω^{PD}. No remeshing is required for the FE mesh and the discretization of Ω^{FE} remains unchanged from the beginning till the end of the simulation. Meanwhile, Ω^{PD} follows the crack propagation and relocates each time Eq. (6.17) is violated (see Figure 6.24 (A) and (G)). The crack path can be traced from the trail of enrichment functions, which gives the name Peridynamic snail to the algorithm. In total, $15{,}148$ dofs are used at the end of the simulation ($6{,}544$ PD dofs and $8{,}604$ FE dofs). This reduction is caused by the variation of the area of Ω^{PD} from the initial to the final configuration (see Figure 6.24 (B) and (H)).

A load increment is also isolated before and after the application of the relocation method in Figure 6.24 (C) – (F). The load increment 0.58 is initially solved with the current XFEM-PD configuration and the crack propagation is approximated. In Figure 6.24 (C) and (D) the current XFEM-PD configuration and a close-up near the PD domain are plotted, respectively. At the end of this solution step, some of the particles damaged due to the crack propagation violate the expansion trigger. Ω^{PD} is expanded and load increment 0.58 is solved again. With the expanded PD domain, the expansion trigger is not activated after the crack propagation and the solution is accepted. The contraction step is subsequently used and the new XFEM-PD configuration and a close-up near the PD domain are plotted in Figure 6.24 (E) and (F) respectively.

The reaction force generated during the analysis at the corner of the beam is plotted in Figure 6.25. The peak force is $20.90 \cdot 10^{-3}\mathrm{N}$, observed when $\delta_y = 0.4725 \cdot 10^{-3}\mathrm{mm}$. After this point crack propagation occurs and the reaction force is reduced. For comparison, the analysis is repeated using a coarser PD grid in Ω^{PD} with $\Delta x^{PD} = 3 \cdot 10^{-3}\mathrm{mm}$ as well as a PD only model with $\Delta x^{PD} = 2.5 \cdot 10^{-3}\mathrm{mm}$. The PD horizon was kept the same and equal to $\delta = 4\Delta x^{PD}$ in all models. The results are in very close agreement for all cases. The PD only model

estimates the peak force to be $20.44 \cdot 10^{-3}\mathrm{N}$ at $\delta_y = 0.4875 \cdot 10^{-3}\mathrm{mm}$ (i.e. two load increments later) while for the XFEM-PD model with the coarser grid the peak force is $20.89 \cdot 10^{-3}\mathrm{N}$ at $\delta_y = 0.4650 \cdot 10^{-3}\mathrm{mm}$.

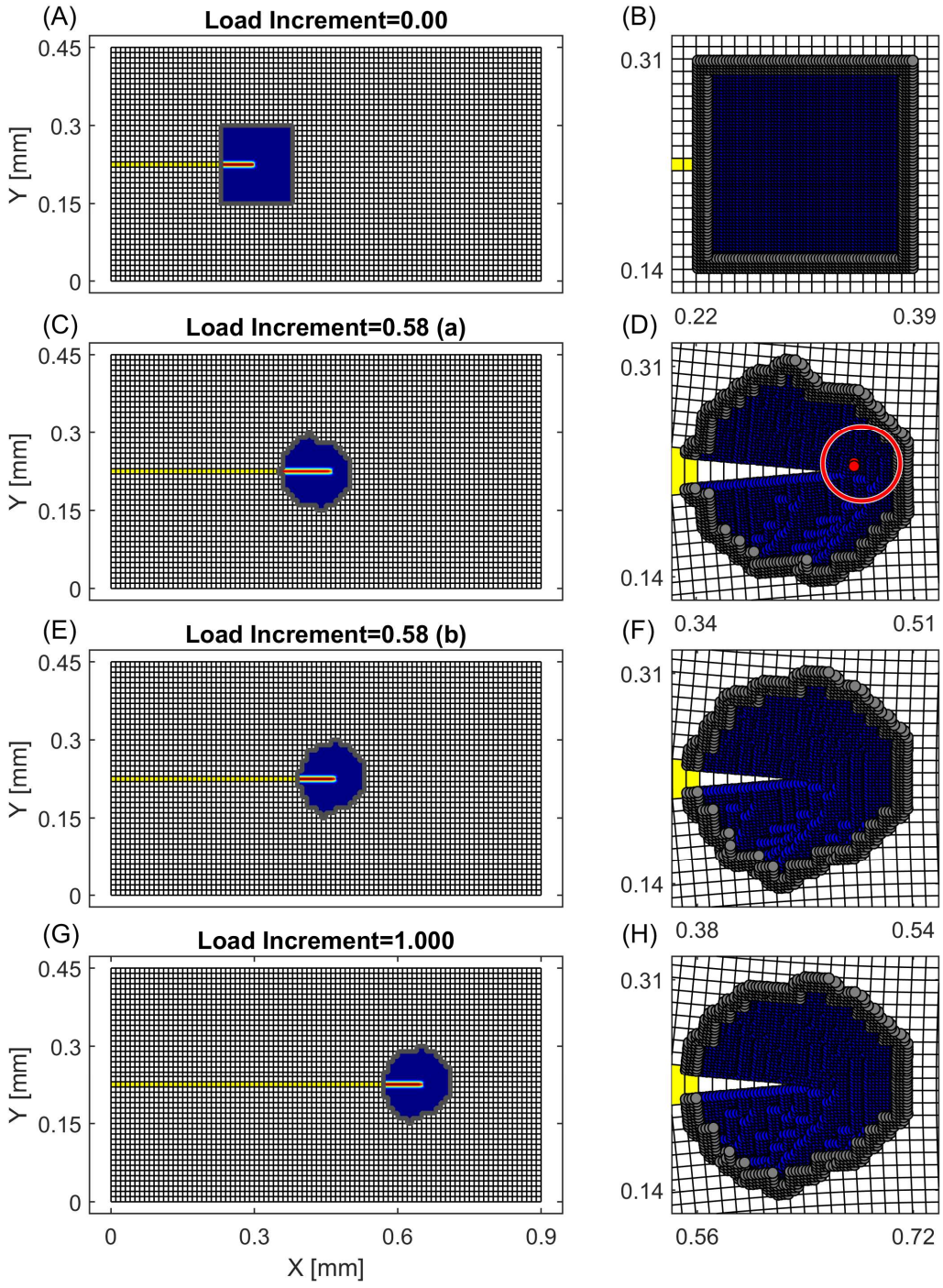

Figure 6.24: (Left column): Adaptive relocation of Ω^{PD} and tip tracking during crack propagation at different load increments. For clarity, the local damage index is plotted in Ω^{PD} to indicate the crack

location. (Right column): Close up at the coupling interface indicating the PD particles and the FEs. The displacements have been magnified by a factor of 50.

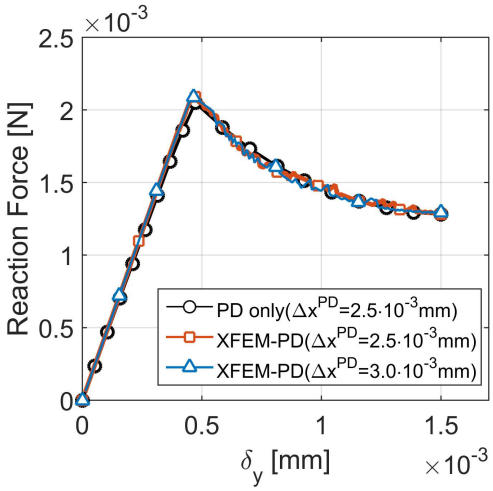

Figure 6.25: Comparison of the reaction force between the proposed method and a PD only solution.

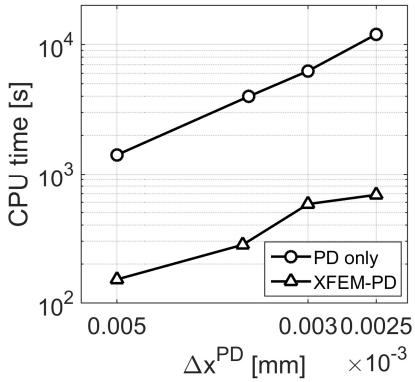

Figure 6.26: Comparison of the CPU time required to solve the resulting system of equations when the PD only and the proposed approaches are used, for different Δx^{PD}.

The relative difference of the peak reaction force predicted by the proposed method and a PD only model is approximately 2.25%, when the same grid spacing is used. The PD only model however led to a total of $131{,}040$ dofs for the discretization of the problem domain. This reduction of the dofs leads to significant computational savings, as illustrated in Figure 6.26. The effective speed-up of the solution varies between 9.3 to 17.4 times faster, depending on the discretization selected. Thus, despite having to manage the relocation of Ω^{PD} and to repeat load increments when the expansion trigger is tripped, the proposed method can accelerate crack propagation simulations. Compared to the example presented in section 6.2, the computational efficiency of the proposed method is pronounced as the reduction of the

total dofs is higher and the Newton-Raphson solver had to be invoked multiple times due to the incremental application of the load.

6.4.2 *Example 2: Dynamic Example of a Centrally Cracked Plate*

Often, it is required to address problems that contain multiple crack tips, either due to the existence of multiple edge breaking cracks (see e.g. Figure 6.16) or because the crack is embedded into the body. To this end, a plate containing a central crack is considered here, to illustrate the ability of the proposed methodology to monitor and follow the evolution of multiple tips. The same example has been presented in [7] where a PD only model was implemented for the simulation of the crack propagation. For comparison, the example is recreated here using the XFEM-PD model with the adaptive relocation algorithm.

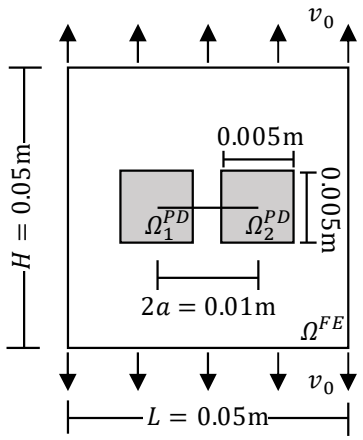

Figure 6.27: Schematic illustration of the plate with a central crack.

The inertia forces are not neglected in this example and the plate behaves elastically with Young's modulus $E = 192\ \text{GPa}$, Poisson's ratio $v = 1/3$ and density $\rho = 7850\ \text{kg/m}^3$. Following [7], the critical bond elongation is set to $s_0 = 0.04472$ and the plate thickness to $h = 1 \cdot 10^{-4}\text{m}$. The total duration of the analysis is $t_{tot} = 16.6 \cdot 10^{-6}\text{s}$ with $\Delta t = 1 \cdot 10^{-8}\text{s}$ and a prescribed velocity $v_0 = 20\ \text{m/s}$ is applied at the top and bottom faces of the plate. The discretization length is set to $\Delta x^{PD} = \Delta y^{PD} = 1.02 \cdot 10^{-4}\text{m}$ and $\Delta x^{FE} = \Delta y^{FE} = 1 \cdot 10^{-3}\text{m}$ for Ω^{PD} and Ω^{FE}, respectively. For consistency and to ensure comparability of the results obtained using the proposed approach with those reported in [7], $c(\boldsymbol{\xi})$ is assumed uniform (Eq. (3.11)) and the PD horizon is set to $\delta = 3\Delta x^{PD}$.

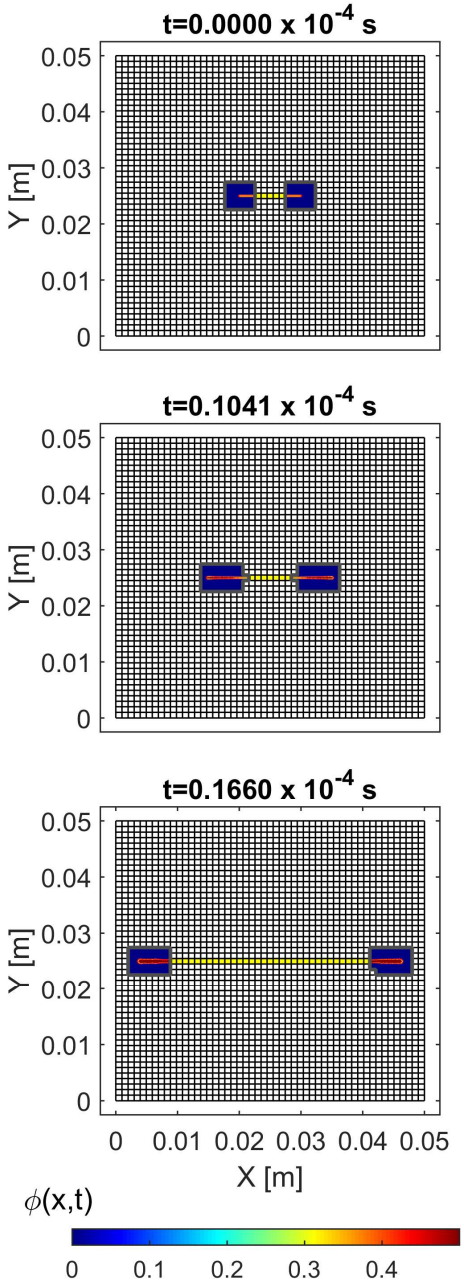

Figure 6.28: Crack location at time instants $t = 0\text{s},\ 0.1041 \cdot 10^{-4}\text{s}$ and $0.1660 \cdot 10^{-4}\text{s}$. The local damage index $\phi(\boldsymbol{x}, t)$ is plotted to indicate the location of Ω^{PD} and the crack.

The tips at both ends of the crack are monitored and the PD domain relocates according to their propagation. It is of interest to ensure that only the tips are covered within Ω^{PD} and not the whole crack. Multiple PD patches, or subdomains Ω_i^{PD}, can be defined depending on the number of tips. Each subdomain Ω_i^{PD} can expand and contract independently to each other. Here, the patches are square with side 0.005m, centered at the location of each crack tip and

Ω^{PD} is defined as $\Omega^{PD} = \Omega_1^{PD} \cup \Omega_2^{PD}$. The geometry and loading conditions are illustrated schematically in Figure 6.27. Although in this example the number of patches and their initial location were pre-defined and specifically constructed, these patches can emanate naturally through the expansion/contraction process in more complex problems. This property is presented in the following section where the dynamic crack branching problem is considered.

The central difference scheme is used for the time marching during the analysis. Contrary to the static problem, the expansion and the contraction triggers need not be evaluated at each time increment due to the small time step of the explicit solver. A sampling rate of 1/20 steps is used to monitor the crack location and check if expansion is required. Additionally, both the expansion and the contraction steps are executed after the current time step is finished.

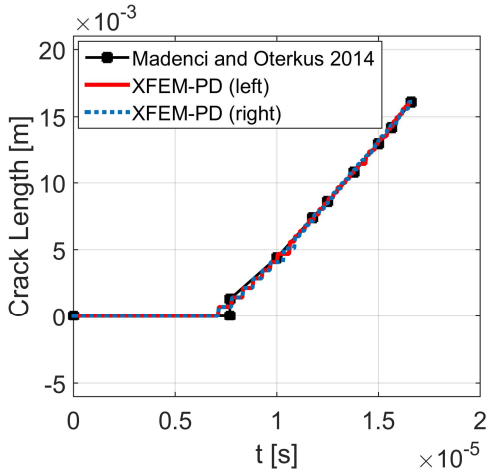

Figure 6.29: Comparison of the crack propagation with the results presented by Madenci and Oterkus in [7].

The velocity applied on the top and bottom faces of the plate stretch the plate in the vertical direction. The cark evolution is presented in Figure 6.28 at three different time instants. Each of the PD subdomains Ω_1^{PD} and Ω_2^{PD} follows the propagation of the tip they contain and adaptively relocate when it reaches close to the coupling interface (indicated with a grey line in the same figure). The location of each tip is monitored using the tracking algorithm discussed earlier and the crack length versus time is plotted in Figure 6.29 for both tips. For the material and loading parameters selected in this problem, crack propagation is expected in the horizontal direction in a self-similar manner. The proposed methodology was able to capture the self-similar growth of the crack while relocating Ω^{PD} during the analysis. The results are also in very good agreement with those reported by Madenci and Oterkus in [7]. A difference between the results is observed at $t = 0.77 \cdot 10^{-5}$s. In the results reported in [7] the crack length suddenly increases while in the present study this effect was not captured.

This difference probably originates due to differences in the way the tip location is monitored, and the sampling rate of the measurements taken. The proposed method is thus capable of monitoring multiple tips and adaptively relocate each individual subdomain that Ω^{PD} contains.

The results plotted in Figure 6.5 and Figure 6.6 indicate that the coupling approach can lead to reflections of small amplitude and sufficiently accurate energy transferring between the two models. In the example addressed here, apart from the external loading, pulses are generated at each tip during crack growth. Since Ω^{PD} is enclosed in Ω^{FE} the reflection from these pulses become trapped. This situation can lead to the energy entrapment that was discussed in section 5.5.3.

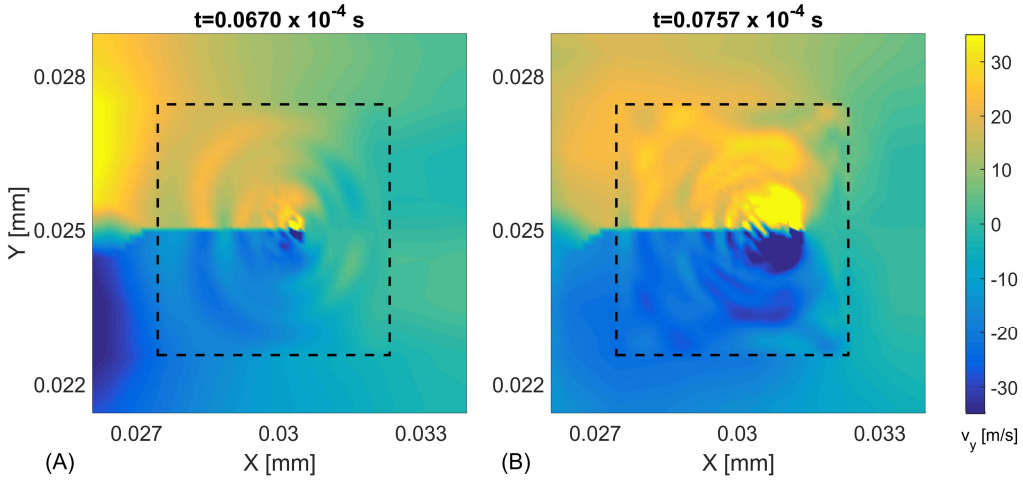

Figure 6.30: Plots of v_y near the right crack tip during the initial stages of the crack growth. The coupling interface is indicated with a black dashed line.

Although it is not easy to isolate these reflections, the vertical component of the velocity v_y near the tip at the right side of the plate is plotted in Figure 6.30. As the crack starts to grow pulses are generated and propagate towards the coupling interface (see Figure 6.30 (A)). At a later time instant, these pulses cross the interface and reflections appear inside Ω^{PD}. These reflections can be seen near the top and bottom faces in Figure 6.30 (B). The sudden and rapid nature of fracture excites a broad spectrum of frequencies. In Ω^{PD} the discretization is one order of magnitude smaller than Ω^{FE}. A possible explanation for these reflections is that part of the frequency spectrum that was excited by the crack extension is above the cut-off frequency of the discretized model in Ω^{FE}. As these frequencies cannot enter Ω^{FE} they become trapped in Ω^{PD}.

The results illustrated in Figure 6.29, indicate that these reflections did not affect significantly the propagation of each crack tip. Inevitably however, during the contraction step a region of

Ω^{PD} that contains reflections is switched to Ω^{FE}. Because of the interpolation and the least squares fitting that take place, these reflections are *smoothed* during the transition. It is of interest to evaluate whether significant energy is lost during the simulation because of this approximation. During crack growth, there is energy loss due to the removal of the broken bonds from the simulation. Additionally, using the current problem set-up, energy is constantly provided into the system. This can make evaluation of the energy loss due to the switch from PD to FEs difficult. Thus, we modify the problem and instead of a constant velocity, a distributed load f_y is applied at the top and bottom faces of the plate with:

$$f_y = \begin{cases} f_{max} & t \leq 6 \cdot 10^{-4}\ \mathrm{s} \\ 0 & \text{otherwise} \end{cases}, \tag{6.29}$$

where, $f_{max} = 8\ \mathrm{kN/m}$. All other parameters in the analysis remain the same as before apart from the total duration of the simulation that is increased to $t_{tot} = 20 \cdot 10^{-6}\mathrm{s}$.

Using the modified loading from Eq. (6.29), crack propagation is again self-similar but crack growth is arrested after each side of the crack has extended by $6.93 \cdot 10^{-3}\mathrm{m}$. To evaluate the influence of the expansion/contraction process the analysis is repeated two times: **i**) the first time the proposed methodology is implemented with the new loading. The dimensions and the location of Ω^{PD} are the same as illustrated in Figure 6.27. **ii**) The second time, the dimensions of Ω^{PD} are selected as such that it contains both the initial and the final crack location. The height of Ω^{PD} is kept the same but the length is extended to $0.01\ \mathrm{m}$ on each side. As such, in the second case the extension/contraction steps are not required. The initial and final configurations for each case are illustrated in Figure 6.31. By comparing the total energy in each case, it is attempted to obtain an indication of the induced error because of the smoothing of the reflections during the contraction step.

The total energy in each case is plotted in Figure 6.32. Based on the total energy in the system three distinct areas can be observed. The first is the initial stage where energy is provided into the system. At approximately $t = 0.6 \cdot 10^{-5}\mathrm{s}$, crack propagation is observed, and the total energy of the system reduces. Crack arrest takes place at approximately $t = 1.34 \cdot 10^{-5}\mathrm{s}$ and the total energy remains constant for the remaining simulation. The two cases capture the same behaviour and the computed total energy is in close agreement. Comparing the two curves the maximum value of the absolute relative error is $4.1 \cdot 10^{-3}$. As such, the expansion/contraction process does not lead to significant variations in the energy of the system despite the reflections being smoothed during the contraction step.

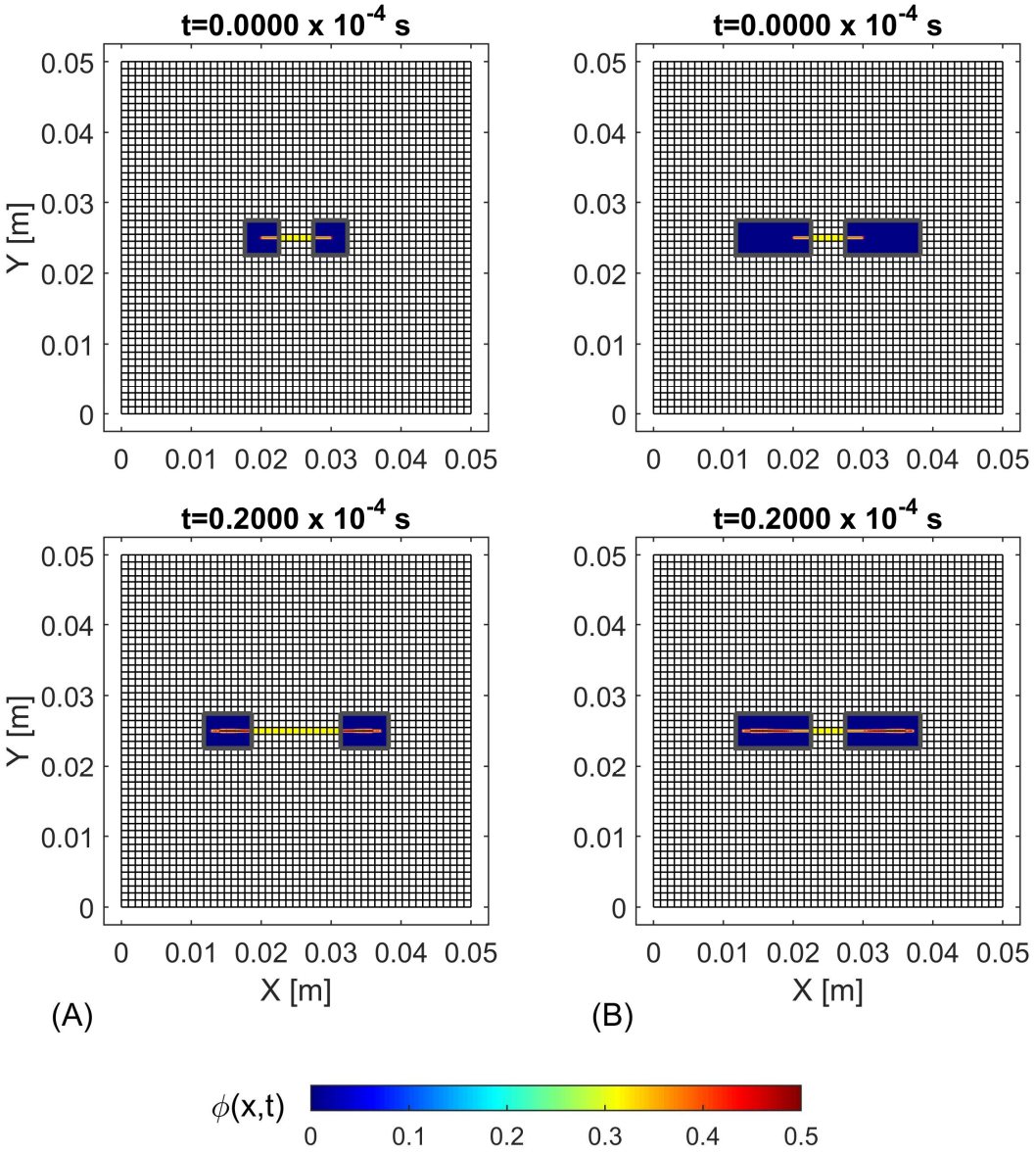

Figure 6.31: Initial and final configuration when (A): Ω^{PD} is initially small and the expansion/contractions steps are executed for the relocations and (B): Ω^{PD} is constructed as such that contain both the initial and the final location of the crack.

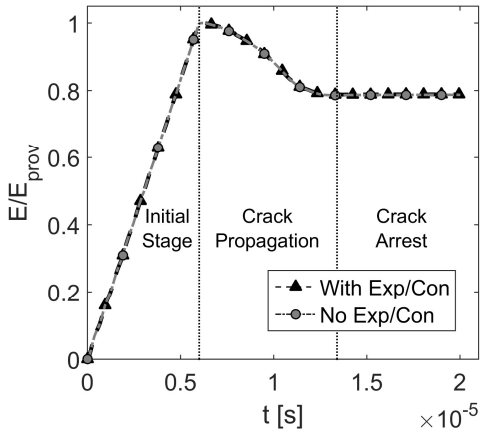

Figure 6.32: Comparison of the total energy computed when i) the proposed method with the expansion/contraction steps is used and ii) when Ω^{PD} is specifically constructed to include both the initial and the final location of the crack.

6.4.3 *Example 3: Dynamic Crack Branching*

Although the previous two examples where useful to highlight key advantages of the proposed methodology, they referred to simple mode I cases where the crack propagates in a straight line. As a final example, the case of dynamic crack branching is included. Many researchers have simulated numerically this problem using a variety of tools to gain understanding on the fundamental mechanisms behind the branching phenomenon (see e.g. [91,109,164,236]). Specifically, in the contributions by Ha and Bobaru [86] and Bobaru and Zhang [30], the application of the PD theory for crack branching applications is discussed in detail. Here the dynamic crack branching problem is used to illustrate the ability of the XFEM-PD model to adaptively relocate and follow the damage evolution when complex crack patterns emerge. It is also used to illustrate the ability of Ω^{PD} to split into different subdomains, each following the propagation of a different crack tip, through the implementation of the expansion/contraction steps.

Consider a rectangular plate with an edge-breaking pre-existing crack. The plate is made of soda-lime glass and it is assumed to behave elastically with Young's modulus $E = 72\ \mathrm{GPa}$, Poisson's ratio $\nu = 1/3$, density $\rho = 2440\ \mathrm{kg/m^3}$ and energy release rate $G_C = 135\ \mathrm{N/mm}$. It is also assumed that plane stress conditions apply. The initial length of the crack is $a = 0.05\ \mathrm{m}$ while the length and the height of the plate are $L = 0.1\ \mathrm{m}$ and $H = 0.04\ \mathrm{m}$, respectively. The geometry and loading conditions of the problem are illustrated schematically in Figure 6.33.

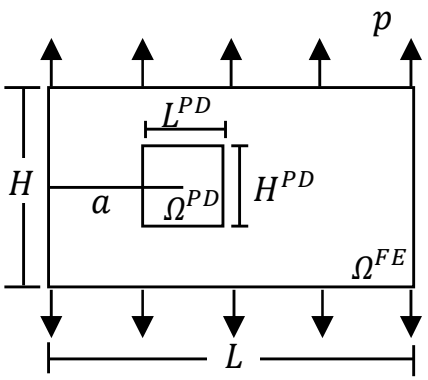

Figure 6.33: Schematic illustration of the problem set-up for the dynamic branching example.

The example presented here is taken from [86] where m and δ convergence studies were conducted. Based on the numerical results in [86], it was observed that if a pressure $p = 14\ \mathrm{MPa}$ is applied at the top and bottom faces of the plate, the crack will propagate initially on a horizontal line and then branch into two cracks. The final crack pattern will change depending on the value of the load applied.

The discretization length of Ω^{FE} and Ω^{PD} is set to $\Delta x^{FE} = \Delta y^{FE} = 7.5 \cdot 10^{-4}\mathrm{m}$ and $\Delta x^{PD} = \Delta y^{PD} = 1.25 \cdot 10^{-4}\ \mathrm{m}$ and the PD horizon is defined as $\delta = 4\Delta x^{PD}$. The discretization used in Ω^{PD} is the finer case that was presented during the converge study in [86]. The total duration of the simulation is $t_{total} = 4 \cdot 10^{-5}\mathrm{s}$ with time step equal to $\Delta t = 2.5 \cdot 10^{-8}\mathrm{s}$. The bond constant is assumed uniform and Eqs. (3.11) and (3.18) are used for the computation of $c(\boldsymbol{\xi})$ and s_0, respectively. Similar to the previous examples, Ω^{PD} is constructed initially as a square with $L^{PD} = H^{PD} = 0.01\mathrm{m}$, centered at the location of the tip. In total $30{,}204$ dofs are used for the discretization of the problem, $15{,}488$ for Ω^{PD} and $14{,}716$ for Ω^{FE} ($14{,}472$ standard and 244 enriched dofs). For comparison, if a PD only approach was adopted for the whole problem a total of $515{,}200$ dofs would be required. Because the crack pattern is more complex in this example, the contraction step is executed when three expansion steps have been completed. This allows Ω^{PD} to first follow the propagation of the crack and adapt to the complex geometry near the branching area and then it is contracted to reduce the total number of dofs.

The local damage index $\phi(\boldsymbol{x}, t)$ is plotted in Figure 6.34 at $t = 0.1950 \cdot 10^{-4}\mathrm{s}$. Although $\phi(\boldsymbol{x}, t)$ is not defined in the classical elasticity, a zero value is used in Ω^{FE} to indicate the undamaged area. A white and a grey solid line is used to indicate the current and the initial location of $\partial\Omega_2$ and a green line is used to indicate the location of the crack in Ω^{FE}. During

the initial steps, the crack has propagated to the right following a straight path. Prior to the branching, the damage area near the crack tip becomes wider, as illustrated in Figure 6.34.

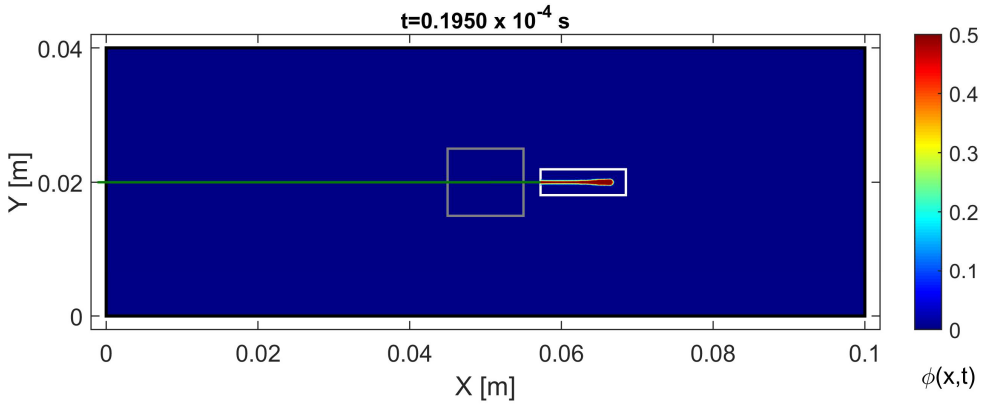

Figure 6.34: Surface plot of the local damage index illustrating the initial propagation of the crack.

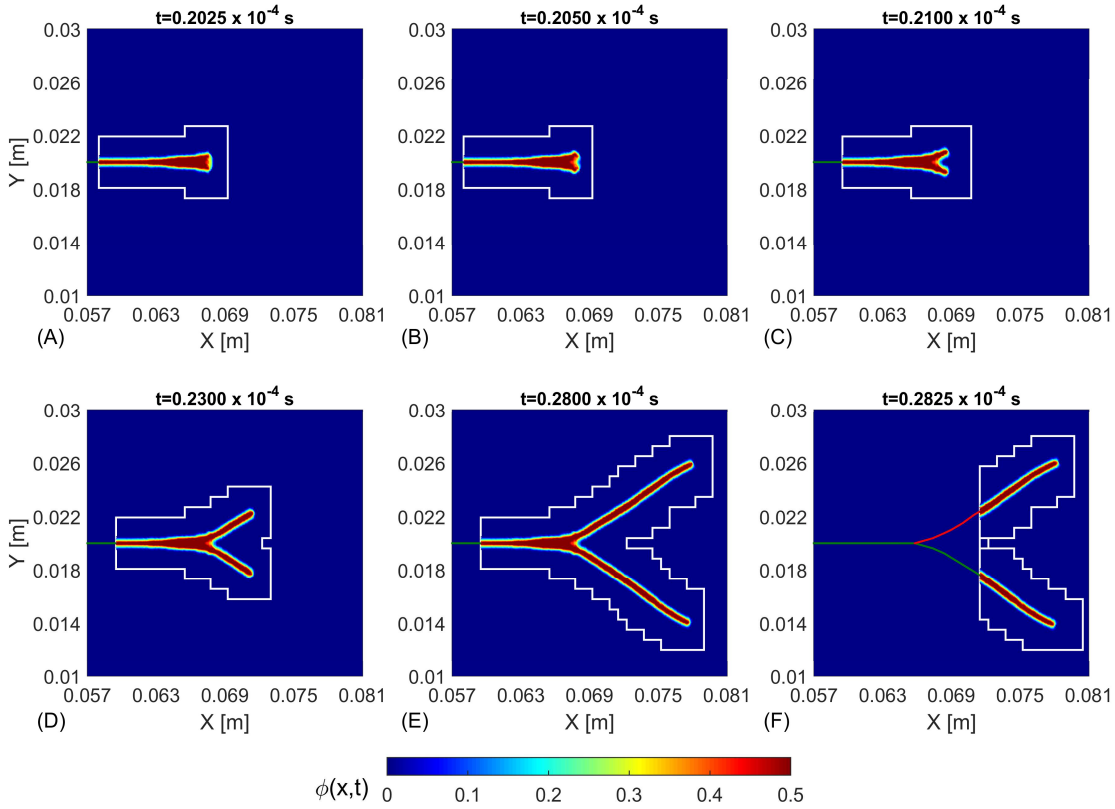

Figure 6.35: Adaptive relocation and splitting of Ω^{PD} during branching.

The onset of branching and the adaptive relocation of Ω^{PD} that follows the complex pattern and eventually splits into two subdomains is illustrated in Figure 6.35. It is difficult to define the exact time and location that crack branching takes place. Based on the damage plots in Figure 6.35 (A) and (B) an estimation between $t = 20.00 \sim 20.50$ μs and $x = 6.7 \sim 6.73$ μm

can be made. These values are in close agreement with the results reported in [86] where it is reported that crack branching takes place between $t = 20.50 \sim 21.50\ \mu s$ and is located approximately at $x = 6.80\ \mu m$. As discussed in [86], dynamic crack branching is affected by the reflections of the stress waves from the geometrical boundaries.

Creating automatically specific patches, that conform to the geometry of the branching crack can be challenging. By applying the expansion step, Ω^{PD} can change in size and shape to follow the evolution of the damage. This can be seen in Figure 6.35 (A) – (E). Since no information regarding the number and location of the cracks is required, the expansion step can capture complex patterns. A restriction was applied on the contraction step to allow for a smooth transition from PD to FE near the branching site. When branching is identified, the contraction step can only be executed when the new interface will be located away from that location (see Figure 6.35 (F)). From Figure 6.35 (A) – (F) it can be also seen how the initial Ω^{PD} is split into two subdomains, each one following a crack tip. The splitting of Ω^{PD} is better illustrated in Figure 6.36 where the final configuration is plotted. Additionally, the deformed plate is plotted in Figure 6.37, where the displacements have been magnified by a factor of 20. The path each branch followed is indicated with a green and red solid line.

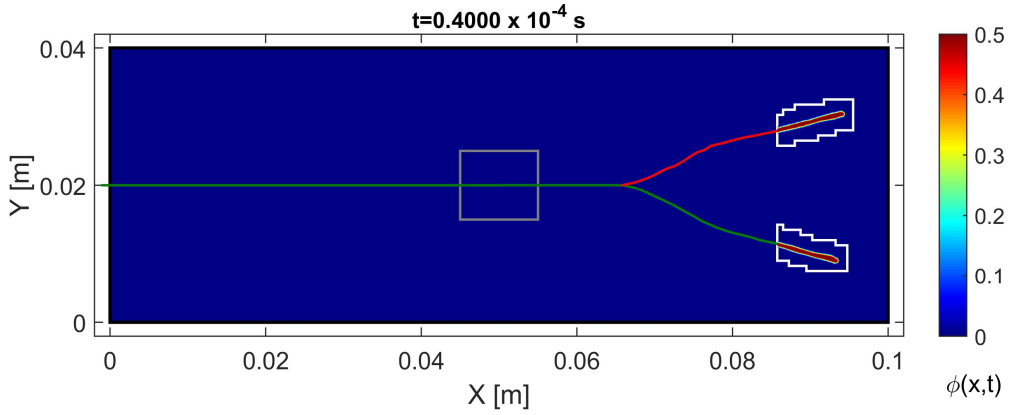

Figure 6.36: Final crack path and location of Ω^{PD}.

The final crack path that was obtained using the proposed methodology is compared with the path reported by Ha and Bobaru [86] in Figure 6.38. Because the path from [86] is inferred from a figure, to improve the fidelity of the comparison, the simulation is also repeated here using a PD only model. The discretization parameters of the PD only model are the same as those used for Ω^{PD} in the XFEM-PD model. It is noted that solid green and red lines are used to indicate the main and the second branch of the crack, respectively. The predicted crack paths are in close agreement for all cases considered. It is possible to capture the location

where the branching occurs as well as the same change of propagation angle following the branching event.

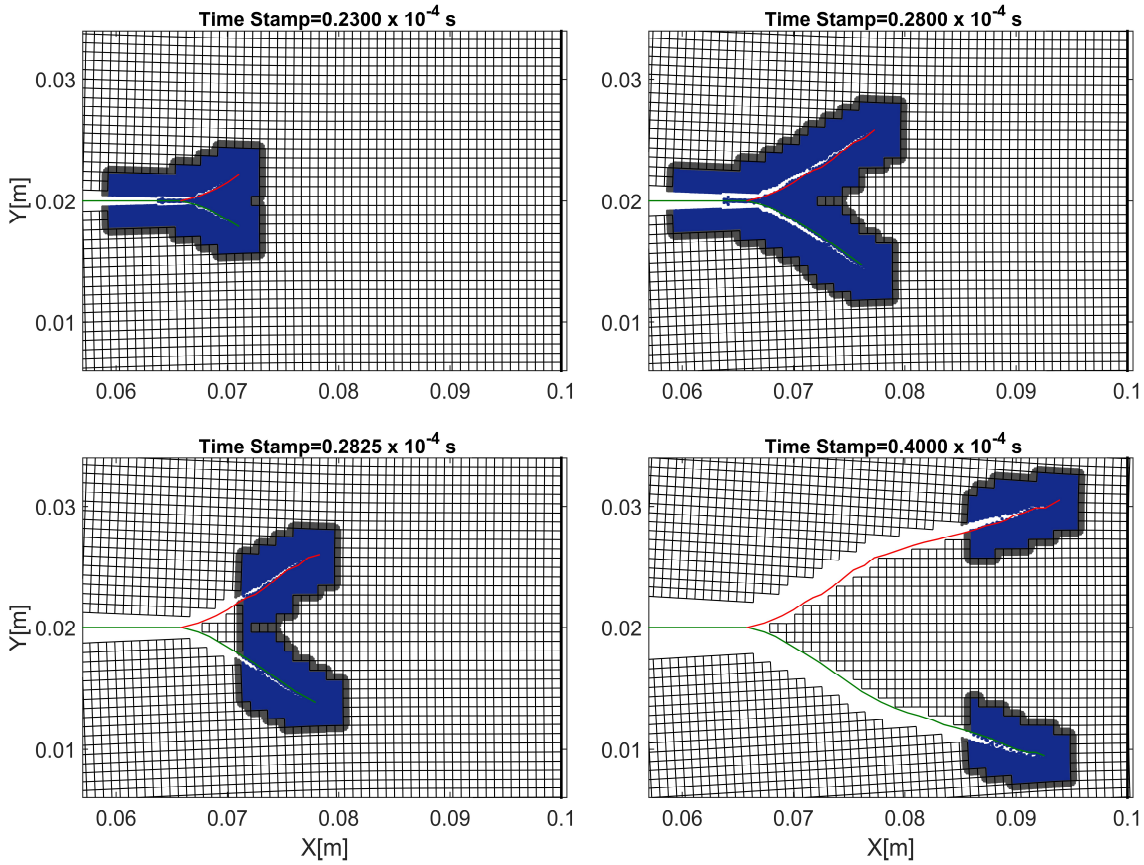

Figure 6.37: Illustration of the deformed plate at different time instants. Displacements have been magnified by a factor of 20.

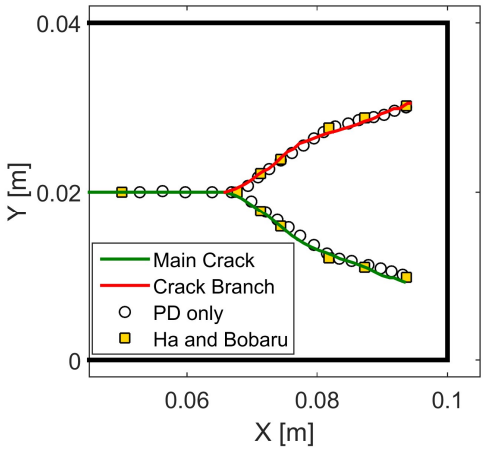

Figure 6.38: Comparison of the final crack path as predicted using the proposed method, a PD only model and the results presented in [86].

The maximum theoretically attainable crack propagation is speed is the Rayleigh wave speed c_R. Numerous experimental observations suggest that the propagation speed is limited in the region of $0.4c_R \sim 0.7c_R$ [159,237]. When the propagation speed reaches this value, branching typically occurs. The crack propagation speed computed using the proposed method is plotted in Figure 6.39. In the same figure the propagation speed for the same discretization parameters from [86] is included. In soda lime glass, terminal velocities between $1460{\sim}1600\ \mathrm{m/s}$ have been reported by various experimental investigations [238]. For consistency, the max propagation speed of $v_c = 1580\ \mathrm{m/s}$ is indicated in Figure 6.39, as this value was used in [86]. The results from the proposed method follow the same trend as those reported in the literature. The propagation speed approaches v_c prior to crack branching at approximately $t = 1.92 \cdot 10^{-5}\mathrm{s}$, followed by a reduction in the propagation speed. Additionally, the same fluctuations in speed are observed comparatively to [86]. As discussed in [86] and [30], these fluctuations can be correlated to the concertation or dispersion of the stress waves that reflect from the boundaries. It evident that although the trend is followed between the two curves, the curve of the present model is shifted slightly to the left. This is also collaborated by the fact that in our simulations the branching event took place earlier. Small differences in the results were expected because when the proposed method is used, the loading and the geometrical boundaries are defined on Ω^{FE}. Furthermore, use of classical elasticity to model the bulk of the material induces differences in the wave propagation characteristics. Nevertheless, the when the XFEM-PD model is used with the adaptive relocation algorithm to recreate the problem, the results are comparable with those obtained using a PD only solution.

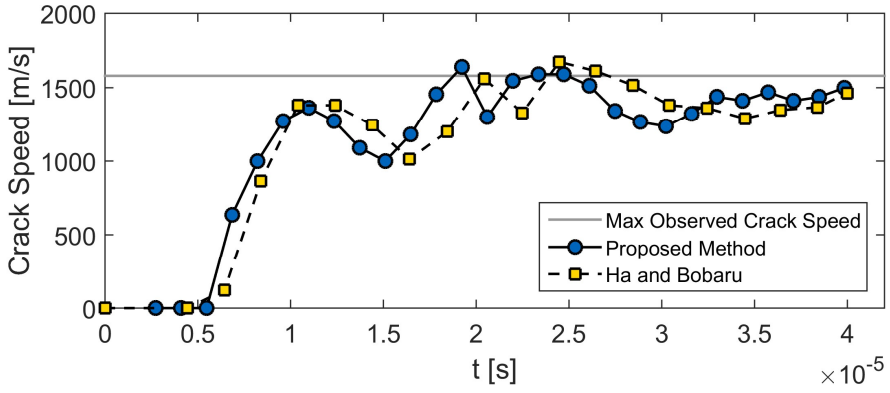

Figure 6.39: Comparison of the crack propagation speed observed when the proposed method is implemented compared to Ha and Bobaru [86]. The maximum crack speed that was observed during experimental studies is indicated with a grey line.

7 Conclusions and Future Work

7.1 Remarks

Focus of the present study is the combination of the FE method with the recently developed PD theory to simulate fracture. First, the two models are implemented sequentially, on different fields, to predict the nucleation and the evolution of cracks in ceramic materials under thermal stresses. The FE method is used to approximate the temperature field and subsequently, PD is used to simulate the thermal cracking of alumina (Al_2O_3) specimens. The advantage of this set-up is that the nucleation and the propagation of multiple cracks is captured from the PD model while the well-established FE method is used for the efficient solution of a nonlinear heat transfer problem. The results from the cold shock analyses illustrate that this uncoupled methodology is capable of producing comparable accuracy to similar numerical investigations and is able to reproduce the experimental observations [182]. Furthermore, the importance of considering the temperature dependency of the thermal and mechanical properties and the effects associated with radiative heat transfer, is demonstrated. In this case, the predicted crack lengths indicate a better correlation to the experimental measurements, particular for the longer crack-length classes. When hot shock conditions are used the model predicted (as expected) cracking of the material originating from its interior. The incorporation of the temperature dependency of the material properties leads to the manifestation of additional damage mechanisms at the surface of the specimen. These mechanisms are in accordance with reports of spalling due to the development of high compressive stresses [175], [195]. Finally the onset of a crack at the corner of the specimen could be related to the appearance of high shear stresses at the same location, as reported in [168] where a FE approach is adopted to simulate the thermomechanical problem.

Despite using an uncoupled thermomechanical approach for the thermal cracking problem, the results, albeit accurate, highlight the computational restrictions entailed with the implementation of the PD model. A concurrent combination of the PD theory with classical elasticity and the coupling of PD grids with FE meshes could alleviate this problem. In total three approaches are formulated to study the spurious reflections that appear during dynamic simulations when such couplings are considered. Although these reflections could be important, e.g. when energy is released during crack propagation, and cannot be avoided completely, they can be minimized through careful set up and calibration of the coupling procedure and model parameters. The first coupling approach presented is the simplest one and used mainly for comparison purposes. Its implementation is not recommended as it requires conforming meshes, posing difficulties for 2D and 3D applications [239]. The second

and third approach can be extended to problems with higher dimensions more efficiently [5,117,118,240], as both of them allow the independent discretization of Ω^{PD} and Ω^{FE}. The coupling approaches are compared through numerical tests in a 1D bar for pulses with different shapes and frequency contents. Initially, the energy drift is computed in the time domain for incident pulses with modular and Gaussian shape.

The numerical tests are then continued in the frequency domain where the discrete PD model is coupled with continuum models. This configuration allowed for a systematic accuracy assessment of each coupling approach by comparing the transmission and reflection coefficients in an infinite bar. Closed form solutions are derived for Coupling Cases 1, 2 and 3 with a linear blending function. For Coupling Case 3 with a cubic blending function, the solution in Ω^{coupl} is approximated numerically. The discretization size and the value of the PD horizon are of outmost importance as they control the characteristics of the dispersion curve and the cut-off frequency of the numerical solution. The results indicate that the third coupling case with a cubic blending function leads to the most accurate energy transmission. Comparable accuracy can be achieved when the second coupling case is used. This approach is simpler to formulate, less demanding (computationally) and does not entail ambiguities with regards to the optimal overlapping length and the selection of blending functions. Compared to the Coupling Case 3, the accuracy of the second coupling case is more sensitive to the PD skin effect and appropriate corrections must be employed.

The second coupling case is also extended to 2D problems to illustrate the significance of considering the cut-off frequencies of both the finer (PD) and the coarser (FE) models. A radially loaded hole in an infinite domain is used as an example. The introduction of a PML around the plate allowed to truncate the computational domain and remove the reflections from the boundary conditions. This example is used to illustrate that in cases where Ω^{PD} is enclosed by Ω^{FE}, and the pulse source is located within Ω^{PD} (e.g. dynamic crack propagation), energy entrapment can be observed if the coupling between the two models is not accurate. In the example presented, if the discretization in Ω^{FE} is too coarse, approximately 16% of the total energy remains trapped in Ω^{PD}. This is attributed to the cut-off frequency of the FE model being below the frequency content of the input pulse. During dynamic crack propagation, the sudden evolution of a crack will generate pulses that excite a broader spectrum of frequencies in Ω^{PD}.

Finally, Coupling Case 2 is modified to allow the introduction of the XFEM enrichment and avoid the requirement of computing the intersection of the coupling interface with each bond that connects a ghost with a normal particle. With this modification, instead of applying the

bond forces on the coupling interface, they are applied at the particle location and they are distributed to the nodes through FE shape functions. This notion is similar to the VL coupling presented in [121]. The discretization of the coupled models remains independent while the operations required to achieve the coupling are reduced. Additionally, the original formulation of the PD theory is used instead of the linearized. Simple static and dynamic examples are solved numerically using the coupled methodology and the results are compared to those obtained from elasticity. Accurate energy transmission is achieved between the models while the amplitude of the reflections is kept small.

For fracture problems, the introduction of the XFEM enrichment allows the appearance of discontinuous displacement fields within Ω^{FE} and limits the use of the PD model only near the vicinity of the crack tip. Heaviside functions are used to enrich the basis functions of the finite elements that are cut by the crack body. Crack tip enrichment, based on solutions from linear elastic fracture mechanics that is typically employed in XFEM to capture the stress/strain singularity, is avoided by switching to a nonlocal particle approach. Following this approach, Ω^{PD} is also employed away from boundary conditions and geometrical boundaries that can be cumbersome for the PD theory. A static example with two edge breaking cracks is used to evaluate the effectiveness of the coupled model in the presence of strong discontinuities. A convergence study based on the J contour integral is preformed for the comparison of the XFEM – PD model and the PD only model. The results indicate that the XFEM – PD model can achieve the same level of accuracy compared to the PD only model, while reducing significantly the total number of dofs.

Lastly, the ability of the proposed XFEM – PD model to adaptively relocate Ω^{PD} and Ω^{FE}, following the damage evolution process, is presented. This is carried out through the implementation of expansion and contraction steps that constitute a switch from FE to PD and from PD to FE, respectively. The introduction of the XFEM enrichment allows the FE nodal positions to be independent with regards to the location of the fracture. Re-meshing during propagation or the construction of specific meshes that conform the crack geometry is avoided. A simple method to track the location of the crack tip using the Laplacian of the local damage index $\phi(\boldsymbol{x}^{PD}, t)$, is also presented. Using this method, it is possible to monitor the propagation of multiple cracks as well as capture the crack branching location. Because Ω^{PD} moves through this expansion/contraction process, leaving behind it a trail of Heaviside functions, the algorithm is termed the "*Peridynamic snail*".

The adaptive relocation process is successfully applied in many crack propagation problems, including dynamic crack branching. In all cases presented, the results are compared with

similar solutions obtained using PD only models and results from the available literature. The ability of PD to naturally accommodate discontinuous fields and simulate complex crack patterns is exploited while switching to classical elasticity at locations away from the area of interest. Compared to a PD only approach, the total number of dofs is reduced significantly leading to a more tractable system, both in terms of CPU time needed and required memory resources. The a-priori determination of the computational speed-up between the proposed approach and a full PD model is not straightforward as it can be case specific. Nevertheless, the results of this study highlight that a coupled XFEM-PD model with the ability to relocate during propagation can potentially lead to significant computational savings.

The key advantages and observations behind the proposed approach are:

i) A PD patch is employed around the crack tip. The PD patch covers sufficiently the vicinity of the crack tip but remains always as small as possible to avoid excessive computational cost.

ii) Since the crack body away from the tip remains in the domain where classical continuum elasticity is used, treatment of the discontinuous displacement field is required. This is handled by adding the shifted Heaviside step function enrichment according to XFEM. Crack tip enrichments or incorporation of *a-priori* solutions to capture the stress state near the tip are not required since this part is handled by the PD model.

iii) The existence of crack tip(s) is allowed only in Ω^{PD}. If a crack propagates the PD patch will also follow the propagation and the crack is free to evolve anywhere in the problem domain regardless of the initial position of Ω^{PD}. The propagation length and direction are captured by the PD model and knowledge of the final crack path is not required.

iv) Limiting the area where the PD theory is applied can lead to significant improvement of the overall computational cost of the solution, both in terms of memory requirements and CPU time.

v) The expansion/contraction procedure allows to first capture the crack pattern and then relocate as necessary, with the ability of splitting in case the initial crack branches. Furthermore, in static problems where the final crack length is not known, the expansion step can be repeated as many times as necessary till the current step solution is accepted.

vi) Switching to a nonlocal model near the crack tip introduces an internal length scale to the simulation. The microstructure of the material can thus be incorporated in the model resulting to multiscale simulations.

7.2 Recommendations for Future Work

One study area, that could also be the extension of the present methodology, is the introduction of microstructure within the PD model. The reduction of the computational cost allows implementation of a much denser discretization grid. In [98] for example, fracture in a polycrystalline materials was simulated using the PD theory by defining crystals with orthotropic behaviour in the lattice and assigning a random orientation to each crystal. Such approach can be adopted within Ω^{PD}. This poses however the following challenge; what are the properties of the bulk material that is contained in Ω^{FE}? One possible approach would be to either create a FE mesh that is adequately fine and conforms to the geometry of each crystal or use XFEM to capture the crystal boundaries using enrichment functions. The other possibility would be to assume homogenized properties in Ω^{FE} to avoid the spatial resolution of each crystal. In this case however, the reflections at the interface must be re-evaluated as the coupling interface will also be an interface between dissimilar materials.

Such an extension is also interesting for the thermal cracking of ceramics, which is a topic with numerous industrial applications. Incorporation of a polycrystalline structure could be used to study the effect of grain size on the thermal resistance of alumina. Additionally, a fully coupled thermomechanical model could be used to repeat the hot shock case and study in more detail the appearance of damage at the surface of the specimen.

It is worthwhile to point out here some disadvantages of the proposed relocation method that can form the basis for future modifications and studies. The first one has to do with the tracking of the crack front in 3D configurations, which will now be a line and not a point. False front identification, due to inaccuracies of the herein proposed algorithm, could lead to improper relocation of Ω^{PD} and induce errors in the definition of the Heaviside functions, impairing significantly the accuracy of the results. In fact, the requirement to track the crack location is restrictive on its own. The ability of the PD theory to simulate fracture without requiring information on the exact crack location is one of its attractive and desirable properties.

Another disadvantage arises due to the algorithmic realization of the expansion and contraction steps that require the execution of multiple conditional and looping statements. The extension, scalability and efficiency of such algorithm to a highly parallelized platform for large scale simulations is not straightforward. For example, Mossaiby et. al. [241] demonstrate significant computational gains through the execution of PD algorithms using graphics processing units (GPUs). The performance of the methodology on such platforms needs to be studied. On the other hand, GPUs are usually limited in terms of available memory. Thus,

methodologies like the one presented here, capable of reducing significantly the total number of dofs, can be very appealing.

References

[1] A.R. Khoei, Extended finite element method: theory and applications, John Wiley & Sons, 2014.
[2] T.L. Anderson, Fracture mechanics: fundamentals and applications, CRC press, 2005.
[3] D. Broek, Elementary engineering fracture mechanics, Springer Science & Business Media, 2012.
[4] P.-A. Guidault, O. Allix, L. Champaney, C. Cornuault, A multiscale extended finite element method for crack propagation, Computer Methods in Applied Mechanics and Engineering. 197 (2008) 381–399.
[5] F. Bobaru, J.T. Foster, P.H. Geubelle, P.H. Geubelle, S.A. Silling, (first), Handbook of Peridynamic Modeling, (2016).
[6] S.A. Silling, Reformulation of elasticity theory for discontinuities and long-range forces, Journal of the Mechanics and Physics of Solids. 48 (2000) 175–209.
[7] E. Madenci, E. Oterkus, Peridynamic theory and its applications, Springer, 2014.
[8] A.A. Griffith, The phenomena of rupture and flow in solids, Philosophical Transactions of the Royal Society of London. Series A, Containing Papers of a Mathematical or Physical Character. 221 (1921) 163–198.
[9] G.R. Irwin, Onset of fast crack propagation in high strength steel and aluminum alloys, Sagamore Research Conference Proceedings. 2 (1956) 289–305.
[10] H. Westergaard, Bearing Pressures and Cracks, Journal of Applied Mechanics. 18 (1939).
[11] G.R. Irwin, Plastic Zone Near a Crack and Fracture Toughness., Sagamore Research Conference Proceedings. 4 (1961) 63–78.
[12] D.S. Dugdale, Yielding of steel sheets containing slits, Journal of the Mechanics and Physics of Solids. 8 (1960) 100–104.
[13] A. Wells, Unstable crack propagation in metals: cleavage and fast fracture, in: 1961.
[14] J.R. Rice, A path independent integral and the approximate analysis of strain concentration by notches and cracks, in: ASME, 1968.
[15] P.C. Paris, M.P. Gomez, W.E. Anderson, A rational analytic theory of fatigue, The Trend in Engineering. 13 (1961) 9–14.
[16] T. Rabczuk, Computational methods for fracture in brittle and quasi-brittle solids: state-of-the-art review and future perspectives, ISRN Applied Mathematics. 2013 (2013).
[17] R. Chandwani, M. Wiehahn, C. Timbrell, 3D Fracture mechanics in ANSYS, in: 2004.
[18] J. Fish, T. Belytschko, A first course in finite elements, John Wiley & Sons, 2007.
[19] J.T. Katsikadelis, Boundary elements: theory and applications, Elsevier, 2002.
[20] E. Oñate, Structural analysis with the finite element method. Linear statics: volume 2: beams, plates and shells, Springer Science & Business Media, 2013.
[21] R. Henshell, K. Shaw, Crack tip finite elements are unnecessary, International Journal for Numerical Methods in Engineering. 9 (1975) 495–507.
[22] B. Moran, C. Shih, A general treatment of crack tip contour integrals, International Journal of Fracture. 35 (1987) 295–310.
[23] G.I. Barenblatt, The formation of equilibrium cracks during brittle fracture. General ideas and hypotheses. Axially-symmetric cracks, Journal of Applied Mathematics and Mechanics. 23 (1959) 622–636.
[24] X.-P. Xu, A. Needleman, Numerical simulations of dynamic interfacial crack growth allowing for crack growth away from the bond line, International Journal of Fracture. 74 (1996) 253–275.

[25] G.T. Camacho, M. Ortiz, Computational modelling of impact damage in brittle materials, International Journal of Solids and Structures. 33 (1996) 2899–2938.
[26] R. de Borst, M.A. Gutiérrez, G.N. Wells, J.J. Remmers, H. Askes, Cohesive-zone models, higher-order continuum theories and reliability methods for computational failure analysis, International Journal for Numerical Methods in Engineering. 60 (2004) 289–315.
[27] N. Chandra, H. Li, C. Shet, H. Ghonem, Some issues in the application of cohesive zone models for metal–ceramic interfaces, International Journal of Solids and Structures. 39 (2002) 2827–2855.
[28] A. Agwai, I. Guven, E. Madenci, Predicting crack propagation with peridynamics: a comparative study, International Journal of Fracture. 171 (2011) 65–78.
[29] M. Zaccariotto, F. Luongo, U. Galvanetto, Examples of applications of the peridynamic theory to the solution of static equilibrium problems, The Aeronautical Journal. 119 (2015) 677–700.
[30] F. Bobaru, G. Zhang, Why do cracks branch? A peridynamic investigation of dynamic brittle fracture, International Journal of Fracture. 196 (2015) 59–98.
[31] T. Belytschko, T. Black, Elastic crack growth in finite elements with minimal remeshing, International Journal for Numerical Methods in Engineering. 45 (1999) 601–620.
[32] T. Belytschko, R. Gracie, G. Ventura, A review of extended/generalized finite element methods for material modeling, Modelling and Simulation in Materials Science and Engineering. 17 (2009) 043001.
[33] J. Dolbow, N. Moës, T. Belytschko, Modeling fracture in Mindlin–Reissner plates with the extended finite element method, International Journal of Solids and Structures. 37 (2000) 7161–7183.
[34] P.F. Liu, B.J. Zhang, J.Y. Zheng, Finite element analysis of plastic collapse and crack behavior of steel pressure vessels and piping using XFEM, Journal of Failure Analysis and Prevention. 12 (2012) 707–718.
[35] A. Yazid, N. Abdelkader, H. Abdelmadjid, A state-of-the-art review of the X-FEM for computational fracture mechanics, Applied Mathematical Modelling. 33 (2009) 4269–4282.
[36] T. Rabczuk, S. Bordas, G. Zi, On three-dimensional modelling of crack growth using partition of unity methods, Computers & Structures. 88 (2010) 1391–1411.
[37] J. Bellec, J. Dolbow, A note on enrichment functions for modelling crack nucleation, Communications in Numerical Methods in Engineering. 19 (2003) 921–932.
[38] H. Ren, X. Zhuang, C. Anitescu, T. Rabczuk, An explicit phase field method for brittle dynamic fracture, Computers & Structures. 217 (2019) 45–56.
[39] S. Zhou, T. Rabczuk, X. Zhuang, Phase field modeling of quasi-static and dynamic crack propagation: COMSOL implementation and case studies, Advances in Engineering Software. 122 (2018) 31–49.
[40] G.A. Francfort, J.-J. Marigo, Revisiting brittle fracture as an energy minimization problem, Journal of the Mechanics and Physics of Solids. 46 (1998) 1319–1342.
[41] M.A. Msekh, J.M. Sargado, M. Jamshidian, P.M. Areias, T. Rabczuk, Abaqus implementation of phase-field model for brittle fracture, Computational Materials Science. 96 (2015) 472–484.
[42] J.-Y. Wu, V.P. Nguyen, C.T. Nguyen, D. Sutula, S. Bordas, S. Sinaie, Phase field modeling of fracture, Advances in Applied Mechancis: Multi-Scale Theory and Computation. 52 (2018).
[43] G.-R. Liu, Meshfree methods: moving beyond the finite element method, Taylor & Francis, 2009.

[44] A. Shojaei, B. Boroomand, F. Mossaiby, A simple meshless method for challenging engineering problems, Engineering Computations. (2015).
[45] T.-P. Fries, H.G. Matthies, Classification and overview of meshfree methods, Department of Mathematics and Computer Science, Technical University of Braunschweig. (2003).
[46] T. Belytschko, Y.Y. Lu, L. Gu, Element-free Galerkin methods, International Journal for Numerical Methods in Engineering. 37 (1994) 229–256.
[47] E. Oñate, S. Idelsohn, O. Zienkiewicz, R. Taylor, A finite point method in computational mechanics. Applications to convective transport and fluid flow, International Journal for Numerical Methods in Engineering. 39 (1996) 3839–3866.
[48] J.J. Monaghan, An introduction to SPH, Comput. Phys. Comm. 48 (1988) 89–96.
[49] S.N. Atluri, T. Zhu, A new meshless local Petrov-Galerkin (MLPG) approach in computational mechanics, Computational Mechanics. 22 (1998) 117–127.
[50] W.K. Liu, C. Oberste-Brandenburg, Reproducing kernel and wavelet particle methods, in: Publ by ASME, 1993: pp. 39–55.
[51] T. Rabczuk, S.P. Xiao, M. Sauer, Coupling of mesh-free methods with finite elements: basic concepts and test results, Communications in Numerical Methods in Engineering. 22 (2006) 1031–1065.
[52] J. Fish, Multiscale methods: bridging the scales in science and engineering, Oxford University Press on Demand, 2010.
[53] P.A. Gourgiotis, A. Piccolroaz, Steady-state propagation of a mode II crack in couple stress elasticity, International Journal of Fracture. 188 (2014) 119–145.
[54] G.A. Maugin, Generalized continuum mechanics: what do we mean by that?, in: Mechanics of Generalized Continua, Springer, 2010: pp. 3–13.
[55] E. Cosserat, F. Cosserat, Théorie des corps déformables, Paris. 3 (1909) 17–29.
[56] A.R. Hadjesfandiari, G.F. Dargush, Evolution of generalized couple-stress continuum theories: a critical analysis, ArXiv Preprint ArXiv:1501.03112. (2014).
[57] R.A. Toupin, Elastic materials with couple-stresses, Archive for Rational Mechanics and Analysis. 11 (1962) 385–414.
[58] R.D. Mindlin, H.F. Tiersten, Effects of couple-stresses in linear elasticity, Archive for Rational Mechanics and Analysis. 11 (1962) 415–448.
[59] D.C. Lam, F. Yang, A. Chong, J. Wang, P. Tong, Experiments and theory in strain gradient elasticity, Journal of the Mechanics and Physics of Solids. 51 (2003) 1477–1508.
[60] R.D. Mindlin, Micro-structure in linear elasticity, Archive for Rational Mechanics and Analysis. 16 (1964) 51–78.
[61] R.D. Mindlin, Second gradient of strain and surface-tension in linear elasticity, International Journal of Solids and Structures. 1 (1965) 417–438.
[62] N. Fleck, G. Muller, M. Ashby, J. Hutchinson, Strain gradient plasticity: theory and experiment, Acta Metallurgica et Materialia. 42 (1994) 475–487.
[63] A.C. Eringen, Theory of micropolar elasticity, in: Microcontinuum Field Theories, Springer, 1999: pp. 101–248.
[64] H.-T. Thai, T.P. Vo, T.-K. Nguyen, S.-E. Kim, A review of continuum mechanics models for size-dependent analysis of beams and plates, Composite Structures. 177 (2017) 196–219.
[65] H. Askes, I.M. Gitman, Review and critique of the stress gradient elasticity theories of Eringen and Aifantis, in: Mechanics of Generalized Continua, Springer, 2010: pp. 203–210.
[66] H. Askes, E.C. Aifantis, Gradient elasticity in statics and dynamics: an overview of formulations, length scale identification procedures, finite element implementations and new results, International Journal of Solids and Structures. 48 (2011) 1962–1990.

[67] E.C. Aifantis, On the role of gradients in the localization of deformation and fracture, International Journal of Engineering Science. 30 (1992) 1279–1299.
[68] I.G. Kevrekidis, C.W. Gear, G. Hummer, Equation-free: The computer-aided analysis of complex multiscale systems, AIChE Journal. 50 (2004) 1346–1355.
[69] B.N. Cox, H. Gao, D. Gross, D. Rittel, Modern topics and challenges in dynamic fracture, Journal of the Mechanics and Physics of Solids. 53 (2005) 565–596.
[70] H. Talebi, M. Silani, S.P. Bordas, P. Kerfriden, T. Rabczuk, A computational library for multiscale modeling of material failure, Computational Mechanics. 53 (2014) 1047–1071.
[71] M.J. Buehler, H. Gao, Modeling dynamic fracture using large-scale atomistic simulations, Dynamic Fracture Mechanics. (2006) 1.
[72] F.F. Abraham, R. Walkup, H. Gao, M. Duchaineau, T.D. De La Rubia, M. Seager, Simulating materials failure by using up to one billion atoms and the world's fastest computer: Work-hardening, Proceedings of the National Academy of Sciences. 99 (2002) 5783–5787.
[73] P. Aubertin, J. Réthoré, R. de Borst, A coupled molecular dynamics and extended finite element method for dynamic crack propagation, International Journal for Numerical Methods in Engineering. 81 (2010) 72–88.
[74] R. Gracie, T. Belytschko, Concurrently coupled atomistic and XFEM models for dislocations and cracks, International Journal for Numerical Methods in Engineering. 78 (2009) 354–378.
[75] P. Aubertin, J. Réthoré, R. De Borst, Energy conservation of atomistic/continuum coupling, International Journal for Numerical Methods in Engineering. 78 (2009) 1365–1386.
[76] K. Fackeldey, Challenges in atomistic-to-continuum coupling, Mathematical Problems in Engineering. 2015 (2015).
[77] A.C. Eringen, D. Edelen, On nonlocal elasticity, International Journal of Engineering Science. 10 (1972) 233–248.
[78] R. Maranganti, P. Sharma, Length scales at which classical elasticity breaks down for various materials, Physical Review Letters. 98 (2007) 195504.
[79] Z.P. Bažant, M. Jirásek, Nonlocal integral formulations of plasticity and damage: survey of progress, Journal of Engineering Mechanics. 128 (2002) 1119–1149.
[80] J. Reddy, S. Pang, Nonlocal continuum theories of beams for the analysis of carbon nanotubes, Journal of Applied Physics. 103 (2008) 023511.
[81] F. Bobaru, W. Hu, The meaning, selection, and use of the peridynamic horizon and its relation to crack branching in brittle materials, International Journal of Fracture. 176 (2012) 215–222.
[82] O. Weckner, S.A. Silling, Determination of nonlocal constitutive equations from phonon dispersion relations, International Journal for Multiscale Computational Engineering. 9 (2011).
[83] W. Hu, Y.D. Ha, F. Bobaru, S.A. Silling, The formulation and computation of the nonlocal J-integral in bond-based peridynamics, International Journal of Fracture. 176 (2012) 195–206.
[84] S.A. Silling, E. Askari, A meshfree method based on the peridynamic model of solid mechanics, Computers & Structures. 83 (2005) 1526–1535.
[85] M. Zimmermann, A continuum theory with long-range forces for solids, (2005).
[86] Y.D. Ha, F. Bobaru, Studies of dynamic crack propagation and crack branching with peridynamics, International Journal of Fracture. 162 (2010) 229–244.
[87] F. Bobaru, Y.D. Ha, Adaptive refinement and multiscale modeling in 2D peridynamics, (2011).

[88] F. Bobaru, M. Yang, L.F. Alves, S.A. Silling, E. Askari, J. Xu, Convergence, adaptive refinement, and scaling in 1D peridynamics, International Journal for Numerical Methods in Engineering. 77 (2009) 852–877.
[89] H. Ren, X. Zhuang, T. Rabczuk, Dual-horizon peridynamics: A stable solution to varying horizons, Computer Methods in Applied Mechanics and Engineering. 318 (2017) 762–782.
[90] H. Ren, X. Zhuang, Y. Cai, T. Rabczuk, Dual-horizon peridynamics, International Journal for Numerical Methods in Engineering. 108 (2016) 1451–1476.
[91] D. Dipasquale, M. Zaccariotto, U. Galvanetto, Crack propagation with adaptive grid refinement in 2D peridynamics, International Journal of Fracture. 190 (2014) 1–22.
[92] E. Emmrich, O. Weckner, The peridynamic equation of motion in non-local elasticity theory, in: 2006.
[93] S.A. Silling, O. Weckner, E. Askari, F. Bobaru, Crack nucleation in a peridynamic solid, International Journal of Fracture. 162 (2010) 219–227.
[94] S.A. Silling, Dynamic fracture modeling with a meshfree peridynamic code, Computational Fluid and Solid Mechanics. 2003 (2003) 641–644.
[95] S.A. Silling, M. Zimmermann, R. Abeyaratne, Deformation of a peridynamic bar, Journal of Elasticity. 73 (2003) 173–190.
[96] Y.D. Ha, F. Bobaru, Studies of dynamic crack propagation and crack branching with peridynamics, International Journal of Fracture. 162 (2010) 229–244.
[97] E. Oterkus, E. Madenci, O. Weckner, S. Silling, P. Bogert, A. Tessler, Combined finite element and peridynamic analyses for predicting failure in a stiffened composite curved panel with a central slot, Composite Structures. 94 (2012) 839–850.
[98] D. De Meo, N. Zhu, E. Oterkus, Peridynamic Modeling of Granular Fracture in Polycrystalline Materials, Journal of Engineering Materials and Technology. (2016).
[99] E. Askari, F. Bobaru, R.B. Lehoucq, M.L. Parks, S.A. Silling, O. Weckner, Peridynamics for multiscale materials modeling, in: Journal of Physics: Conference Series, IOP Publishing, 2008: p. 012078.
[100] D. De Meo, C. Diyaroglu, N. Zhu, E. Oterkus, M.A. Siddiq, Modelling of stress-corrosion cracking by using peridynamics, International Journal of Hydrogen Energy. 41 (2016) 6593–6609.
[101] S.R. Chowdhury, P. Roy, D. Roy, J. Reddy, A peridynamic theory for linear elastic shells, International Journal of Solids and Structures. 84 (2016) 110–132.
[102] C. Diyaroglu, E. Oterkus, S. Oterkus, E. Madenci, Peridynamics for bending of beams and plates with transverse shear deformation, International Journal of Solids and Structures. 69 (2015) 152–168.
[103] M. Taylor, D.J. Steigmann, A two-dimensional peridynamic model for thin plates, Mathematics and Mechanics of Solids. 20 (2015) 998–1010.
[104] J. O'Grady, J. Foster, Peridynamic plates and flat shells: A non-ordinary, state-based model, International Journal of Solids and Structures. 51 (2014) 4572–4579.
[105] R.W. Macek, S.A. Silling, Peridynamics via finite element analysis, Finite Elements in Analysis and Design. 43 (2007) 1169–1178.
[106] S.A. Silling, M. Epton, O. Weckner, J. Xu, E. Askari, Peridynamic states and constitutive modeling, Journal of Elasticity. 88 (2007) 151–184.
[107] W. Gerstle, N. Sau, S. Silling, Peridynamic modeling of concrete structures, Nuclear Engineering and Design. 237 (2007) 1250–1258.
[108] F. Han, G. Lubineau, Y. Azdoud, Adaptive coupling between damage mechanics and peridynamics: a route for objective simulation of material degradation up to complete failure, Journal of the Mechanics and Physics of Solids. (2016).

[109] H. Ren, X. Zhuang, Y. Cai, T. Rabczuk, Dual-horizon peridynamics, International Journal for Numerical Methods in Engineering. 108 (2016) 1451–1476.
[110] T. Belytschko, J.-H. Song, Coarse-graining of multiscale crack propagation, International Journal for Numerical Methods in Engineering. 81 (2010) 537–563.
[111] V.P. Nguyen, M. Stroeven, L.J. Sluys, Multiscale continuous and discontinuous modeling of heterogeneous materials: a review on recent developments, Journal of Multiscale Modelling. 3 (2011) 229–270.
[112] O. Lloberas-Valls, D.J. Rixen, A. Simone, L.J. Sluys, Multiscale domain decomposition analysis of quasi-brittle heterogeneous materials, International Journal for Numerical Methods in Engineering. 89 (2012) 1337–1366.
[113] A. Shojaei, M. Zaccariotto, U. Galvanetto, Coupling of 2D discretized Peridynamics with a meshless method based on classical elasticity using switching of nodal behaviour, Engineering Computations. (2017).
[114] M.F. Horstemeyer, Multiscale modeling: a review, in: Practical Aspects of Computational Chemistry, Springer, 2009: pp. 87–135.
[115] R.E. Miller, E.B. Tadmor, A unified framework and performance benchmark of fourteen multiscale atomistic/continuum coupling methods, Modelling and Simulation in Materials Science and Engineering. 17 (2009) 053001.
[116] B. Kilic, E. Madenci, Coupling of peridynamic theory and the finite element method, Journal of Mechanics of Materials and Structures. 5 (2010) 707–733.
[117] M. Zaccariotto, T. Mudric, D. Tomasi, A. Shojaei, U. Galvanetto, Coupling of FEM meshes with Peridynamic grids, Computer Methods in Applied Mechanics and Engineering. 330 (2018) 471–497.
[118] U. Galvanetto, T. Mudric, A. Shojaei, M. Zaccariotto, An effective way to couple FEM meshes and Peridynamics grids for the solution of static equilibrium problems, Mechanics Research Communications. 76 (2016) 41–47.
[119] P. Guidault, T. Belytschko, Bridging domain methods for coupled atomistic–continuum models with L2 or H1 couplings, International Journal for Numerical Methods in Engineering. 77 (2009) 1566–1592.
[120] P.T. Bauman, H.B. Dhia, N. Elkhodja, J.T. Oden, S. Prudhomme, On the application of the Arlequin method to the coupling of particle and continuum models, Computational Mechanics. 42 (2008) 511–530.
[121] W. Liu, J.-W. Hong, A coupling approach of discretized peridynamics with finite element method, Computer Methods in Applied Mechanics and Engineering. 245 (2012) 163–175.
[122] M. Xu, T. Belytschko, Conservation properties of the bridging domain method for coupled molecular/continuum dynamics, International Journal for Numerical Methods in Engineering. 76 (2008) 278–294.
[123] P. Seleson, S. Beneddine, S. Prudhomme, A force-based coupling scheme for peridynamics and classical elasticity, Computational Materials Science. 66 (2013) 34–49.
[124] B. Kilic, E. Madenci, Coupling of peridynamic theory and the finite element method, Journal of Mechanics of Materials and Structures. 5 (2010) 707–733.
[125] F. Han, G. Lubineau, Coupling of nonlocal and local continuum models by the Arlequin approach, International Journal for Numerical Methods in Engineering. 89 (2012) 671–685.
[126] H.B. Dhia, G. Rateau, The Arlequin method as a flexible engineering design tool, International Journal for Numerical Methods in Engineering. 62 (2005) 1442–1462.
[127] M. Di Paola, G. Failla, M. Zingales, The mechanically-based approach to 3D non-local linear elasticity theory: Long-range central interactions, International Journal of Solids and Structures. 47 (2010) 2347–2358.

[128] G. Lubineau, Y. Azdoud, F. Han, C. Rey, A. Askari, A morphing strategy to couple non-local to local continuum mechanics, Journal of the Mechanics and Physics of Solids. 60 (2012) 1088–1102.
[129] A. Shojaei, T. Mudric, M. Zaccariotto, U. Galvanetto, A coupled meshless finite point/Peridynamic method for 2D dynamic fracture analysis, International Journal of Mechanical Sciences. 119 (2016) 419–431.
[130] M. Zaccariotto, D. Tomasi, U. Galvanetto, An enhanced coupling of PD grids to FE meshes, Mechanics Research Communications. 84 (2017) 125–135.
[131] W. Sun, J. Fish, Superposition-based coupling of peridynamics and finite element method, Computational Mechanics. 64 (2019) 231–248.
[132] S.A. Silling, F. Bobaru, Peridynamic modeling of membranes and fibers, International Journal of Non-Linear Mechanics. 40 (2005) 395–409.
[133] S.A. Silling, Linearized theory of peridynamic states, Journal of Elasticity. 99 (2010) 85–111.
[134] A. Agwai, I. Guven, E. Madenci, Predicting crack propagation with peridynamics: a comparative study, International Journal of Fracture. 171 (2011) 65–78.
[135] I.N. Giannakeas, T.K. Papathanasiou, H. Bahai, Simulation of thermal shock cracking in ceramics using bond-based peridynamics and FEM, Journal of the European Ceramic Society. 38 (2018) 3037–3048.
[136] B. Kilic, E. Madenci, Peridynamic theory for thermomechanical analysis, IEEE Transactions on Advanced Packaging. 33 (2010) 97–105.
[137] B. Kilic, E. Madenci, Prediction of crack paths in a quenched glass plate by using peridynamic theory, International Journal of Fracture. 156 (2009) 165–177.
[138] S. Oterkus, E. Madenci, A. Agwai, Fully coupled peridynamic thermomechanics, Journal of the Mechanics and Physics of Solids. 64 (2014) 1–23.
[139] S.F. Henke, S. Shanbhag, Mesh sensitivity in peridynamic simulations, Computer Physics Communications. 185 (2014) 181–193.
[140] W. Liu, J.W. Hong, Discretized peridynamics for linear elastic solids, Computational Mechanics. 50 (2012) 579–590.
[141] Y.D. Ha, F. Bobaru, Characteristics of dynamic brittle fracture captured with peridynamics, Engineering Fracture Mechanics. 78 (2011) 1156–1168.
[142] W. Hu, Y.D. Ha, F. Bobaru, S.A. Silling, The formulation and computation of the nonlocal J-integral in bond-based peridynamics, International Journal of Fracture. 176 (2012) 195–206.
[143] Q.V. Le, F. Bobaru, Surface corrections for peridynamic models in elasticity and fracture, Computational Mechanics. (2017) 1–20.
[144] W. Gerstle, N. Sau, S.A. Silling, Peridynamic modeling of plain and reinforced concrete structures, in: SMiRT18, Int. Conf. Structural Mech. Reactor Technol, 2005.
[145] B. Kilic, E. Madenci, An adaptive dynamic relaxation method for quasi-static simulations using the peridynamic theory, Theoretical and Applied Fracture Mechanics. 53 (2010) 194–204.
[146] Q. Le, W. Chan, J. Schwartz, A two-dimensional ordinary, state-based peridynamic model for linearly elastic solids, International Journal for Numerical Methods in Engineering. 98 (2014) 547–561.
[147] D. Levy, Introduction to numerical analysis, Department of Mathematics and Center for Scientific Computation and Mathematical Modeling, CSCAMM, University of Maryland. (2010).
[148] D.J. Littlewood, Roadmap for peridynamic software implementation, SAND Report, Sandia National Laboratories, Albuquerque, NM and Livermore, CA. (2015).

[149] K. Chopra Anil, Dynamics of structures, Theory and Application to Earthquake Engineering. Prentice Hall, New Jersey. (1995).
[150] K.F. Graff, Wave motion in elastic solids, Courier Corporation, 2012.
[151] S.S. Rao, F.F. Yap, Mechanical vibrations, Prentice Hall Upper Saddle River, 2011.
[152] T.J. Hughes, The finite element method: linear static and dynamic finite element analysis, Courier Corporation, 2012.
[153] Y. Fung, P. Tong, X. Chen, Classical and computational solid mechanics, World Scientific Publishing Company, 2017.
[154] K.-J. Bathe, Finite element procedures, Klaus-Jurgen Bathe, 2006.
[155] N. Moës, J. Dolbow, T. Belytschko, A finite element method for crack growth without remeshing, International Journal for Numerical Methods in Engineering. 46 (1999) 131–150.
[156] Z. Zhuang, Z. Liu, B. Cheng, J. Liao, Extended Finite Element Method: Tsinghua University Press Computational Mechanics Series, Academic Press, 2014.
[157] T. Belytschko, C. Parimi, N. Moës, N. Sukumar, S. Usui, Structured extended finite element methods for solids defined by implicit surfaces, International Journal for Numerical Methods in Engineering. 56 (2003) 609–635.
[158] T. Belytschko, N. Moës, S. Usui, C. Parimi, Arbitrary discontinuities in finite elements, International Journal for Numerical Methods in Engineering. 50 (2001) 993–1013.
[159] A.J. Rosakis, Intersonic shear cracks and fault ruptures, Advances in Physics. 51 (2002) 1189–1257.
[160] J.-H. Song, H. Wang, T. Belytschko, A comparative study on finite element methods for dynamic fracture, Computational Mechanics. 42 (2008) 239–250.
[161] C. Daux, N. Moës, J. Dolbow, N. Sukumar, T. Belytschko, Arbitrary branched and intersecting cracks with the extended finite element method, International Journal for Numerical Methods in Engineering. 48 (2000) 1741–1760.
[162] G. Zi, J.-H. Song, E. Budyn, S.-H. Lee, T. Belytschko, A method for growing multiple cracks without remeshing and its application to fatigue crack growth, Modelling and Simulation in Materials Science and Engineering. 12 (2004) 901.
[163] D. Xu, Z. Liu, X. Liu, Q. Zeng, Z. Zhuang, Modeling of dynamic crack branching by enhanced extended finite element method, Computational Mechanics. 54 (2014) 489–502.
[164] T. Belytschko, H. Chen, J. Xu, G. Zi, Dynamic crack propagation based on loss of hyperbolicity and a new discontinuous enrichment, International Journal for Numerical Methods in Engineering. 58 (2003) 1873–1905.
[165] T. Elguedj, A. Gravouil, H. Maigre, An explicit dynamics extended finite element method. Part 1: mass lumping for arbitrary enrichment functions, Computer Methods in Applied Mechanics and Engineering. 198 (2009) 2297–2317.
[166] T. Menouillard, J. Rethore, A. Combescure, H. Bung, Efficient explicit time stepping for the eXtended Finite Element Method (X-FEM), International Journal for Numerical Methods in Engineering. 68 (2006) 911–939.
[167] H.-A. Bahr, H. Balke, M. Kuna, H. Liesk, Fracture analysis of a single edge cracked strip under thermal shock, Theoretical and Applied Fracture Mechanics. 8 (1987) 33–39.
[168] T.K. Papathanasiou, F. Dal Corso, A. Piccolroaz, Thermo-mechanical response FEM simulation of ceramic refractories undergoing severe temperature variations, Journal of the European Ceramic Society. 36 (2016) 2329–2340.
[169] C.P. Jiang, X.F. Wu, J. Li, F. Song, Y.F. Shao, X.H. Xu, P. Yan, A study of the mechanism of formation and numerical simulations of crack patterns in ceramics subjected to thermal shock, Acta Materialia. 60 (2012) 4540–4550.

[170] P.K. Panda, T.S. Kannan, J. Dubois, C. Olagnon, G. Fantozzi, Thermal shock and thermal fatigue study of ceramic materials on a newly developed ascending thermal shock test equipment, Science and Technology of Advanced Materials. 3 (2002) 327–334.
[171] C.B. Carter, M.G. Norton, Ceramic materials: science and engineering, Springer Science & Business Media, 2007.
[172] X. Wu, C. Jiang, F. Song, J. Li, Y. Shao, X. Xu, P. Yan, Size effect of thermal shock crack patterns in ceramics and numerical predictions, Journal of the European Ceramic Society. 35 (2015) 1263–1271.
[173] P. Sicsic, J.-J. Marigo, C. Maurini, Initiation of a periodic array of cracks in the thermal shock problem: a gradient damage modeling, Journal of the Mechanics and Physics of Solids. 63 (2014) 256–284.
[174] J.-C. Han, B.-L. Wang, Thermal shock resistance of ceramics with temperature-dependent material properties at elevated temperature, Acta Materialia. 59 (2011) 1373–1382.
[175] T.J. Lu, N.A. Fleck, The thermal shock resistance of solids, Acta Materialia. 46 (1998) 4755–4768.
[176] Z.P. Bažant, H. Ohtsubo, K. Aoh, Stability and post-critical growth of a system of cooling or shrinkage cracks, International Journal of Fracture. 15 (1979) 443–456.
[177] G.A. Schneider, G. Petzow, Thermal shock and thermal fatigue behavior of advanced ceramics, Springer Science & Business Media, 2013.
[178] I. Jones, Impulse response model of thermal striping for hollow cylindrical geometries, Theoretical and Applied Fracture Mechanics. 43 (2005) 77–88.
[179] H.-A. Bahr, G. Fischer, H.-J. Weiss, Thermal-shock crack patterns explained by single and multiple crack propagation, Journal of Materials Science. 21 (1986) 2716–2720.
[180] G. Carta, I. Jones, M. Brun, N. Movchan, A. Movchan, Crack propagation induced by thermal shocks in structured media, International Journal of Solids and Structures. 50 (2013) 2725–2736.
[181] J. Li, F. Song, C. Jiang, A non-local approach to crack process modeling in ceramic materials subjected to thermal shock, Engineering Fracture Mechanics. 133 (2015) 85–98.
[182] J. Li, F. Song, C. Jiang, Direct numerical simulations on crack formation in ceramic materials under thermal shock by using a non-local fracture model, Journal of the European Ceramic Society. 33 (2013) 2677–2687.
[183] B. Bourdin, J.-J. Marigo, C. Maurini, P. Sicsic, Morphogenesis and propagation of complex cracks induced by thermal shocks, Physical Review Letters. 112 (2014) 014301.
[184] I. Özdemir, W. Brekelmans, M.G. Geers, FE2 computational homogenization for the thermo-mechanical analysis of heterogeneous solids, Computer Methods in Applied Mechanics and Engineering. 198 (2008) 602–613.
[185] M. Nieves, A. Movchan, I. Jones, Asymptotic study of a thermoelastic problem in a semi-infinite body containing a surface-breaking crack and small perforations, The Quarterly Journal of Mechanics & Applied Mathematics. 64 (2011) 349–369.
[186] F. Damhof, W. Brekelmans, M. Geers, Experimental analysis of the evolution of thermal shock damage using transit time measurement of ultrasonic waves, Journal of the European Ceramic Society. 29 (2009) 1309–1322.
[187] A.M. Hofmeister, Thermal diffusivity and thermal conductivity of single-crystal MgO and Al2O3 and related compounds as a function of temperature, Physics and Chemistry of Minerals. 41 (2014) 361–371.
[188] J.G. Hemrick, R.B. Dinwiddie, E.R. Loveland, A. Prigmore, Development of a test technique to determine the thermal diffusivity of large refractory ceramic test specimens, International Journal of Applied Ceramic Technology. 9 (2012) 108–114.

[189] P. Auerkari, Mechanical and physical properties of engineering alumina ceramics, Technical Research Centre of Finland Finland, 1996.
[190] R. Morrell, Handbook of properties of technical and engineering ceramics, Hmso, 1987.
[191] Z. Zhou, F. Song, Y. Shao, S. Meng, C. Jiang, J. Li, Characteristics of the surface heat transfer coefficient for Al 2 O 3 ceramic in water quench, Journal of the European Ceramic Society. 32 (2012) 3029–3034.
[192] W.J. Lee, Y. Kim, E. Case, The effect of quenching media on the heat transfer coefficient of polycrystalline alumina, Journal of Materials Science. 28 (1993) 2079–2083.
[193] J. Webb, K. Jakus, J. Ritter, R-curve and subcritical crack growth behavior at elevated temperatures in coarse grain alumina, Acta Materialia. 44 (1996) 2259–2264.
[194] A. Polyanin, Handbook of linear partial differential equations for engineers and scientists. 2002, Bovs Raton: Chapman&Hall/CRC. (n.d.).
[195] W.D. Kingery, Factors affecting thermal stress resistance of ceramic materials, Journal of the American Ceramic Society. 38 (1955) 3–15.
[196] M. Nieves, A. Movchan, I. Jones, Analytical model of thermal striping for a micro-cracked solid, International Journal of Solids and Structures. 49 (2012) 1189–1194.
[197] R. Becker, R.J. Lucas, An assessment of peridynamics for pre and post failure deformation, Army Research Lab Aberdeen Proving Ground MD Weapons and Materials Research Directorate, 2011.
[198] K. Ravi-Chandar, Dynamic fracture, Elsevier, 2004.
[199] A.J. Rosakis, Intersonic shear cracks and fault ruptures, Advances in Physics. 51 (2002) 1189–1257.
[200] W. Zhang, N. Doynov, M. Wolf, O. Dreibati, R. Ossenbrink, V. Michailov, Investigation of the Thermal Shock Behavior of Ceramic Using a Combination of Experimental Testing and FE-Simulation Methods, Advanced Engineering Materials. 15 (2013) 480–484.
[201] R. Benz, A. Naoumidis, H. Nickel, Thermal shock testing of ceramics with pulsed laser irradiation, Journal of Nuclear Materials. 150 (1987) 128–139.
[202] S. Akiyama, S. Amada, A new method to evaluate the thermal shock resistance of ceramics by laser pulse irradiation, Fusion Science and Technology. 23 (1993) 426–434.
[203] E. Brochen, S. Clasen, E. Dahlem, C. Dannert, Determination of the Thermal Shock Resistance of Refractories, (n.d.).
[204] S. Xiao, T. Belytschko, A bridging domain method for coupling continua with molecular dynamics, Computer Methods in Applied Mechanics and Engineering. 193 (2004) 1645–1669.
[205] P. Guidault, T. Belytschko, On the L2 and the H1 couplings for an overlapping domain decomposition method using Lagrange multipliers, International Journal for Numerical Methods in Engineering. 70 (2007) 322–350.
[206] K. Chopra Anil, Dynamics of structures, Theory and Application to Earthquake Engineering. Prentice Hall, New Jersey. (1995).
[207] F. Bobaru, W. Hu, The meaning, selection, and use of the peridynamic horizon and its relation to crack branching in brittle materials, International Journal of Fracture. 176 (2012) 215–222.
[208] K. Fackeldey, Challenges in atomistic-to-continuum coupling, Mathematical Problems in Engineering. 2015 (2015).
[209] M. Jirásek, Nonlocal theories in continuum mechanics, Acta Polytechnica. 44 (2004).
[210] K. Dayal, Leading-order nonlocal kinetic energy in peridynamics for consistent energetics and wave dispersion, Journal of the Mechanics and Physics of Solids. 105 (2017) 235–253.

[211] Y. Mikata, Analytical solutions of peristatic and peridynamic problems for a 1D infinite rod, International Journal of Solids and Structures. 49 (2012) 2887–2897.
[212] S.N. Butt, J.J. Timothy, G. Meschke, Wave dispersion and propagation in state-based peridynamics, Computational Mechanics. 60 (2017) 725–738.
[213] A. Ben-Menahem, S.J. Singh, Seismic waves and sources, Springer Science & Business Media, 2012.
[214] V.F. Zaitsev, A.D. Polyanin, Handbook of exact solutions for ordinary differential equations, CRC press, 2002.
[215] L. Debnath, D. Bhatta, Integral transforms and their applications, Chapman and Hall/CRC, 2006.
[216] A. Shojaei, U. Galvanetto, T. Rabczuk, A. Jenabi, M. Zaccariotto, A generalized finite difference method based on the Peridynamic differential operator for the solution of problems in bounded and unbounded domains, Computer Methods in Applied Mechanics and Engineering. (2018).
[217] J.-P. Berenger, A perfectly matched layer for the absorption of electromagnetic waves, Journal of Computational Physics. 114 (1994) 185–200.
[218] F. Collino, C. Tsogka, Application of the perfectly matched absorbing layer model to the linear elastodynamic problem in anisotropic heterogeneous media, Geophysics. 66 (2001) 294–307.
[219] R. Matzen, An efficient finite element time-domain formulation for the elastic second-order wave equation: A non-split complex frequency shifted convolutional PML, International Journal for Numerical Methods in Engineering. 88 (2011) 951–973.
[220] S.S. Madsen, S. Krenk, O. Hededal, Perfectly Matched Layer (PML) for transient wave propagation in a moving frame of reference, in: 2013: pp. 4379–4388.
[221] M. Kuzuoglu, R. Mittra, Frequency dependence of the constitutive parameters of causal perfectly matched anisotropic absorbers, IEEE Microwave and Guided Wave Letters. 6 (1996) 447–449.
[222] R.A. Wildman, G.A. Gazonas, A perfectly matched layer for peridynamics in two dimensions, Journal of Mechanics of Materials and Structures. 7 (2013) 765–781.
[223] T. Ni, M. Zaccariotto, Q.-Z. Zhu, U. Galvanetto, Static solution of crack propagation problems in Peridynamics, Computer Methods in Applied Mechanics and Engineering. 346 (2019) 126–151.
[224] M. Dorduncu, A. Barut, E. Madenci, N.D. Phan, Peridynamic augmented XFEM, in: 2017: p. 0656.
[225] E. Madenci, A. Barut, M. Futch, Peridynamic differential operator and its applications, Computer Methods in Applied Mechanics and Engineering. 304 (2016) 408–451.
[226] I.N. Giannakeas, T.K. Papathanasiou, H. Bahai, On the Reflection and Transmission of Waves in a 1D Coupled FE-Peridynamic Model, 6th European Conference on Computational Mechanics (ECCM 6). (2018).
[227] S.A. Silling, R.B. Lehoucq, Peridynamic theory of solid mechanics, Advances in Applied Mechanics. 44 (2010) 73–168.
[228] E. Madenci, S. Oterkus, Ordinary state-based peridynamics for plastic deformation according to von Mises yield criteria with isotropic hardening, Journal of the Mechanics and Physics of Solids. 86 (2016) 192–219.
[229] T.L. Anderson, T. Anderson, Fracture mechanics: fundamentals and applications, CRC press, 2005.
[230] É. Béchet, H. Minnebo, N. Moës, B. Burgardt, Improved implementation and robustness study of the X-FEM for stress analysis around cracks, International Journal for Numerical Methods in Engineering. 64 (2005) 1033–1056.

[231] Y. Azdoud, F. Han, G. Lubineau, The morphing method as a flexible tool for adaptive local/non-local simulation of static fracture, Computational Mechanics. 54 (2014) 711–722.
[232] F. Han, G. Lubineau, Y. Azdoud, A. Askari, A morphing approach to couple state-based peridynamics with classical continuum mechanics, Computer Methods in Applied Mechanics and Engineering. 301 (2016) 336–358.
[233] G. Lubineau, Y. Azdoud, F. Han, C. Rey, A. Askari, A morphing strategy to couple non-local to local continuum mechanics, Journal of the Mechanics and Physics of Solids. 60 (2012) 1088–1102.
[234] I.N. Giannakeas, T.K. Papathanasiou, H. Bahai, Simulation of thermal shock cracking in ceramics using bond-based peridynamics and FEM, Journal of the European Ceramic Society. (2017).
[235] T. Rabczuk, Computational methods for fracture in brittle and quasi-brittle solids: state-of-the-art review and future perspectives, ISRN Applied Mathematics. 2013 (2013).
[236] J. Song, T. Belytschko, Cracking node method for dynamic fracture with finite elements, International Journal for Numerical Methods in Engineering. 77 (2009) 360–385.
[237] K. Ravi-Chandar, Dynamic fracture, Elsevier, 2004.
[238] G.D. Quinn, On terminal crack velocities in glasses, International Journal of Applied Glass Science. 10 (2019) 7–16. https://doi.org/10.1111/ijag.13042.
[239] J. Fish, Multiscale methods: bridging the scales in science and engineering, Oxford University Press on Demand, 2010.
[240] H. Qiao, Q. Yang, W. Chen, C. Zhang, Implementation of the Arlequin method into ABAQUS: Basic formulations and applications, Advances in Engineering Software. 42 (2011) 197–207.
[241] F. Mossaiby, A. Shojaei, M. Zaccariotto, U. Galvanetto, Opencl implementation of a high performance 3d peridynamic model on graphics accelerators, Computers & Mathematics with Applications. 74 (2017) 1856–1870.

Appendix A: Derivation of $G_n(x)$ Expressions

The expressions for function $G_n(x)$, $n = \delta/\Delta x$ that appear in Eq. (5.29) are derived here for $n = 1, 2, 3$ and 4. Consider a series of particles that are used to discretize a 1D bar, as illustrated in Figure A.1. The number of bonds connected to each particle depends on the value n. For simplicity it is assumed that the grid in uniform and a constant micromodulus function is used. This leads to, $\|\boldsymbol{x}_{k-1}-\boldsymbol{x}_k\| = \|\boldsymbol{x}_{k+1}-\boldsymbol{x}_k\| = \Delta x$, , $\|\boldsymbol{x}_{k-2}-\boldsymbol{x}_k\| = \|\boldsymbol{x}_{k+2}-\boldsymbol{x}_k\| = 2\Delta x$, $\|\boldsymbol{x}_{k-3}-\boldsymbol{x}_k\| = \|\boldsymbol{x}_{k+3}-\boldsymbol{x}_k\| = 3\Delta x$, $\|\boldsymbol{x}_{k-4}-\boldsymbol{x}_k\| = \|\boldsymbol{x}_{k+4}-\boldsymbol{x}_k\| = 4\Delta x$, $c_{i,j} = c = \frac{2E}{A\delta^2}$ and $V_i = V$. The equation of motion for a particle can then be written as:

$$\rho\ddot{\boldsymbol{d}}_i = \sum cv_{i,j}\frac{\boldsymbol{d}_j - \boldsymbol{d}_i}{\|\boldsymbol{x}_j-\boldsymbol{x}_i\|}V_j \tag{A.1}$$

where, the volume correction has also been included. Using Eq. (A.1) we write the equation of motion of a particle k for different values of n. Solutions with the form $\boldsymbol{d} = De^{i(\omega t+\kappa)}$ are assumed to extract the dispersion relationship in each case. The following expressions are used:

$$e^{\iota\alpha} + e^{-\iota\alpha} = 2\cos(\alpha) \tag{A.1}$$
$$\cos(2\alpha) = 1 - 2\sin^2(\alpha)$$
$$\sin(2\alpha) = 2\cos(\alpha)\sin(\alpha)$$
$$\sin(3\alpha) = 3\sin(\alpha) - 4\sin^3(\alpha)$$

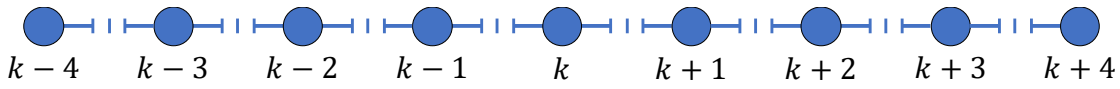

Figure A.1: Particle numbering in a 1D problem.

- $\boldsymbol{n = 1}$

The equation of motion for particle k is written as:

$$\rho\ddot{\boldsymbol{d}}_k = cv_{k-1,k}\frac{\boldsymbol{d}_{k-1} - \boldsymbol{d}_k}{\|\boldsymbol{x}_{k-1}-\boldsymbol{x}_k\|}V_k + cv_{k+1,k}\frac{\boldsymbol{d}_{k+1} - \boldsymbol{d}_k}{\|\boldsymbol{x}_{k+1}-\boldsymbol{x}_k\|}V_k = \frac{C}{2}(\boldsymbol{d}_{k-1} - 2\boldsymbol{d}_k + \boldsymbol{d}_{k+1}) \tag{A.2}$$

where, $v_{k-1,k} = v_{k+1,k} = 0.5$ and $C = cV/\Delta x$. Then using $\boldsymbol{d} = De^{i(\omega t+\kappa x)}$ in the expression above we get:

$$-\omega^2\rho = 0.5C(e^{\iota\kappa\Delta x} - 2 + e^{-\iota\kappa\Delta x}) = 0.5C(2\cos(\kappa\Delta x) - 2) = C(\cos(\kappa\Delta x) - 1)$$
$$= -2C\sin^2\left(\frac{\kappa\Delta x}{2}\right) \tag{A.3}$$

From the last expression we get that:

$$\omega = \sqrt{\frac{2C}{\rho}}\sin\left(\frac{\kappa\Delta x}{2}\right) = \sqrt{\frac{2C}{\rho}}\sin\left(\frac{\kappa\Delta x}{2}\right)G_1\left(\frac{\kappa\Delta x}{2}\right), \tag{A.4}$$

with $G_1\left(\frac{\kappa\Delta x}{2}\right) = 1$.

- $\boldsymbol{n = 2}$

The equation of motion for particle k is written as:

$$\rho\ddot{\boldsymbol{d}}_k = C(0.25\boldsymbol{d}_{k-2} + \boldsymbol{d}_{k-1} - 2.5\boldsymbol{d}_k + \boldsymbol{d}_{k+1} + 0.25\boldsymbol{d}_{k+2})$$
$$= \frac{C}{4}(\boldsymbol{d}_{k-2} + 4\boldsymbol{d}_{k-1} - 10\boldsymbol{d}_k + 4\boldsymbol{d}_{k+1} + \boldsymbol{d}_{k+2}) \tag{A.5}$$

where, $v_{k-2,k} = v_{k+2,k} = 0.5$. Then using $\boldsymbol{d} = De^{i(\omega t+\kappa x)}$ in the expression above we get:

$$-\omega^2\rho = 0.25C(e^{\iota\kappa 2\Delta x} + e^{-\iota\kappa 2\Delta x} + 4e^{\iota\kappa\Delta x} + 4e^{-\iota\kappa\Delta x} - 10)$$
$$= 0.25C(2\cos(\kappa 2\Delta x) - 2 + 8\cos(\kappa\Delta x) - 8)$$
$$= 0.25C(-4\sin^2(2\theta) - 16\sin^2(\theta)) = -C(\sin^2(2\theta) + 4\sin^2(\theta)) \tag{A.6}$$
$$= -C(4\sin^2(\theta)\cos^2(\theta) + 4\sin^2(\theta))$$
$$= -2C\sin^2(\theta)\,(2\cos^2(\theta) + 2)$$

where, $\theta = \frac{\kappa\Delta x}{2}$ was used. From the last expression we get that:

$$\omega = \sqrt{\frac{2C}{\rho}}\sin\left(\frac{\kappa\Delta x}{2}\right)\sqrt{2\cos^2\left(\frac{\kappa\Delta x}{2}\right) + 2} = \sqrt{\frac{2C}{\rho}}\sin\left(\frac{\kappa\Delta x}{2}\right)G_2\left(\frac{\kappa\Delta x}{2}\right), \tag{A.7}$$

with $G_2\left(\frac{\kappa\Delta x}{2}\right) = \sqrt{2\cos^2\left(\frac{\kappa\Delta x}{2}\right) + 2}$.

- $\boldsymbol{n = 3}$

The equation of motion for particle k is written as:

$$\rho\ddot{\boldsymbol{d}}_k = \frac{C}{6}(\boldsymbol{d}_{k-3} + 3\boldsymbol{d}_{k-2} + 6\boldsymbol{d}_{k-1} - 20\boldsymbol{d}_k + 6\boldsymbol{d}_{k+1} + 3\boldsymbol{d}_{k+2} + \boldsymbol{d}_{k+3}) \tag{A.8}$$

where, $v_{k-3,k} = v_{k+3,k} = 0.5$. Then using $\boldsymbol{d} = De^{i(\omega t+\kappa x)}$ in the expression above we get:

$$
\begin{aligned}
-\omega^2\rho &= \frac{C}{6}(e^{\iota\kappa 3\Delta x} + e^{-\iota\kappa 3\Delta x} + 3e^{\iota\kappa 2\Delta x} + 3e^{-\iota\kappa 2\Delta x} + 6e^{\iota\kappa\Delta x} + 6e^{-\iota\kappa\Delta x} - 20) \\
&= \frac{C}{6}(2\cos(\kappa 3\Delta x) - 2 + 6\cos(\kappa 2\Delta x) - 6 + 12\cos(\kappa\Delta x) - 12) \\
&= \frac{C}{6}(-4\sin^2(3\theta) - 12\sin^2(2\theta) - 24\sin^2(\theta)) \\
&= -\frac{2C}{6}(2\sin^2(3\theta) + 6\sin^2(2\theta) + 12\sin^2(\theta))
\end{aligned}
\tag{A.9}
$$

Then, using:

$$
\begin{aligned}
\sin^2(3\theta) &= \sin^2(\theta)\,(16\sin^4(\theta) - 24\sin^2(\theta) + 9) \\
\sin^2(2\theta) &= 4\sin^2(\theta)\cos^2(\theta)
\end{aligned}
\tag{A.10}
$$

in the above we get:

$$
\begin{aligned}
\omega^2\rho = \frac{2C}{6}&(\sin^2(\theta)\,(32\sin^4(\theta) - 48\sin^2(\theta) + 18) + 24\sin^2(\theta)\cos^2(\theta) \\
&+ 12\sin^2(\theta)) \\
&= 2C\sin^2(\theta)\left(\frac{32}{6}\sin^4(\theta) - 8\sin^4(\theta) + 3 + 4\cos^2(\theta) + 2\right)
\end{aligned}
\tag{A.11}
$$

From the last expression we get:

$$
\begin{aligned}
\omega &= \sqrt{\frac{2C}{\rho}}\sin(\theta)\sqrt{\frac{32}{6}\sin^4(\theta) - 8\sin^4(\theta) + 4\cos^2(\theta) + 5} \\
&= \sqrt{\frac{2C}{\rho}}\sin\left(\frac{\kappa\Delta x}{2}\right)G_3\left(\frac{\kappa\Delta x}{2}\right),
\end{aligned}
\tag{A.12}
$$

with $G_3\left(\frac{\kappa\Delta x}{2}\right) = \sqrt{\frac{32}{6}\sin^4(\theta) - 8\sin^4(\theta) + 4\cos^2(\theta) + 5}$.

- $\boldsymbol{n = 4}$

The equation of motion for particle k is written as:

$$
\begin{aligned}
\rho\ddot{\boldsymbol{d}}_k = \frac{C}{24}&(3\boldsymbol{d}_{k-4} + 8\boldsymbol{d}_{k-3} + 12\boldsymbol{d}_{k-2} + 24\boldsymbol{d}_{k-1} - 94\boldsymbol{d}_k + 24\boldsymbol{d}_{k+1} + 12\boldsymbol{d}_{k+2} \\
&+ 8\boldsymbol{d}_{k+3} + 3\boldsymbol{d}_{k+4})
\end{aligned}
\tag{A.13}
$$

where, $v_{k-4,k} = v_{k+4,k} = 0.5$. Then using $\boldsymbol{d} = De^{i(\omega t + \kappa\ )}$ in the expression above we get:

$$
\begin{aligned}
-\omega^2\rho = \frac{C}{24}(&3e^{\iota\kappa 4\Delta x} + 3e^{-\iota\kappa 4\Delta x} - 6 + 8e^{\iota\kappa 3\Delta x} + 8e^{-\iota\kappa 3\Delta x} - 16 + 12e^{\iota\kappa 2\Delta x} \\
&+ 12e^{-\iota\kappa 2\Delta x} - 24 + 24e^{\iota\kappa\Delta x} + 24e^{-\iota\kappa\Delta} - 48) \\
&= \frac{C}{24}(6\cos(\kappa 4\Delta x) - 6 + 16\cos(\kappa 3\Delta x) - 16 + 24\cos(\kappa 2\Delta x) - 24 \\
&+ 48\cos(\kappa\Delta x) - 48) \\
&= \frac{C}{24}(-12\sin^2(4\theta) - 32\sin^2(3\theta) - 48\sin^2(2\theta) - 96\sin^2(\theta))
\end{aligned}
\tag{A.14}
$$

Then using also $\sin^2(4\theta) = 4\sin^2(2\theta)\cos^2(2\theta) = 16\sin^2(\theta)\cos^2(\theta)\cos^2(2\theta)$ we get:

$$
\begin{aligned}
\omega^2\rho = \frac{C}{24}\big(&192\sin^2(\theta)\cos^2(\theta)\cos^2(2\theta) \\
&+ 32\sin^2(\theta)(16\sin^4(\theta) - 24\sin^2(\theta) + 9) + 192\sin^2(\theta)\cos^2(\theta) \\
&+ 96\sin^2(\theta)\big) \\
&= \frac{C}{24}\big(192\sin^2(\theta)\cos^2(\theta)\cos^2(2\theta) \\
&+ \sin^2(\theta)(512\sin^4(\theta) - 768\sin^2(\theta) + 288) \\
&+ 192\sin^2(\theta)\cos^2(\theta) + 96\sin^2(\theta)\big) \\
&= 2C\sin^2(\theta)\left(4\cos^2(\theta)\cos^2(2\theta) + \frac{32}{3}\sin^4(\theta) - 16\sin^2(\theta)\right. \\
&\left. + 4\cos^2(\theta) + 8\right)
\end{aligned}
\tag{A.15}
$$

From the last expression we get:

$$
\begin{aligned}
\omega &= \sqrt{\frac{2C}{\rho}}\sin(\theta)\sqrt{4\cos^2(\theta)\cos^2(2\theta) + \frac{32}{3}\sin^4(\theta) - 16\sin^2(\theta) + 4\cos^2(\theta) + 8} \\
&= \sqrt{\frac{2C}{\rho}}\sin\left(\frac{\kappa\Delta x}{2}\right)G_4\left(\frac{\kappa\Delta x}{2}\right),
\end{aligned}
\tag{A.16}
$$

with $G_4\left(\frac{\kappa\Delta x}{2}\right) = \sqrt{4\cos^2(\theta)\cos^2(2\theta) + \frac{32}{3}\sin^4(\theta) - 16\sin^2(\theta) + 4\cos^2(\theta) + 8}$.